Tumor Necrosis Factor-Regulated Granuloma Formation in Tuberculosis: Multi-Scale Modeling and Experiments

by

Mohammad Fallahi Sichani

A dissertation submitted in partial fulfillment
of the requirements for the degree of
Doctor of Philosophy
(Chemical Engineering)
in The University of Michigan
2012

Doctoral Committee:

Professor Jennifer J. Linderman, Chair
Professor Denise E. Kirschner
Professor Steve L. Kunkel
Assistant Professor Lola Eniola-Adefeso

به نام آن که دل پروانه اوست

Khaju Bridge, Isfahan, Iran (built in 1650)
(http://en.wikipedia.org/wiki/File:Khaju_Bridje_at_night.jpg)

To my mother whose prayers have always followed me and my dreams.

To my father whose support and encouragement has always helped me dream big dreams.

To my sisters and brothers who have always supported me with their love.

Acknowledgements

I would like to thank my advisors, Professor Jennifer Linderman and Professor Denise Kirschner for their support and guidance throughout my graduate work. They have served as models for me in their research excellence, leadership and professional integrity. I am grateful to Professor Steve Kunkel for his support during my experimental research. I am thankful to Professor Lola Eniola-Adefeso for her support as my doctoral committee member. I would like to thank Dr. Simeone Marino for helpful discussions we had on mathematical modeling and sensitivity analysis. Without his expertise, I would not have been able to analyze my computational models comprehensively. I am grateful to Dr. Matthew Schaller for his great help during my experimental work, and Mohammed El-Kebir and Paul Wolberg for their invaluable help with my computational work. Without them I could not have accomplished what I have done. I am grateful to Professor JoAnne Flynn whom I have consulted on this research and without her expertise I would not have been able to tackle such a multi-disciplinary project. I would like to thank Dr. Khamir Mehta and Dr. Amir Haji-Akbari for their help on computational modeling during initial phases of my research. I am thankful to Joe Waliga for management of Movies and Supplementary Materials at http://malthus.micro.med.umich.edu/lab/movies/. I would also like to thank all of the Linderman and Kirschner group members past and present: Rachel Dudek, Nick Cilfone, Laura Chang, and Danielle Trakimas. Finally, I acknowledge my funding sources for making this work possible: NIH, Rackham International Student and Predoctoral Fellowships.

Table of Contents

List of Figures

Figure

List of Figures (continued)

List of Figures (continued)

List of Tables

Table

List of Appendices

Appendix

Chapter 1

Introduction

1.1 Specific aims and significance of this work

Tuberculosis (TB) granulomas are organized collections of immune cells composed of macrophages, lymphocytes and other cells that form in the lung in response to *Mycobacterium tuberculosis* (Mtb) infection. A granuloma, the pathologic hallmark of TB, serves to focus the host immune response, contain infection and pathology, and provide a niche for the bacillus to persist within the host. If granulomas are capable of inhibiting or killing most of the Mtb present, humans develop a clinically latent infection. However, if granulomas are impaired in function, infection progresses, granulomas enlarge and bacteria seed new granulomas; this results in progressive pathology and disease, i.e. active tuberculosis. In clinical latency, immunologic perturbation at the level of the granuloma can result in reactivation of infection. In humans, there are a variety of granuloma types, even within the lungs of a single host.

Multiple immune factors, including various cells (macrophages, T cells, B cells, neutrophils) and molecules (cytokines, chemokines, effector molecules) control host responses to Mtb infection, including the formation of granulomas. The roles and interactions of these factors within a granuloma are complex and challenging to address by experimental methods alone. One such factor, tumor necrosis factor-α (TNF), is a protein produced primarily by activated monocytes and macrophages. TNF regulates inflammatory immune responses via activating multiple signaling pathways such as the

NF-κB signaling pathway and the apoptotic pathway. A major challenge in studying the role of TNF in immunity to Mtb is that direct measurement of TNF levels and TNF activities within a granuloma is very difficult. Computational approaches, however, can be used to dissect the temporal and spatial aspects of granuloma formation and function. The overall goal of this research is to use a systems biology approach that integrates experimental and computational work to address critical questions necessary to understanding TNF-regulated granuloma formation and function during Mtb infection. Such understanding is essential to development of strategies for prevention and treatment. In particular, this work elucidates mechanisms at multiple biological scales (molecular, cellular and tissue) that control TNF availability and TNF activities within a granuloma in order to understand how a granuloma forms in response to Mtb infection and maintains its structural integrity during the latent infection as well as how treatment with anti-TNF therapies results in TB reactivation. This work is divided into three aims:

Aim 1. ***Identification of key processes that control TNF availability in a TB granuloma:*** Availability of TNF within a TB granuloma has been proposed to have a key role in the protective immunity to Mtb [1], although measuring the true TNF production and consumption within a granuloma is not yet feasible. Further, it is not clear what factors regulate TNF availability in a granuloma. To address these questions, we calculated the TNF concentration in a granuloma using a differential equation model that considers a simple representation of the spatial structure of a granuloma at steady state and includes TNF/TNF receptor (TNFR) binding and trafficking processes (i.e. synthesis, internalization, recycling, and degradation of ligands and receptors)[2]. We measured critical model parameters (identified by sensitivity analysis) using a simple experimental

system for granuloma formation in mice. We induced granuloma formation in mice by injecting Sepharose beads covalently coupled to mycobacterial antigen [3,4]. Model analysis by using the experimental data suggested that there is a TNF concentration gradient in granulomas. The development and detailed analyses of the mathematical model and the experimental granuloma model are described in Chapter 2.

Aim 2. ***Multi-scale computational modeling of TNF-regulated granuloma formation in the lung:*** Identification of a TNF concentration gradient in TB granulomas (as described in Aim 1) leads us to new unanswered questions that are critical to understanding the role of TNF in immunity to Mtb: What factors control such a gradient during a long-term immune response to Mtb infection? How does this gradient regulate TNF-associated processes and ultimately translate to the outcome of infection? What is the impact of dynamics of TNF-associated molecular scale processes on the long-term immune response to Mtb? Finally, are there TNF-level processes that, if targeted, could present new strategies for disease control and therapy? These questions invoke multiple biological scales (in length and time) that are currently difficult to address experimentally. To address these questions, we developed multi-scale computational models that describe the immune response to Mtb in the lung over three biological length scales: molecular (via deterministic ODEs), cellular and tissue (via stochastic agent-based modeling) [5]. Using these models, we predicted the impact of TNFR dynamics and TNF-induced NF-κB signaling dynamics on the outcome of infection at the level of a granuloma. The development and detailed analyses of these models that combine deterministic and stochastic sub-models are described in Chapters 3, 4 and 5. Combining deterministic and stochastic modeling can also be helpful in studying the role of receptor

organization on the cell membrane in determining the outcomes of receptor signaling [6] as described in Chapter 7.

Aim 3. ***Identification of mechanisms by which TNF-neutralizing drugs induce TB reactivation:*** Increased rates of TB reactivation have been reported in humans suffering from inflammatory disorders such as rheumatoid arthritis (RA) and psoriasis and treated with TNF-neutralizing drugs. Higher rates are observed with anti-TNF antibody-type drugs (e.g. infliximab) as compared with the TNF receptor fusion protein-type drug (etanercept). Mechanisms driving differential reactivation rates and differences in drug action are not known. We used the multi-scale computational model of granuloma formation [5] (described in Aim 2) to investigate these mechanisms, as this model provides detailed information regarding the spatial and temporal dynamics of TNF during development of a granuloma in lung tissue. We incorporated TNF-neutralizing drugs and their relevant pharmacokinetic (PK) and pharmacodynamic (PD) properties into the model and identified functional and biochemical characteristics underlying the higher likelihood of TB reactivation that occurs for some TNF-neutralizing drugs. The findings of Aim 3 (Chapter 6) can be used to guide future development of safer anti-TNF drugs for inflammatory disease treatment.

1.2 Experimental background

1.2.1 Tuberculosis and granuloma formation

Tuberculosis (TB), a disease caused by the intracellular pathogen *Mycobacterium tuberculosis* (Mtb), is responsible for 2-3 million deaths per year. In the presence of an effective immune response, only 5-10% of infected people develop clinical signs of

active TB (known as primary TB). However, immunological testing provides evidence of a state of latent infection, with no clinical symptoms, in one third of the world population [7]. Latent TB represents a steady state in which the host controls the infection but is unable to clear it, allowing bacteria to survive at relatively constant, but low levels [8]. Latent infection may reactivate to active disease (reactivation TB) with an average 10% per lifetime frequency, as a result of, for example, age, impaired immunity (as in the case of HIV co-infection), malnutrition, or anti-inflammatory drug administration that interferes with host immunity [9-11].

Mtb is inhaled as droplets from the atmosphere, taken up by phagocytic cells such as alveolar macrophages and dendritic cells and transported across the alveolar epithelium into the lung. Although many bacilli may be destroyed by alveolar macrophages, a fraction of bacilli may survive and begin to replicate in macrophages, initiating an inflammatory response that involves recruitment of additional macrophages and other immune cells to site of infection (Fig. 1.1). Dendritic cells that engulf bacteria migrate to the local lymph nodes and bronchus-associated lymphoid tissue, where they present the processed antigens to T cells [12]. In the lymph node, the T cell response takes at least 2 weeks to be primed [13-15]. Priming is defined as the stimulation of naïve T cells as a result of presentation of antigens by antigen-presenting cells (e.g. dendritic cells). Primed T cells then migrate to the lung and are recruited to site of infection under the influence of chemokines released by infected macrophages and dendritic cells [16,17]. T cells in the lung then contribute to killing of infected macrophages (by cytotoxic T cells) or to activating macrophages to efficiently kill extracellular and intracellular bacteria.

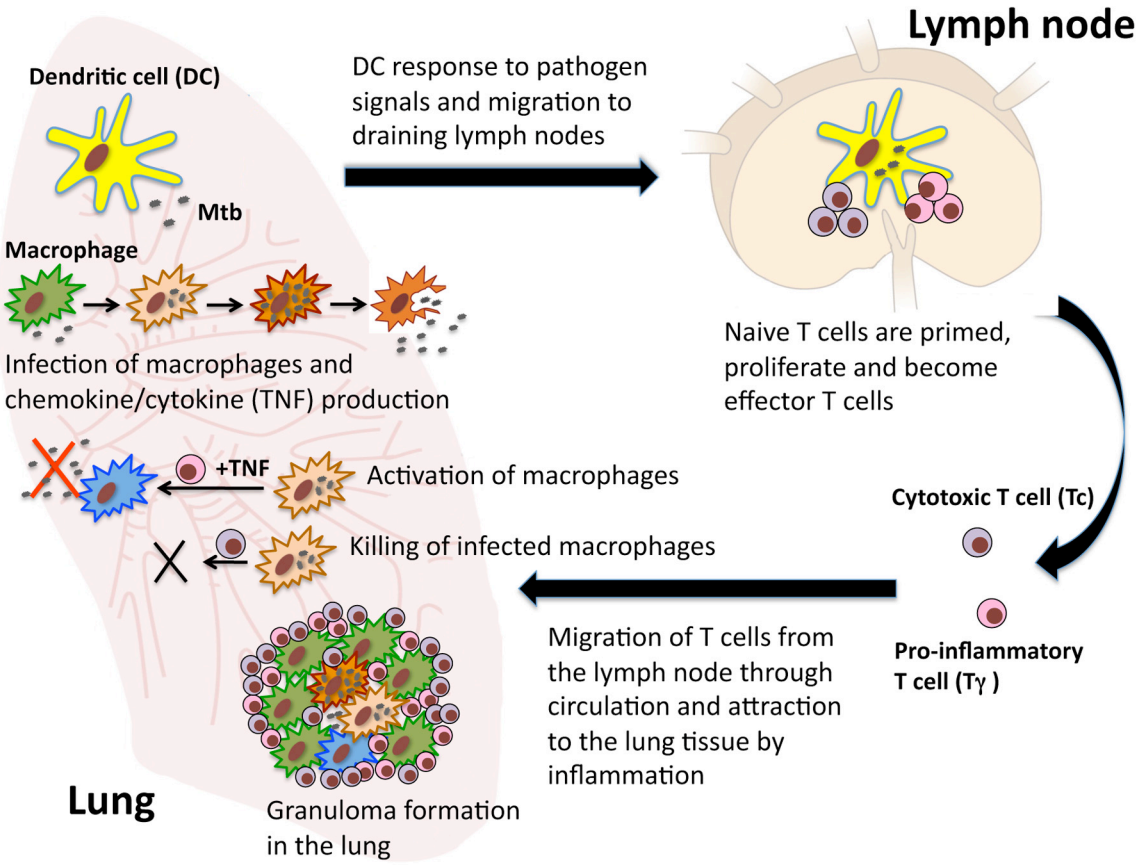

Fig. 1.1 A schematic overview of the immune response initiated as a result of Mtb infection. See text for detailed description of immunological processes involved in immune response to Mtb.

A key outcome of Mtb infection that arises as a result of the immune response within the host is the formation of aggregates of immune cells and bacteria called granulomas in the lungs. The granuloma is known as the pathological hallmark of TB. Granulomas initially form as a result of macrophage responses, including recruitment of macrophages to site of infection, bacteria uptake by macrophages and dispersion of bacteria in tissue due to death of infected macrophages [18]. This stage of infection is generally accompanied by bacterial expansion until the T cell response is initiated. The initiation of the antigen-specific T cell response and recruitment of CD4+ effector T cells (pro-inflammatory T cells, or T_γ cells) and CD8+ effector T cells (cytotoxic T cell, or T_c cells) to site of infection then may halt bacteria growth, leading to control of infection in

granulomas [19,20]. TB granulomas, especially in humans as well as guinea pig and non-human primate models, form as organized spherical structures composed of a core of bacteria, macrophages and dendritic cells surrounded by a ring of lymphocytes, including T cells and B cells [21-27]. The classic caseous granuloma observed in humans and monkeys may also include an area of dead tissue (grossly resembling cheese). Granulomas act to immunologically restrain and physically contain Mtb infection. Latent and active TB in humans comprise a heterogeneous mixture of granulomas (for review, see [28]) that provide a range of physiological microenvironments associated with bacterial replication, persistence and killing (Fig. 1.2). Understanding and dissecting mechanisms, both host and bacterial, that occur during granuloma formation and function and within the different types of granulomas will lead to a better understanding of TB. This in turn will direct development of new therapeutic and preventive strategies to treat this complex disease [29,30].

1.2.2 Key cellular and molecular players in a granuloma

Advances made during the past decade revealed an extensive complexity and a wide range of immune components involved in the immune response to Mtb. These components include various immune cells (e.g. CD4+ and CD8+ T cells), chemokines (e.g. CCL2, CCL5, CXCL9 and CXCL10), and cytokines (e.g. IFN-γ, TNF and IL-10) that play key roles in control of granuloma formation and function during the immune response to Mtb (reviewed in [11,16,21,31-33]). The precise roles and functions of these cells and molecules are still being defined.

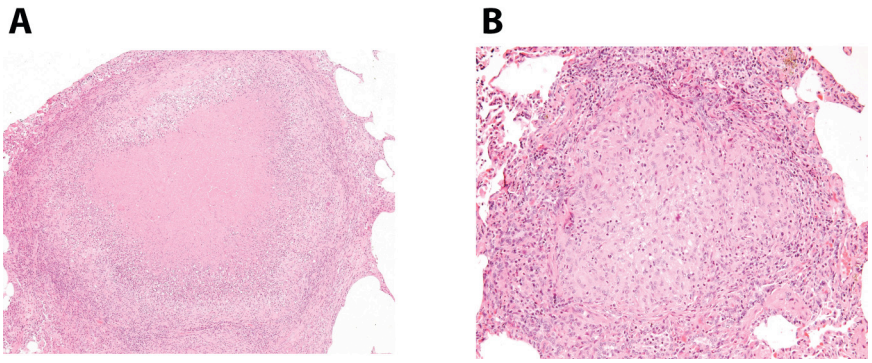

Fig. 1.2 Microscopic histopathology images of different types of tuberculosis granulomas from lungs of monkeys infected with Mtb. (A) A caseous granuloma consisting of a central area of caseum surrounded by a mantle of epithelioid macrophages and peripherally located cuff of lymphocytes from a monkey with active disease, 5x H&E. (B) A well-circumscribed non-necrotizing (solid cellular) granuloma consisting of a core of epithelioid macrophages and peripheral lymphocytes from a monkey with active disease 5X H&E. Granuloma images are taken from [34]**.**

Various experimental models and clinical observations established the important role of CD4+ and CD8+ T cells in defense against TB, although the mechanisms by which these cells provide protection are not completely understood. CD4+ T cells recognize foreign peptides in the context of the major histocompatibility complex (MHC) class II membrane molecules presented by dendritic cells and macrophages. The primary effector function of CD4+ T cells is believed to be production of IFN-γ that contributes to activation of macrophages and elimination of bacteria [35,36]. Besides producing IFN-γ and possibly other cytokines, these cells may contribute to controlling Mtb infection in other ways such as induction of apoptosis in infected macrophages [11,37,38]. CD8+ T cells have also been found to be associated with the granulomatous response. This subset of T cells recognizes foreign antigens degraded within the cytoplasm of dendritic cells or macrophages and presented on the cell membrane in the context of MHC class I antigens. CD8+ T cells can produce cytokines and act as cytotoxic cells. CD8+ T cells take advantage of an antimicrobial pathway mediated by perforin and granulysin that

contributes to lysis of infected macrophages and killing of intracellular bacteria [39]. Current knowledge of the relevance of the perforin/granulysin pathway *in vivo* is limited, as mice apparently do not have a gene or homolog for granulysin. The role of B cells in TB remain controversial, with some studies supporting that these cells are important contributors to protection [40]. The pro-inflammatory cytokine TNF is produced by a variety of immune cells, especially infected and activated macrophages and pro-inflammatory T cells, and functions as a critical component of the immune response to Mtb [41,42].

1.2.3 TNF biology and its role in the immune response to Mtb

TNF is expressed as a 26 kDa membrane-bound precursor protein (membrane-bound TNF or mTNF) which can be cleaved by proteolytic activity of a metalloproteinase TNF-α converting enzyme (TACE) and released as a 17 kDa subunit (soluble TNF or sTNF) to extracellular spaces [43,44]. Both sTNF and mTNF are trimeric in their mature bioactive form [45]. The wide range of TNF activities is explained by the presence of two types of TNF receptors on cell membranes: TNF receptor type 1 (TNFR1; also referred to as p55 or CD120a) and TNF receptor type 2 (TNFR2; also called p75 or CD120b) [46]. TNFR1 is constitutively expressed on almost all nucleated cell types, whereas TNFR2 is typically expressed on immune cells [47]. While mTNF activates both TNF receptors, sTNF has been shown to predominantly stimulate TNFR1 and has limited signaling capacities on TNFR2. This difference has been attributed to the difference in the stability (half-life) of the ligand/receptor complexes [48-51].

The binding of TNF to TNFR1 induces a number of intracellular events that ultimately result in activation of the two major transcription factors, NF-κB and c-Jun that are responsible for the inducible expression of genes important for a wide range of cellular activities, including immune and inflammatory responses [52]. Stimulation of TNFR1 can also lead to activation of the caspase-mediated apoptotic pathway, in particular when NF-κB pathway is compromised [47,53]. The binding of TNF to TNFR2 can also activate the NF-κB signaling pathway. However, TNFR2 lacks the ability to directly activate the apoptotic pathway [54].

TNF has been identified as one of the important mediators of protective immunity to intracellular pathogens including mycobacteria. The protective role of TNF has been mostly attributed to the soluble form (sTNF) and its interaction with TNFR1. However, mice expressing a non-cleavable mTNF mutant have been shown to be able to efficiently induce a cell-mediated immune response with development of granulomas in response to *Mycobacterium bovis* BCG, while all TNF-deficient mice have succumbed to infection. The protective effect of mTNF has been shown to be mediated through TNFR2 signaling [55]. On the other hand, although these mice have been reported to show higher survival and enhanced resistance than TNF-deficient mice to Mtb, they have ultimately died from infection [55,56]. Another study on the role of TNF in the immunologic maintenance of Mtb infection within pulmonary granulomas in mice has indicated that mTNF on cells from the lungs of infected mice are transient and quickly cleaved by TACE [57]. This finding highlights the role of sTNF in the immune response against Mtb.

TNF functions as part of the immune response to Mtb infection via several mechanisms. TNF (in conjunction with the cytokine IFN-γ) induces macrophage

activation to kill bacteria [58-60], enhances immune cell recruitment to site of infection [61], and augments chemokine expression by macrophages through activation of the NF-κB signaling pathway [62]. TNF can also mediate cell death via inducing the caspase-mediated apoptotic pathway [63,64]. Experimental data identifying the roles of TNF in immunity to Mtb include: TNF knockout/neutralization experiments in mice and monkeys [1,41,65,66], and TNF receptor 1 (TNFR1) knockout experiments in mice [41]. The use of TNF inhibitors as treatment for inflammatory diseases in humans has also confirmed that TNF is a major player in the protective immune response against TB [67]. The incidence of active TB is increased in patients with rheumatoid arthritis (RA) and psoriasis receiving treatment with TNF inhibitors [67-70]. These observations support a central role for TNF in maintaining immunity to Mtb. However, TNF has numerous functions in the human immune response and sorting out which are the relevant mechanisms is difficult *in vivo*.

1.2.4 Experimental models of tuberculosis granulomas

Experimental animal models of TB are central to our understanding of TB, including the pathogenesis, pathology, and immunology of this disease. A chief advantage of animal models is the ability to obtain samples from the site of disease, i.e. the lung and thoracic lymph nodes, including granulomas. This is extremely challenging in human studies, and a good animal model that is similar to humans can provide an opportunity to assess immunological events involved within the Mtb infection [9]. There are various well-characterized animal models that are susceptible to infection with Mtb and thus can be used for TB research (reviewed in [71]). These models can be selected depending on the

type of research questions being addressed, cost, and availability of reagents and Biosafety Level 3 (BSL3) facilities.

The most commonly used animal model is the mouse. An advantage for using this animal model in TB research is that a great variety of reagents especially genetically modified animals (lacking different molecules, cytokines, or cell types) are available. Pathology in mice includes many elements of human disease such as the cytokine and chemokine pattern associated with the granulomatous response, and the presence of epithelioid cells, and multinucleate giant cells. However, there are obvious differences in the immunopathology of the disease after low-dose aerosol administration with Mtb compared with human disease [27]. Unlike human granulomas, murine granulomas lack calcification, cavitation and caseous necrosis. T cells acquire a peripheral distribution in human granulomas. In mice, however, incoming T cells and B cells drive well into the center of lesions, where they aggregate in large numbers. Further, unlike in humans where latent infection is observed in the majority of cases, there is no true latent infection in mice. Mice become chronically and progressively infected with Mtb, and every infected mouse eventually succumbs to the disease. Thus, studying mouse granulomas as a model for human granulomas can be problematic, since many of the features and microenvironments of human granulomas are absent in mice. These differences may impact on the ability of immune cells to interact and may provide different environmental cues to the bacillus.

In addition to the mouse model infected with mycobacterium, the use of *in vivo* mouse models using non-replicating agents [3,33,72] provide unique insight into processes involved in granuloma formation and function. For example, mycobacterial

antigen-coated beads are used to induce pulmonary granulomas with cytokine and cellular patterns that closely match those in an active mycobacterial infection [3,4,33,73,74]. Although this model does not include live mycobacteria (which definitely can affect the immune response), it is able to provide many of the features of an Mtb lung granulomatous response that can be investigated only over a two-week period without requiring BSL3 facilities.

Guinea pigs have long been recognized as animal models that are highly susceptible to Mtb infection with a shorter time course of infection and a higher speed of granuloma development compared with the standard laboratory mouse models [27]. Thus, they have been used extensively in TB research, especially for vaccine studies [75,76]. The granulomas in guinea pigs include inflammation similar to mice, but also more structured caseous and mineralized granulomas. Lymphocytes in the guinea pig granulomas occupy a more peripheral position, maybe because of the presence of the central caseation. Although there are several elegant studies on the pathologic features of guinea pig granulomas [77-79], the available reagents for immunologic analyses such as cytokine measurement and immunohistochemistry, as well as reagents for *in vivo* manipulation of the host are limited.

Rabbits are also used in TB research [80-83]. For most studies in rabbits, *M. bovis* is used. Rabbits are extremely susceptible to *M. bovis* and the pathology in these animals is remarkably similar to that in human TB lungs. Despite their susceptibility to *M. bovis*, however, rabbits are relatively resistant to many laboratory strains of Mtb. Granulomas with similar organization to human granulomas, with caseous necrosis and cavity

formation are observed in these animals. However, the lack of immune reagents limits this model, as does the size and containment needs of rabbits.

Another useful model for TB that has been developed over the past 15 years is zebrafish. This model has many attractive features [84]. For example, zebrafish embryos are optically transparent. This allows for a variety of unique experimental approaches to study TB pathogenesis, including vital microscopy. Zebrafish develop TB-like disease when infected with *M. marinum*, the closest genetic relative of Mtb. Although, there are differences that may contribute to difficulty in translating the findings to human TB, there are similarities between zebrafish granulomas and human granulomas. Infection of adult zebrafish produces caseous granulomas that are primarily composed of macrophages [18]. The ability to manipulate the fish genetically and to examine the contributions of genes in high-throughput, forward genetic screens has provided valuable insights into the host-pathogen interaction of mycobacterial infections. Further, zebrafish can be infected and monitored during early development when adaptive immunity has not yet developed. This allows us to study the role of innate and adaptive immunity to infection separately.

Non-human primates (NHPs) were used years ago for the study of TB, for both vaccine and drug testing [85]. However, the expense and difficulty in maintaining animals in BSL3 facilities lead to the demise of monkeys as a model for studying TB. In recent years, however, there has been a resurgence of interest in using these animals for TB research, as new data revealed substantial similarities among outcomes of Mtb infection in humans and monkeys [34]. Low dose infection of cynomolgus macaques with Mtb results in the full spectrum of human infection outcomes, from latent to active TB [34,86]. The granulomas can be solid, necrotic, caseous, or cavitory, even within the

same monkey. Furthermore, reactivation of latent Mtb infection in monkeys has been demonstrated after TNF neutralization [1], CD4+ T cell depletion and Simian immunodeficiency virus (SIV) co-infection (as a model of TB and AIDS) [87,88]. There are several attractive features of the macaque as a model of TB. First, this is the only animal model of latent TB. The full spectrum of human pathology is also observed in the macaque, with all varieties of granulomas observed, in both lungs and lymph nodes, and cavity formation [28,34]. Second, the reagents for immunologic and pathologic analysis are readily available and in many cases cross-reactive human reagents can be used. These features make macaque an important and useful model for studying human TB. However, there are several limitations to this model system. The primary limitations are the expense of buying and maintaining monkeys, the difficulties in housing monkeys in BSL3 facilities, the limitations on obtaining monkeys, and the necessarily small sample sizes. Further, there is extensive genetic variability among monkeys, requiring larger cohorts of animals to obtain statistically significant results.

1.3 Computational background

1.3.1 Computational models of tuberculosis granulomas

Experimental models of TB have been and will continue to be successful and necessary tools to exploring infection with Mtb. However, despite decades of research on TB, our understanding of the factors that lead to active, latent, and reactivation TB remain very much incomplete. For example, it is not clear which collection of immune factors is responsible for determining whether an individual develops active or latent TB. One difficulty is that studies in animal models (and also humans) are often focused on only

one or two factors at a time. Although single-component studies (e.g. single-gene knockout models) in animals are necessary, it can be difficult to integrate these studies in the context of a very complex immune response such as TB. In particular, the complexity of granulomas and the immune interactions contributing to granuloma formation and function can be difficult to assess by using only experimental methods. Indeed, integration of data from experimental studies of isolated components is necessary to gain insight into the interplay of various components of the immune response during granuloma formation. Systems biology is an approach whereby such data can be integrated [89]. A critical step toward this goal is to create mathematical and computational models that reflect human biology, providing an opportunity to perform experiments that are not feasible *in vitro* or *in vivo*.

Mathematical and computational modeling provides a unique approach to studying the behavior of complex biological systems. These methods can be used to better explore hypothesized mechanisms, generate and test new hypotheses, run virtual (*in silico*) experiments, interpret data, motivate particular experiments, and suggest new drug targets. A series of mathematical and computational models have been developed to investigate the host response to Mtb infection [2,5,90-101]. In particular, model-based analysis of the formation and function of a TB granuloma contributes to understanding the mechanisms that control the immune response to Mtb [90-93,95,101]. These models complement experimental approaches and can be used to address questions in TB that are difficult or currently impossible to approach experimentally. The high cost and time investment needed to fully explore many interacting immune factors and various outcomes involved within the Mtb-host interactions in an experimental setting are factors

that should promote the use of computational models. Building computational models can also allow us to integrate data derived from experiments on different tissues, different biological scales (e.g. molecular or cellular) and different time scales into a comprehensive picture of the immune response to Mtb.

Differential equation (DE)-based models typically describe a deterministic relationship among several continuously varying quantities (e.g., numbers of cells, concentrations of molecules, etc.) and their rates of change in space and/or time. DE-based models have been developed for studying temporal dynamics of cytokines and effector cells during the immune response to Mtb [96,97,102,103]. These models are based on known interactions of immune cells in the lung during Mtb infection. Experimental data are used to estimate parameter values. When data are not available, uncertainty and sensitivity analyses are used to define parameter spaces. Uncertainty analysis is performed to investigate the uncertainty in the model output that results from uncertainty in input parameter values. Sensitivity analysis is then used to quantify how input uncertainty (e.g., biological variability coupled to unknown ranges of variation for model parameters) affects model outcomes and to identify critical model parameters. Once validated against experimental data, the models are used to make novel predictions about dynamics, progression of infection and potential therapies. Examples of contributions these models have made to our understanding of TB include identifying the critical impact of delays in either dendritic cell migration to the draining lymph node or T cell trafficking to the site of infection on the outcome of infection [102], and identifying the key role of cytokine IL-10 in balancing macrophage phenotypes in the lung and lymph nodes [103]. DE models can also be used to examine spatial aspects of the

immune response, including analysis of the process of granuloma formation and cytokine availability in a granuloma [2,95].

In contrast to DE-based models, agent-based models (ABMs, also known as individual based models) are rule-based models that capture a variety of stochastic and discrete events occurring in the immune system [104-108]. An ABM has the following components: *agents* (e.g. immune cells, bacteria), the *environment* where agents reside (e.g. a two-dimensional grid representing a section of lung tissue), the *rules* that govern the dynamics of agents, including movements, actions and interactions between agents as well as between agents and environment, and *time-scales* on which the rules are executed. In an ABM, the local, possibly stochastic interactions occurring at the level of agents lead to global, system-wide dynamics and emergent spatial and temporal patterns. Hence, ABMs are particularly useful for studying complex systems such as TB granulomas in which cell heterogeneity and spatial interactions are important.

First- and second-generation ABMs have been developed to describe the immune response to Mtb and to identify mechanisms that control granuloma formation and function [90,91]. Next-generation granuloma ABMs have been developed in response to new biological data that indicated the importance of including additional cell types (e.g. effector CD8+ T cells and regulatory T cells), cytokines (e.g. TNF, IL-10), and chemokines (e.g. CCL2, CCL5 and CXCL9) [5,90,101]. These models are the first to track the dynamics of formation and maintenance of a granuloma in space and time, simultaneously providing critical details regarding cellular interactions and molecular concentrations. There are no experimental methods to obtain these detailed, continuous data in primates.

As a complex process, granuloma models include parameters describing a large number of biological events. Hence, it is critical to understand the role that each of these parameters plays in determining how a granuloma functions. A number of useful and powerful tools have been developed to analyze these complex model systems. One approach is to perform *virtual* deletion and depletion experiments that mimic experimental gene knockout or molecule depletion studies [90]. Loss of activity is achieved by setting relevant parameters (e.g. probabilities or rate constants) to zero or raising relevant thresholds to an unattainable level. Virtual deletion refers to the loss of activity from the beginning of simulation and virtual depletion refers to the loss of activity after establishment of a granuloma. A second approach is to use uncertainty and sensitivity analysis techniques that have been adapted for use in agent-based models [109].

1.3.2 Uncertainty and sensitivity analysis

When computational models include parameters describing a large number of known biological processes, it is critical to understand the role that each of these parameters plays in determining output. Sensitivity analysis is a technique to identify critical parameters of a model and quantify how input uncertainty impacts model outputs. Latin hypercube sampling (LHS) is an algorithm that allows multiple parameters to be varied and sampled simultaneously in a computationally efficient manner [110]. It has been shown to be more than one order of magnitude more efficient than random sampling methods [111-113]. Briefly, each input parameter is assigned a range. Each parameter's value range is divided into *N* equal probable segments according to a specified

probability distribution function (e.g. uniform distribution) for that parameter. A random value is then chosen from each segment, so that each parameter becomes a vector of *N* values. The *N* values of the parameter vectors are then randomly paired to generate an *N* by *X* input matrix, where *X* is the number of parameters to be varied. The model simulations are run using each of the *N* parameter sets, generating a vector of *N* solutions (model outputs). Then, we can use statistical techniques to identify parameters that are most important in determining model outputs. For example, correlation coefficients can be calculated to identify parameters whose variation is strongly correlated with variations in an output of interest. For nonlinear monotonic systems, partial rank correlation coefficient (PRCC) is an appropriate choice [111]. PRCC values vary between -1 (perfect negative correlation) and +1 (perfect positive correlation) and can be differentiated based on *p*-values derived from Student's *t* test. The choice of the number of simulations is determined by the desired significance level for the PRCC [110]. LHS sensitivity analysis with PRCC calculation has been particularly adapted for application to ABMs such as the granuloma model [114].

1.4 References

1. Lin PL, Myers A, Smith L, Bigbee C, Bigbee M, et al. (2010) Tumor necrosis factor neutralization results in disseminated disease in acute and latent mycobacterium tuberculosis infection with normal granuloma structure in a cynomolgus macaque model. Arthritis Rheum 62: 340-350.

2. Fallahi-Sichani M, Schaller MA, Kirschner DE, Kunkel SL, Linderman JJ (2010) Identification of key processes that control tumor necrosis factor availability in a tuberculosis granuloma. PLoS Comput Biol 6: e1000778.

3. Chensue SW, Warmington K, Ruth J, Lincoln P, Kuo MC, et al. (1994) Cytokine responses during mycobacterial and schistosomal antigen-induced pulmonary granuloma formation. production of Th1 and Th2 cytokines and relative contribution of tumor necrosis factor. Am J Pathol 145: 1105-1113.

4. Chensue SW, Warmington KS, Ruth JH, Lincoln P, Kunkel SL (1995) Cytokine function during mycobacterial and schistosomal antigen-induced pulmonary granuloma formation. local and regional participation of IFN-gamma, IL-10, and TNF. J Immunol 154: 5969-5976.

5. Fallahi-Sichani M, El-Kebir M, Marino S, Kirschner DE, Linderman JJ (2011) Multiscale computational modeling reveals a critical role for TNF-{alpha} receptor 1 dynamics in tuberculosis granuloma formation. J Immunol 186: 3472-3483.

6. Fallahi-Sichani M, Linderman JJ (2009) Lipid raft-mediated regulation of G-protein coupled receptor signaling by ligands which influence receptor dimerization: A computational study. PLoS One 4: e6604.

7. Mortellaro A, Robinson L, Ricciardi-Castagnoli P (2009) Spotlight on mycobacteria and dendritic cells: Will novel targets to fight tuberculosis emerge?. EMBO Mol Med 1: 19-29.

8. Russell DG, Barry CE,3rd, Flynn JL (2010) Tuberculosis: What we don't know can, and does, hurt us. Science 328: 852-856.

9. Lin PL, Flynn JL (2010) Understanding latent tuberculosis: A moving target. J Immunol 185: 15-22.

10. Russell DG (2007) Who puts the tubercle in tuberculosis?. Nat Rev Microbiol 5: 39-47.

11. Flynn JL (2004) Immunology of tuberculosis and implications in vaccine development. Tuberculosis (Edinb) 84: 93-101.

12. Bhatt K, Hickman SP, Salgame P (2004) Cutting edge: A new approach to modeling early lung immunity in murine tuberculosis. J Immunol 172: 2748-2751.

13. Wolf AJ, Desvignes L, Linas B, Banaiee N, Tamura T, et al. (2008) Initiation of the adaptive immune response to mycobacterium tuberculosis depends on antigen production in the local lymph node, not the lungs. J Exp Med 205: 105-115.

14. Lazarevic V, Nolt D, Flynn JL (2005) Long-term control of mycobacterium tuberculosis infection is mediated by dynamic immune responses. J Immunol 175: 1107-1117.

15. Chackerian AA, Alt JM, Perera TV, Dascher CC, Behar SM (2002) Dissemination of mycobacterium tuberculosis is influenced by host factors and precedes the initiation of T-cell immunity. Infect Immun 70: 4501-4509.

16. Cooper AM (2009) Cell-mediated immune responses in tuberculosis. Annu Rev Immunol 27: 393-422.

17. Lambrecht BN, Prins JB, Hoogsteden HC (2001) Lung dendritic cells and host immunity to infection. Eur Respir J 18: 692-704.

18. Clay H, Volkman HE, Ramakrishnan L (2008) Tumor necrosis factor signaling mediates resistance to mycobacteria by inhibiting bacterial growth and macrophage death. Immunity 29: 283-294.

19. Davis JM, Ramakrishnan L (2009) The role of the granuloma in expansion and dissemination of early tuberculous infection. Cell 136: 37-49.

20. Bold TD, Ernst JD (2009) Who benefits from granulomas, mycobacteria or host?. Cell 136: 17-19.

21. Algood HM, Chan J, Flynn JL (2003) Chemokines and tuberculosis. Cytokine Growth Factor Rev 14: 467-477.

22. Morel PA, Ta'asan S, Morel BF, Kirschner DE, Flynn JL (2006) New insights into mathematical modeling of the immune system. Immunol Res 36: 157-165.

23. Davis JM, Ramakrishnan L (2008) "The very pulse of the machine": The tuberculous granuloma in motion. Immunity 28: 146-148.

24. Tsai MC, Chakravarty S, Zhu G, Xu J, Tanaka K, et al. (2006) Characterization of the tuberculous granuloma in murine and human lungs: Cellular composition and relative tissue oxygen tension. Cell Microbiol 8: 218-232.

25. Ulrichs T, Kosmiadi GA, Trusov V, Jorg S, Pradl L, et al. (2004) Human tuberculous granulomas induce peripheral lymphoid follicle-like structures to orchestrate local host defence in the lung. J Pathol 204: 217-228.

26. Lin PL, Pawar S, Myers A, Pegu A, Fuhrman C, et al. (2006) Early events in mycobacterium tuberculosis infection in cynomolgus macaques. Infect Immun 74: 3790-3803.

27. Turner OC, Basaraba RJ, Frank AA & Orme IM (2003) in *Granulomatous infections and inflammations: cellular and molecular mechanisms,* ed Boros DL (ASM Press, Washington, D.C.), pp 65-84.

28. Flynn JL & Klein E (2010) in *A color atlas of comparative pulmonary tuberculosis histopathology,* eds Leong J, Dartois V & Dick T (CRC Press, Taylor & Francis Publishers, Boca Raton), pp 83-106.

29. Barry CE,3rd, Boshoff HI, Dartois V, Dick T, Ehrt S, et al. (2009) The spectrum of latent tuberculosis: Rethinking the biology and intervention strategies. Nat Rev Microbiol 7: 845-855.

30. Kirschner DE, Young D, Flynn JL (2010) Tuberculosis: Global approaches to a global disease. Curr Opin Biotechnol 21: 524-531.

31. Co DO, Hogan LH, Il-Kim S, Sandor M (2004) T cell contributions to the different phases of granuloma formation. Immunol Lett 92: 135-142.

32. Baumann S, Nasser Eddine A, Kaufmann SH (2006) Progress in tuberculosis vaccine development. Curr Opin Immunol 18: 438-448.

33. Chensue SW & Kunkel SL (2003) in *Granulomatous infections and inflammations: cellular and molecular mechanisms,* ed Boros DL (ASM Press, Washington, D.C.), pp 29-64.

34. Lin PL, Rodgers M, Smith L, Bigbee M, Myers A, et al. (2009) Quantitative comparison of active and latent tuberculosis in the cynomolgus macaque model. Infect Immun 77: 4631-4642.

35. Cooper AM, Dalton DK, Stewart TA, Griffin JP, Russell DG, et al. (1993) Disseminated tuberculosis in interferon gamma gene-disrupted mice. J Exp Med 178: 2243-2247.

36. Flynn JL, Chan J, Triebold KJ, Dalton DK, Stewart TA, et al. (1993) An essential role for interferon gamma in resistance to mycobacterium tuberculosis infection. J Exp Med 178: 2249-2254.

37. Gallegos AM, van Heijst JW, Samstein M, Su X, Pamer EG, et al. (2011) A gamma interferon independent mechanism of CD4 T cell mediated control of M. tuberculosis infection in vivo. PLoS Pathog 7: e1002052.

38. Torrado E, Cooper AM (2011) What do we really know about how CD4 T cells control mycobacterium tuberculosis?. PLoS Pathog 7: e1002196.

39. Stegelmann F, Bastian M, Swoboda K, Bhat R, Kiessler V, et al. (2005) Coordinate expression of CC chemokine ligand 5, granulysin, and perforin in CD8+ T cells provides a host defense mechanism against mycobacterium tuberculosis. J Immunol 175: 7474-7483.

40. Maglione PJ, Chan J (2009) How B cells shape the immune response against mycobacterium tuberculosis. Eur J Immunol 39: 676-686.

41. Flynn JL, Goldstein MM, Chan J, Triebold KJ, Pfeffer K, et al. (1995) Tumor necrosis factor-alpha is required in the protective immune response against mycobacterium tuberculosis in mice. Immunity 2: 561-572.

42. Saunders BM, Briscoe H, Britton WJ (2004) T cell-derived tumour necrosis factor is essential, but not sufficient, for protection against mycobacterium tuberculosis infection. Clin Exp Immunol 137: 279-287.

43. Korner H, Sedgwick JD (1996) Tumour necrosis factor and lymphotoxin: Molecular aspects and role in tissue-specific autoimmunity. Immunol Cell Biol 74: 465-472.

44. Newton RC, Solomon KA, Covington MB, Decicco CP, Haley PJ, et al. (2001) Biology of TACE inhibition. Ann Rheum Dis 60 Suppl 3: iii25-32.

45. Smith RA, Baglioni C (1987) The active form of tumor necrosis factor is a trimer. J Biol Chem 262: 6951-6954.

46. Vandenabeele P, Declercq W, Beyaert R, Fiers W (1995) Two tumour necrosis factor receptors: Structure and function. Trends Cell Biol 5: 392-399.

47. Wajant H, Pfizenmaier K, Scheurich P (2003) Tumor necrosis factor signaling. Cell Death Differ 10: 45-65.

48. Grell M, Douni E, Wajant H, Lohden M, Clauss M, et al. (1995) The transmembrane form of tumor necrosis factor is the prime activating ligand of the 80 kDa tumor necrosis factor receptor. Cell 83: 793-802.

49. Grell M, Wajant H, Zimmermann G, Scheurich P (1998) The type 1 receptor (CD120a) is the high-affinity receptor for soluble tumor necrosis factor. Proc Natl Acad Sci U S A 95: 570-575.

50. Decoster E, Vanhaesebroeck B, Vandenabeele P, Grooten J, Fiers W (1995) Generation and biological characterization of membrane-bound, uncleavable murine tumor necrosis factor. J Biol Chem 270: 18473-18478.

51. Krippner-Heidenreich A, Tubing F, Bryde S, Willi S, Zimmermann G, et al. (2002) Control of receptor-induced signaling complex formation by the kinetics of ligand/receptor interaction. J Biol Chem 277: 44155-44163.

52. Chen G, Goeddel DV (2002) TNF-R1 signaling: A beautiful pathway. Science 296: 1634-1635.

53. Micheau O, Tschopp J (2003) Induction of TNF receptor I-mediated apoptosis via two sequential signaling complexes. Cell 114: 181-190.

54. Till A, Rosenstiel P, Krippner-Heidenreich A, Mascheretti-Croucher S, Croucher PJ, et al. (2005) The met-196 -> arg variation of human tumor necrosis factor receptor 2

(TNFR2) affects TNF-alpha-induced apoptosis by impaired NF-kappaB signaling and target gene expression. J Biol Chem 280: 5994-6004.

55. Allie N, Alexopoulou L, Quesniaux VJ, Fick L, Kranidioti K, et al. (2008) Protective role of membrane tumour necrosis factor in the host's resistance to mycobacterial infection. Immunology 125: 522-534.

56. Olleros ML, Guler R, Vesin D, Parapanov R, Marchal G, et al. (2005) Contribution of transmembrane tumor necrosis factor to host defense against mycobacterium bovis bacillus calmette-guerin and mycobacterium tuberculosis infections. Am J Pathol 166: 1109-1120.

57. Plessner HL, Lin PL, Kohno T, Louie JS, Kirschner D, et al. (2007) Neutralization of tumor necrosis factor (TNF) by antibody but not TNF receptor fusion molecule exacerbates chronic murine tuberculosis. J Infect Dis 195: 1643-1650.

58. Harris J, Hope JC, Keane J (2008) Tumor necrosis factor blockers influence macrophage responses to mycobacterium tuberculosis. J Infect Dis 198: 1842-1850.

59. Gutierrez MG, Mishra BB, Jordao L, Elliott E, Anes E, et al. (2008) NF-kappa B activation controls phagolysosome fusion-mediated killing of mycobacteria by macrophages. J Immunol 181: 2651-2663.

60. Mosser DM, Edwards JP (2008) Exploring the full spectrum of macrophage activation. Nat Rev Immunol 8: 958-969.

61. Zhou Z, Connell MC, MacEwan DJ (2007) TNFR1-induced NF-kappaB, but not ERK, p38MAPK or JNK activation, mediates TNF-induced ICAM-1 and VCAM-1 expression on endothelial cells. Cell Signal 19: 1238-1248.

62. Algood HM, Lin PL, Yankura D, Jones A, Chan J, et al. (2004) TNF influences chemokine expression of macrophages in vitro and that of CD11b+ cells in vivo during mycobacterium tuberculosis infection. J Immunol 172: 6846-6857.

63. Keane J, Shurtleff B, Kornfeld H (2002) TNF-dependent BALB/c murine macrophage apoptosis following mycobacterium tuberculosis infection inhibits bacillary growth in an IFN-gamma independent manner. Tuberculosis (Edinb) 82: 55-61.

64. Keane J, Balcewicz-Sablinska MK, Remold HG, Chupp GL, Meek BB, et al. (1997) Infection by mycobacterium tuberculosis promotes human alveolar macrophage apoptosis. Infect Immun 65: 298-304.

65. Chakravarty SD, Zhu G, Tsai MC, Mohan VP, Marino S, et al. (2008) Tumor necrosis factor blockade in chronic murine tuberculosis enhances granulomatous inflammation and disorganizes granulomas in the lungs. Infect Immun 76: 916-926.

66. Roach DR, Bean AG, Demangel C, France MP, Briscoe H, et al. (2002) TNF regulates chemokine induction essential for cell recruitment, granuloma formation, and clearance of mycobacterial infection. J Immunol 168: 4620-4627.

67. Keane J, Gershon S, Wise RP, Mirabile-Levens E, Kasznica J, et al. (2001) Tuberculosis associated with infliximab, a tumor necrosis factor alpha-neutralizing agent. N Engl J Med 345: 1098-1104.

68. Wallis RS, Broder M, Wong J, Lee A, Hoq L (2005) Reactivation of latent granulomatous infections by infliximab. Clin Infect Dis 41 Suppl 3: S194-8.

69. Keane J (2005) TNF-blocking agents and tuberculosis: New drugs illuminate an old topic. Rheumatology (Oxford) 44: 714-720.

70. Winthrop KL (2006) Risk and prevention of tuberculosis and other serious opportunistic infections associated with the inhibition of tumor necrosis factor. Nat Clin Pract Rheumatol 2: 602-610.

71. Flynn JL, Tsenova L, Izzo A & Kaplan G (2008) in *Handbook of tuberculosis: Immunology and Cell Biology,* eds Kaufmann SHE & Britton WJ (Wiley-VCH, pp 389-417.

72. Bowdish DM, Sakamoto K, Kim MJ, Kroos M, Mukhopadhyay S, et al. (2009) MARCO, TLR2, and CD14 are required for macrophage cytokine responses to mycobacterial trehalose dimycolate and mycobacterium tuberculosis. PLoS Pathog 5: e1000474.

73. Chensue SW, Warmington K, Ruth JH, Lukacs N, Kunkel SL (1997) Mycobacterial and schistosomal antigen-elicited granuloma formation in IFN-gamma and IL-4 knockout mice: Analysis of local and regional cytokine and chemokine networks. J Immunol 159: 3565-3573.

74. Qiu B, Frait KA, Reich F, Komuniecki E, Chensue SW (2001) Chemokine expression dynamics in mycobacterial (type-1) and schistosomal (type-2) antigen-elicited pulmonary granuloma formation. Am J Pathol 158: 1503-1515.

75. Orme IM (2006) Preclinical testing of new vaccines for tuberculosis: A comprehensive review. Vaccine 24: 2-19.

76. Helke KL, Mankowski JL, Manabe YC (2006) Animal models of cavitation in pulmonary tuberculosis. Tuberculosis (Edinb) 86: 337-348.

77. Turner OC, Basaraba RJ, Orme IM (2003) Immunopathogenesis of pulmonary granulomas in the guinea pig after infection with mycobacterium tuberculosis. Infect Immun 71: 864-871.

78. Hoff DR, Ryan GJ, Driver ER, Ssemakulu CC, De Groote MA, et al. (2011) Location of intra- and extracellular M. tuberculosis populations in lungs of mice and guinea pigs during disease progression and after drug treatment. PLoS One 6: e17550.

79. Basaraba RJ (2008) Experimental tuberculosis: The role of comparative pathology in the discovery of improved tuberculosis treatment strategies. Tuberculosis (Edinb) 88 Suppl 1: S35-47.

80. Subbian S, Tsenova L, O'Brien P, Yang G, Koo MS, et al. (2011) Phosphodiesterase-4 inhibition combined with isoniazid treatment of rabbits with pulmonary tuberculosis reduces macrophage activation and lung pathology. Am J Pathol 179: 289-301.

81. Via LE, Lin PL, Ray SM, Carrillo J, Allen SS, et al. (2008) Tuberculous granulomas are hypoxic in guinea pigs, rabbits, and nonhuman primates. Infect Immun 76: 2333-2340.

82. Allison MJ, Zappasodi P, Lurie MB (1962) Host-parasite relationships in natively resistant and susceptible rabbits on quantitative inhalation of tubercle bacilli. their significance for the nature of genetic resistance. Am Rev Respir Dis 85: 553-569.

83. Dannenberg AM (1994) in *Tuberculosis: Pathogenesis, Protection, and Control,* ed Bloom BR (American Society for Microbiology, Washington, D.C.), pp 149-156.

84. Cosma CL, Swaim LE, Volkman H, Ramakrishnan L, Davis JM (2006) Zebrafish and frog models of mycobacterium marinum infection. Curr Protoc Microbiol Chapter 10: Unit 10B.2.

85. Flynn JL (2006) Lessons from experimental mycobacterium tuberculosis infections. Microbes Infect 8: 1179-1188.

86. Capuano SV,3rd, Croix DA, Pawar S, Zinovik A, Myers A, et al. (2003) Experimental mycobacterium tuberculosis infection of cynomolgus macaques closely resembles the various manifestations of human M. tuberculosis infection. Infect Immun 71: 5831-5844.

87. Mattila JT, Diedrich CR, Lin PL, Phuah J, Flynn JL (2011) Simian immunodeficiency virus-induced changes in T cell cytokine responses in cynomolgus macaques with latent mycobacterium tuberculosis infection are associated with timing of reactivation. J Immunol 186: 3527-3537.

88. Diedrich CR, Mattila JT, Klein E, Janssen C, Phuah J, et al. (2010) Reactivation of latent tuberculosis in cynomolgus macaques infected with SIV is associated with early peripheral T cell depletion and not virus load. PLoS One 5: e9611.

89. Fallahi-Sichani M, Marino S, Flynn JL, Linderman JJ & Kirschner DE (in press) in *Systems biology of tuberculosis,* eds McFadden J, Beste D & Kierzek A (Springer), A systems biology approach for understanding granuloma formation and function in tuberculosis.

90. Ray JC, Flynn JL, Kirschner DE (2009) Synergy between individual TNF-dependent functions determines granuloma performance for controlling mycobacterium tuberculosis infection. J Immunol 182: 3706-3717.

91. Segovia-Juarez JL, Ganguli S, Kirschner D (2004) Identifying control mechanisms of granuloma formation during M. tuberculosis infection using an agent-based model. J Theor Biol 231: 357-376.

92. Warrender C, Forrest S, Koster F (2006) Modeling intercellular interactions in early mycobacterium infection. Bull Math Biol 68: 2233-2261.

93. Bru A, Cardona PJ (2010) Mathematical modeling of tuberculosis bacillary counts and cellular populations in the organs of infected mice. PLoS One 5: e12985.

94. Ganguli S, Gammack D, Kirschner DE (2005) A metapopulation model of granuloma formation in the lung during infection with mycobacterium tuberculosis. Math Biosci Eng 2: 535-560.

95. Gammack D, Doering CR, Kirschner DE (2004) Macrophage response to mycobacterium tuberculosis infection. J Math Biol 48: 218-242.

96. Marino S, Sud D, Plessner H, Lin PL, Chan J, et al. (2007) Differences in reactivation of tuberculosis induced from anti-TNF treatments are based on bioavailability in granulomatous tissue. PLoS Comput Biol 3: 1909-1924.

97. Sud D, Bigbee C, Flynn JL, Kirschner DE (2006) Contribution of CD8+ T cells to control of mycobacterium tuberculosis infection. J Immunol 176: 4296-4314.

98. Wigginton JE, Kirschner D (2001) A model to predict cell-mediated immune regulatory mechanisms during human infection with mycobacterium tuberculosis. J Immunol 166: 1951-1967.

99. Magombedze G, Garira W, Mwenje E (2006) Modelling the human immune response mechanisms to mycobacterium tuberculosis infection in the lungs. Math Biosci Eng 3: 661-682.

100. Day J, Friedman A, Schlesinger LS (2009) Modeling the immune rheostat of macrophages in the lung in response to infection. Proc Natl Acad Sci U S A 106: 11246-11251.

101. Marino S, El-Kebir M, Kirschner D (2011) A hybrid multi-compartment model of granuloma formation and T cell priming in tuberculosis. J Theor Biol 280: 50-62.

102. Marino S, Pawar S, Fuller CL, Reinhart TA, Flynn JL, et al. (2004) Dendritic cell trafficking and antigen presentation in the human immune response to mycobacterium tuberculosis. J Immunol 173: 494-506.

103. Marino S, Myers A, Flynn JL, Kirschner DE (2010) TNF and IL-10 are major factors in modulation of the phagocytic cell environment in lung and lymph node in tuberculosis: A next-generation two-compartmental model. J Theor Biol 265: 586-598.

104. An G, Mi Q, Dutta-Moscato J, Vodovotz Y (2009) Agent-based models in translational systems biology. Wiley Interdiscip Rev Syst Biol Med 1: 159-171.

105. Marino S, Linderman JJ, Kirschner DE (2011) A multifaceted approach to modeling the immune response in tuberculosis. Wiley Interdiscip Rev Syst Biol Med 3: 479-489.

106. Kirschner DE, Linderman JJ (2009) Mathematical and computational approaches can complement experimental studies of host-pathogen interactions. Cell Microbiol 11: 531-539.

107. Young D, Stark J, Kirschner D (2008) Systems biology of persistent infection: Tuberculosis as a case study. Nat Rev Microbiol 6: 520-528.

108. Bauer AL, Beauchemin CA, Perelson AS (2009) Agent-based modeling of host-pathogen systems: The successes and challenges. Inf Sci (Ny) 179: 1379-1389.

109. Marino S, Hogue IB, Ray CJ, Kirschner DE (2008) A methodology for performing global uncertainty and sensitivity analysis in systems biology. J Theor Biol 254: 178-196.

110. Blower SM, Dowlatabadi H (1994) Sensitivity and uncertainty analysis of complex models of disease transmission: An HIV model, as an example. Int Stat Rev 62: 229-243.

111. Helton JC, Davis FJ (2002) Illustration of sampling-based methods for uncertainty and sensitivity analysis. Risk Analysis 22: 591-622.

112. Iman RL, Helton JC (1988) An investigation of uncertainty and sensitivity analysis techniques for computer models. Risk Analysis 8: 71-90.

113. McKay MD, Beckman RJ, Conover WJ (1979) A comparison of three methods for selecting values of input variables in the analysis of output from a computer code. Technometrics 21: pp. 239-245.

114. Marino S, Hogue IB, Ray CJ, Kirschner DE (2008) A methodology for performing global uncertainty and sensitivity analysis in systems biology. J Theor Biol 254: 178-196.

Chapter 2

Identification of key processes that control tumor necrosis factor availability in a tuberculosis granuloma

2.1 Introduction

Tuberculosis (TB) is caused by a highly successful bacterium, *Mycobacterium tuberculosis* (Mtb), and is responsible for three million deaths per year [1]. 5-10% of infected people fail to control the infection and progress to primary TB disease [2]. A state of latent infection with no clinical symptoms is achieved in most people and may be maintained for the lifetime of the host. However, latent infection can be reactivated years later leading to active tuberculosis. The risk of reactivation is increased in latently infected persons who are elderly, immunocompromised (e.g. due to HIV co-infection), malnourished or taking specific drugs [3,4]. A key outcome of Mtb infection that arises as a result of the immune response within the host is the formation of aggregates of immune cells and bacteria called granulomas in the lungs. TB granulomas, especially in humans as well as guinea pig and non-human primate models, form as organized spherical structures composed of a core of bacteria, macrophages and dendritic cells (DCs) surrounded by a ring of lymphocytes, including T cells and B cells [2,5-10]. In an infected host with latent infection, the micro-environment created within a granuloma provides appropriate conditions for containment of bacteria [11,12].

Tumor necrosis factor-α (TNF) is a well-studied inflammatory cytokine that is produced by immune cells, especially activated macrophages and monocytes. TNF is

expressed as a 26 kDa membrane-bound precursor protein (membrane-bound TNF; mTNF) that can be cleaved by proteolytic activity of a metalloproteinase TNF-α converting enzyme (TACE) and released as a 17 kDa subunit (soluble TNF; sTNF) into extracellular spaces [13,14]. Both sTNF and mTNF are trimeric in their mature bioactive form [15] and function by binding to one of the two types of TNF receptors on cells: TNF receptor type 1 (TNFR1; also referred to as p55 or CD120a) and TNF receptor type 2 (TNFR2; also called p75 or CD120b) [16]. Although the two receptors are co-expressed on the surface of most cell types, TNFR1 has been identified as the primary signaling receptor through which most of the inflammatory responses attributed to TNF occur [17]. TNF affects the immune response to Mtb through several mechanisms, including induction of macrophage activation [18], apoptosis [19,20], and chemokine expression [21]. Further, numerous reports have begun to reveal the role of TNF in granuloma formation as well as in maintenance of granulomas in latent TB [11,18,22-24]. There are conflicting data, however, regarding the role of TNF in granulomas and Mtb infection and this has arisen because of cross-species comparisons. In humans, anti-inflammatory TNF-neutralizing drugs such as infliximab and etanercept are associated with an increased risk of latent TB reactivation, although the level of susceptibility depends on the drug [25,26]. Granuloma formation in mice that lack TNF or TNFR1 has been reported to be aberrant or delayed [18]. Neutralization of TNF in mice with chronic infection leads to disorganization of granulomas, increase in bacterial load and subsequent death [23]. However, TNF neutralization in monkeys results in both exacerbation of primary disease and reactivation of latent infection without affecting the granuloma architecture seen in primary and latent TB [27]. Overall, it is clear that TNF

plays an important role in TB infection dynamics. Further, TNF availability, i.e. the amount of TNF available to cells in the granuloma, has been reported to be crucial in control of TB infection [28,29], but there are still open questions regarding the mechanisms controlling TNF availability and the influence of TNF availability on granuloma function.

To elucidate the mechanisms by which availability of TNF in a granuloma is controlled, we focus on TNF interactions with immune cells that comprise a granuloma. We are interested particularly in TNF receptor dynamics. Receptor/ligand interactions at the cell membrane are responsible for initiating intracellular signaling pathways and ultimately the cell response to the external stimulus. However, trafficking events (defined here to include synthesis, internalization, recycling and degradation of ligands and receptors) have been demonstrated to take place under normal physiological conditions and can influence the availability of ligand, the number of ligand-bound receptors and thus receptor-mediated cell responses [30,31]. TNF/TNFR trafficking processes have been studied in a variety of human and mouse cell lines [32-36]. For example, a whole-cell kinetic analysis of TNF/TNFR system with fitting to experimental data on human lung adenocarcinoma A549 cells has shown that the simplest model that reasonably explains the behavior of this system includes receptor synthesis and turn-over, TNF/TNFR association and dissociation as well as TNF/TNFR complex internalization, degradation and recycling of free receptors to the cell membrane [36].

The influence of the dynamics of TNF/TNFR trafficking processes on the availability of TNF in a TB granuloma has never been studied. Thus, we develop a reaction/diffusion-based partial differential equation (PDE) model that describes a TB

granuloma as a continuous collection of immune cells forming concentric layers and includes TNF/TNFR binding and trafficking processes. Our multi-scale model is focused on TNF/TNFR-level reactions and interactions, while using a coarse-grain description of the cellular-level details representing a snapshot in time of a granuloma comprised of a static number of immune cells. To analyze the model, we use estimations for TNF/TNFR-associated parameter values from literature and then employ an artificial experimental mouse model of TB granuloma (Fig. 2.1) to quantitatively measure critical model parameters identified by sensitivity analysis. The artificial model of granuloma formation is induced in mice following injection of Sepharose beads covalently coupled to *Mycobacterium* purified protein derivative (PPD) antigen. This model is an appropriate choice for our study as it provides cytokine and cellular patterns that closely match those in an active mycobacterial infection [37-41]. Thus our mathematical model also accounts for a bead at the center of the granuloma (Fig. 2.1). We use our model to answer the following questions: What are the most important processes that control TNF availability in a granuloma? Are there likely to be gradients of TNF within a TB granuloma? How does the specific organization of immune cells in the granuloma, i.e. a core of macrophages and DCs surrounded by a mantle of lymphocytes, influence the fraction of TNF-bound receptors and thus TNF signaling for each cell type? And ultimately, how might the neutralization power of TNF-neutralizing drugs in a TB granuloma be affected by their TNF binding properties?

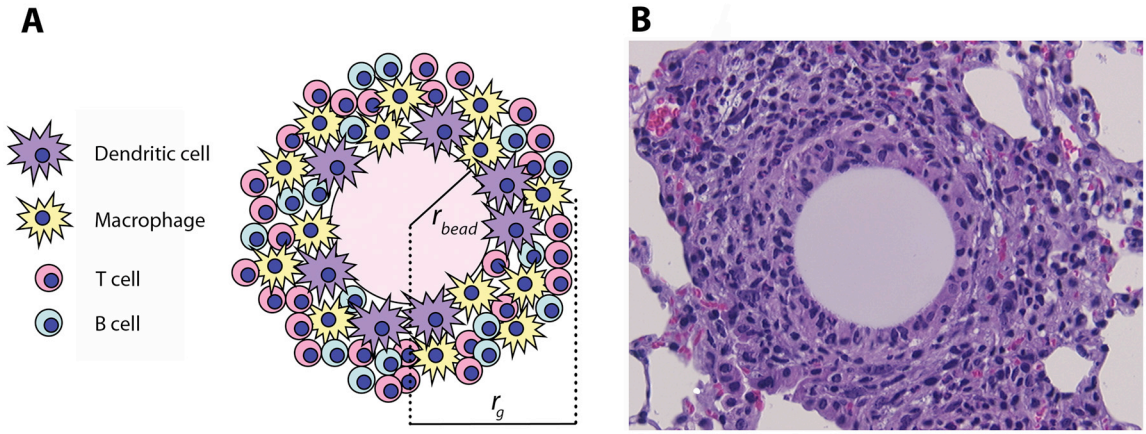

Fig. 2.1 PPD antigen-bead pulmonary granuloma model. (A) Schematic representation (r_{bead}: radius of bead, r_g: radius of granuloma) and (B) histological appearance of an artificial pulmonary granuloma induced in mouse 4 days after injection of PPD-coated beads [37,38,41] (H&E staining; magnification: ×800).

2.2 Methods

2.2.1 TNF/TNFR kinetics at the single-cell level

The binding interactions and reactions controlling TNF/TNFR dynamics at the single-cell level regardless of the cell type are illustrated in Fig. 2.2A. TNF is first synthesized by TNF-producing cells as a membrane-bound precursor form (mTNF) that can then be processed and released as a soluble form (sTNF) into extracellular spaces. This processing occurs via a cell-associated metalloproteinase called TACE [13,14]. Two types of TNF receptors (TNFR1 and TNFR2) are synthesized and expressed on the cell surface as free receptors. Soluble TNF (sTNF) reversibly binds to TNFRs on the cell membrane or degrades [16,42,43]. sTNF-bound cell surface TNFR1 internalizes and sTNF-bound cell surface TNFR2 may undergo internalization or shedding into extracellular spaces [44]. Internalized receptors may degrade or recycle to the cell membrane where they can re-bind to sTNF [36]. Ligand-free TNFRs also turn over (internalize) [34,36]. Intact sTNF may dissociate from the shed sTNF/TNFR2 complex in the extracellular space [45]. We modeled these molecular processes based on mass

action kinetics as shown in Table 2.1; definitions and values of the rate constants are given in Table 2.2.

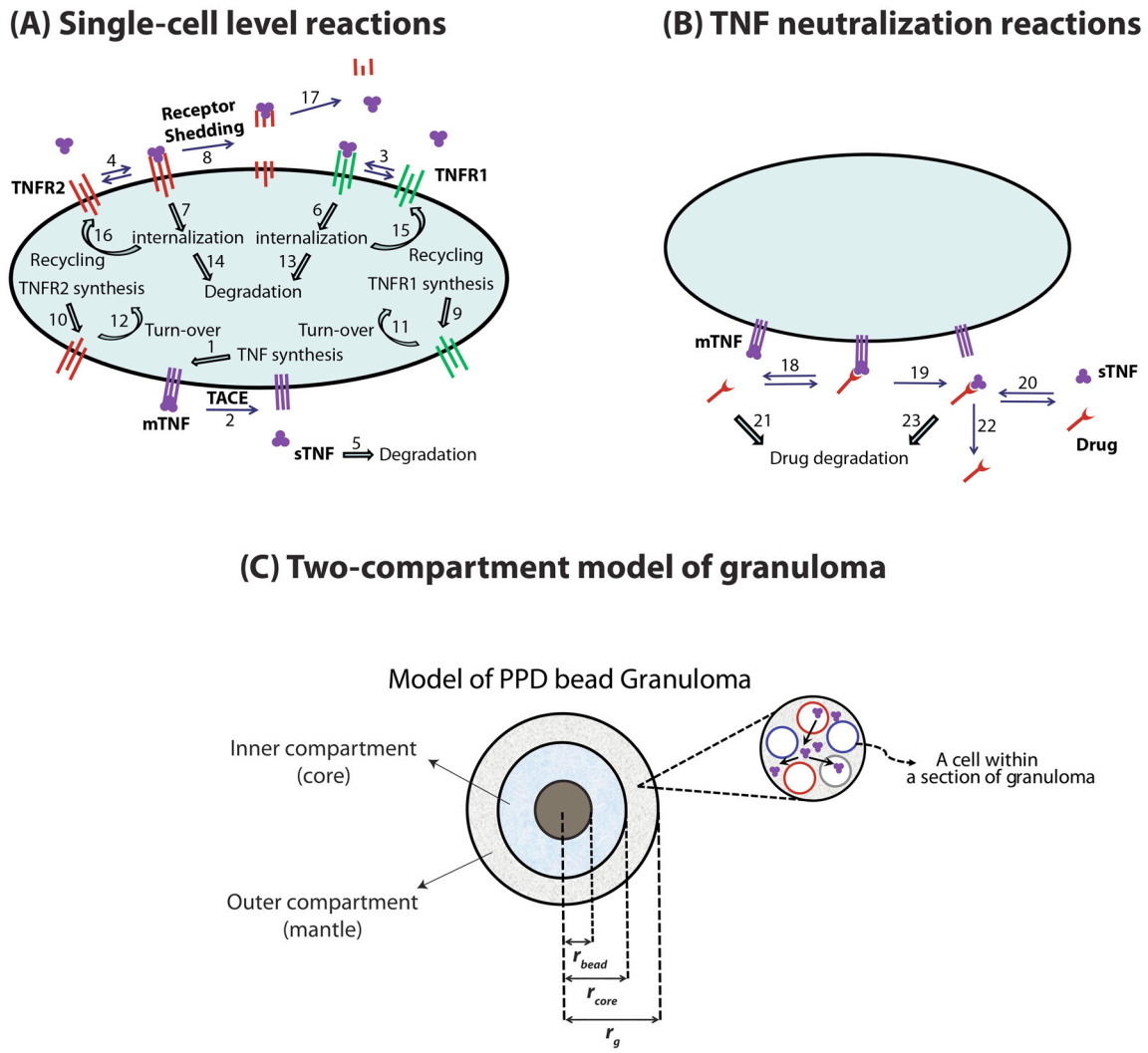

Fig. 2.2 Schematic representation of the granuloma model. (A) Binding interactions and reactions controlling TNF/TNFR dynamics at the single-cell level, including synthesis of TNFR1, TNFR2 and mTNF, sTNF release to the extracellular space under the effect of TACE activity, reversible binding of sTNF to TNFR1 and TNFR2, sTNF degradation, internalization of free and sTNF-bound TNFR1 and TNFR2, degradation of internalized TNFR1 and TNFR2, recycling of internalized TNFR1 and TNFR2, shedding of sTNF-bound TNFR2 and release of sTNF from the shed sTNF/TNFR2 complex. (B) TNF neutralization-associated reactions, including reversible binding of drug to mTNF and sTNF, release of drug-bound TNF from the membrane to the extracellular space and drug degradation. (C) Two-compartment model of granuloma that includes a bead of radius r_{bead} surrounded by the inner compartment populated by macrophages and DCs and the outer compartment composed of lymphocytes. Numbers in (A) and (B) represent model reactions as listed in Table 2.1.

Table 2.1 Definition of reaction species, model reactions and their rates (v_i).

Reaction species

mTNF	Membrane-bound TNF	$sTNF/TNFR1_i$	Internalized sTNF/TNFR1 complex
sTNF	Extracellular soluble TNF	$sTNF/TNFR2_i$	Internalized sTNF/TNFR2 complex
TNFR1	Cell surface TNF receptor 1	$sTNF/TNFR2_{shed}$	Shed sTNF/TNFR2 complex
TNFR2	Cell surface TNF receptor 2	*Drug*	TNF-neutralizing drug
sTNF/TNFR1	sTNF/TNFR1 complex on the membrane	*mTNF/Drug*	mTNF/Drug complex on the membrane
sTNF/TNFR2	sTNF/TNFR2 complex on the membrane	*sTNF/Drug*	Extracellular sTNF/Drug complex

Base model reactions

1	*mTNF synthesis* $v_1 = k_{synth}$	10	*TNFR2 synthesis* $v_{10} = V_{r2}$
2	$mTNF \rightarrow sTNF$ $v_2 = k_{TACE}[mTNF]$	11	$TNFR1 \rightarrow TNFR1_i$ $v_{11} = k_{i1}[TNFR1]$
3	$sTNF + TNFR1 \leftrightarrow sTNF/TNFR1$ $v_3 = k_{on1}[sTNF][TNFR1] - k_{off1}[sTNF/TNFR1]$	12	$TNFR2 \rightarrow TNFR2_i$ $v_{12} = k_{i2}[TNFR2]$
4	$sTNF + TNFR2 \leftrightarrow sTNF/TNFR2$ $v_4 = k_{on2}[sTNF][TNFR2] - k_{off2}[sTNF/TNFR2]$	13	$sTNF/TNFR1_i \rightarrow degradation$ $v_{13} = k_{deg1}[sTNF/TNFR1_i]$
5	$sTNF \rightarrow degradation$ $v_5 = k_{deg}[sTNF]$	14	$sTNF/TNFR2_i \rightarrow degradation$ $v_{14} = k_{deg2}[sTNF/TNFR2_i]$
6	$sTNF/TNFR1 \rightarrow sTNF/TNFR1_i$ $v_6 = k_{int1}[sTNF/TNFR1]$	15	$sTNF/TNFR1_i \rightarrow TNFR1$ $v_{15} = k_{rec1}[sTNF/TNFR1_i]$
7	$sTNF/TNFR2 \rightarrow sTNF/TNFR2_i$ $v_7 = k_{int2}[sTNF/TNFR2]$	16	$sTNF/TNFR2_i \rightarrow TNFR2$ $v_{16} = k_{rec2}[sTNF/TNFR2_i]$
8	$sTNF/TNFR2 \rightarrow sTNF/TNFR2_{shed}$ $v_8 = k_{shed}[sTNF/TNFR2]$	17	$sTNF/TNFR2_{shed} \rightarrow sTNF + TNFR2_{shed}$ $v_{17} = k_{off2}[sTNF/TNFR2_{shed}]$
9	*TNFR1 synthesis* $v_9 = V_{r1}$		

TNF neutralization reactions

18*	$mTNF + Drug \leftrightarrow mTNF/Drug$ $v_{18} = k_{on\_TNF/Drug}[mTNF][Drug] - k_{off\_TNF/Drug}[mTNF/Drug]$	21	$Drug \rightarrow degradation$ $v_{21} = k_{deg\_Drug}[Drug]$
19	$mTNF/Drug \rightarrow sTNF/Drug$ $v_{19} = k_{TACE}[mTNF/Drug]$	22	$sTNF/Drug \rightarrow Drug$ (sTNF degradation) $v_{22} = k_{deg}[sTNF/Drug]$
20*	$sTNF + Drug \leftrightarrow sTNF/Drug$ $v_{20} = k_{on\_TNF/Drug}[sTNF][Drug] - k_{off\_TNF/Drug}[sTNF/Drug]$	23	$sTNF/Drug \rightarrow degradation$ $v_{23} = k_{deg\_Drug}[sTNF/Drug]$

* Sequential binding of drug to sTNF and mTNF for drugs with TNF binding ratio of greater than 1:1 was modeled similarly.

Table 2.2 Model parameters, definitions and values estimated from literature.

Parameter	Parameter description	Value*	Reference
k_{synth_in} (#/cell.s)	Average rate of mTNF synthesis in the inner compartment	10^{-2}-1	See text
k_{synth_out} (#/cell.s)	Average rate of mTNF synthesis in the outer compartment	0-10^{-1}	See text
R_{1_out} (#/cell)	TNFR1 density in the outer compartment	500-5000	[33,46,47]
R_{1_in} (#/cell)	TNFR1 density in the inner compartment	500-5000	[33,46,47]
R_{2_out} (#/cell)	TNFR2 density in the outer compartment	500-5000	[33,46,47]
R_{2_in} (#/cell)	TNFR2 density in the inner compartment	500-5000	[33,46,47]
f	Fraction of granuloma in the outer compartment	0.4-0.7	[7,41]
D_1 (cm^2/s) †	Diffusion coefficient of sTNF	10^{-8}-10^{-7} (5.2×10^{-8})	[48,49]
D_2 (cm^2/s) †	Diffusion coefficient of shed TNF/TNFR2 complex	10^{-8}-10^{-7} (3.2×10^{-8})	[48,49]
ϕ ‡	Volume fraction of the extracellular space per granuloma volume	0.2-0.3 (0.2)	[50,51]
d_G (#/mm^2)	Density of granulomas in the lung tissue cross section	0.5-30 (1)	[52,53]
ρ (cell/l)	Mean cell number density in the tissue	6×10^{12}	[41]
r_g (μm)	Granuloma radius	100	[41]
r_m (μm) §	Half mean distance between granulomas	$1000\times(\pi d_G)^{-0.5}$	
r_{bead} (μm)	Bead radius	40	
r_{core} (μm)	Radius of the inner compartment	$[r_g^3-f(r_g^3-r_{bead}^3)]^{1/3}$	
N_{av} (mol^{-1})	Avogadro's number	6.02×10^{23}	
k_{TACE} (s^{-1})	Rate constant for TNF release by TACE activity	10^{-4}-10^{-3} (4.4×10^{-4})	[14,54,55]
k_{deg} (s^{-1})	sTNF degradation rate constant	4.58×10^{-4}	[56]
K_{d1} (M)	Equilibrium dissociation constant of sTNF/TNFR1	10^{-12}-10^{-10} (1.9×10^{-11})	[33,42]
K_{d2} (M)	Equilibrium dissociation constant of sTNF/TNFR2	10^{-10}-10^{-9} (4.2×10^{-10})	[33,42,57]
k_{on1} ($M^{-1}s^{-1}$)	sTNF/TNFR1 association rate constant	10^7-10^8 (2.8×10^7)	[42]
k_{on2} ($M^{-1}s^{-1}$)	sTNF/TNFR2 association rate constant	10^7-10^8 (3.5×10^7)	[42]
k_{off1} (s^{-1})	sTNF/TNFR1 dissociation rate constant	$k_{on1}\times K_{d1}$	
k_{off2} (s^{-1})	sTNF/TNFR2 dissociation rate constant	$k_{on2}\times K_{d2}$	
k_{int1} (s^{-1})	TNFR1 internalization rate constant	5×10^{-4}-1.5×10^{-3} (7.7×10^{-4})	[42,44]
k_{int2} (s^{-1})	TNFR2 internalization rate constant	3.9×10^{-4}-5×10^{-4} (4.6×10^{-4})	[57]
k_{shed} (s^{-1})	TNFR2 shedding rate constant	3.9×10^{-4}-1.5×10^{-3} (5×10^{-4})	[44,54]
k_{rec1} (s^{-1})	TNFR1 recycling rate constant	8.8×10^{-5}-5.5×10^{-4} (1.8×10^{-5})	[34,36]
k_{rec2} (s^{-1})	TNFR2 recycling rate constant	8.8×10^{-5}-5.5×10^{-4} (1.8×10^{-5})	[34,36]
k_{t1} (s^{-1})	TNFR1 turn-over rate constant	3×10^{-4}-5×10^{-4} (3.8×10^{-4})	[34,36]
k_{t2} (s^{-1})	TNFR2 turn-over rate constant	3×10^{-4}-5×10^{-4} (3.8×10^{-4})	[34,36]
k_{deg1} (s^{-1})	TNFR1 degradation rate constant	10^{-5}-10^{-4} (5×10^{-5})	[32-34,36]
k_{deg2} (s^{-1})	TNFR2 degradation rate constant	10^{-5}-10^{-4} (5×10^{-5})	[32-34,36]
V_{r1_in} (#/cell.s)	Cell surface TNFR1 synthesis rate constant in the inner compartment	$k_{t1}\times R_{1\_in}$	
V_{r1_out} (#/cell.s)	Cell surface TNFR1 synthesis rate constant in the outer compartment	$k_{t1}\times R_{1\_out}$	
V_{r2_in} (#/cell.s)	Cell surface TNFR2 synthesis rate constant in the inner compartment	$k_{t2}\times R_{2\_in}$	
V_{r2_out} (#/cell.s)	Cell surface TNFR2 synthesis rate constant in the outer compartment	$k_{t2}\times R_{2\_out}$	

* The 25 parameters used for sensitivity analysis are indicated by their ranges of values. Values in parentheses are used to generate other model results.

† Diffusion coefficients of the soluble species in granuloma were estimated in line with estimates for diffusible factors of similar molecular weight in tumors [48,49].

‡ Consistent with extracellular volume fraction estimated for multi –cellular tumor spheroids [50,51].

§ Half mean distance between granulomas were calculated from the granuloma density assessed for 2D sections of the lung tissue [52,53] and assumed to be consistent in 3D.

2.2.2 TNF neutralization kinetics

Several TNF-neutralizing drugs have been developed and they work to interfere with TNF activity and thus are used to control inflammation in human diseases such as rheumatoid arthritis and Crohn's disease. These drugs are composed of either monoclonal antibodies (e.g. infliximab) or receptor fusion molecules (e.g. etanercept) that specifically bind TNF, acting as a competitive inhibitor for TNF binding to cell surface TNFRs and eventually neutralizing its functions [58,59].

To study the effect of TNF-neutralizing drugs of various properties on TNF/TNFR dynamics, we modeled a hypothetical drug as an agent that binds to sTNF or both sTNF and mTNF molecules and also inhibits sTNF binding to both TNFRs. We captured TNF neutralization-associated reactions (schematically shown in Fig. 2.2B) in our model, including reversible binding of drug to mTNF and sTNF [59,60], release of drug-bound mTNF into extracellular spaces due to TACE activity, and drug or TNF/drug complex degradation [61] based on mass action kinetics as shown in Table 2.1. Definitions and values of drug-specific parameters are given in Table 2.3.

Table 2.3 TNF neutralization-associated parameters, definitions, and values.

Parameter	Parameter description	Value	Reference
D_{drug} (cm^2/s) *	Diffusion coefficient of drug	2.3×10^{-8}	[48,49]
k_c (cm/s) †	Drug permeability in granuloma	9×10^{-7}	[62]
C_0 (M) ‡	Average drug concentration in the lung tissue	1×10^{-7}	[63,64]
$k_{on\_TNF/Drug}$ ($M^{-1}s^{-1}$)	TNF/drug association rate constant	10^4-10^6	[60,65,66]
$k_{off\_TNF/Drug}$ (s^{-1})	TNF/drug dissociation rate constant	10^{-5}-10^{-3}	[60,65,66]
k_{deg_Drug} (s^{-1})	Drug degradation rate constant	1×10^{-6}	[59]

* Diffusion coefficient of the drug in granuloma was estimated in line with estimates for diffusible factors of similar molecular weight in tumors [48,49].
† Drug permeability in granuloma was estimated based on permeability of bifunctional antibodies in tumors [62].
‡ Drug concentration in the lung was estimated based on approximate blood concentration of TNF-neutralizing drugs. For most antibodies, tissue/blood concentration ratios are in the range of 0.1-0.5 [64].

2.2.3 Two-compartment model of granuloma

To study the influence of TNF/TNFR dynamics on the availability of TNF within the multi-cellular structure of the granuloma, TNF/TNFR-associated molecular processes described at the single-cell level were incorporated into a coarse-grain multi-cellular model of a TB granuloma. The model represents a snapshot in time of a granuloma and is composed of an organized collection of a static number of immune cells surrounding a PPD-coated bead. Within this collection, TNF is produced by TNF-producing immune cells, diffuses in extracellular spaces and interacts with TNFR-expressing cells. We modeled the granuloma as a spherical continuum consisting of two cellular compartments. The inner compartment includes evenly distributed macrophages and DCs that form the core of the granuloma, and the outer compartment or mantle is comprised of evenly distributed T cells and B cells (Fig. 2.2C). This is consistent with the structure observed for classical TB granulomas that are comprised of aggregates of macrophages and DCs with a characteristic cuff of lymphocytes, including T cells and B cells on the periphery [2,6]. Discrete cells are not explicitly considered in this model; each cell-associated species (e.g. cell surface TNF receptor, internalized TNF-bound

receptor, etc) is treated as a spatially immobile agent whose concentration in space is expressed by a continuous variable, whereas unbound extracellular sTNF and shed receptors are free to diffuse. Thus, the model includes reaction-diffusion equations for extracellular sTNF and shed receptor concentrations, and basic reaction equations for other species as listed in Table 2.4. Definitions and values of model parameters are given in Table 2.2.

Table 2.4 Model equations. TNF neutralization reactions are distinguished from other reactions by bold font.

$$\frac{\partial[mTNF]}{\partial t} = v_1 - v_2 - \boldsymbol{v_{18}}$$

$$\frac{\partial[sTNF]}{\partial t} = \frac{D_1}{r^2}\frac{\partial}{\partial r}\left(r^2 \frac{\partial[sTNF]}{\partial r}\right) + \left(\frac{\rho}{\phi N_{av}}\right)(v_2 - v_3 - v_4) - v_5 + v_{17} - \boldsymbol{v_{20}}$$

$$\frac{\partial[TNFR1]}{\partial t} = v_9 - v_3 - v_{11} + v_{15}$$

$$\frac{\partial[TNFR2]}{\partial t} = v_{10} - v_4 - v_{12} + v_{16}$$

$$\frac{\partial[sTNF/TNFR1]}{\partial t} = v_3 - v_6$$

$$\frac{\partial[sTNF/TNFR2]}{\partial t} = v_4 - v_7 - v_8$$

$$\frac{\partial[sTNF/TNFR1_i]}{\partial t} = v_6 - v_{13} - v_{15}$$

$$\frac{\partial[sTNF/TNFR2_i]}{\partial t} = v_7 - v_{14} - v_{16}$$

$$\frac{\partial[sTNF/TNFR2_{shed}]}{\partial t} = \frac{D_2}{r^2}\frac{\partial}{\partial r}\left(r^2 \frac{\partial[sTNF/TNFR2_{shed}]}{\partial r}\right) + \left(\frac{\rho}{\phi N_{av}}\right)v_8 - v_{17}$$

$$\frac{\partial[\boldsymbol{Drug}]}{\partial t} = \frac{\boldsymbol{D_{drug}}}{r^2}\frac{\partial}{\partial r}\left(r^2 \frac{\partial[\boldsymbol{Drug}]}{\partial r}\right) - \left(\frac{\rho}{\phi N_{av}}\right)\boldsymbol{v_{18}} - \boldsymbol{v_{20}} - \boldsymbol{v_{21}} + \boldsymbol{v_{22}}$$

$$\frac{\partial[\boldsymbol{mTNF/Drug}]}{\partial t} = \boldsymbol{v_{18}} - \boldsymbol{v_{19}}$$

$$\frac{\partial[\boldsymbol{sTNF/Drug}]}{\partial t} = \frac{\boldsymbol{D_{drug}}}{r^2}\frac{\partial}{\partial r}\left(r^2 \frac{\partial[\boldsymbol{sTNF/Drug}]}{\partial r}\right) + \left(\frac{\rho}{\phi N_{av}}\right)\boldsymbol{v_{19}} + \boldsymbol{v_{20}} - \boldsymbol{v_{23}} - \boldsymbol{v_{22}}$$

To maintain the consistency of the mathematical model with the experimental mouse bead model of granuloma that we study, the granuloma is comprised of a bead of radius r_{bead} surrounded by cellular layers of the inner and outer compartments with radii of r_{core} and r_g, respectively (Fig. 2.2C). We assumed no flux of sTNF at $r = r_{bead}$ and at r

= r_m, a distance equal to half the mean distance between granulomas, due to symmetry with tissue surrounding adjacent granulomas. Initial conditions for TNFRs are specified as:

$$[TNFR1]\,(r,\,0) = \begin{array}{ll} R_{1\_in}: & r_{bead} < r \le r_{core} \\ R_{1\_out}: & r_{core} < r \le r_g \end{array} \tag{2.1}$$

$$[TNFR2]\,(r,\,0) = \begin{array}{ll} R_{2\_in}: & r_{bead} < r \le r_{core} \\ R_{2\_out}: & r_{core} < r \le r_g \end{array} \tag{2.2}$$

where R_{1_in}, R_{1_out}, R_{2_in} and R_{2_out} are the average TNFR1 and TNFR2 densities on the membrane of cells in the inner and outer compartments. These parameters were set equal to the steady state concentrations of cell surface TNFRs in each compartment in the absence of TNF and are controlled by the rates of receptor synthesis and turnover of free receptors as indicated in Table 2.2. Similarly, we assumed the steady state concentration of mTNF (found from Equation 2.3) in each compartment as the initial value of mTNF for that compartment (Equation 2.4).

$$\left.\frac{d[mTNF]}{dt}\right|_{sready\text{-}state} = k_{synth} - k_{TACE}[mTNF]_{steady-state} = 0 \tag{2.3}$$

$$[mTNF]\,(r,\,0) = [mTNF]_{steady-state} = \begin{array}{ll} k_{synth\_in}/k_{TACE}: & r_{bead} < r \le r_{core} \\ k_{synth\_out}/k_{TACE}: & r_{core} < r \le r_g \end{array} \tag{2.4}$$

Initial concentrations of other species were set to zero, as cell-associated mTNF is the initial source of the whole TNF in the granuloma.

The PDE model was solved numerically using COMSOL Multiphysics 3.4 (COMSOL AB, Stockholm, Sweden) with MATLAB 7.5 (The MathWorks, Natick, MA). Simulations were run until a steady state was reached (approximately 12 hours of real time). Because TNF-associated molecular level processes studied here occur

significantly faster than cellular level events that may change the structure of a granuloma (e.g. cell recruitment, migration and death), we assumed that the structure of granuloma is not changed during the 12-hour time course of simulations.

2.2.4 Distinct cell types and cellular organization in the granuloma model

To study the influence that specific cellular organizations may have on the availability of TNF within a TB granuloma, we explicitly incorporated major granuloma-comprising cell types (determined from experiments performed herein), including macrophages, DCs, T cells and B cells into our mathematical model of a granuloma. We defined a metric, *separation index* (*s*), to present the level of separation between different cell types in a granuloma, defined as:

$$s = \frac{l_o - l_g}{1 - l_g} \tag{2.5}$$

where l_o, l_g are the lymphocyte (T cells and B cells) fractions in the outer compartment and in the whole granuloma, respectively. Thus a separation index of 0 is equivalent to a totally mixed cellular organization, whereas a separation index of 1 represents a separate cellular organization approximately as observed in human and non-human primate models of TB in which DCs and macrophages reside in the inner compartment (core) and lymphocytes compose the outer compartment (mantle). A schematic representation of the effect of changing *s* on cellular organization of the bead granuloma is shown in Appendix A (Fig. A.1). Some model parameters were also defined or modified based on consideration of the cellular organization in the model as shown in Appendix A (Table A.1). For example, using the mean cell volume in each compartment, cell number

densities in the inner and outer compartments (ρ_{in} and ρ_{out}) are computed and replace general cell density ρ in diffusion equations of Table 2.4.

We assumed that some TNF/TNFR kinetic parameters, including the rate constants for TNF release by TACE activity, TNF/TNFR association and dissociation as well as TNFR internalization, shedding, degradation and recycling have the same values for different cell types. This assumption is based on consistency of experimental data on measurement or estimation of values of these parameters for a variety of cell types including various cell lines expressing TNF and/or TNF receptors with one another as well as other data on similar mammalian cell surface receptors [14,30,32-34,36,42,44,54,55,57,67]. However, the rate of synthesis of TNF and TNFRs depends on the cell type (see Results). Thus, when different cell types are considered, average rates of mTNF synthesis in granuloma compartments can be computed as follows:

$$k_{synth\_in} = (1-s)(f_B k_B + f_{CD4} k_{CD4} + f_{CD8} k_{CD8}) + \frac{[1-l_g(1-s)](f_{Mac} k_{Mac} + f_{mDC} k_{mDC} + f_{pDC} k_{pDC})}{1-l_g} \quad (2.6)$$

$$k_{synth\_out} = \frac{[l_g(1-s)+s](f_B k_B + f_{CD4} k_{CD4} + f_{CD8} k_{CD8})}{l_g} + (1-s)(f_{Mac} k_{Mac} + f_{mDC} k_{mDC} + f_{pDC} k_{pDC}) \quad (2.7)$$

where definitions of parameters are given in Appendix A (Table A.1). Similarly, average values of TNFR1 and TNFR2 densities in each compartment can be computed.

2.2.5 Model outputs

The protective role of TNF in immunity to Mtb infection has been shown to depend primarily on the soluble form (sTNF) and its interactions with TNFR1 [18,68], suggesting that the spatial profile of sTNF concentration and the fraction of sTNF-bound

cell surface TNFR1 are model outputs of interest. Therefore, we introduce four steady-state spatially averaged metrics to characterize our simulation results for availability of TNF in a granuloma. These metrics were used to perform sensitivity analysis and include: sTNF-bound fraction of cell surface TNFR1 in the whole granuloma (output 1), granuloma core (inner compartment; output 2) and mantle (outer compartment; output 3) as well as free sTNF concentration in the whole granuloma (output 4).

2.2.6 Sensitivity analysis

To identify parameters that significantly influence the outcomes of the two-compartment model of a granuloma, we used Latin hypercube sampling (LHS) [69-73] to sample values of 25 parameters from the ranges (with uniform distributions) listed in Table 2.2. Ranges of TNF/TNFR affinity and kinetic parameter values were obtained from a variety of literature data from different cell lines. However, no experimental values are available for several other parameters, including the rate of mTNF synthesis and TNFR densities as well as cell fractions and densities in a granuloma. Thus, relevant ranges of values of these parameters, though not derived from TB granulomas, were used for sensitivity analysis. For example, reported rates of TNF synthesis by activated cultured immune cells [28,38], receptor densities on human monocytes and lymphocytes [33,46,47], and immune cell fractions in the lungs of Mtb infected or mycobacterial antigen activated mice [7,41] were used.

To reduce the number of parameters in LHS simulations, we replaced distinct cell type fractions with a general parameter f defined as the fraction of granuloma in the outer compartment. The parameter f directly determines the thickness of the inner and

outer compartments as indicated in Appendix A (Fig. A.1). The rate of mTNF synthesis and density of TNF receptors were sampled independently as average values of these parameters in each compartment (k_{synth_in}, k_{synth_out}, R_{1_in}, R_{1_out}, R_{2_in}, R_{2_out}). Thus, these parameters together with f determine the overall rate of TNF and TNFR expression in the granuloma. Note that the separation index (s) defined above is not used in the absence of distinct cell types (i.e. for the sensitivity analysis described here). Simulations sampled each parameter 1000 times, producing 1000 solutions to the model equations. To determine the correlation between parameter values and each of the model outputs, partial rank correlation coefficient (PRCC) values were calculated [69,70,74]. PRCC values vary between -1 (perfect negative correlation) and 1 (perfect positive correlation) and can be differentiated based on p-values derived from Student's t test. The choice of number of simulations (N) is determined by the desired significance level for the PRCC [69,75] and here $N = 1000$ implies that PRCC values above +0.09 or below -0.09 are significantly different from zero ($p < 0.001$). Model parameters then were categorized for their significance in affecting the model outputs based on their PRCC values.

2.2.7 Simulation of TNF neutralization in granuloma

To study the effect of TNF-neutralizing drugs of various properties on TNF availability in a granuloma, the model was run in the absence of drug until a steady state was reached and then the drug was added. We modeled the drug source as a concentration C_0 in the surrounding tissue with a flux into a granuloma that is dependent on drug permeability k_c and the drug gradient at granuloma radius $r = r_g$:

$$D_{drug}\left.\frac{\partial[Drug]}{\partial r}\right|_{r=r_g} = k_c(C_0 - [Drug]_{r=r_g}) \tag{2.8}$$

C_0 was considered constant within the time course of simulation that is significantly shorter than the decay time reported for TNF-neutralizing drugs [59,63]. Equations describing drug/TNF interactions and reactions are listed in Table 2.4. Drug-associated model parameters are listed in Table 2.3. To compare the influence of drugs with different properties (parameters) on availability of TNF in a granuloma, TNF neutralization efficiency, E, was defined as a function of the ratio of the spatially averaged steady-state concentration of sTNF before drug addition to the spatially averaged concentration of sTNF when drug exerts its steady state maximum effect, i.e. approximately 6 hours after drug addition.

$$E = 1 - \frac{\int_{r_{bead}}^{r_g} [sTNF]\big|_{t=6\text{ hours}}(4\pi r^2)dr}{\int_{r_{bead}}^{r_g} [sTNF]\big|_{t=0}(4\pi r^2)dr} \tag{2.9}$$

where $t = 0$ stands for the steady state condition at which drug was added.

2.2.8 Mouse model of TB granuloma

We use an artificial mouse model of TB granuloma that has been demonstrated to provide a well-circumscribed lung granuloma typified by a type 1 cytokine phenotype characterized in TB [38]. Briefly, granulomas were induced in pre-sensitized CBA/J mice lungs following i.v. injection of 6000 Sepharose 4B beads (in 0.5 ml of PBS) covalently coupled to *Mycobacterium* purified protein derivative (PPD) as previously described [38,40,41,76]. After 2 days, PPD-coated beads are surrounded by immune cells including macrophages, DCs, T cells and B cells. PPD-bead granulomas achieve their maximal size on day 4 and gradually diminish thereafter [38]. To measure

parameters of interest in PPD bead granulomas, groups of mice were sacrificed at 2 and 4 days after bead injection. Intact granulomas were isolated following homogenization of lungs in cold RPMI-1640 medium (BioWhittaker) in a Waring blender with a narrow-bottom stainless steel cup. Granuloma cells were obtained following a 30-minute treatment of isolated granulomas in a solution of RPMI supplemented with 10% fetal calf serum (FCS), 1 mg/ml collagenase A (Roche) and 30 μg/ml bovine pancreatic DNase I (Sigma) at 37^{o}C and used for further experiments.

2.2.9 Cellular composition of PPD bead granulomas

To identify the cellular composition of PPD bead granulomas, we used multi-color flow cytometry with fluorescing antibodies specific for immune cell markers, including macrophages, DCs, T cells and B cells. Other immune cells such as neutrophils and eosinophils were not quantified as they have been shown to constitute only a tiny fraction of PPD bead granulomas [41]. The following antibodies/conjugates were used for staining of the cells: anti-CD11b-APC (BD Pharmingen), anti-CD11c-FITC (BD Pharmingen), anti-F4/80-APC-Cy7 (eBioscience), anti-B220-PerCP-Cy5.5 (BioLegend), anti-CD4-PE-Cy7 (BD Pharmingen) and anti-CD8a-Biotin (BD Pharmingen)/ Streptavidin-Pacific Orange (Invitrogen). Dead cells were identified and excluded from analysis by staining with the Live/Dead Fixable Violet Dead Cell Stain Kit (Invitrogen). 2×10^5 events were counted using a BD-LSRII system flow cytometer (BD Biosciences). F4/80$^+$ CD11b$^+$ macrophage, B220$^+$ CD11c$^+$ lymphoid dendritic cell (pDC), CD11b$^+$ CD11c$^+$ myeloid dendritic cell (mDC), B220$^+$ B cell, CD4$^+$ T cell and CD8$^+$ T cell populations were gated following compensation for fluorochrome spectral overlaps. Cell

fractions in granulomas were identified following analysis by FlowJo software (Treestar, Ashland, OR).

2.2.10 TNF receptor quantification

To quantify the number of TNFR1 and TNFR2 molecules on the membrane of each cell type, we used quantitative flow cytometry with Phycoerythrin (PE)-conjugated anti-TNFR1 or -TNFR2 antibodies (BioLegend), together with staining of cell-specific markers as described above. Thus, cell suspensions at a concentration of 1×10^6 cells per volume of 200 μl were stained with saturating concentrations of antibodies that were identified to be 2 mg/l for anti-TNFR1 and 1 mg/l for anti-TNFR2 antibodies. We generated a calibration plot from the fluorescence intensity measurements on Quanti-BRITE PE-conjugated standard micro-beads (BD Biosciences). This plot was used (after compensation for fluorochrome spectral overlaps) to quantify TNFR1 and TNFR2 densities on the membrane of granuloma macrophages, mDCs, pDCs, B cells, CD4 and CD8 T cells based on the PE mean fluorescence intensities.

2.2.11 Quantification of the rate of TNF synthesis

Because TNF is initially synthesized as a membrane-bound molecule (mTNF), we can also use quantitative flow cytometry to quantify the rate of TNF synthesis by granuloma-comprising cells, including macrophages, DCs, B cells and T cells. Live granuloma cells were first isolated (from the lungs of a group of 10 mice) by using a Dead Cell Removal Kit (Miltenyi Biotec) and incubated at 37^oC in a 5% CO_2 humidified environment for 4-5 hours. TNF-α proteinase inhibitor-1 (TAPI-1; Calbiochem) at a

concentration of 100 μM was added to inhibit TNF release from cell membranes [54,77]. PE-conjugated anti-TNF antibody (BioLegend) was then used to stain 1×10^6 cells at a sequence of time-points within a 3 hour period of TACE inhibition at 37°C.

The rate of mTNF synthesis for distinct TNF-producing cell types was derived by nonlinear regression of the experimental data to an equation of the form $y = ae^{bt} + c$ as the general form of Equation 2.10 (which is derived from Equation 2.3) using MATLAB. Parameters a, b, c then were used to calculate k'_{TACE} and k_{synth}.

$$[mTNF] = ([mTNF]_0 - \frac{k_{synth}}{k'_{TACE}})e^{-k'_{TACE}t} + \frac{k_{synth}}{k'_{TACE}} \tag{2.10}$$

where $[mTNF]_0$ is the steady-state initial number of mTNF on the cell membrane and k'_{TACE} is the TNF release rate constant in the presence of TAPI-1 ($k'_{TACE} \leq k_{TACE}$). Knowing k_{synth} and the steady-state initial number of mTNF $[mTNF]_0$, the value of k_{TACE} can be calculated from:

$$[mTNF]_0 = \frac{k_{synth}}{k_{TACE}} \tag{2.11}$$

2.3 Results

2.3.1 TNF availability within a granuloma

To understand the extent to which granuloma properties (e.g. cellular composition, TNFR expression and the rate constant for receptor internalization) impact the availability of TNF, simulations were run for different values of model parameters within ranges given in Table 2.2. Although TNF exists in different forms in the granuloma, the amount of TNF associated with TNF receptors, and in particular TNFR1, has been identified as a primary factor that determines the outcomes of TNF signaling in

the granuloma [18,78]. Thus, we present steady state model predictions for spatial profile of the fraction of sTNF-bound TNFR1 in a granuloma using several different sample sets of values for model parameters within ranges specified in Table 2.2 (Fig. 2.3). Simulation results for the spatial profiles of other forms of TNF in the model (soluble and cell-associated sTNF-bound TNFR2 and internalized sTNF-bound TNFRs) are presented in Appendix A. Our modeling results demonstrate that TNF availability in granuloma compartments is dramatically influenced by the values of model parameters, including rate constants for TNF/TNFR trafficking events, TNFR densities and the rate of TNF synthesis in granuloma compartments. However, modeling results here are limited in their applicability due to parameter uncertainty, especially uncertainty in the level of TNF and TNFR expression by distinct granuloma-comprising cells. Therefore, we next turn to the identification of critical model parameters that influence the outcome of the model, TNF availability and binding to TNFRs in the granuloma.

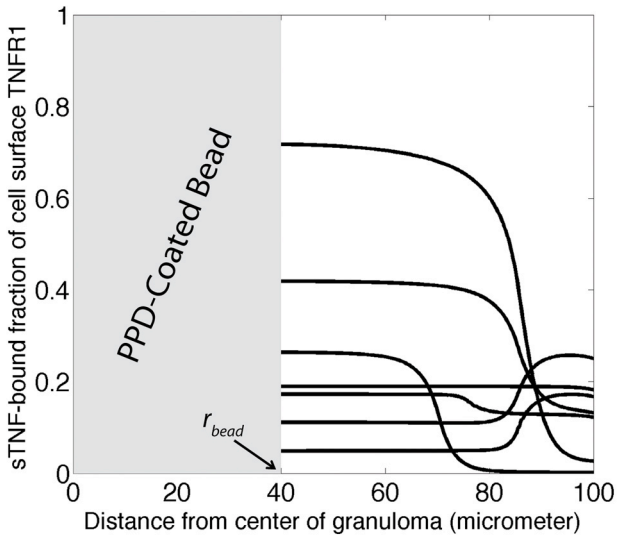

Fig. 2.3 Simulation results for the steady-state profile of sTNF-bound fraction of cell surface TNFR1 in a granuloma using seven different sample sets of parameter values within ranges specified in Table 2.2. Arrow indicates radius of the bead (r_{bead}). Parameter values for the particular curves shown are listed in Appendix A (Table A.2).

2.3.2 Sensitivity analysis: identifying critical model parameters that influence TNF availability

To identify parameters that significantly influence the availability of TNF within a granuloma, sensitivity of the outputs of the model describing TNF trafficking in a granuloma to changes of input parameters was explored. Table 2.5 indicates significant PRCC values for model parameters and outputs. For example, the average sTNF-bound fraction of cell surface TNFR1 in the whole granuloma (output 1) was shown to be significantly influenced by a variety of parameters, including the average rate of mTNF synthesis in the inner and outer compartments (k_{synth_in} and k_{synth_out}), the average TNFR1 density in the inner and outer compartments (R_{1_in}, R_{1_out}), the outer compartment fraction of granuloma (f) as well as both TNF receptor affinities for sTNF (K_{d1} and K_{d2}) and the rate constant for TNF-induced internalization of TNFR1 (k_{int1}). Indeed, using

different values of these particular parameters as inputs leads to outputs similar to those shown in Fig. 2.3 (data not shown). Thus, experimentally determined values of these parameters are required for generation of useful model predictions.

Table 2.5 Significant PRCC values for model parameters and four spatially averaged steady-state outputs: (1) sTNF-bound fraction of cell surface TNFR1 in the whole granuloma, (2) sTNF-bound fraction of cell surface TNFR1 in the inner compartment, (3) sTNF-bound fraction of cell surface TNFR1 in the outer compartment, (4) sTNF concentration in the whole granuloma. Non-significant PRCC values are not indicated.

Parameter	Parameter description	Output (1)	Output (2)	Output (3)	Output (4)
k_{synth_in}	Average rate of mTNF synthesis in the inner compartment	0.93**	0.93**	0.71**	0.88**
k_{synth_out}	Average rate of mTNF synthesis in the outer compartment	0.31**		0.82**	0.29**
R_{1_out}	TNFR1 density in the outer compartment	-0.76**		-0.85**	-0.29**
R_{1_in}	TNFR1 density in the inner compartment	-0.62**	-0.86**	-0.54**	-0.76**
R_{2_out}	TNFR2 density in the outer compartment			-0.17**	
R_{2_in}	TNFR2 density in the inner compartment	-0.09*	-0.15**	0.25**	
f	Fraction of granuloma in the outer compartment	-0.49**		-0.32**	-0.36**
D_1	Diffusion coefficient of sTNF			0.19**	
D_2	Diffusion coefficient of shed TNF/TNFR2 complex			0.08*	
ϕ	Volume fraction of the extracellular space per granuloma volume				
d_G	Density of granulomas in the lung tissue				
k_{TACE}	Rate constant for TNF release by TACE activity				
K_{d1}	Equilibrium dissociation constant of sTNF/TNFR1	-0.12**	-0.18**	0.16**	0.72**
K_{d2}	Equilibrium dissociation constant of sTNF/TNFR2	0.14**	0.18**		0.09*
k_{on1}	sTNF/TNFR1 association rate constant				-0.47**
k_{on2}	sTNF/TNFR2 association rate constant				
k_{int1}	TNFR1 internalization rate constant	-0.76**	-0.72**	-0.75**	-0.42**
k_{int2}	TNFR2 internalization rate constant				
k_{shed}	TNFR2 shedding rate constant				
k_{rec1}	TNFR1 recycling rate constant				-0.09*
k_{rec2}	TNFR2 recycling rate constant				0.09*
k_{t1}	TNFR1 turn-over rate constant				
k_{t2}	TNFR2 turn-over rate constant				
k_{deg1}	TNFR1 degradation rate constant				
k_{deg2}	TNFR2 degradation rate constant				

* 0.001 < p-value < 0.05
** p-value < 0.001

Parameters that positively correlate with the sTNF-bound fraction of cell surface TNFR1 in the whole granuloma (output 1 in Table 2.5) include the rate of mTNF synthesis in both compartments and the equilibrium dissociation constant of TNFR2 (K_{d2}) as a competitor of TNFR1 for binding to sTNF. Conversely, TNFR1 internalization rate constant k_{int1}, TNFR1 density in both compartments, equilibrium dissociation constant of TNFR1 (K_{d1}), and the outer compartment fraction of granuloma f negatively correlate with this same output. Although greater affinity of TNFR1 for sTNF enhances the level of sTNF binding to TNFR1 in the core of granuloma (output 2) as the major TNF-producing compartment, it reduces the access of TNFR1 on the membrane of cells in the outer compartment to diffusing sTNF (output 3). Thus, increasing the effective diffusion coefficient of sTNF in the granuloma increases the sTNF-bound fraction of receptors in the outer compartment. Diffusion of shed sTNF-bound TNFR2 complex from the inner compartment to the outer compartment of granuloma can also explain the positive correlation of TNFR2 density in the core with the sTNF-bound fraction of TNFR1 in the outer compartment (output 3), while it is negatively correlated with the same response in the inner compartment (output 2) due to competition between receptors for binding to sTNF. Significant correlations of model parameters with the level of free sTNF concentration in the granuloma (output 4) are qualitatively similar to their correlations with output 1, except for K_{d1} and sTNF/TNFR1 association rate constant k_{on1} that are, respectively, positively and negatively correlated with output 4.

Applicability of the model will require that we have accurate values of the significant parameters found via sensitivity analysis or else we will have to consider the

wide range of possibilities hinted at in Fig. 2.3. There are two different classes of these significant parameters. One class includes parameters associated with TNF/TNFR interactions and intracellular trafficking. The parameters of this class have been theoretically estimated or experimentally measured in multiple cell lines expressing TNF receptors. These studies show that the time scales and thus the rates of significant TNF/TNFR-associated processes identified above are consistent over different cell lines. For example, the obtained TNF/TNFR association and dissociation rate constants for TNFR1 and TNFR2 on a variety of cell lines, including U937, HeLa, and KYM-1 cells were found to be similar and consistent with the data on mouse embryonic fibroblasts [42,67]. Further, internalization of the sTNF/TNFR1 complex has been shown to occur with a half-time of 10-20 minutes which gives an average value of 7.7×10^{-4} s^{-1} for the TNFR1 internalization rate constant [42,44]. The values of these parameters are given in Table 2.2 (in parentheses). The second class of significant parameters are the ones for which no experimental values are available and include cellular fractions, the rate of mTNF synthesis and TNFR densities on immune cells in a TB granuloma. Thus, we measure the values of these parameters in an experimental model of TB granuloma.

2.3.3 Cellular composition of PPD bead granulomas

We used an artificial model of TB granuloma developed in mice following injection of PPD-coated beads to measure model parameters of interest. To identify the cellular composition of PPD bead granulomas, multi-color flow cytometry with fluorescing antibodies for specific immune cell surface markers was used as described in Methods. Fig. 2.4 indicates experimental data on fractions of the major granuloma-comprising

immune cells, including DCs, macrophages, T cells and B cells, that compose approximately 80% of the total cell population of day 2 and day 4 granulomas. Macrophages and B cells were observed to be the largest cell populations in isolated granulomas. A small but statistically significant increase ($p < 0.001$) in the percentage of both CD4 and CD8 T cells which represent the adaptive immune response was observed in day 4 granulomas compared with day 2 granulomas. On the other hand, macrophages and DCs were shown to form a slightly smaller portion of day 4 granuloma cell population. The percentage of B cells in granulomas did not significantly change from day 2 to day 4. Cellular composition of the granuloma and the increase in the level of T cell recruitment with time are qualitatively consistent with the experimental data on the infiltration of immune cells into the lungs of mice infected with Mtb as well as data on granulomas induced in lungs of Mtb-infected monkeys, although T cell recruitment occurs in a shorter time scale for PPD bead granulomas [7,9].

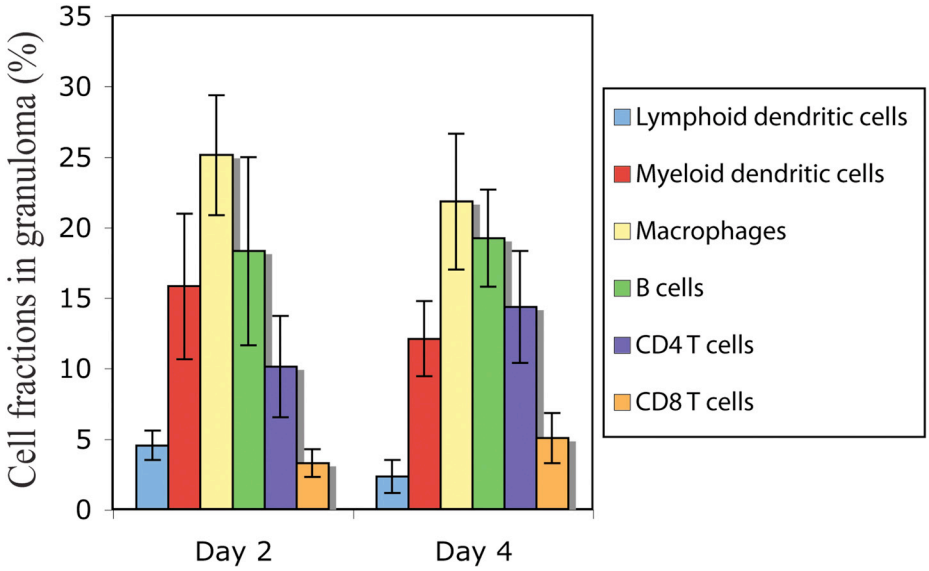

Fig. 2.4 Cellular fractions in PPD bead granulomas at 2 and 4 days of granuloma formation in thirty CBA/J mice quantified by multi-color flow cytometry. Results are expressed as the percentage of each cell type in the total population of granuloma cells. Error bars represent standard deviation from the mean.

2.3.4 Quantification of TNFR densities

The average numbers of TNFR1 and TNFR2 molecules on the membrane of day 2 and day 4 granuloma-comprising immune cells were quantified by flow cytometry using standard PE-conjugated beads as described in Methods. DCs, macrophages and B cells were found to be the major TNFR-expressing cells in granulomas with average TNFR1 density of the order of 10^3 molecules per cell and a lower level of expression for TNFR2 (Table 2.6). Further, except for lymphoid DCs and B cells that show a significant decrease with time, the level of TNFR expression was similar for day 2 and day 4 granuloma cells.

Table 2.6 Average numbers of TNF receptors per cell quantified by multi-color flow cytometry for different types of granuloma-comprising immune cells isolated from 15 mice.

Cell type	Number of receptors at day 2		Number of receptors at day 4	
	TNFR1	TNFR2	TNFR1	TNFR2
Lymphoid dendritic cells	4600 ± 1100	1900 ± 600	1700 ± 500	1700 ± 1100
Myeloid dendritic cells	1500 ± 400	500 ± 200	1700 ± 400	700 ± 300
Macrophage	1000 ± 300	400 ± 200*	1000 ± 300	500 ± 200
B cells	1100 ± 600	900 ± 200	500 ± 200	200 ± 100*
CD4 T cells	300 ± 100*	400 ± 100*	200 ± 100*	200 ± 100*
CD8 T cells	300 ± 100*	200 ± 100*	100 ± 100*	200 ± 100*

* PE fluorescence intensity was smaller than the fluorescence intensity of the QuantiBRITE standard beads with the smallest number of conjugated PE molecules.

2.3.5 Quantification of the rate of mTNF synthesis

Using TAPI-1 as a TACE inhibitor to suppress the release of TNF from the membrane of TNF-expressing cells over a 3 hour time course, the rates of mTNF synthesis k_{synth} by different types of immune cells in granulomas isolated at 2 and 4 days were measured by flow cytometry as described in Methods. TAPI-1 was shown to partially suppress the TACE-mediated release of TNF from the cell membrane, so that the rate constant for TNF release after addition of TAPI-1 k'_{TACE} was not zero. Thus, the rate of mTNF synthesis by each cell type was quantified by fitting experimental data to Equation 2.10 as described in Methods and shown in Fig. 2.5. The results of the fit for k_{synth}, k_{TACE} and k'_{TACE} from three experiments are averaged and reported in Table 2.7. Interestingly, PPD-bead granuloma T cells and B cells did not express quantifiable amounts of mTNF, although proinflammatory T cells have been reported to produce TNF in Mtb-infected mice [79]. To our knowledge, this is the first experimental quantification of the rate of TNF synthesis by granuloma-comprising immune cells.

Table 2.7 Average rate of mTNF synthesis and average rate constant for TNF release quantified by multi-color flow cytometry for different types of TNF-expressing immune cells (isolated from 10 mice) isolated from day 2 and 4 granulomas.

Cell type	k_{synth} (#/cell.sec) day 2	k_{synth} (#/cell.sec) day 4	k_{TACE} (s^{-1})*	k'_{TACE} (s^{-1})*
Lymphoid dendritic cells	1.01 ± 0.74	0.81 ± 0.35	$(4.23 \pm 1.23) \times 10^{-4}$	$(3.27 \pm 0.87) \times 10^{-4}$
Myeloid dendritic cells	0.26 ± 0.21	0.21 ± 0.05	$(4.49 \pm 1.86) \times 10^{-4}$	$(3.09 \pm 1.45) \times 10^{-4}$
Macrophage	0.17 ± 0.09	0.15 ± 0.03	$(4.55 \pm 1.36) \times 10^{-4}$	$(3.18 \pm 1.16) \times 10^{-4}$

* Values of k_{TACE} and k'_{TACE} were averaged over all data on day 2 and day 4 granuloma cells.

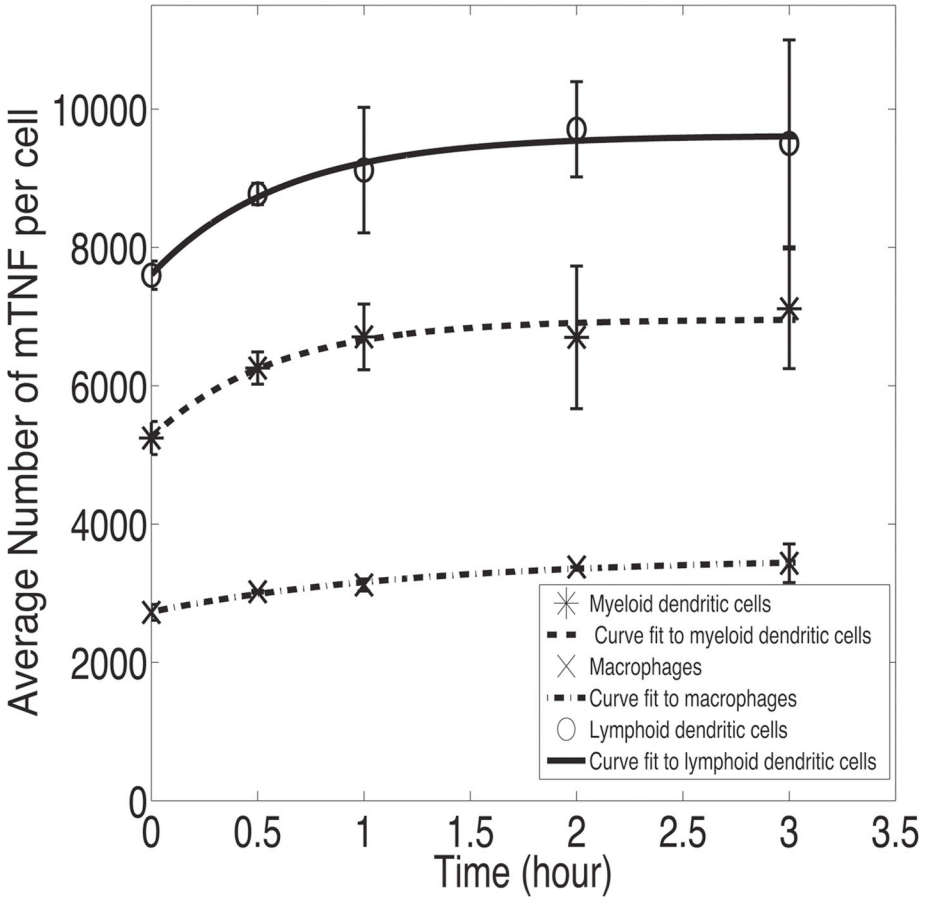

Fig. 2.5 Quantification of the rate of mTNF synthesis by each cell type. Experimental data on the number of mTNF molecules on the surface of each cell type after addition of TAPI-1 were fitted to Equation 2.10 to estimate k_{synth} for that cell type. Displayed data represent TNF synthesis by day 4 granuloma cells for three hours in the presence of TAPI-1. Error bars indicate standard deviations. Values of R^2 for curve fitting for mDCs, macrophages and pDCs are 0.97, 0.99 and 0.98, respectively.

2.3.6 TNF/TNFR binding and trafficking dynamics and cellular organization control TNF availability within a granuloma

In general, the differences between experimental data on day 2 and 4 granulomas, although significant, are fairly small. Thus, using our data on cellular composition, cell-specific rates of mTNF synthesis and TNFR densities from day 4 PPD-bead granulomas as well as literature data on TNF/TNFR kinetic parameter estimates as inputs to our model, we studied mechanisms that control steady state TNF availability within a TB granuloma. Here we illustrate the role of two important factors, (i) molecular level processes governing TNF/TNFR interactions and intracellular dynamics and (ii) cellular organization within the granuloma, in regulating TNF availability within a granuloma.

To study the influence of TNF-associated molecular level processes on the availability of TNF, and thus TNF signaling within a TB granuloma, the distribution of sTNF in a granuloma was calculated by comparing modeling results in the presence of TNF intracellular trafficking with results of the model in the absence of TNF/TNFR internalization and shedding or TNF binding to TNF receptors. Fig. 2.6A compares the spatial distributions of free sTNF at steady state for each case. TNF/TNFR reactions and interactions significantly affect the available amount of sTNF in a granuloma. Reversible binding of sTNF to cell surface receptors can reduce the amount of available extracellular sTNF in the granuloma by approximately two-fold. However, other molecular processes including the intracellular trafficking of TNF lead to a dramatic decrease of up to two orders of magnitude in the extracellular concentration of sTNF compared with the case in which TNF is produced and diffuses in a granuloma without binding to cell surface receptors. This result is consistent with experimental data on the

role of TNFRs in modulating the biologic activity of TNF where a reduction of more than one order of magnitude in serum TNF levels of LPS-challenged control mice compared with TNFR-deficient mice has been observed [17].

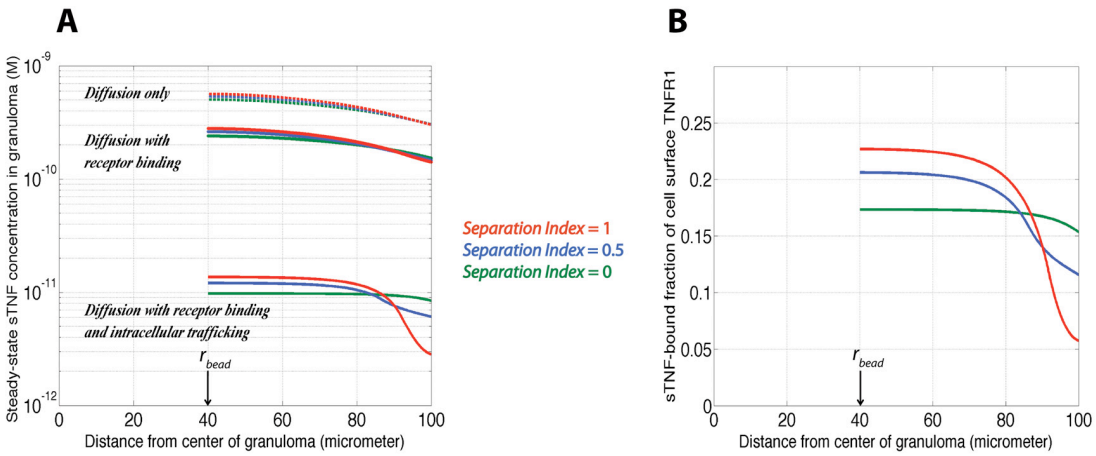

Fig. 2.6 Granuloma model predictions: for (A) the effects of receptor binding, intracellular trafficking of TNF and cellular organization within granuloma (represented by separation) on the steady state spatial distribution of free sTNF in a granuloma, and (B) the effect of separation between different cell types in a granuloma on the spatial concentration of sTNF-bound cell surface TNFR1. Parameter values for the rate of mTNF synthesis (and similarly for TNFR densities) in each compartment were computed via Equations 2.6 and 2.7, using experimental data for day 4 granulomas presented in Fig. 2.4 and Tables 2.6 and 2.7. Other parameter values are as listed in Table 2.2. The qualitative aspects of these plots are similar for day 2 granulomas.

Numerous studies have shown that TB granulomas, especially in humans as well as guinea pig and non-human primate models [9,10], form as organized structures composed of a core of macrophages and DCs surrounded by a ring of lymphocytes. However, the effect of such a specific cellular organization on trafficking and availability of cytokines, in particular TNF, in the granuloma microenvironment has not been studied. To demonstrate the effect of spatial organization of immune cells on TNF availability in a granuloma, we performed simulations for varying levels of separation index (*s*) between populations of macrophages/DCs and lymphocytes within the granuloma (see Methods for more information). Our modeling results show that in the

presence of TNF/TNFR binding and intracellular trafficking, the organization of cells within a granuloma significantly influences the availability of TNF. As such, greater levels of separation between macrophages/DCs and lymphocytes (separation index close to or at 1) result in steeper gradients of TNF concentration in the granuloma (Fig. 2.6A). When the granuloma is organized in this way, the granuloma core (which is completely or almost completely composed of macrophages and DCs) is exposed to a higher concentration of TNF, while the mantle (which is composed of lymphocytes) is exposed to a lower concentration of TNF in comparison with the case of a zero separation index (reflecting a well-mixed cellular organization). A similar effect is observed for the number of sTNF-bound cell surface TNFR1 that controls the type and level of TNF-induced cell response in the granuloma (Fig. 2.6B). For sufficiently large separation indices, a greater fraction of TNFR1 molecules on the membrane of macrophages and DCs in the granuloma core bind to sTNF in comparison with lymphocytes in the outer compartment. These results demonstrate that molecular level processes, including TNF intracellular trafficking and TNF receptor recycling, together with how immune cells (with different levels of TNF and TNF receptor expression) are organized within the granuloma control the amount of available TNF for each cell type and thus cell-specific TNF signaling.

2.3.7 Effect of TNF-neutralizing drugs on availability of TNF within a granuloma

In order to study the effects of TNF-neutralizing drugs with various properties on the availability of TNF in a granuloma, we model a hypothetical TNF-neutralizing drug as an agent that diffuses from surrounding tissue into the granuloma, binds to TNF

molecules and inhibits sTNF from binding to TNF receptors. We investigated how the efficiency of TNF neutralization (defined by Equation 2.9) by anti-TNF drugs is influenced by drug properties, including drug/TNF association and dissociation kinetics, drug ability to bind to mTNF, and drug/TNF binding stoichiometry. Three classes of hypothetical drugs with defined properties were modeled loosely based on properties of human TNF-neutralizing drugs (e.g. infliximab and etanercept) and their efficiencies of TNF neutralization were compared. Since the general behavior of all classes of drugs was shown to be independent of cellular organization in the granuloma (data not shown), model results for a separation index of one are discussed below.

Class 1: drug binding to only sTNF at a binding ratio of 1:1

We first consider a drug that binds to sTNF with a binding ratio of 1:1, inhibiting it from binding to both TNFR1 and TNFR2. The effects of varying association and dissociation rate constants ($k_{on\_sTNF/drug}$ and $k_{off\_sTNF/drug}$) for sTNF and drug are shown in Fig. 2.7A. Model results show that depending on sTNF/drug association and dissociation rate constants, 0% - 50% of total available sTNF in a granuloma can be neutralized. As expected, drugs with greater affinities for sTNF more efficiently neutralize TNF in the granuloma. Interestingly, increasing $k_{on\_sTNF/drug}$ without changing drug affinity leads to an increase in the drug neutralization efficiency (Fig. 2.7D, Class 1). This is because drugs compete with cell surface TNFRs for binding to sTNF and thus a drug with a greater $k_{on\_sTNF/drug}$ can neutralize larger amounts of sTNF.

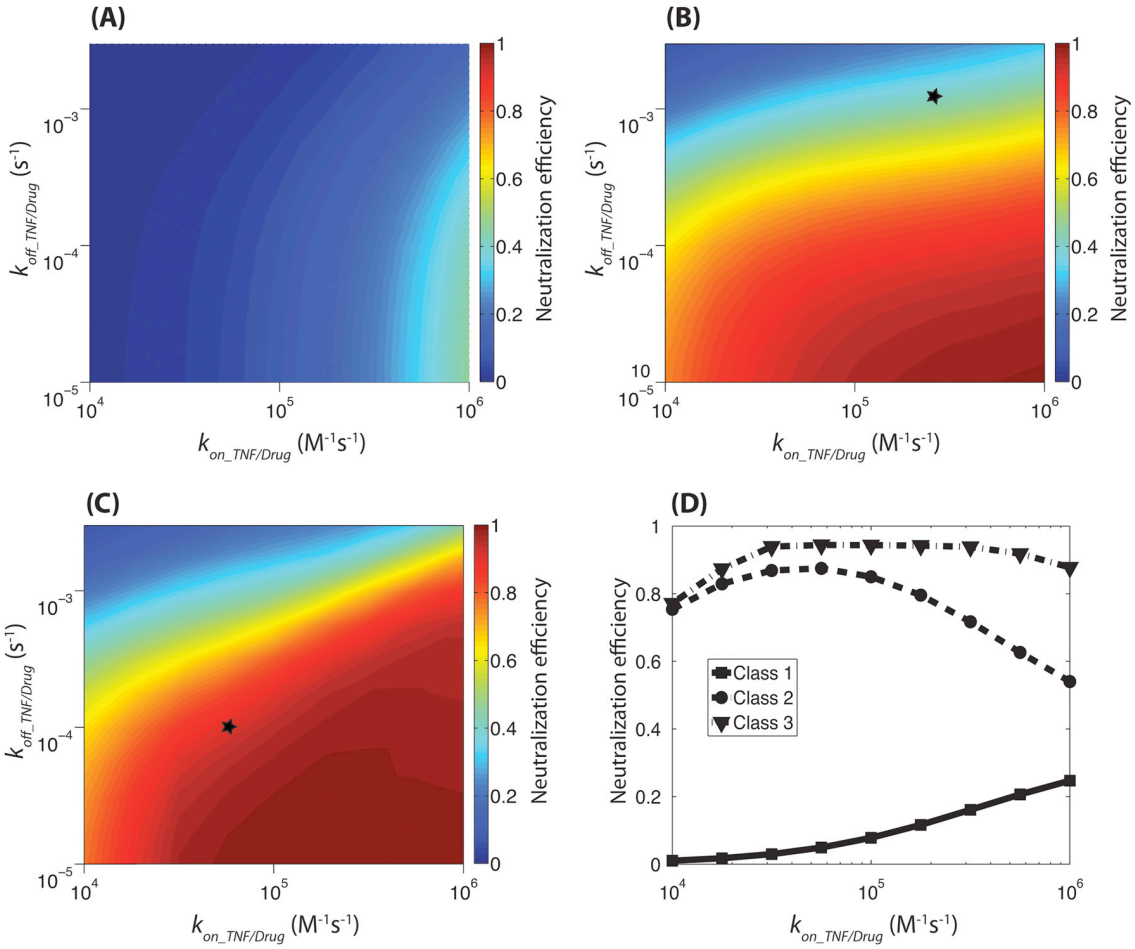

Fig. 2.7 Model predictions for the effect of TNF-neutralizing drugs with various properties on the availability of TNF within a granuloma. (A) Class 1: the drug can only bind to sTNF with a binding ratio of 1:1. (B) Class 2: the drug can bind to both mTNF and sTNF with a binding ratio of 1:1. The star shows the location of a drug with TNF binding kinetics similar to etanercept. (C) Class 3: the drug can bind to both mTNF and sTNF with a binding ratio of 3:1. The star shows the location of a drug with TNF binding kinetics similar to infliximab. (D) Model predictions for the effect of TNF/drug association rate constant on neutralization efficiency of drugs of different classes but identical affinities ($K_{d\_Drug} = k_{off\_TNF/Drug}/k_{on\_TNF/Drug} = 10^{-9}$ M). Model parameter values are the same as Fig. 2.6. TNF neutralization-associated parameter values are as listed in Table 2.3.

Class 2: drug binding to both sTNF and mTNF at a binding ratio of 1:1

We next consider a drug that binds to both sTNF and mTNF with a binding ratio of 1:1. We assumed identical association and dissociation rate constants for drug binding to mTNF and sTNF. TACE activity was considered independent of whether mTNF is bound to drug or not. Model results show that at all values of TNF/drug association and

dissociation rate constants, a drug with the ability to bind to both sTNF and mTNF is more efficient in neutralizing TNF in a granuloma compared with a drug that can only bind to sTNF (compare Fig. 2.7A and 2.7B). In other words, our model results demonstrate that even if sTNF is considered as the primary form of TNF that controls TNF-mediated signaling in granuloma cells, binding to mTNF is an important determinant of TNF neutralization power of the drug. This can be explained by rapid binding of diffusing drug molecules to mTNF in the absence of competition effects of cell surface TNFRs. However, similar to the case of Class 1 drug tested, TNF neutralization most efficiently occurs for a drug with the highest affinity for TNF.

Interestingly, among drugs with a constant affinity of $K_d = 10^{-9}$ M there is an optimum in neutralization efficiency that occurs for a drug with approximate values of $k_{on\_TNF/drug} = 5.6\times10^{4}$ $M^{-1}s^{-1}$ and $k_{off\_TNF/drug} = 5.6\times10^{-5}$ s^{-1} (Fig. 2.7D, Class 2). To explain this result, we need to note that an mTNF/drug complex can be released into extracellular spaces due to TACE activity and then acts as a source for sTNF in the granuloma. When TNF/drug association is sufficiently rapid, drug binding to mTNF occurs before mTNF can be released into extracellular spaces. Thus, a significant proportion of sTNF in the granuloma is produced only after dissociation of sTNF from mTNF/drug complexes that are released from the cell membrane. In other words, the drug exerts a delay in the release of available sTNF from the cell membrane. Under these conditions, increasing TNF/drug dissociation rate constant increases the amount of sTNF dissociated from extracellular TNF/drug complexes and reduces the efficiency of TNF neutralization. This can explain why a drug of Class 2 type with intermediate values of TNF association and dissociation rate constants can more efficiently neutralize

TNF compared with drugs of the same Class with the same affinity for TNF but higher values of these rate constants.

Class 3: drug binding to both sTNF and mTNF at a binding ratio of 3:1

Finally, we considered a drug that binds to both trimeric sTNF and mTNF molecules that possess three binding sites for the drug. An sTNF molecule with either one, two or three drug molecules bound is neutralized and not able to bind TNFR1 or TNFR2. This assumption helps us compare modeling results for TNF neutralization by different classes of drugs. Further, this assumption is consistent with experimental data indicating that only trimeric TNF is biologically active and that both monomeric TNF and artificially prepared dimeric TNF do not efficiently trigger TNF signaling in cells [80,81]. We investigated the effect of multiple binding sites for drug binding to TNF and formation of larger drug/TNF complexes on the efficiency of TNF neutralization in a granuloma. Model results show that at large values of TNF/drug association rate constant, a higher binding ratio (i.e. 3:1) increases the efficiency of TNF neutralization in comparison to a drug of Class 2 type with a binding ratio of 1:1 (compare Fig. 2.7B and 2.7C). However, binding stoichiometry does not significantly influence the level of TNF neutralization at low values of TNF/drug association rate constant, where TNFRs dominate the drug in competition for binding to sTNF (Fig. 2.7C). An optimum in neutralization efficiency amongst Class 3 drugs of the same affinity $K_d = 10^{-9}$ occurs in the same range of TNF/drug association and dissociation rate constants as observed for Class 2 (Fig. 2.7D).

2.4 Discussion

We have developed a two-compartment mathematical model that captures the structural features of a TB granuloma based on an experimental mouse PPD bead model and also includes molecular processes that govern the intracellular and extracellular trafficking of TNF. The model includes fine grain details at the level of TNF receptor dynamics, while using a coarse grain description for cellular level details representing a snapshot in time of a granuloma comprised of a static number of immune cells. This is based on a significant difference between the time-scale of TNF/TNFR associated molecular processes studied here and cellular level events that may change the structure of a granuloma (e.g. cell recruitment, migration and death).

The detailed consideration of synthesis, diffusion, receptor binding and intracellular trafficking of TNF within the heterogeneous three-dimensional structure of a granuloma distinguishes our model from a previous study by Marino *et al* on the role of TNF in host defense against TB [28]. The model developed by Marino *et al* describes the temporal dynamics of the immune response to Mtb infection in active and latent phases within a time course of 500 days by inclusion of TNF immunological functions on macrophages and T cells. However, we focus in this study on a snapshot in time of a granuloma to study the steady state spatial distribution of available TNF. We used results of our model sensitivity analysis as a novel tool to lead experiments to measure critical model parameters in artificial granulomas induced in the lungs of mice following injection of mycobacterial PPD-coated beads. Finally, whereas TNF neutralization has been simulated by Marino *et al* via removing fractions of available sTNF and/or mTNF, we studied the effects of TNF-neutralizing drugs by incorporation of their mTNF and/or

sTNF binding kinetics and stoichiometry.

Model analysis helped us characterize two mechanisms for controlling the availability of TNF within a granuloma. These mechanisms include intracellular trafficking of TNF via internalization of recyclable TNFRs, and specific cellular organization within the granuloma, i.e. the level of separation between different classes of cells. Further, we demonstrated that for the resulting effect of cellular organization on spatial distribution of available TNF in the granuloma to be significant, intracellular trafficking of TNF is essential (Fig. 2.6A). Hence, the spatial heterogeneity in the level of TNF and TNFR expression, and thus the amount of TNF internalization that occurs as a result of specific organization of different cell types in the granuloma controls the spatial distribution of the available amount of TNF for signaling for each specific cell type.

For sufficiently large values of the separation index in the granuloma, the model predicts significantly greater levels of sTNF binding to TNFR1 on the membrane of macrophages/DCs in the core compared with lymphocytes in the mantle (Fig. 2.6B), which might be important for spatially coordinating the TNF-induced immunological functions for cells in a granuloma. Rangamani and Sirovich have recently shown via mathematical modeling that the induction of the two major TNF-induced signaling pathways, the caspase-mediated apoptotic pathway and the NF-κB-mediated survival pathway, are primarily controlled at the level of TNF/TNFR1 interactions [82]. As such, very low initial concentrations of TNF (i.e. less than 10^{-11} M) that can activate only a limited number of cell surface TNFR1 molecules are not capable of inducing apoptosis in the cells [67]. However, efficient NF-κB activation has been reported at TNF

concentrations as low as 10^{-13} M based on both modeling [83] and experimental analysis of TNF signaling in HL60 cells and 3T3 mouse embryonic fibroblasts [56,84]. Further, TNF/TNFR2 interactions have been shown to enhance TNFR1-dependent activation of caspase-mediated apoptotic pathway [85,86]. These suggest a differential induction of apoptotic and survival signaling pathways between the granuloma core that is comprised of macrophages/DCs and the surrounding ring of lymphocytes.

The hypothesis of differential induction of TNF-mediated signaling pathways for classical granulomas such as ones observed particularly in human, nonhuman primate and guinea pig models of TB [9,10] has immunological implications. Whereas TNF-induced apoptosis of granuloma core macrophages that contain pathogenic mycobacteria is required for antigen cross-presentation and subsequent T cell priming and helps eliminate the pathogen [87,88], lymphocyte (especially CD4 and CD8 T cell) death by TNF-induced apoptosis has been reported as one of the important components of an ineffective immune response against mycobacterial infections [89,90]. However, the TNF-induced survival signaling pathway is required for retaining T cells at the developing granuloma site where they produce IFN-γ, activating macrophages in synergy with TNF to kill intracellular infections [91]. Thus, our novel hypothesis is that a separate cellular organization in the granuloma may favor an efficient immune response via spatially coordinating the TNF-induced immunological functions in the granuloma (Fig. 2.8). Consistent with our hypothesis, very few apoptotic lymphocytes in classical TB granulomas induced in the guinea pig have been detected and most apoptotic cells have been seen close to the core of granulomas [92]. Further, because cellular organization undergoes dynamic changes with granuloma development and at

different stages of immune response (innate versus adaptive) to TB infection, it can be a factor controlling the diverse activities of TNF according to the stage of infection in the lung tissue.

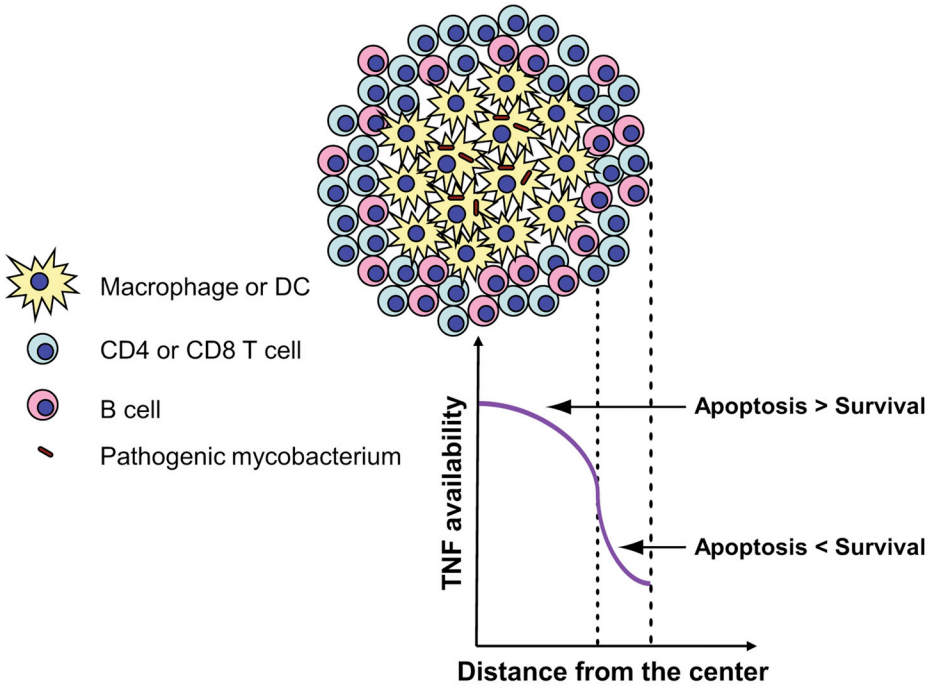

Fig. 2.8 Spatial coordination of the TNF-induced immunological functions in a classical granuloma composed of a core of macrophages and DCs surrounded by a ring of lymphocytes. Great availability of TNF in the core of granuloma (together with TNF-induced TNFR2 activation) can turn on the TNFR1-dependent caspase-mediated apoptotic pathway that favors antigen cross-presentation as well as elimination of the pathogen inside the granuloma. Low level of TNF availability in the mantle of granuloma is sufficient to turn on the NF-κB signaling which favors cell survival and expression of pro-inflammatory genes but not the apoptotic pathway.

Finally, we used the model to predict and analyze the effects of TNF-neutralizing drugs with different properties on the availability of TNF within a developed granuloma. Average serum concentration of two murine analogs of human TNF blockers, infliximab and etanercept, after a single dose of drug, has been reported to be on the order of 10^{-7}-10^{-6} M [63]. Using this reported concentration to estimate the tissue level concentration

of these drugs (Table 2.3), we demonstrated that the efficiency of TNF neutralization within the granuloma not only depends on the affinity of the drug for TNF, but also on the ability of the drug to bind to mTNF versus sTNF, the rate constants for drug/TNF association and dissociation reactions as well as the drug/TNF binding stoichiometry (Fig. 2.7).

We can use these modeling results to generate a hypothesis regarding experimentally observed differences in the neutralizing power of the two major human TNF blockers, infliximab and etanercept, based on their TNF binding specificities. Infliximab is a chimeric monoclonal TNF antibody that binds potently to both sTNF and mTNF. Up to three infliximab molecules can bind to one trimeric TNF molecule. Etanercept is a TNF receptor p75-IgG fusion protein that can also bind to both trimeric sTNF and mTNF, however, with a binding molar ratio of 1:1 and has greater TNF association and dissociation rate constants in comparison with infliximab [60,65,66]. Hence, based on the classification of TNF-neutralizing drugs we presented in this paper, infliximab and etanercept can be considered as drugs of Class 3 and Class 2 types, respectively. Given the TNF binding stoichiometries and reported TNF association/dissociation rate constants for infliximab and etanercept (infliximab: $k_{on\_TNF/drug} = 5.7 \times 10^4\ M^{-1}s^{-1}$, $k_{off\_TNF/drug} = 1.1 \times 10^{-4}\ s^{-1}$ and etanercept: $k_{on\_TNF/drug} = 2.6 \times 10^5\ M^{-1}s^{-1}$, $k_{off\_TNF/drug} = 1.3 \times 10^{-3}\ s^{-1}$) [65], our granuloma model predicts TNF neutralization efficiencies of 0.90 and 0.39 for drugs with identical TNF binding properties to infliximab and etanercept, respectively; these efficiencies are marked with stars on Fig. 2.7B, C. This is consistent with the reported higher TNF neutralization power of the TNF antibody (analog of infliximab) in comparison with the TNF receptor

fusion molecule (analog of etenercept) in chronically Mtb-infected mice [93]. Although decreased penetration of the receptor fusion molecule into the lungs compared with antibody has been hypothesized to be a reason for the higher TNF neutralization power of antibody [93], we did not observe a significant change in the neutralization efficiency of simulated drug analogs by changing drug permeability in the granuloma (k_c) by up to two order of magnitude (data not shown). Thus, the difference in binding properties of infliximab and etanercept must be considered when explaining the higher rate of TB reactivation induced from infliximab treatments in comparison with etanercept, although we anticipate that differential functional properties such as induction of apoptosis in TNF-producing cells by infliximab but not etanercept further influence the outcome of anti-TNF treatments [58,94].

Although we have focused this study primarily on molecular and cellular scale processes within a snapshot of time in a granuloma, it will be necessary to consider multiple time and length scales (including dynamics in the lymphatic system) to further examine the role of TNF and anti-TNF therapies in the process of granuloma development and maintenance [95]. This is the focus of our studies as described in Chapters 3-5.

2.5 References

1. Mortellaro A, Robinson L, Ricciardi-Castagnoli P (2009) Spotlight on mycobacteria and dendritic cells: Will novel targets to fight tuberculosis emerge?. EMBO Mol Med 1: 19-29.

2. Algood HM, Chan J, Flynn JL (2003) Chemokines and tuberculosis. Cytokine Growth Factor Rev 14: 467-477.

3. Russell DG (2007) Who puts the tubercle in tuberculosis?. Nat Rev Microbiol 5: 39-47.

4. Flynn JL (2004) Immunology of tuberculosis and implications in vaccine development. Tuberculosis (Edinb) 84: 93-101.

5. Morel PA, Ta'asan S, Morel BF, Kirschner DE, Flynn JL (2006) New insights into mathematical modeling of the immune system. Immunol Res 36: 157-165.

6. Davis JM, Ramakrishnan L (2008) "The very pulse of the machine": The tuberculous granuloma in motion. Immunity 28: 146-148.

7. Tsai MC, Chakravarty S, Zhu G, Xu J, Tanaka K, et al. (2006) Characterization of the tuberculous granuloma in murine and human lungs: Cellular composition and relative tissue oxygen tension. Cell Microbiol 8: 218-232.

8. Ulrichs T, Kosmiadi GA, Trusov V, Jorg S, Pradl L, et al. (2004) Human tuberculous granulomas induce peripheral lymphoid follicle-like structures to orchestrate local host defence in the lung. J Pathol 204: 217-228.

9. Lin PL, Pawar S, Myers A, Pegu A, Fuhrman C, et al. (2006) Early events in mycobacterium tuberculosis infection in cynomolgus macaques. Infect Immun 74: 3790-3803.

10. Turner OC, Basaraba RJ, Frank AA & Orme IM (2003) in *Granulomatous infections and inflammations: cellular and molecular mechanisms,* ed Boros DL (ASM Press, Washington, D.C.), pp 65-84.

11. Egen JG, Rothfuchs AG, Feng CG, Winter N, Sher A, et al. (2008) Macrophage and T cell dynamics during the development and disintegration of mycobacterial granulomas. Immunity 28: 271-284.

12. Ulrichs T, Kaufmann SH (2006) New insights into the function of granulomas in human tuberculosis. J Pathol 208: 261-269.

13. Korner H, Sedgwick JD (1996) Tumour necrosis factor and lymphotoxin: Molecular aspects and role in tissue-specific autoimmunity. Immunol Cell Biol 74: 465-472.

14. Newton RC, Solomon KA, Covington MB, Decicco CP, Haley PJ, et al. (2001) Biology of TACE inhibition. Ann Rheum Dis 60 Suppl 3: iii25-32.

15. Smith RA, Baglioni C (1987) The active form of tumor necrosis factor is a trimer. J Biol Chem 262: 6951-6954.

16. Vandenabeele P, Declercq W, Beyaert R, Fiers W (1995) Two tumour necrosis factor receptors: Structure and function. Trends Cell Biol 5: 392-399.

17. Peschon JJ, Torrance DS, Stocking KL, Glaccum MB, Otten C, et al. (1998) TNF receptor-deficient mice reveal divergent roles for p55 and p75 in several models of inflammation. J Immunol 160: 943-952.

18. Flynn JL, Goldstein MM, Chan J, Triebold KJ, Pfeffer K, et al. (1995) Tumor necrosis factor-alpha is required in the protective immune response against mycobacterium tuberculosis in mice. Immunity 2: 561-572.

19. Keane J, Shurtleff B, Kornfeld H (2002) TNF-dependent BALB/c murine macrophage apoptosis following mycobacterium tuberculosis infection inhibits bacillary growth in an IFN-gamma independent manner. Tuberculosis (Edinb) 82: 55-61.

20. Keane J, Balcewicz-Sablinska MK, Remold HG, Chupp GL, Meek BB, et al. (1997) Infection by mycobacterium tuberculosis promotes human alveolar macrophage apoptosis. Infect Immun 65: 298-304.

21. Algood HM, Lin PL, Yankura D, Jones A, Chan J, et al. (2004) TNF influences chemokine expression of macrophages in vitro and that of CD11b+ cells in vivo during mycobacterium tuberculosis infection. J Immunol 172: 6846-6857.

22. Lin PL, Plessner HL, Voitenok NN, Flynn JL (2007) Tumor necrosis factor and tuberculosis. J Investig Dermatol Symp Proc 12: 22-25.

23. Chakravarty SD, Zhu G, Tsai MC, Mohan VP, Marino S, et al. (2008) Tumor necrosis factor blockade in chronic murine tuberculosis enhances granulomatous inflammation and disorganizes granulomas in the lungs. Infect Immun 76: 916-926.

24. Clay H, Volkman HE, Ramakrishnan L (2008) Tumor necrosis factor signaling mediates resistance to mycobacteria by inhibiting bacterial growth and macrophage death. Immunity 29: 283-294.

25. Keane J, Gershon S, Wise RP, Mirabile-Levens E, Kasznica J, et al. (2001) Tuberculosis associated with infliximab, a tumor necrosis factor alpha-neutralizing agent. N Engl J Med 345: 1098-1104.

26. Winthrop KL (2006) Risk and prevention of tuberculosis and other serious opportunistic infections associated with the inhibition of tumor necrosis factor. Nat Clin Pract Rheumatol 2: 602-610.

27. Lin PL, Myers A, Smith L, Bigbee C, Bigbee M, et al. (2010) Tumor necrosis factor neutralization results in disseminated disease in acute and latent mycobacterium tuberculosis infection with normal granuloma structure in a cynomolgus macaque model. Arthritis Rheum 62: 340-350.

28. Marino S, Sud D, Plessner H, Lin PL, Chan J, et al. (2007) Differences in reactivation of tuberculosis induced from anti-TNF treatments are based on bioavailability in granulomatous tissue. PLoS Comput Biol 3: 1909-1924.

29. Ray JC, Flynn JL, Kirschner DE (2009) Synergy between individual TNF-dependent functions determines granuloma performance for controlling mycobacterium tuberculosis infection. J Immunol 182: 3706-3717.

30. Lauffenburger D, Linderman JJ (1993) Receptors: models for binding, trafficking, and signaling. New York: Oxford University Press.

31. Rippley RK, Stokes CL (1995) Effects of cellular pharmacology on drug distribution in tissues. Biophys J 69: 825-839.

32. Tsujimoto M, Yip YK, Vilcek J (1985) Tumor necrosis factor: Specific binding and internalization in sensitive and resistant cells. Proc Natl Acad Sci U S A 82: 7626-7630.

33. Imamura K, Spriggs D, Kufe D (1987) Expression of tumor necrosis factor receptors on human monocytes and internalization of receptor bound ligand. J Immunol 139: 2989-2992.

34. Vuk-Pavlovic S, Kovach JS (1989) Recycling of tumor necrosis factor-alpha receptor in MCF-7 cells. FASEB J 3: 2633-2640.

35. Pan W, Tu H, Yu C, Hsuchou H, Yang Y, et al. (2007) Differential role of TNF receptors in cellular trafficking of intact TNF. Cell Physiol Biochem 20: 559-568.

36. Bajzer Z, Myers AC, Vuk-Pavlovic S (1989) Binding, internalization, and intracellular processing of proteins interacting with recycling receptors. A kinetic analysis. J Biol Chem 264: 13623-13631.

37. Chensue SW & Kunkel SL (2003) in *Granulomatous infections and inflammations: cellular and molecular mechanisms,* ed Boros DL (ASM Press, Washington, D.C.), pp 29-64.

38. Chensue SW, Warmington K, Ruth J, Lincoln P, Kuo MC, et al. (1994) Cytokine responses during mycobacterial and schistosomal antigen-induced pulmonary granuloma formation. production of Th1 and Th2 cytokines and relative contribution of tumor necrosis factor. Am J Pathol 145: 1105-1113.

39. Chensue SW, Warmington KS, Ruth JH, Lincoln P, Kunkel SL (1995) Cytokine function during mycobacterial and schistosomal antigen-induced pulmonary granuloma formation. local and regional participation of IFN-gamma, IL-10, and TNF. J Immunol 154: 5969-5976.

40. Chensue SW, Warmington K, Ruth JH, Lukacs N, Kunkel SL (1997) Mycobacterial and schistosomal antigen-elicited granuloma formation in IFN-gamma and IL-4 knockout mice: Analysis of local and regional cytokine and chemokine networks. J Immunol 159: 3565-3573.

41. Qiu B, Frait KA, Reich F, Komuniecki E, Chensue SW (2001) Chemokine expression dynamics in mycobacterial (type-1) and schistosomal (type-2) antigen-elicited pulmonary granuloma formation. Am J Pathol 158: 1503-1515.

42. Grell M, Wajant H, Zimmermann G, Scheurich P (1998) The type 1 receptor (CD120a) is the high-affinity receptor for soluble tumor necrosis factor. Proc Natl Acad Sci U S A 95: 570-575.

43. Adamson GM, Billings RE (1994) Tumor necrosis factor: Receptor binding and expression of receptors in cultured mouse hepatocytes. J Pharmacol Exp Ther 269: 367-373.

44. Higuchi M, Aggarwal BB (1994) TNF induces internalization of the p60 receptor and shedding of the p80 receptor. J Immunol 152: 3550-3558.

45. Aderka D, Engelmann H, Maor Y, Brakebusch C, Wallach D (1992) Stabilization of the bioactivity of tumor necrosis factor by its soluble receptors. J Exp Med 175: 323-329.

46. Pocsik E, Mihalik R, Ali-Osman F, Aggarwal BB (1994) Cell density-dependent regulation of cell surface expression of two types of human tumor necrosis factor receptors and its effect on cellular response. J Cell Biochem 54: 453-464.

47. van Riemsdijk-Van Overbeeke IC, Baan CC, Knoop CJ, Loonen EH, Zietse R, et al. (2001) Quantitative flow cytometry shows activation of the TNF-alpha system but not of the IL-2 system at the single cell level in renal replacement therapy. Nephrol Dial Transplant 16: 1430-1435.

48. Nugent LJ, Jain RK (1984) Extravascular diffusion in normal and neoplastic tissues. Cancer Res 44: 238-244.

49. Pluen A, Boucher Y, Ramanujan S, McKee TD, Gohongi T, et al. (2001) Role of tumor-host interactions in interstitial diffusion of macromolecules: Cranial vs. subcutaneous tumors. Proc Natl Acad Sci U S A 98: 4628-4633.

50. Wenning LA, Murphy RM (1999) Coupled cellular trafficking and diffusional limitations in delivery of immunotoxins to multicell tumor spheroids. Biotechnol Bioeng 62: 562-575.

51. Chen KC, Kim J, Li X, Lee B (2008) Modeling recombinant immunotoxin efficacies in solid tumors. Ann Biomed Eng 36: 486-512.

52. Guler R, Olleros ML, Vesin D, Parapanov R, Garcia I (2005) Differential effects of total and partial neutralization of tumor necrosis factor on cell-mediated immunity to mycobacterium bovis BCG infection. Infect Immun 73: 3668-3676.

53. Watson VE, Hill LL, Owen-Schaub LB, Davis DW, McConkey DJ, et al. (2000) Apoptosis in mycobacterium tuberculosis infection in mice exhibiting varied immunopathology. J Pathol 190: 211-220.

54. Crowe PD, Walter BN, Mohler KM, Otten-Evans C, Black RA, et al. (1995) A metalloprotease inhibitor blocks shedding of the 80-kD TNF receptor and TNF processing in T lymphocytes. J Exp Med 181: 1205-1210.

55. Solomon KA, Covington MB, DeCicco CP, Newton RC (1997) The fate of pro-TNF-alpha following inhibition of metalloprotease-dependent processing to soluble TNF-alpha in human monocytes. J Immunol 159: 4524-4531.

56. Cheong R, Bergmann A, Werner SL, Regal J, Hoffmann A, et al. (2006) Transient IkappaB kinase activity mediates temporal NF-kappaB dynamics in response to a wide range of tumor necrosis factor-alpha doses. J Biol Chem 281: 2945-2950.

57. Pennica D, Lam VT, Mize NK, Weber RF, Lewis M, et al. (1992) Biochemical properties of the 75-kDa tumor necrosis factor receptor. characterization of ligand binding, internalization, and receptor phosphorylation. J Biol Chem 267: 21172-21178.

58. Ehlers S (2003) Role of tumour necrosis factor (TNF) in host defence against tuberculosis: Implications for immunotherapies targeting TNF. Ann Rheum Dis 62 Suppl 2: ii37-42.

59. Tracey D, Klareskog L, Sasso EH, Salfeld JG, Tak PP (2008) Tumor necrosis factor antagonist mechanisms of action: A comprehensive review. Pharmacol Ther 117: 244-279.

60. Scallon B, Cai A, Solowski N, Rosenberg A, Song XY, et al. (2002) Binding and functional comparisons of two types of tumor necrosis factor antagonists. J Pharmacol Exp Ther 301: 418-426.

61. Jit M, Henderson B, Stevens M, Seymour RM (2005) TNF-alpha neutralization in cytokine-driven diseases: A mathematical model to account for therapeutic success in rheumatoid arthritis but therapeutic failure in systemic inflammatory response syndrome. Rheumatology (Oxford) 44: 323-331.

62. Baxter LT, Yuan F, Jain RK (1992) Pharmacokinetic analysis of the perivascular distribution of bifunctional antibodies and haptens: Comparison with experimental data. Cancer Res 52: 5838-5844.

63. Filler SG, Solis NV, Guo J, Doellgast G, Ruiz-Garcia A, et al. (2007) Pharmacokinetics of murine p75-fc fusion protein and MP6-XT22 anti-murine TNF-alpha mAb in mice. J Investig Dermatol Symp Proc 12: 52-56.

64. Lobo ED, Hansen RJ, Balthasar JP (2004) Antibody pharmacokinetics and pharmacodynamics. J Pharm Sci 93: 2645-2668.

65. Kim MS, Lee SH, Song MY, Yoo TH, Lee BK, et al. (2007) Comparative analyses of complex formation and binding sites between human tumor necrosis

factor-alpha and its three antagonists elucidate their different neutralizing mechanisms. J Mol Biol 374: 1374-1388.

66. Kaymakcalan Z, Sakorafas P, Bose S, Scesney S, Xiong L, et al. (2009) Comparisons of affinities, avidities, and complement activation of adalimumab, infliximab, and etanercept in binding to soluble and membrane tumor necrosis factor. Clin Immunol 131: 308-316.

67. Till A, Rosenstiel P, Krippner-Heidenreich A, Mascheretti-Croucher S, Croucher PJ, et al. (2005) The met-196 -> arg variation of human tumor necrosis factor receptor 2 (TNFR2) affects TNF-alpha-induced apoptosis by impaired NF-kappaB signaling and target gene expression. J Biol Chem 280: 5994-6004.

68. Olleros ML, Guler R, Vesin D, Parapanov R, Marchal G, et al. (2005) Contribution of transmembrane tumor necrosis factor to host defense against mycobacterium bovis bacillus calmette-guerin and mycobacterium tuberculosis infections. Am J Pathol 166: 1109-1120.

69. Blower SM, Dowlatabadi H (1994) Sensitivity and uncertainty analysis of complex models of disease transmission: An HIV model, as an example. Int Stat Rev 62: 229-243.

70. Marino S, Hogue IB, Ray CJ, Kirschner DE (2008) A methodology for performing global uncertainty and sensitivity analysis in systems biology. J Theor Biol 254: 178-196.

71. Kinzer-Ursem TL, Linderman JJ (2007) Both ligand- and cell-specific parameters control ligand agonism in a kinetic model of g protein-coupled receptor signaling. PLoS Comput Biol 3: e6.

72. Chang ST, Linderman JJ, Kirschner DE (2008) Effect of multiple genetic polymorphisms on antigen presentation and susceptibility to mycobacterium tuberculosis infection. Infect Immun 76: 3221-3232.

73. Chang ST, Linderman JJ, Kirschner DE (2005) Multiple mechanisms allow mycobacterium tuberculosis to continuously inhibit MHC class II-mediated antigen presentation by macrophages. Proc Natl Acad Sci U S A 102: 4530-4535.

74. Fallahi-Sichani M, Linderman JJ (2009) Lipid raft-mediated regulation of G-protein coupled receptor signaling by ligands which influence receptor dimerization: A computational study. PLoS One 4: e6604.

75. Marino S, Hogue IB, Ray CJ, Kirschner DE (2008) A methodology for performing global uncertainty and sensitivity analysis in systems biology. J Theor Biol 254: 178-196.

76. Chiu BC, Freeman CM, Stolberg VR, Hu JS, Komuniecki E, et al. (2004) The innate pulmonary granuloma: Characterization and demonstration of dendritic cell recruitment and function. Am J Pathol 164: 1021-1030.

77. Mohler KM, Sleath PR, Fitzner JN, Cerretti DP, Alderson M, et al. (1994) Protection against a lethal dose of endotoxin by an inhibitor of tumour necrosis factor processing. Nature 370: 218-220.

78. Jacobs M, Togbe D, Fremond C, Samarina A, Allie N, et al. (2007) Tumor necrosis factor is critical to control tuberculosis infection. Microbes Infect 9: 623-628.

79. Hoang TT, Nansen A, Roy S, Billeskov R, Aagaard C, et al. (2009) Distinct differences in the expansion and phenotype of TB10.4 specific CD8 and CD4 T cells after infection with mycobacterium tuberculosis. PLoS One 4: e5928.

80. Menart V, Gaberc-Porekar V, Jevsevar S, Pernus M, Meager A, et al. (2000) Early events in TNFa-p55 receptor interations--experiments with TNF dimers. Pflugers Arch 439: R113-5.

81. Corti A, Fassina G, Marcucci F, Barbanti E, Cassani G (1992) Oligomeric tumour necrosis factor alpha slowly converts into inactive forms at bioactive levels. Biochem J 284 (Pt 3): 905-910.

82. Rangamani P, Sirovich L (2007) Survival and apoptotic pathways initiated by TNF-alpha: Modeling and predictions. Biotechnol Bioeng 97: 1216-1229.

83. Lipniacki T, Puszynski K, Paszek P, Brasier AR, Kimmel M (2007) Single TNFalpha trimers mediating NF-kappaB activation: Stochastic robustness of NF-kappaB signaling. BMC Bioinformatics 8: 376.

84. Hohmann HP, Remy R, Poschl B, van Loon AP (1990) Tumor necrosis factors-alpha and -beta bind to the same two types of tumor necrosis factor receptors and maximally activate the transcription factor NF-kappa B at low receptor occupancy and within minutes after receptor binding. J Biol Chem 265: 15183-15188.

85. Fotin-Mleczek M, Henkler F, Samel D, Reichwein M, Hausser A, et al. (2002) Apoptotic crosstalk of TNF receptors: TNF-R2-induces depletion of TRAF2 and IAP proteins and accelerates TNF-R1-dependent activation of caspase-8. J Cell Sci 115: 2757-2770.

86. Wajant H, Pfizenmaier K, Scheurich P (2003) Tumor necrosis factor signaling. Cell Death Differ 10: 45-65.

87. Kundu M, Pathak SK, Kumawat K, Basu S, Chatterjee G, et al. (2009) A TNF- and c-cbl-dependent FLIP(S)-degradation pathway and its function in mycobacterium tuberculosis-induced macrophage apoptosis. Nat Immunol 10: 918-926.

88. Schaible UE, Winau F, Sieling PA, Fischer K, Collins HL, et al. (2003) Apoptosis facilitates antigen presentation to T lymphocytes through MHC-I and CD1 in tuberculosis. Nat Med 9: 1039-1046.

89. Seah GT, Rook GA (2001) Il-4 influences apoptosis of mycobacterium-reactive lymphocytes in the presence of TNF-alpha. J Immunol 167: 1230-1237.

90. Kremer L, Estaquier J, Wolowczuk I, Biet F, Ameisen JC, et al. (2000) Ineffective cellular immune response associated with T-cell apoptosis in susceptible mycobacterium bovis BCG-infected mice. Infect Immun 68: 4264-4273.

91. Co DO, Hogan LH, Il-Kim S, Sandor M (2004) T cell contributions to the different phases of granuloma formation. Immunol Lett 92: 135-142.

92. Turner OC, Basaraba RJ, Orme IM (2003) Immunopathogenesis of pulmonary granulomas in the guinea pig after infection with mycobacterium tuberculosis. Infect Immun 71: 864-871.

93. Plessner HL, Lin PL, Kohno T, Louie JS, Kirschner D, et al. (2007) Neutralization of tumor necrosis factor (TNF) by antibody but not TNF receptor fusion molecule exacerbates chronic murine tuberculosis. J Infect Dis 195: 1643-1650.

94. Wallis RS, Ehlers S (2005) Tumor necrosis factor and granuloma biology: Explaining the differential infection risk of etanercept and infliximab. Semin Arthritis Rheum 34: 34-38.

95. Kirschner DE, Chang ST, Riggs TW, Perry N, Linderman JJ (2007) Toward a multiscale model of antigen presentation in immunity. Immunol Rev 216: 93-118.

Chapter 3

Multi-scale computational modeling reveals a critical role for TNF receptor 1 dynamics in tuberculosis granuloma formation

3.1 Introduction

Tuberculosis (TB), a disease caused by the intracellular pathogen *Mycobacterium tuberculosis* (Mtb), is responsible for 2-3 million deaths per year. In the presence of an effective immune response, only 5-10% of infected people develop clinical signs of active TB (known as primary TB). However, immunological testing provides evidence of a state of latent infection, with no clinical symptoms, in one third of the world population [1]. Latent TB represents a state of equilibrium in which the host controls the infection but is unable to clear it, allowing bacteria to survive at relatively constant but low levels [2]. Latent infection may reactivate to active disease (reactivation TB) with an average 10% per lifetime frequency, as a result of, for example, age, impaired immunity (as in the case of HIV co-infection), malnutrition, or anti-inflammatory drug administration that interferes with host immunity [3].

The key pathological feature of TB that arises as a result of the immune response is the formation of aggregates of bacteria and immune cells within the lung called granulomas. TB granulomas, especially in humans, form as organized spherical structures composed of bacteria, a macrophage-rich core including resting, infected and activated macrophages, and a surrounding mantle of lymphocytes. Granulomas act to immunologically restrain and physically contain Mtb infection [4-10]. Latent and active

TB in humans comprise a heterogeneous mixture of granulomas in both lung and lymph nodes that provide a range of physiological microenvironments associated with bacterial replication, persistence and killing. Characterization of different types of granulomas will provide a framework for understanding the immunobiology of TB that can lead to the development of new strategies for control and therapy [11,12].

In addition to cellular components, studies in animal models and humans have identified a variety of cytokines involved in granuloma formation and function, including tumor necrosis factor-α (TNF) and interferon-γ (IFN-γ) (reviewed in [13]). These molecules are secreted from cellular sources (macrophages and T cells) as a result of Mtb infection, interact with receptors on target cells, trigger intracellular signaling pathways, and induce cell responses that ultimately contribute to formation of granulomas and immunologic control of Mtb infection [13-15]. One can hypothesize that molecular scale processes that lie between the availability of particular extracellular cytokines and the final cytokine-mediated response may influence the outcome of Mtb infection. Receptor/ligand binding and *trafficking* (defined here to include synthesis, internalization, recycling and degradation of the ligand and receptors) are a group of molecular scale processes that take place under physiological conditions and are believed to play a major role in receptor-mediated cell responses [16]. However, the significance of trafficking processes in controlling the effect of cytokines on the host immune response (TB immune response in particular) has never been studied. Hence, a multi-scale approach that considers events at the molecular, cellular and tissue scales is required for comprehensive analysis of the role of cytokines in the complex immune response to Mtb.

Our study is focused on TNF interactions with immune cells that form a granuloma. The pleiotropic cytokine TNF is produced by a variety of immune cells, especially infected and activated macrophages and pro-inflammatory T cells [17,18], and functions as part of the immune response to Mtb infection via several mechanisms. TNF (in conjunction with the cytokine IFN-γ) induces macrophage activation [19-21], enhances immune cell recruitment to the site of infection [22], and augments chemokine expression by macrophages through activation of the NF-κB signaling pathway [23]. TNF can also mediate cell death via inducing the caspase-mediated apoptotic pathway [24,25]. Data identifying the roles of TNF include: TNF knockout/neutralization experiments in mice and monkeys [17,26-28], TNF receptor 1 (TNFR1) knockout experiments in mice [17], and mathematical modeling studies [29,30]. Despite this wealth of information on the critical role of TNF in immunity to Mtb, many fundamental questions remain unanswered regarding the mechanisms that regulate TNF activity at different biological scales. For example, it is not known how the dynamics of molecular events such as TNF/TNFR binding and trafficking influence a granuloma's ability to control Mtb infection. We have recently suggested via mathematical modeling that organization of immune cells as well as the processes of TNF/TNFR binding and trafficking control steady state TNF availability within an existing granuloma. This results from a TNF concentration gradient that is created with the highest concentration at the core of granuloma (see Chapter 2 and [31]). However, important unanswered questions remain: What factors control such a gradient during a long-term immune response to Mtb infection that includes formation and maintenance of granulomas? How does this gradient regulate TNF-associated processes and ultimately translate to the

outcome of Mtb infection? Is there an inter-play between TNF availability and bacterial load in a granuloma? Are there TNF-level processes that, if targeted, could present new strategies for disease therapy?

These questions invoke multiple biological scales (in length and time) are currently difficult to address experimentally. Hence, a systems biology approach that incorporates computational modeling to generate and test hypotheses, run virtual experiments, and make experimentally testable predictions is uniquely suited to address these questions. We develop a multi-scale computational model that describes the immune response to Mtb in the lung over three biological length scales: molecular, cellular and tissue. We use the model to track formation and maintenance of a granuloma in space and time. The model captures the dynamics of TNF/TNFR interactions that occur on the second to minute time scales within the long-term immune response to Mtb infection, a complex process that lasts for months to years. We identify TNF-associated processes that influence infection outcome at the granuloma scale as well as predicting cellular scale processes that influence TNF availability. Finally, we identify processes that regulate TNF concentration and cellular behaviors and thus influence the outcome of infection within a granuloma.

3.2 Methods

3.2.1 An overview of the multi-scale granuloma model

To build a multi-scale model necessary to address the questions herein regarding TNF-regulated immune responses to Mtb infection in the lung, we need to first have working models at both the cellular/tissue scale and the molecular/single-cell scale. We briefly

describe these models below and then describe our approach for linking them. Cellular and tissue scale dynamics are captured via a set of well-described interactions between immune cells and Mtb at the site of infection using stochastic simulations in the form of an agent-based model (ABM). Single-cell molecular scale processes that control TNF/TNFR binding and trafficking for each individual cell are captured by a set of nonlinear ordinary differential equations (ODEs). Fig. 3.1 indicates how these models exist separately and how they are linked into a single multi-scale granuloma model. The linkage is achieved via TNF-induced cell responses (i.e. apoptosis and NF-κB activation) that are modeled as Poisson processes with rate parameters computed as functions of molecular concentrations from the ODE model. Further details of the rules, equations and parameters of the multi-scale model are described below and in Appendix B.

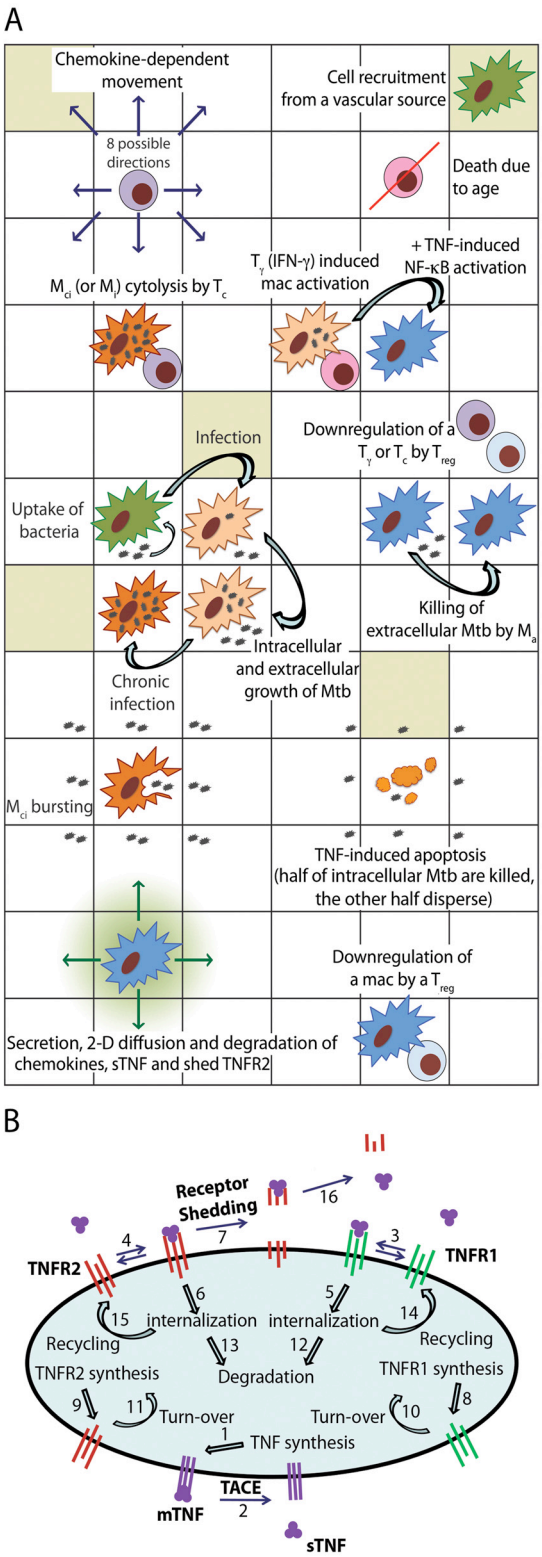

Fig. 3.1 Schematic representation of the multi-scale model of the immune response to Mtb infection in the lung. (A) An overview of selected cell-level ABM rules based on known immunological activities and interactions. (B) Schematic representation of binding interactions and reactions controlling TNF/TNFR dynamics at the single-cell level with numbers that represent model processes as listed in Appendix B (Table B.3).

3.2.2 Cellular/tissue scale model

The two-dimensional (2-D) ABM used in this study is an updated version of our previous model that captures cellular scale interactions leading to a tissue-level readout, namely granuloma formation in response to Mtb infection in primates [30]. Because multi-scale analysis of the long-term immune response to Mtb is the aim of this study, an extensive sensitivity analysis is required. Therefore, choosing a 2-D model that can be used to run a large number of simulations in a reasonable timeframe is key for our study. A comparison with a simple three-dimensional version has shown that our 2-D model can capture important dynamics of Mtb infection [32]. Fig. 3.1A depicts a schematic overview of selected immunological interactions tracked at the cellular scale. A full description of all ABM rules that reflect known biological activities is provided in Supporting Text and significant updates to the original model are highlighted. Briefly, rule events include: chemotactic movement and recruitment of immune cells to site of infection, intracellular and extracellular growth of Mtb, phagocytosis of bacteria by macrophages, cell death and apoptosis, macrophage/T-cell interactions such as cytolytic functions of cytotoxic T cells (T_c) and IFN-γ based activation of macrophages by pro-inflammatory T cells (T_γ), down-regulation of immune cells by regulatory T cells (T_{reg}), secretion of chemokines, and caseation.

One important simplification in our model is the choice to include only cell types with well-characterized roles in Mtb granulomas (macrophages, T_c, T_γ and T_{reg} cells). Cell types that may have important roles but are not sufficiently characterized at this point to include in mechanistic ways in the model include neutrophils (with protective roles in early infection that may be immunomodulatory in nature [33-35]), multi-nucleate

giant cells (may modulate chemokine production [36,37]), dendritic cells (for optimal antigenic stimulation of T cells [38,39]), and foamy cells (possible nutrient source for bacteria [40,41]). Future work can easily incorporate them into the model when more mechanistic data become available.

3.2.3 Molecular/single-cell scale TNF/TNFR model

The kinetic processes of TNF/TNFR binding and trafficking (synthesis, internalization, recycling and degradation of ligand and receptors) occurring in individual cells within a granuloma can be described by ODEs (see Chapter 2 and [31]). As schematically shown in Fig. 3.1B, TNF is first synthesized by TNF-producing cells, including infected macrophages, chronically infected macrophages, NF-κB-activated resting macrophages, activated macrophages and T cells as a membrane-bound precursor form (mTNF) that can then be processed and released as a soluble form (sTNF) into extracellular spaces. Two types of TNF receptors (TNFR1 and TNFR2) are synthesized and expressed on the cell membrane. The equations describing TNF/TNFR processes for an individual cell are detailed in Appendix B (Tables B.3, B.4).

3.2.4 Linking the individual models via sTNF-induced cell responses

Activation of the two major TNF-induced signaling pathways, the caspase-mediated apoptotic pathway and the NF-κB pathway, are both controlled at the level of sTNF/TNFR1 interactions and thus serve as the link between the molecular/single-cell scale TNF/TNFR kinetic model and the cellular/tissue scale model. The NF-κB signaling pathway is initiated by sTNF-bound cell surface TNFR1 and apoptosis depends on the

internalized sTNF/TNFR1 complexes [42-44]. As reported in the literature, NF-κB activation of macrophages is a necessary but not sufficient factor in successful immune response to mycobacterial infection. Its role includes induction of a variety of inflammatory-related genes such as TNF and chemokines as well as controlling phagolysosome fusion-mediated killing of mycobacteria by activated macrophages [20,45]. TNF-induced apoptosis of macrophages kills intracellular bacteria and is associated with a better outcome of infection [3]. In addition to sTNF, mTNF has also been shown to contribute in part to control of Mtb infection in mice [46-48]. However, experimental data regarding molecular and cellular-level details of mTNF-mediated signaling and reverse signaling in Mtb immune responses are limited. Thus, at this time we only consider sTNF/TNFR1-mediated signaling in our model.

A recent study has shown that TNF-induced NF-κB activation is a process with a discrete nature at the single-cell level, with fewer cells responding at lower doses [49]. Accordingly, we describe TNF-induced NF-κB activation for each individual macrophage as a Poisson process with a probability determined within each time-step (Δt), based on a Poisson rate parameter that is a function of the NF-κB activation rate constant ($k_{NF\text{-}\kappa B}$), the concentration of cell surface sTNF/TNFR1 complexes [sTNF/TNFR1], and the concentration threshold for cell surface sTNF/TNFR1 ($\tau_{NF\text{-}\kappa B}$):

$$P_{NF-\kappa B} = \begin{cases} 0 & ; [sTNF/TNFR1] < \tau_{NF-\kappa B} \\ 1 - e^{-k_{NF-\kappa B}([sTNF/TNFR1]-\tau_{NF-\kappa B})\Delta t} & ; [sTNF/TNFR1] \geq \tau_{NF-\kappa B} \end{cases} \quad (3.1)$$

Similarly, we model TNF-induced apoptosis for each individual cell (macrophage and T cell) by:

$$P_{apopt} = \begin{cases} 0 & ; [sTNF/TNFR1_i] < \tau_{apopt} \\ 1 - e^{-k_{apopt}([sTNF/TNFR1_i]-\tau_{apopt})\Delta t} & ; [sTNF/TNFR1_i] \geq \tau_{apopt} \end{cases} \quad (3.2)$$

We use a Poisson process with a probability computed as a function of the apoptosis rate constant (k_{apopt}), the concentration of internalized sTNF/TNFR1 complexes [sTNF/TNFR1$_i$], and the concentration threshold for internalized sTNF/TNFR1 (τ_{apopt}). Scale-linking parameters, or simply *linking parameters*, i.e. TNF-response parameters (defined here to include parameters introduced in Equations 3.1 and 3.2), are listed in Appendix B (Table B.5).

To analyze how TNF affects infected versus resting macrophages in a granuloma, we define *infected:resting cell ratios*, $R_{apoptosis}$ and $R_{NF\text{-}\kappa B}$, as follows. $R_{apoptosis}$ is defined as the ratio of the number of infected macrophages that undergo TNF-mediated apoptosis to the number of resting macrophages that undergo TNF-mediated apoptosis during a 200-day period post-infection. $R_{NF\text{-}\kappa B}$ is similarly defined as the number of infected macrophages that undergo TNF-mediated NF-κB activation to the number of resting macrophages that undergo TNF-mediated NF-κB activation during a 200-day period post-infection.

3.2.5 Parameter estimation and control experiments

We estimate ABM parameter values from literature data as described in detail by Ray *et al* [30]. When data are not available, we use uncertainty analysis to explore the entire parameter space of possible model outcomes as described in [50]. Cell-specific TNFR densities and rate constants for TNF/TNFR processes are estimated based on experimental data from our group [31], as described in Chapter 2, and other groups as indicated in Appendix B (B.2). Values of parameters used to describe TNF-induced cell responses, including NF-κB activation and apoptosis (i.e. linking parameters) are

estimated via uncertainty analysis by varying parameter values in ranges that are qualitatively consistent with experimental and modeling data on time-scales and thresholds for TNF-induced cell responses [49,51,52].

Using the above methods, we specify a baseline set of parameter values that robustly leads to control of infection in granulomas with organized structures as reported for humans and non-human primates (see Appendix B, Tables B.1, B.2 and B.5). We then explore parameter changes that shift infection outcome to clearance or uncontrolled growth of Mtb. To further test the ability of the model to predict different infection outcomes under pathological conditions compatible with both experimental and previous modeling data on granuloma formation, we simulate gene knockouts of previously identified essential components of the Mtb immune response (e.g. TNF, IFN-γ and T cell knockouts). To do this, we set relevant probabilities or rate constants to zero from the beginning of simulations.

3.2.6 Sensitivity analysis

When computational models include parameters describing a large number of known biological processes, it is critical to understand the role that each of these parameters plays in determining output. Sensitivity analysis is a technique to identify critical parameters of a model and quantify how input uncertainty impacts model outputs. Latin hypercube sampling (LHS) is an algorithm that allows multiple parameters to be varied and sampled simultaneously in a computationally efficient manner [53]. We use LHS sensitivity analysis as described for application to ABMs [50] to analyze the impact of TNF/TNFR trafficking and TNF response (linking) parameter values as well as TNF-

independent and cellular scale parameter values, as listed in Appendix B (Tables B.1, B.2 and B.5), on model outputs. For clarity, these outputs are grouped, as TNF function-related outputs (total number of TNF-induced events, including NF-κB activation and apoptosis in different types of cells), cellular-level outputs (total bacteria, macrophage and T cell numbers), tissue-level outputs (granuloma size and caseation area) and average tissue concentrations of TNF and chemokines. The correlation of model outputs with each parameter is quantified via calculation of a partial rank correlation coefficient (PRCC). PRCC values vary between -1 (perfect negative correlation) and +1 (perfect positive correlation) and can be differentiated based on *p*-values derived from Student's *t* test. LHS simulations sampled each parameter 250 times. Each sampled parameter set was run 4 times and averages of the outputs were used to calculate PRCC values. The choice of the number of simulations is determined by the desired significance level for the PRCC [50,53]. Here, 250 runs imply that PRCC values above +0.24 or below -0.24 are significantly different from zero ($p < 0.001$). To study how processes at different scales interact with each other, we analyze the effect of parameters associated with each scale on the outputs of the same scale (intra-scale sensitivity analysis) as well as on the outputs of the other scale (inter-scale sensitivity analysis).

3.2.7 Computer simulations and visualization

The model was implemented in C++. We use Qt, a C++ framework for developing cross-platform applications with a graphical user interface (GUI), to visualize and track different aspects of the granuloma, including the structure and molecular concentration

gradients, as it forms and is maintained. Simulations can be run with or without graphical visualization. Simulations were run on Linux and Mac operating systems.

3.3 Results

3.3.1 Prediction of different infection outcomes at the granuloma level

We first tested whether our multi-scale computational model could capture key features of granuloma formation and maintenance. Using a combination of parameter estimation and uncertainty analysis as described in Methods, we identified a set of baseline values for model parameters, including cellular/tissue scale parameters (see Appendix B, Table B.1), molecular/single-cell scale TNF/TNFR parameters (see Appendix B, Table B.2) and parameters that link the two scales in the model (see Appendix B, Table B.5). This set of parameter values leads to containment: control of Mtb infection within a well-circumscribed granuloma containing stable bacterial levels ($<10^3$ total bacteria) at 200 days post-infection (Fig. 3.2A, B, Movie 1 at http://malthus.micro.med.umich.edu/lab/movies/Multiscale/GranSim/). This recapitulates a state that has been described as an equilibrium between the host and Mtb at the level of single granuloma and is referred to as a solid granuloma with caseous center (Mtb containment) [3,54]. As observed in Movie 1, simulated granulomas form as organized immune structures predominantly composed of uninfected macrophages surrounding a core of bacteria and infected and activated macrophages with T cells localized at the periphery [4-10]. As reported for most animal models of TB, bacterial growth increases logarithmically until reaching a plateau coincident with T cell response initiation [55].

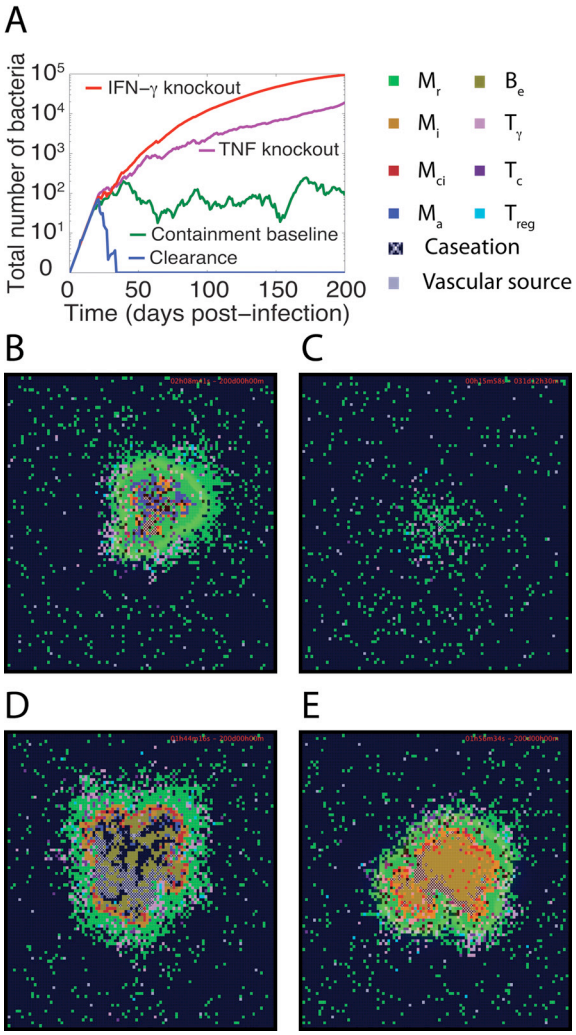

Fig. 3.2 Simulation results for the Mtb dynamics and granuloma structures at 200 days post-infection under different pathological conditions. (A) Changes of total number of Mtb (intracellular and extracellular bacteria, i.e. $B_{int} + B_{ext}$) with time for simulation of containment baseline, a scenario of Mtb clearance, a TNF (or TNFR1) knockout scenario and a IFN-γ knockout scenario. Granuloma snapshots for: (B) a scenario of containment, (C) clearance of Mtb infection in less than five weeks as a result of an efficient immune response, (D) a TNF (or TNFR1) knockout scenario, and (E) an IFN-γ knockout scenario. Cell types and status are shown by different color squares, as indicated in the upper right corner of the figure (M_r: resting macrophage, M_i: infected macrophage, M_{ci}: chronically infected macrophage, M_a: activated macrophage, B_e: extracellular bacteria, T_γ: pro-inflammatory IFN-γ producing T cell, T_c: cytotoxic T cell, T_{reg}: regulatory T cell). Caseation and vascular sources are also indicated.

As observed in non-human primate models as well as in humans, several types of granuloma are observed in Mtb infection [56]. Our multi-scale model is also able to recapitulate different granuloma types with different abilities to control infection as we vary specific parameters identified as important via sensitivity analysis from their

baseline values (see Appendix B, Tables B.1, B.2 and B.5). Cellular scale processes identified to significantly control bacterial numbers, caseation and granuloma size at 200 days post-infection are bacterial growth, T_γ-induced STAT-1 activation of macrophages and T cell movement and recruitment (T_γ cells in particular). These results are highlighted in Table 3.1 and are consistent with available experimental data reviewed in [3,57,58] and our previous modeling studies [30,59]. Greater intracellular Mtb growth rates, in agreement with published data [60], lead to higher bacterial loads and larger granulomas with larger caseation areas. STAT-1 activation of macrophages by IFN-γ producing T_γ cells is required for activation of macrophages and killing of intracellular and extracellular Mtb. Recruitment of IFN-γ producing pro-inflammatory T cells (T_γ cells) to site of infection is a critical component of immunity to Mtb as a smaller TNF/chemokine concentration threshold for T_γ recruitment leads to more efficient responses. Further, the ability of T cells to migrate through a dense uninfected macrophage network surrounding bacteria and infected macrophages at the core of a granuloma helps determine the efficiency of the T cell-mediated immune response to Mtb.

Table 3.1 Model parameters significantly correlated with outputs of interest, bacterial numbers, granuloma size, caseation area and TNF concentration at day 200 post-infection. Detailed sensitivity analysis results are presented in Appendix B (Tables B.6, B.7).

Selected model outputs	Important TNF-independent and cellular scale parameters [*†]	Important TNF/TNFR-associated molecular and linking parameters [*‡]
Total number of bacteria	α_{Bi} (++)	$k_{synthMac}$ (--)
	P_{STAT1} (--)	δ_{TNF} (++)
	T_{moveM} (--)	K_{d1} (+)
	T_{recr} (--)	k_{int1} (+)
	$\tau_{recTgam}$ (++)	$TNFR1_{mac}$ (-)
	D_{chem} (--)	$k_{NF\kappa B}$ (--)
	δ_{chem} (++)	$\tau_{NF\kappa B}$ (++)
Granuloma size	α_{Bi} (++)	$k_{synthMac}$ (--)
	P_{STAT1} (-)	δ_{TNF} (++)
	M_{recr} (++)	K_{d1} (++)
	T_{moveM} (--)	k_{int1} (+)
	T_{recr} (--)	$TNFR1_{mac}$ (--)
	$P_{apop/Fas}$ (-)	$k_{NF\kappa B}$ (--)
	$\tau_{recTgam}$ (++)	$\tau_{NF\kappa B}$ (++)
Caseation	α_{Bi} (++)	$k_{synthMac}$ (--)
	P_{STAT1} (-)	δ_{TNF} (++)
	M_{recr} (++)	K_{d1} (++)
	T_{moveM} (--)	k_{int1} (+)
	T_{recr} (--)	k_{rec1} (++)
	$\tau_{recTgam}$ (++)	$TNFR1_{mac}$ (--)
	δ_{chem} (++)	k_{apop} (-)
	τ_{chem} (+)	$k_{NF\kappa B}$ (--)
		$\tau_{NF\kappa B}$ (++)
Average tissue concentration of sTNF	α_{Bi} (++)	$k_{synthMac}$ (--)
	P_{STAT1} (-)	K_{d1} (+)
	T_{moveM} (--)	$TNFR1_{mac}$ (-)
	T_{recr} (--)	$k_{NF\kappa B}$ (--)
	$\tau_{recTgam}$ (++)	$\tau_{NF\kappa B}$ (+)
	δ_{chem} (++)	
	τ_{chem} (+)	

[*] Only parameters with significant PRCC values are indicated. Significant positive and negative correlations are shown using + and - as follows: -/+: $0.001 < p\text{-value} < 0.01$, --/++: $p\text{-value} < 0.001$.

[†] TNF-independent and cellular scale parameter descriptions are as follows: α_{Bi} intracellular Mtb growth rate, P_{STAT1} probability of STAT-1 activation in M_r or M_i, T_{moveM} probability of T cell moving to a macrophage-containing location, T_{recr} probability of T cell recruitment, M_{recr} probability of M_r recruitment, $\tau_{recTgam}$ TNF/chemokine concentration threshold for T_γ recruitment, $P_{apop/Fas}$ probability of Fas/FasL apoptosis by T_γ, D_{chem} diffusion coefficient of chemokines, δ_{chem} chemokine degradation rate constant. τ_{chem} minimum chemokine concentration detection threshold.

[‡] TNF/TNFR associated parameter descriptions are as follows: $k_{synthMac}$ mTNF synthesis rate for macrophages, δ_{TNF} sTNF degradation rate constant, K_{d1} equilibrium dissociation constant of sTNF/TNFR1, k_{int1} TNFR1 internalization rate constant, k_{rec1} TNFR1 recycling rate constant, $TNFR1_{mac}$ TNFR1 density on the surface of macrophages, k_{apop} rate constant for TNF-induced apoptosis in all cell types, $k_{NF\kappa B}$ rate constant for TNF-induced NF-κB activation in macrophages, $\tau_{NF\kappa B}$ cell surface sTNF/TNFR1 threshold for TNF-induced NF-κB activation.

In addition to containment, we can reproduce other possible outcomes of Mtb infection, including clearance and uncontrolled growth of bacteria, by manipulating values of important model parameters. For example, an increase in the ability of T cells

to penetrate into the site of infection at the core of granuloma by increasing the value of model parameter T_{move}, the probability of a T cell moving onto a macrophage-containing micro-compartment, significantly increases the efficiency of the T cell-mediated response and thus favors Mtb clearance (Fig. 3.2A, C, Movie 2 at http://malthus.micro.med.umich.edu/lab/movies/Multiscale/GranSim/). On the other hand, simulations of gene knockouts of essential components of the Mtb immune response such as TNF or TNFR1 knockouts ($k_{synthMac} = k_{synthTcell} = 0$ or $TNFR1_{mac} = TNFR1_{Tcell} = 0$) and IFN-γ knockout ($P_{STAT1} = 0$) lead to uncontrolled growth of Mtb. This is consistent with a variety of data on the crucial role of these cytokines in immunity to Mtb [3,13,61]. In this case, granulomas that form are greater in size, irregular in structure and include very high numbers of extracellular Mtb, large numbers of infected macrophages and wide-spread caseation (dead tissue caused by multiple deaths of macrophages in tissue usually within the core of the granuloma) (Fig. 3.2A, D, E, Movies 3, 4 at http://malthus.micro.med.umich.edu/lab/movies/Multiscale/GranSim/). Overall, our multi-scale model that includes molecular (TNF-associated), cellular, and tissue scale events predicts dynamics of Mtb infection for different infection scenarios, including containment, clearance and uncontrolled growth of bacteria as well as a variety of structural and functional outcomes that are expected to occur under different pathological conditions. Our results for these conditions are in agreement with our previous study using a model without molecular (TNF-associated) events [30] and a variety of experimental data. We now turn our analysis to the important role that TNF plays, and the factors that affect the ability of TNF to play that role, during the immune response to Mtb.

3.3.2 Cellular scale processes control TNF concentration by affecting bacterial load

We know from experimental studies that artificial manipulation of TNF concentration via anti-TNF treatments negatively affects infection outcome in mice, humans and non-human primates [26,27,62,63]. Are there physiological processes within the granuloma that also affect TNF concentration, and does alteration of those processes similarly affect infection outcome? To answer this question, we used sensitivity analysis to identify critical TNF-independent and cellular scale parameters that influence TNF concentration. Interestingly, processes highlighted in the previous section to be important determinants of bacterial numbers, caseation and granuloma size also significantly impact TNF concentration and thus the number of TNF-induced NF-κB activation and apoptosis events (see Table 3.1 and Appendix B (Table B.6)). This is because TNF production within the granuloma strongly depends on the level of infection. For example, reducing the probability of T cell recruitment (T_{recr}) decreases the level of T cell-mediated macrophage activation, a process that is necessary for limiting Mtb growth in infected macrophages. Therefore, intracellular Mtb can grow, disperse in the tissue after bursting of chronically infected macrophages, and infect more resting macrophages. This ultimately increases the number of extracellular Mtb as well as numbers of infected macrophages that act as further TNF sources in the tissue. TNF also enhances activation and recruitment of immune cells, leading to larger granulomas. This is in agreement with data from animal models that show increased bacterial numbers result in increased inflammation and more immune cell recruitment [64].

3.3.3 TNF/TNFR molecular processes control TNF actions and thus ability of a granuloma to control infection

The analysis above indicates that physiological processes that affect bacterial load indirectly affect TNF concentration. Are there other processes that more directly act on TNF, and would manipulation of those processes alter infection outcome? To answer this question, we performed sensitivity analysis to identify TNF/TNFR-associated molecular scale and linking parameters that influence model outcomes. Both signaling and trafficking processes are identified to significantly influence granuloma function, as indicated in Table 3.1 and Appendix B (Table B.7). TNF-induced NF-κB activation of resting and infected macrophages strongly correlates with bacterial numbers. Increasing the rate constant for TNF-induced NF-κB activation or reducing its cell surface sTNF/TNFR1 concentration threshold leads to faster macrophage NF-κB activation responses by smaller concentrations of available sTNF. Thus, these parameters can significantly influence the outcome of infection. This is consistent with the published data on the role of NF-κB activation of macrophages in killing mycobacteria [20].

Receptor and ligand trafficking processes that strongly influence infection outcome are: mTNF synthesis by infected and activated macrophages, sTNF degradation, TNFR1 affinity for sTNF, TNFR1 density on the membrane of macrophages, and sTNF-induced internalization of TNFR1 (Tables 3.1, Appendix B (Table B.7)). The rate of mTNF synthesis by infected and activated macrophages positively correlates with two key TNF functions (NF-κB activation and apoptosis) and negatively correlates with bacterial load, numbers of infected and chronically infected macrophages as well as granuloma and caseation size. This is consistent with human and animal model data and

our previous studies on the crucial role of TNF in controlling Mtb infection [26,29,30,62,65]. Similarly, the rate of sTNF degradation negatively influences TNF activities and thus positively correlates with bacterial numbers within a granuloma. TNFR1 density on macrophage membranes has a negative impact on bacterial numbers. This is consistent with experimental data on the importance of TNFR1 in controlling Mtb infection [17]. A greater TNFR1 affinity for binding to sTNF (smaller K_{d1}) also enhances the level of TNF-induced NF-κB activation and apoptosis and reduces total bacterial numbers. Internalization of TNFR1 occurs as a result of sTNF binding to TNFR1 on cell membranes and is not only required for TNF-induced apoptosis [42-44], but also reduces sTNF in a granuloma [31]. Thus TNFR1 internalization enhances apoptosis in TNF-secreting infected macrophages but reduces levels of NF-κB activation in non-TNF-secreting resting macrophages by limiting TNF concentrations near these cells (see Appendix B (Table B.7)). Overall, our sensitivity analysis predicts that sTNF-induced TNFR1 internalization increases bacterial levels within a granuloma. We focus our next analysis on potential effects of manipulation in TNFR1 internalization.

3.3.4 TNF/TNFR trafficking dynamics balance inflammation and bacterial killing

The effect of changing the rate constant for TNFR1 internalization on sTNF concentration, recruitment of immune cells, macrophage activation and apoptosis is shown in Fig. 3.3. As described above, sTNF-induced TNFR1 internalization, the key process in TNF/TNFR trafficking, has a significant impact on responses at molecular, cellular and tissue scales. The value of the rate constant for TNFR1 internalization (k_{int1}) controls sTNF concentration dynamics during the immune response to Mtb (Fig. 3.3A).

The physiological rate of TNFR1 internalization (half-time of ~15 min [66,67], k_{int1} = 7.7×10^{-4} s^{-1}) leads to much less extracellular sTNF in the tissue compared with the scenario in which sTNF/TNFR1 complex on the cell membrane is not at all ($k_{int1} = 0$) or is very slowly internalized (half-time of ~115 min, $k_{int1} = 1.0\times10^{-4}$ s^{-1}) (Fig. 3.3B). Although TNF is required for control of Mtb infection and the protective granulomatous response, high concentrations of TNF may lead to excessive inflammation and cause immunopathology [61,68]. Therefore, we predict that TNF/TNFR trafficking plays an important role in preventing excessive inflammation. Indeed, the rate of sTNF-induced internalization of TNFR1 controls the concentration of available TNF in tissue and regulates cell infiltration by affecting the extent and dynamics of TNF-dependent recruitment and activation of immune cells as well as mediating TNF-induced apoptosis (Fig. 3.3C-F). Thus, a hyper-inflammatory state may occur in the absence of a sufficiently rapid sTNF-induced TNFR1 internalization, leading to early and extensive recruitment of macrophages and T cells as well as uncontrolled activation of a large fraction of macrophages that are unable to efficiently undergo apoptosis. Interestingly, increasing TNFR1 internalization rate constant to $k_{int1} = 1.5\times10^{-3}$ s^{-1} (corresponding to a half-time of ~7.7 min) does not have a large effect on either sTNF concentration or immune cell population dynamics but does significantly enhance the number of apoptotic macrophages. However, further analysis reveals that other model outputs may be significantly affected by increasing TNFR1 internalization rate constant.

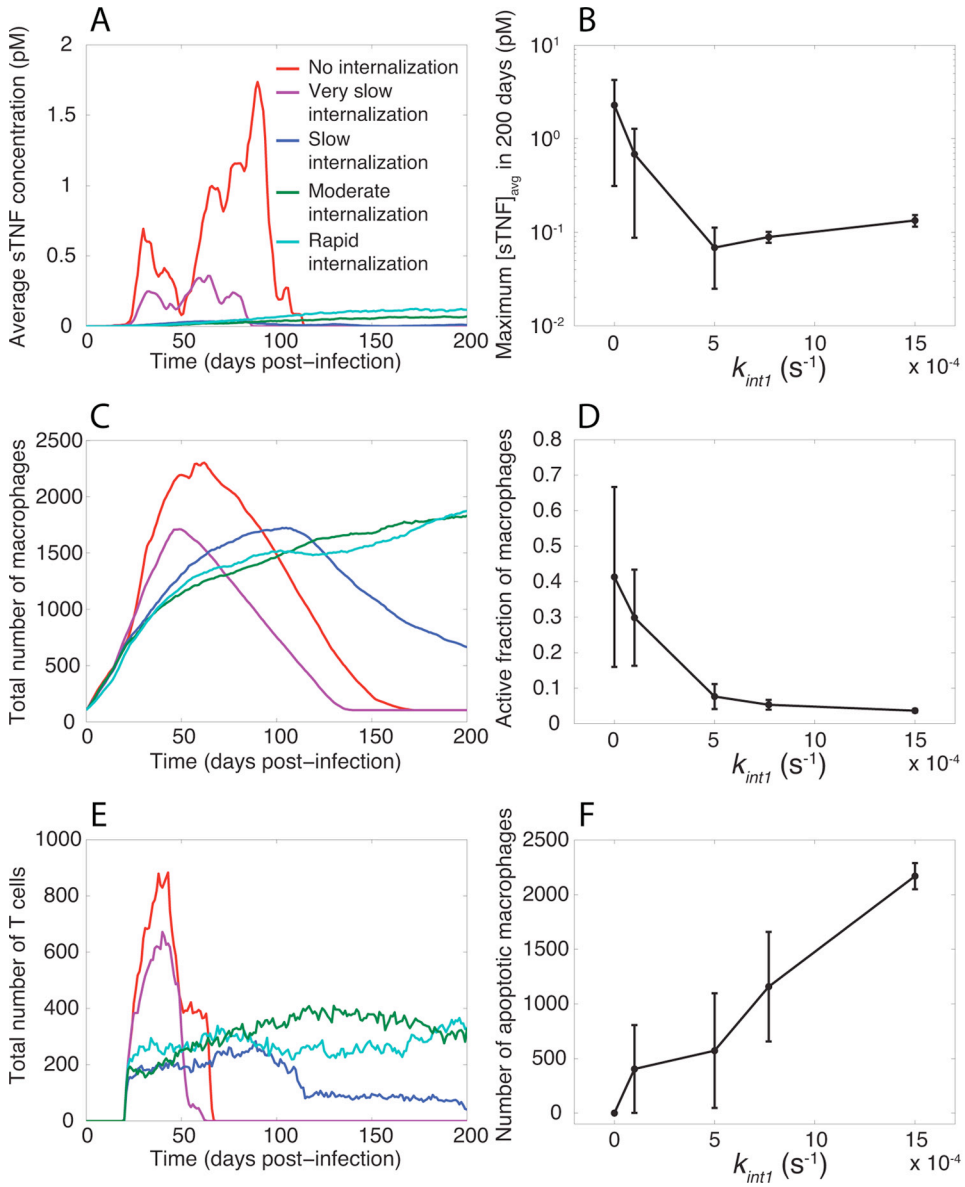

Fig. 3.3 TNFR1 internalization dynamics control sTNF concentration as well as macrophage and T cell recruitment and behavior. Simulation results show: (A) sTNF concentration dynamics, (B) maximum simulated sTNF concentration as a function of TNFR1 internalization rate constant (k_{int1}), (C) macrophage recruitment dynamics, (D) maximum fraction of macrophages that become activated following Mtb infection , (E) T cell recruitment dynamics, (F) TNF-induced macrophage apoptosis within a 200 day period after Mtb infection (No internalization: $k_{int1} = 0$, very slow internalization: $k_{int1} = 1.0\times10^{-4}$ s^{-1}, slow internalization: $k_{int1} = 5.0\times10^{-4}$ s^{-1}, moderate internalization: $k_{int1} = 7.7\times10^{-4}$ s^{-1}, and rapid internalization: $k_{int1} = 1.5\times10^{-3}$ s^{-1}).

In addition to an impact on inflammation, TNF/TNFR trafficking dynamics are capable of exerting a dramatic effect on the bacterial outcome of Mtb infection in a granuloma (Fig. 3.4). Zero to slow rates of sTNF-induced TNFR1 internalization (half-

time of ≥23 min, $k_{int1} \leq 5.0\times10^{-4}$ s^{-1}) favor clearance of bacteria; a moderate (physiological) rate (half-time of ~15 min, $k_{int1} = 7.7\times10^{-4}$ s^{-1}) leads to containment of bacteria, and a rapid rate of TNFR1 internalization (half-time of ~7.7 min. $k_{int1} = 1.5\times10^{-3}$ s^{-1}) results in uncontrolled growth of Mtb within the 200-day period of infection (Fig. 3.4, Movies 5-8 at http://malthus.micro.med.umich.edu/lab/movies/Multiscale/GranSim/). However, zero or very slow rates of TNFR1 internalization (e.g. half-time of ~115 min, $k_{int1} = 1.0\times10^{-4}$ s^{-1}) result in clearance of infection at the expense of extensive inflammation. Thus, our model suggests that there may exist an optimum rate of sTNF-induced TNFR1 internalization that balances the impacts that TNF has on control of Mtb infection and inflammation in tissue. We now investigate mechanisms underlying this balance.

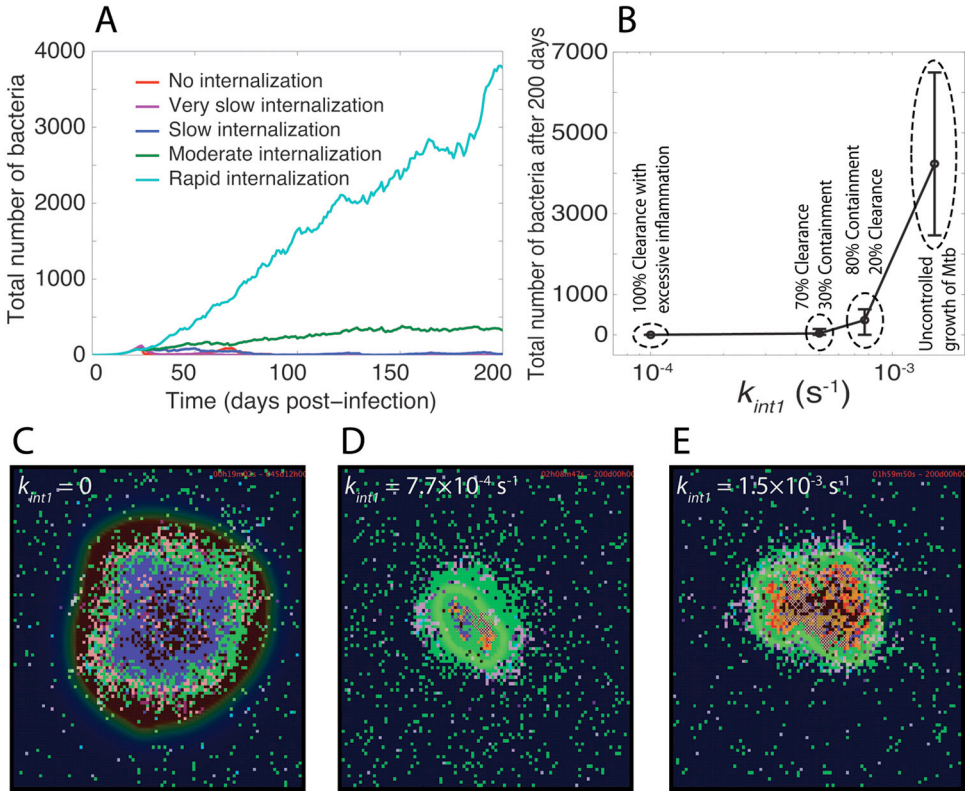

Fig. 3.4 TNFR1 internalization dynamics control bacterial load during Mtb infection. Simulation results show: (A) Mtb dynamics within a 200 day period after Mtb infection, (B) granuloma outcomes and bacterial load 200 days post-infection, (C) granuloma snapshot at the time of Mtb clearance (day 45) in the absence of TNFR1 internalization ($k_{int1} = 0$), (D)-(E) granuloma snapshots 200 days after Mtb infection for moderate ($k_{int1} = 7.7\times10^{-4}\ s^{-1}$) and rapid ($k_{int1} = 1.5\times10^{-3}\ s^{-1}$) rates of TNFR1 internalization. The colors representing cells of different type and status in granuloma snapshots are the same as shown in Fig. 3.2.

3.3.5 Do high rates of TNFR1 internalization and slow rates of TNF synthesis have the same effects?

In the previous section, we showed that the rate of sTNF-induced TNFR1 internalization significantly affects the immune response to Mtb; a small value of TNFR1 internalization rate constant favors Mtb clearance, while increasing the rate of TNFR1 internalization leads to uncontrolled growth of Mtb. One might argue that such an effect is simply attributable to the role of TNFR1 internalization in reducing sTNF concentration in the granuloma, and that therefore an increase or a decrease in the rate of TNF synthesis may

compensate for the effects of increasing or decreasing the rate of TNFR1 internalization. To test this hypothesis, we compare the effects of manipulating rates of TNFR1 internalization and mTNF synthesis by macrophages on model outputs (such as bacterial numbers and inflammation). As indicated in Fig. 3.5A, a zero rate of TNFR1 internalization and a high rate of TNF synthesis both result in Mtb clearance. However, high rates of TNF synthesis, in contrast to very slow or zero rates of TNFR1 internalization, do not lead to dramatic increases in sTNF concentration and macrophage activation (Fig. 3.5B, C). This is because impairing TNFR1 internalization has a negative effect on rates of TNF-induced apoptosis (Fig. 3.5D), a process that has been suggested to be important for controlling the level of inflammation [30]. However, high rates of TNF synthesis favor apoptosis of macrophages and thus do not lead to extensive inflammation.

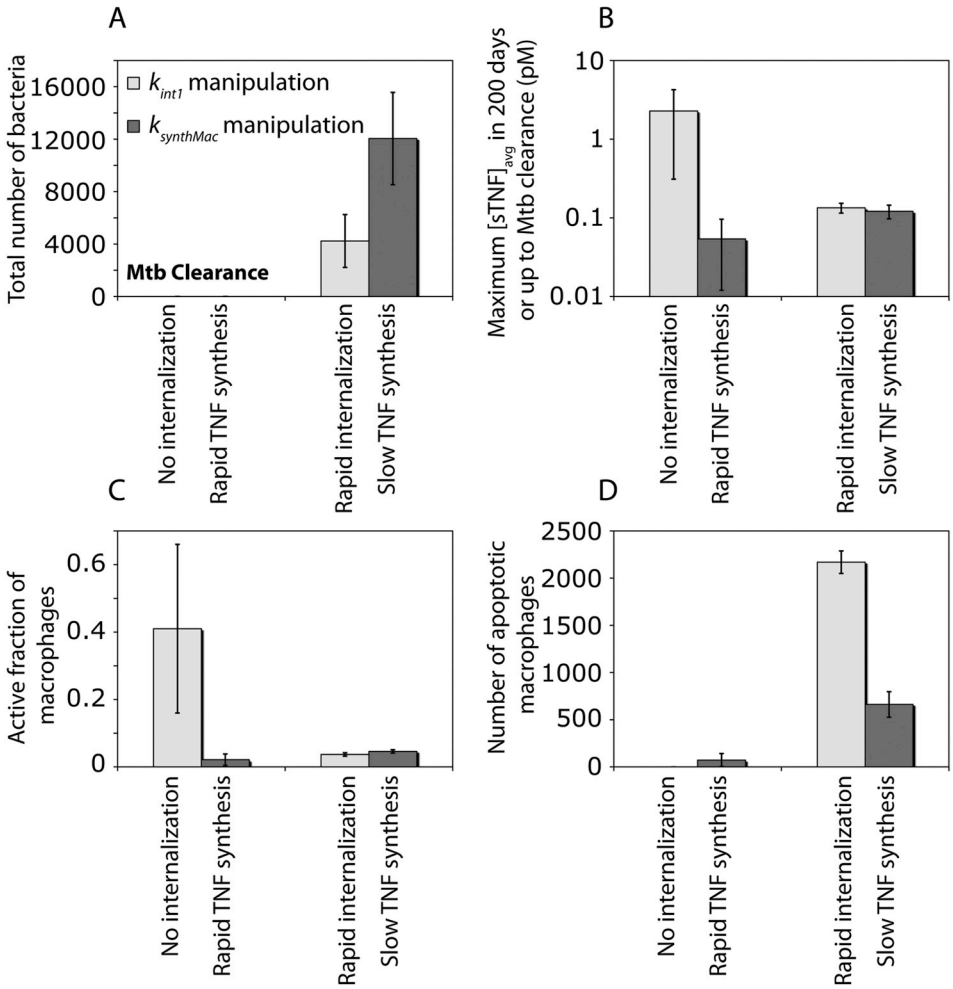

Fig. 3.5 Manipulations in the rate constants for TNFR1 internalization (k_{int1}) and mTNF synthesis ($k_{synthMac}$) lead to different effects on model outputs. Simulation results show the effect of manipulations in k_{int1} and $k_{synthMac}$ on (A) bacterial levels 200 days after Mtb infection, (B) maximum sTNF concentration, (C) maximum fraction of macrophages that become activated following Mtb infection and (D) TNF-induced macrophage apoptosis within a 200-day period after Mtb infection (No internalization: k_{int1} = 0, rapid TNF synthesis : $k_{synthMac}$ = 1 #/cell.s, rapid internalization: k_{int1} = 1.5×10^{-3} s^{-1}, slow TNF synthesis: $k_{synthMac}$ = 0.1 #/cell.s).

On the other hand, a rapid rate of TNFR1 internalization and a small rate of TNF synthesis both result in uncontrolled growth of Mtb, although to different extents (Fig. 3.5A). This difference can be explained by high levels of TNF-induced apoptosis in macrophages (and thus infected macrophages) for high values of TNFR1 internalization rate constant, whereas a small rate of TNF synthesis leads to lower levels of apoptosis

(Fig. 3.5D). Apoptosis of infected macrophages can help with reducing intracellular bacterial burden [25]. Thus, our results suggest that the impact of TNF/TNFR trafficking on Mtb infection is more complex than simply changing the TNF concentration in the granuloma.

3.3.6 TNFR1 internalization controls the spatial range of TNF action within a granuloma

As demonstrated above, sTNF-induced TNFR1 internalization controls both Mtb infection and inflammation in tissue. How does this process play such a key role? Here, we explore the possibility that the spatial range of TNF action underlies the important effects of the rate of TNFR1 internalization on granuloma function. By spatial range of TNF action, we mean the area surrounding the center of granuloma, as indicated in Fig. 3.6A, within which macrophages become activated or undergo apoptosis via autocrine or paracrine stimulation pathways [19,25,69]. As infected macrophages are located in the core of granuloma surrounded by resting macrophages, the spatial range of TNF action is correlated with the infection status of macrophages affected by TNF. Thus, motivated by our sensitivity analysis (Appendix B (Table B.7)), we explore here the possibility that TNF/TNFR trafficking leads to differential effects on TNF-mediated responses in cells of different infection status. We analyzed the infection status of macrophages affected by TNF-induced events (either NF-κB activation or apoptosis) following Mtb infection by computing infected:resting cell ratios, $R_{NF\text{-}\kappa B}$ and $R_{apoptosis}$, as defined in Methods (Fig. 3.6B). These ratios compare TNF effects on infected macrophages versus resting macrophages during the Mtb immune response. Our model predicts a very significant

effect of TNFR1 internalization on both $R_{apoptosis}$ and $R_{NF\text{-}\kappa B}$ (Fig. 3.6B). At very slow rates of sTNF-induced TNFR1 internalization (half-time of ~115 min, $k_{int1} = 1.0\times10^{-4}$ s^{-1}) resting macrophages are the main cells affected by both TNF-mediated apoptosis and NF-κB signaling pathways ($R_{apoptosis}$ and $R_{NF\text{-}\kappa B} << 1$). However, with a dramatic increase in the rate of TNFR1 internalization (to a half-time of ~7.7 min, $k_{int1} = 1.5\times10^{-3}$ s^{-1}), infected macrophages become the main responders to TNF-induced activities ($R_{apoptosis}$ and $R_{NF\text{-}\kappa B} >> 1$). Fig. 3.6C-F display how granulomas are affected by the rate at which sTNF/TNFR1 complexes become internalized; these snapshots are taken early after T cell recruitment to the site of infection. While a significant fraction of resting macrophages surrounding the infected core of granuloma become activated as a result of slow rates of TNFR1 internalization (i.e. there is a greater spatial range of TNF action, as seen in Fig. 3.6C), only a small number of infected macrophages in the core may become activated with a rapid rate of TNFR1 internalization (Fig. 3.6F). Thus, we suggest that the spatial range of TNF action within a granuloma is an important factor that controls the effect of TNFR1 internalization on the bacterial outcome of Mtb infection as well as the level of inflammation in the tissue.

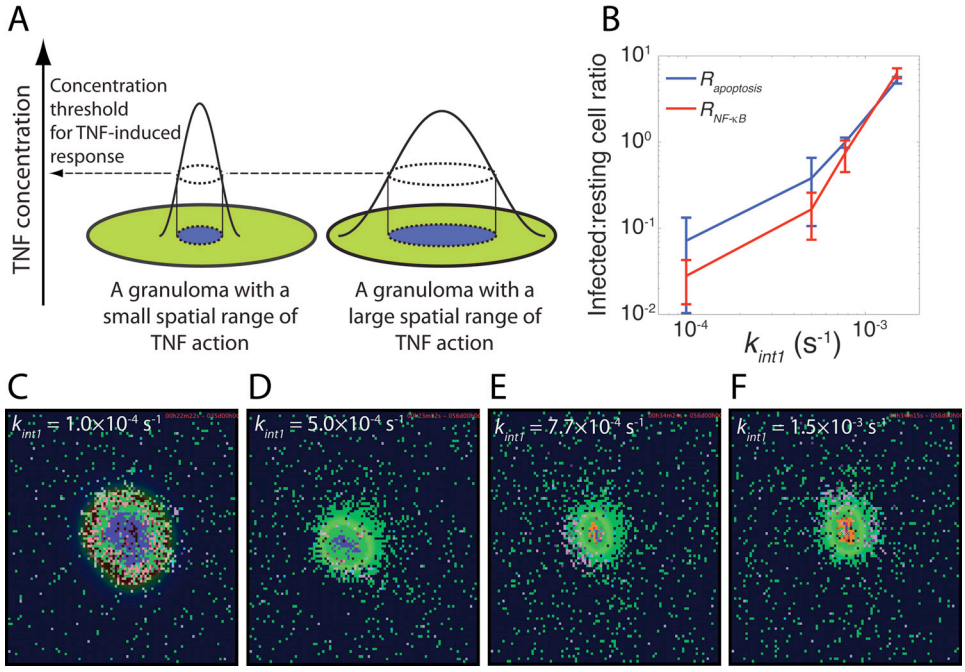

Fig. 3.6 TNFR1 internalization dynamics control the spatial range of TNF action within a granuloma. (A) Schematic definition of spatial range of TNF action in a granuloma, (B) The effect of k_{int1} on $R_{apoptosis}$ and $R_{NF-\kappa B}$, the ratios of total number of TNF-induced (apoptotic and NF-κB activated) infected macrophages to the number of TNF-resting resting macrophages within a 200 day period after Mtb infection, (C)-(F) Granuloma snapshots early after recruitment of T cells for very slow, slow, medium and rapid rates of sTNF-induced TNFR1 internalization. Simulated granuloma snapshots are shown at 5 weeks after Mtb infection, right before clearance of bacteria in (C) and at 8 weeks after Mtb infection in (D-F). The colors representing cells of different type and status in granuloma snapshots are the same as shown in Fig. 3.2.

3.3.7 A robust metric for assessing TNF impact on granuloma function

In the previous section, we demonstrated that the impact of the rate of TNFR1 internalization on bacterial levels in a granuloma is significantly correlated with infection status of macrophages that undergo TNF-mediated apoptosis or NF-κB activation ($R_{apoptosis}$ and $R_{NF-\kappa B}$). Here, we explore the possibility that such a correlation between TNF activities and infection outcome also exists for other processes. We analyzed the effect of varying values of important TNF-associated molecular scale and linking parameters on $R_{apoptosis}$ and $R_{NF-\kappa B}$ during a 200-day period post-infection. A significant correlation was observed between bacterial levels and infected:resting cell ratios, $R_{apoptosis}$

and $R_{NF\text{-}\kappa B}$. As indicated in Fig. 3.7, an increase of one order of magnitude in cell surface sTNF/TNFR1 concentration threshold for NF-κB activation and TNF degradation rate constant, or a decrease of one order of magnitude in NF-κB activation rate constant and the rate of mTNF synthesis by macrophages around baseline parameter values led to significant increases in both $R_{apoptosis}$ and $R_{NF\text{-}\kappa B}$ as well as bacterial levels. Outcomes of uncontrolled growth of Mtb generally occur at $R_{apoptosis}$ and $R_{NF\text{-}\kappa B}$ values of 1-10 or greater, while the chance of achieving clearance is greater for smaller values of these ratios. However, as indicated in Fig. 3.7E, when macrophage TNFR1 density is varied, the correlation between these ratios and bacterial levels (in clearance and containment cases in particular) does not appear very significant. This is probably because TNFR1 density has contradictory effects on TNF functions; although greater TNFR1 densities lead to more sensitive responses to smaller TNF concentrations, at the same time such larger densities enhance TNF uptake by macrophages limiting TNF availability in a granuloma. Overall, we suggest that infected:resting cell ratios we introduced here to compare TNF effects on infected versus resting macrophages, $R_{apoptosis}$ and $R_{NF\text{-}\kappa B}$, translate the effects of a variety of TNF-associated processes to granuloma outcomes.

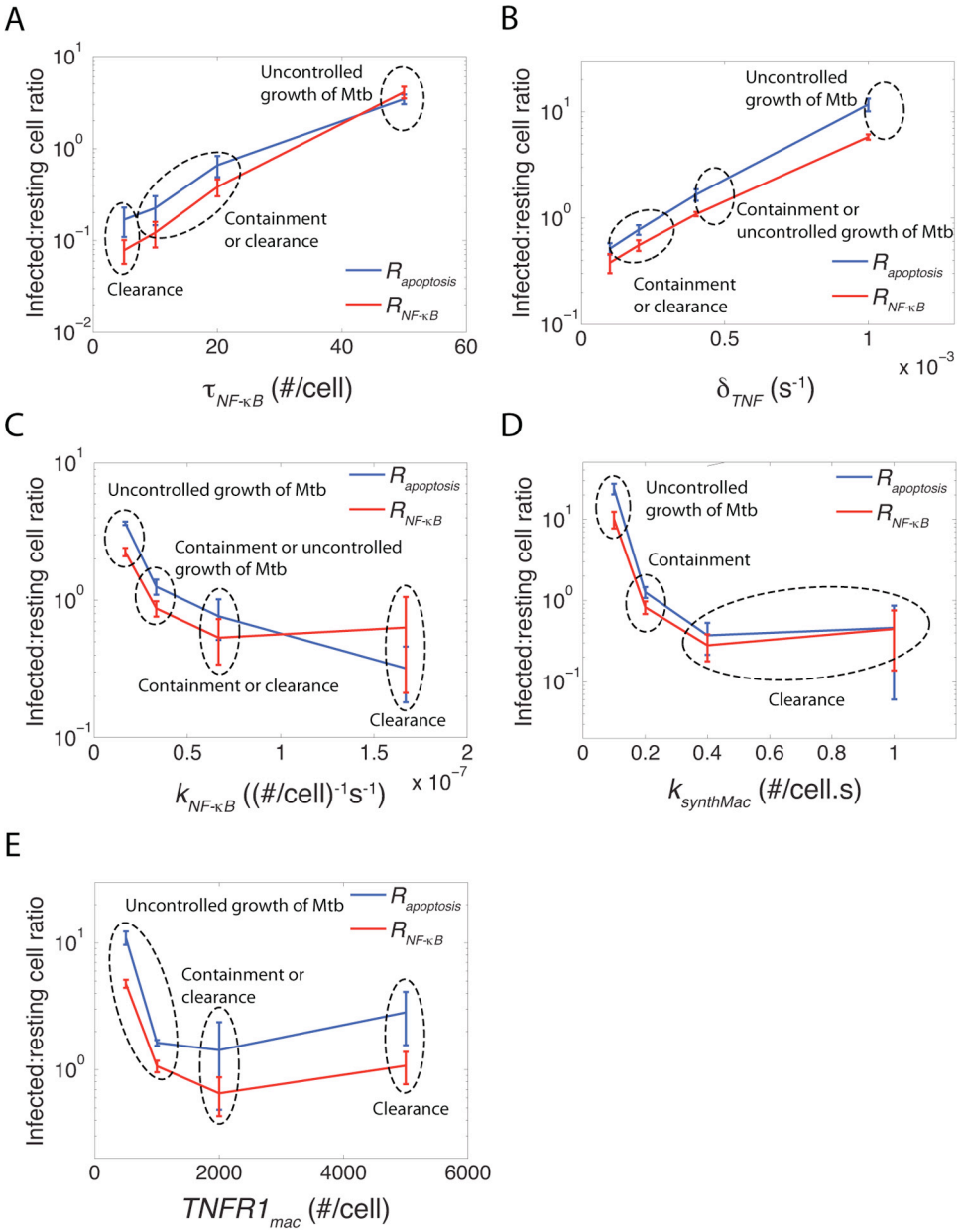

Fig. 3.7 The impact of TNF/TNFR-associated processes on granuloma outcome is correlated with infection status of macrophages that undergo TNF-mediated apoptosis or NF-κB activation. Simulation results show the effect of: (A) cell surface sTNF/TNFR1 concentration threshold for NF-κB activation ($\tau_{NF\text{-}\kappa B}$), (B) sTNF degradation rate constant (δ_{TNF}), (C) NF-κB activation rate constant ($k_{NF\text{-}\kappa B}$), (D) rate of mTNF synthesis by macrophages ($k_{synthMac}$), and (E) macrophage TNFR1 density ($TNFR1_{mac}$) on infected:resting cell ratios $R_{apoptosis}$ and $R_{NF\text{-}\kappa B}$ within a 200-day period after Mtb infection. Also indicated is granuloma outcome (clearance, containment, or uncontrolled growth of Mtb).

3.4 Discussion

TNF was long suggested, based on experimental data from mice, to be essential for formation of granulomas in response to Mtb [17,26,70]. However, recent TNFR1 knockout and TNF neutralization experiments in zebrafish and non-human primate models have shown that TNF, although not required for the formation of a granuloma, is important to restrict mycobacterial growth in a granuloma [27,71]. This suggests that TNF activities *within* a granuloma determine our ability to control Mtb infection. The important questions are, then, how TNF activities influence granuloma function, and what mechanisms control TNF activities in a granuloma during a long-term immune response to Mtb? To answer these questions, we need information about the spatial and temporal dynamics of TNF concentration during granuloma development *in vivo*. These experiments are not at present feasible, and thus, theses questions have remained unanswered. In this study, we use computational modeling/systems biology to address these questions. Our novel hypothesis is that events at different biological scales (molecular, cellular and tissue scales) may influence TNF activities in a granuloma, ultimately determining a granuloma's ability to control infection and inflammation. To address this hypothesis, our model was developed to link the dynamics of molecular scale TNF/TNFR interactions that occur on the second to minute time scales to cellular/tissue scale events that control the long-term immune response to Mtb. One of our interesting findings is that both TNF-independent cellular/tissue scale events (e.g. T cell recruitment or chemotactic movement of immune cells) and TNF-associated molecular scale processes (e.g. mTNF synthesis or TNFR1 internalization) influence TNF availability and activity in the granuloma, but in different ways. TNF-independent cellular scale

processes influence bacterial numbers and that controls TNF availability. However, TNF-associated molecular scale processes directly affect TNF availability and activities that control both the level of inflammation and bacterial numbers. Thus, there is an inter-play between TNF availability and bacterial population at the site of infection that is controlled by the combined effects of molecular and cellular scale processes. An equilibrium state in this inter-play leads to control of infection within a granuloma.

Our model reveals, for the first time, the importance of TNF-associated molecular processes (TNFR1 internalization in particular) in immunity to Mtb. We found that TNFR1 internalization regulates a balance between paracrine and autocrine TNF-induced responses, including NF-κB activation and apoptosis, in resting versus infected macrophages. Because resting macrophages do not express TNF, they become activated by TNF-producing cells only in a paracrine manner. However, infected macrophages express and release TNF to the extracellular space. Hence, they can become activated under the effect of TNF via both autocrine and paracrine pathways. Our results show that TNFR1 internalization favors activation of infected macrophages in an autocrine manner by restricting the diffusion of TNF from TNF-producing cells. TNF-induced activation of resting macrophages in addition to infected macrophages is necessary for controlling Mtb infection. Uncontrolled activation of resting macrophages, on the other hand, may result in excessive inflammation. Thus, a balance between the autocrine and paracrine TNF-induced responses is required for an efficient granuloma response to Mtb and an optimum rate of TNFR1 internalization can provide this balance. This finding can be considered in future studies examining approaches to control and therapy of TB or inhibition of TB

reactivation as several ways have already been proposed to influence the rate of TNFR1 internalization *in vitro* [42,72,73].

Another novel hypothesis from this study is that the efficacy of TNF in controlling Mtb infection is strongly affected by whether or not macrophages induced by TNF-mediated signaling pathways (NF-κB activation and apoptosis) are infected. Bacterial numbers are positively correlated with the ratio of infected macrophages to (uninfected) resting macrophages that become activated by TNF. Thus, we suggest that this ratio is a critical factor that controls the outcome of Mtb infection at the granuloma level. This might be of particular interest in the case of TB reactivation as a result of using TNF-neutralizing drugs (e.g. for treatment of inflammatory diseases such as rheumatoid arthritis and Crohn's disease). As drug penetrates into a granuloma, resting macrophages, compared with infected macrophages in the granuloma core, are exposed to smaller concentrations of TNF and are affected by higher concentrations of the drug. This can potentially impair TNF function, leading to TB reactivation.

Finally, our findings may predict new therapies for control of TB as they suggest novel host targets (e.g. TNFR1 internalization and NF-κB activation) that play key roles in control of Mtb immune response. Further modeling studies including molecular detail of additional processes, such as those involving other cytokines (e.g. IL-10, IL-6 and IL-12) and chemokines, and using a similar approach to that identified here may also identify other important targets for therapy. Our multi-scale computational model also provides a platform at the level of single granuloma to identify and compare therapeutic strategies as well as to investigate mechanisms by which TNF-neutralizing drugs (used to

treat inflammatory diseases) (see Chapter 5) or other drugs that diffuse in TB lesions may interfere with immune response to Mtb and reactivate TB.

3.5 References

1. Mortellaro A, Robinson L, Ricciardi-Castagnoli P (2009) Spotlight on mycobacteria and dendritic cells: Will novel targets to fight tuberculosis emerge?. EMBO Mol Med 1: 19-29.

2. Russell DG, Barry CE,3rd, Flynn JL (2010) Tuberculosis: What we don't know can, and does, hurt us. Science 328: 852-856.

3. Lin PL, Flynn JL (2010) Understanding latent tuberculosis: A moving target. J Immunol 185: 15-22.

4. Algood HM, Chan J, Flynn JL (2003) Chemokines and tuberculosis. Cytokine Growth Factor Rev 14: 467-477.

5. Morel PA, Ta'asan S, Morel BF, Kirschner DE, Flynn JL (2006) New insights into mathematical modeling of the immune system. Immunol Res 36: 157-165.

6. Davis JM, Ramakrishnan L (2008) "The very pulse of the machine": The tuberculous granuloma in motion. Immunity 28: 146-148.

7. Tsai MC, Chakravarty S, Zhu G, Xu J, Tanaka K, et al. (2006) Characterization of the tuberculous granuloma in murine and human lungs: Cellular composition and relative tissue oxygen tension. Cell Microbiol 8: 218-232.

8. Ulrichs T, Kosmiadi GA, Trusov V, Jorg S, Pradl L, et al. (2004) Human tuberculous granulomas induce peripheral lymphoid follicle-like structures to orchestrate local host defence in the lung. J Pathol 204: 217-228.

9. Lin PL, Pawar S, Myers A, Pegu A, Fuhrman C, et al. (2006) Early events in mycobacterium tuberculosis infection in cynomolgus macaques. Infect Immun 74: 3790-3803.

10. Turner OC, Basaraba RJ, Frank AA & Orme IM (2003) in *Granulomatous infections and inflammations: cellular and molecular mechanisms,* ed Boros DL (ASM Press, Washington, D.C.), pp 65-84.

11. Barry CE,3rd, Boshoff HI, Dartois V, Dick T, Ehrt S, et al. (2009) The spectrum of latent tuberculosis: Rethinking the biology and intervention strategies. Nat Rev Microbiol 7: 845-855.

12. Kirschner DE, Young D, Flynn JL (2010) Tuberculosis: Global approaches to a global disease. Curr Opin Biotechnol 21: 524-531.

13. Flynn JL (2004) Immunology of tuberculosis and implications in vaccine development. Tuberculosis (Edinb) 84: 93-101.

14. Cooper AM (2009) Cell-mediated immune responses in tuberculosis. Annu Rev Immunol 27: 393-422.

15. Hanlon AM, Jang S, Salgame P (2002) Signaling from cytokine receptors that affect Th1 responses. Front Biosci 7: d1247-54.

16. Lauffenburger D, Linderman JJ (1993) Receptors: models for binding, trafficking, and signaling. New York: Oxford University Press.

17. Flynn JL, Goldstein MM, Chan J, Triebold KJ, Pfeffer K, et al. (1995) Tumor necrosis factor-alpha is required in the protective immune response against mycobacterium tuberculosis in mice. Immunity 2: 561-572.

18. Saunders BM, Briscoe H, Britton WJ (2004) T cell-derived tumour necrosis factor is essential, but not sufficient, for protection against mycobacterium tuberculosis infection. Clin Exp Immunol 137: 279-287.

19. Harris J, Hope JC, Keane J (2008) Tumor necrosis factor blockers influence macrophage responses to mycobacterium tuberculosis. J Infect Dis 198: 1842-1850.

20. Gutierrez MG, Mishra BB, Jordao L, Elliott E, Anes E, et al. (2008) NF-kappa B activation controls phagolysosome fusion-mediated killing of mycobacteria by macrophages. J Immunol 181: 2651-2663.

21. Mosser DM, Edwards JP (2008) Exploring the full spectrum of macrophage activation. Nat Rev Immunol 8: 958-969.

22. Zhou Z, Connell MC, MacEwan DJ (2007) TNFR1-induced NF-kappaB, but not ERK, p38MAPK or JNK activation, mediates TNF-induced ICAM-1 and VCAM-1 expression on endothelial cells. Cell Signal 19: 1238-1248.

23. Algood HM, Lin PL, Yankura D, Jones A, Chan J, et al. (2004) TNF influences chemokine expression of macrophages in vitro and that of CD11b+ cells in vivo during mycobacterium tuberculosis infection. J Immunol 172: 6846-6857.

24. Keane J, Shurtleff B, Kornfeld H (2002) TNF-dependent BALB/c murine macrophage apoptosis following mycobacterium tuberculosis infection inhibits bacillary growth in an IFN-gamma independent manner. Tuberculosis (Edinb) 82: 55-61.

25. Keane J, Balcewicz-Sablinska MK, Remold HG, Chupp GL, Meek BB, et al. (1997) Infection by mycobacterium tuberculosis promotes human alveolar macrophage apoptosis. Infect Immun 65: 298-304.

26. Chakravarty SD, Zhu G, Tsai MC, Mohan VP, Marino S, et al. (2008) Tumor necrosis factor blockade in chronic murine tuberculosis enhances granulomatous inflammation and disorganizes granulomas in the lungs. Infect Immun 76: 916-926.

27. Lin PL, Myers A, Smith L, Bigbee C, Bigbee M, et al. (2010) Tumor necrosis factor neutralization results in disseminated disease in acute and latent mycobacterium tuberculosis infection with normal granuloma structure in a cynomolgus macaque model. Arthritis Rheum 62: 340-350.

28. Roach DR, Bean AG, Demangel C, France MP, Briscoe H, et al. (2002) TNF regulates chemokine induction essential for cell recruitment, granuloma formation, and clearance of mycobacterial infection. J Immunol 168: 4620-4627.

29. Marino S, Sud D, Plessner H, Lin PL, Chan J, et al. (2007) Differences in reactivation of tuberculosis induced from anti-TNF treatments are based on bioavailability in granulomatous tissue. PLoS Comput Biol 3: 1909-1924.

30. Ray JC, Flynn JL, Kirschner DE (2009) Synergy between individual TNF-dependent functions determines granuloma performance for controlling mycobacterium tuberculosis infection. J Immunol 182: 3706-3717.

31. Fallahi-Sichani M, Schaller MA, Kirschner DE, Kunkel SL, Linderman JJ (2010) Identification of key processes that control tumor necrosis factor availability in a tuberculosis granuloma. PLoS Comput Biol 6: e1000778.

32. Warrender C, Forrest S, Koster F (2006) Modeling intercellular interactions in early mycobacterium infection. Bull Math Biol 68: 2233-2261.

33. Pedrosa J, Saunders BM, Appelberg R, Orme IM, Silva MT, et al. (2000) Neutrophils play a protective nonphagocytic role in systemic mycobacterium tuberculosis infection of mice. Infect Immun 68: 577-583.

34. Seiler P, Aichele P, Bandermann S, Hauser AE, Lu B, et al. (2003) Early granuloma formation after aerosol mycobacterium tuberculosis infection is regulated by neutrophils via CXCR3-signaling chemokines. Eur J Immunol 33: 2676-2686.

35. Zhang X, Majlessi L, Deriaud E, Leclerc C, Lo-Man R (2009) Coactivation of syk kinase and MyD88 adaptor protein pathways by bacteria promotes regulatory properties of neutrophils. Immunity 31: 761-771.

36. Zhu XW, Friedland JS (2006) Multinucleate giant cells and the control of chemokine secretion in response to mycobacterium tuberculosis. Clin Immunol 120: 10-20.

37. Lay G, Poquet Y, Salek-Peyron P, Puissegur MP, Botanch C, et al. (2007) Langhans giant cells from M. tuberculosis-induced human granulomas cannot mediate mycobacterial uptake. J Pathol 211: 76-85.

38. Uehira K, Amakawa R, Ito T, Tajima K, Naitoh S, et al. (2002) Dendritic cells are decreased in blood and accumulated in granuloma in tuberculosis. Clin Immunol 105: 296-303.

39. Giri PK, Schorey JS (2008) Exosomes derived from M. bovis BCG infected macrophages activate antigen-specific CD4+ and CD8+ T cells in vitro and in vivo. PLoS One 3: e2461.

40. Ordway D, Henao-Tamayo M, Orme IM, Gonzalez-Juarrero M (2005) Foamy macrophages within lung granulomas of mice infected with mycobacterium tuberculosis express molecules characteristic of dendritic cells and antiapoptotic markers of the TNF receptor-associated factor family. J Immunol 175: 3873-3881.

41. Peyron P, Vaubourgeix J, Poquet Y, Levillain F, Botanch C, et al. (2008) Foamy macrophages from tuberculous patients' granulomas constitute a nutrient-rich reservoir for M. tuberculosis persistence. PLoS Pathog 4: e1000204.

42. Schutze S, Machleidt T, Adam D, Schwandner R, Wiegmann K, et al. (1999) Inhibition of receptor internalization by monodansylcadaverine selectively blocks p55 tumor necrosis factor receptor death domain signaling. J Biol Chem 274: 10203-10212.

43. Schneider-Brachert W, Tchikov V, Neumeyer J, Jakob M, Winoto-Morbach S, et al. (2004) Compartmentalization of TNF receptor 1 signaling: Internalized TNF receptosomes as death signaling vesicles. Immunity 21: 415-428.

44. Schutze S, Tchikov V, Schneider-Brachert W (2008) Regulation of TNFR1 and CD95 signalling by receptor compartmentalization. Nat Rev Mol Cell Biol 9: 655-662.

45. Gupta S (2002) A decision between life and death during TNF-alpha-induced signaling. J Clin Immunol 22: 185-194.

46. Saunders BM, Tran S, Ruuls S, Sedgwick JD, Briscoe H, et al. (2005) Transmembrane TNF is sufficient to initiate cell migration and granuloma formation and provide acute, but not long-term, control of mycobacterium tuberculosis infection. J Immunol 174: 4852-4859.

47. Fremond C, Allie N, Dambuza I, Grivennikov SI, Yeremeev V, et al. (2005) Membrane TNF confers protection to acute mycobacterial infection. Respir Res 6: 136.

48. Olleros ML, Guler R, Vesin D, Parapanov R, Marchal G, et al. (2005) Contribution of transmembrane tumor necrosis factor to host defense against mycobacterium bovis bacillus calmette-guerin and mycobacterium tuberculosis infections. Am J Pathol 166: 1109-1120.

49. Tay S, Hughey JJ, Lee TK, Lipniacki T, Quake SR, et al. (2010) Single-cell NF-kappaB dynamics reveal digital activation and analogue information processing. Nature 466: 267-271.

50. Marino S, Hogue IB, Ray CJ, Kirschner DE (2008) A methodology for performing global uncertainty and sensitivity analysis in systems biology. J Theor Biol 254: 178-196.

51. Fotin-Mleczek M, Henkler F, Samel D, Reichwein M, Hausser A, et al. (2002) Apoptotic crosstalk of TNF receptors: TNF-R2-induces depletion of TRAF2 and IAP proteins and accelerates TNF-R1-dependent activation of caspase-8. J Cell Sci 115: 2757-2770.

52. Rangamani P, Sirovich L (2007) Survival and apoptotic pathways initiated by TNF-alpha: Modeling and predictions. Biotechnol Bioeng 97: 1216-1229.

53. Blower SM, Dowlatabadi H (1994) Sensitivity and uncertainty analysis of complex models of disease transmission: An HIV model, as an example. Int Stat Rev 62: 229-243.

54. Bold TD, Ernst JD (2009) Who benefits from granulomas, mycobacteria or host?. Cell 136: 17-19.

55. Lazarevic V, Nolt D, Flynn JL (2005) Long-term control of mycobacterium tuberculosis infection is mediated by dynamic immune responses. J Immunol 175: 1107-1117.

56. Lin PL, Rodgers M, Smith L, Bigbee M, Myers A, et al. (2009) Quantitative comparison of active and latent tuberculosis in the cynomolgus macaque model. Infect Immun 77: 4631-4642.

57. Flynn JL, Chan J (2001) Immunology of tuberculosis. Annu Rev Immunol 19: 93-129.

58. Sada-Ovalle I, Chiba A, Gonzales A, Brenner MB, Behar SM (2008) Innate invariant NKT cells recognize mycobacterium tuberculosis-infected macrophages, produce interferon-gamma, and kill intracellular bacteria. PLoS Pathog 4: e1000239.

59. Segovia-Juarez JL, Ganguli S, Kirschner D (2004) Identifying control mechanisms of granuloma formation during M. tuberculosis infection using an agent-based model. J Theor Biol 231: 357-376.

60. Theus S, Eisenach K, Fomukong N, Silver RF, Cave MD (2007) Beijing family mycobacterium tuberculosis strains differ in their intracellular growth in THP-1 macrophages. Int J Tuberc Lung Dis 11: 1087-1093.

61. Lin PL, Plessner HL, Voitenok NN, Flynn JL (2007) Tumor necrosis factor and tuberculosis. J Investig Dermatol Symp Proc 12: 22-25.

62. Keane J, Gershon S, Wise RP, Mirabile-Levens E, Kasznica J, et al. (2001) Tuberculosis associated with infliximab, a tumor necrosis factor alpha-neutralizing agent. N Engl J Med 345: 1098-1104.

63. Winthrop KL (2006) Risk and prevention of tuberculosis and other serious opportunistic infections associated with the inhibition of tumor necrosis factor. Nat Clin Pract Rheumatol 2: 602-610.

64. Flynn JL (2006) Lessons from experimental mycobacterium tuberculosis infections. Microbes Infect 8: 1179-1188.

65. Bean AG, Roach DR, Briscoe H, France MP, Korner H, et al. (1999) Structural deficiencies in granuloma formation in TNF gene-targeted mice underlie the heightened susceptibility to aerosol mycobacterium tuberculosis infection, which is not compensated for by lymphotoxin. J Immunol 162: 3504-3511.

66. Grell M, Wajant H, Zimmermann G, Scheurich P (1998) The type 1 receptor (CD120a) is the high-affinity receptor for soluble tumor necrosis factor. Proc Natl Acad Sci U S A 95: 570-575.

67. Higuchi M, Aggarwal BB (1994) TNF induces internalization of the p60 receptor and shedding of the p80 receptor. J Immunol 152: 3550-3558.

68. Bekker LG, Moreira AL, Bergtold A, Freeman S, Ryffel B, et al. (2000) Immunopathologic effects of tumor necrosis factor alpha in murine mycobacterial infection are dose dependent. Infect Immun 68: 6954-6961.

69. Engele M, Stossel E, Castiglione K, Schwerdtner N, Wagner M, et al. (2002) Induction of TNF in human alveolar macrophages as a potential evasion mechanism of virulent mycobacterium tuberculosis. J Immunol 168: 1328-1337.

70. Algood HM, Lin PL, Flynn JL (2005) Tumor necrosis factor and chemokine interactions in the formation and maintenance of granulomas in tuberculosis. Clin Infect Dis 41 Suppl 3: S189-93.

71. Clay H, Volkman HE, Ramakrishnan L (2008) Tumor necrosis factor signaling mediates resistance to mycobacteria by inhibiting bacterial growth and macrophage death. Immunity 29: 283-294.

72. Schneider-Brachert W, Tchikov V, Merkel O, Jakob M, Hallas C, et al. (2006) Inhibition of TNF receptor 1 internalization by adenovirus 14.7K as a novel immune escape mechanism. J Clin Invest 116: 2901-2913.

73. Neumeyer J, Hallas C, Merkel O, Winoto-Morbach S, Jakob M, et al. (2006) TNF-receptor I defective in internalization allows for cell death through activation of neutral sphingomyelinase. Exp Cell Res 312: 2142-2153.

Chapter 4

The dynamics of TNF-mediated NF-κB signaling control tuberculosis granuloma formation and function

4.1 Introduction

Tuberculosis (TB) is a deadly infectious disease in humans caused by the intracellular pathogen *Mycobacterium tuberculosis* (Mtb). While TB is a global health problem with 2 billion people infected, most are in a latent state, controlling infection [1]. Various immune factors, including immune cells, cytokines and chemokines are known to play key roles in developing protective immune responses against Mtb (reviewed in [2]). Tumor necrosis factor-α (TNF) is an important cytokine for preventing progression of initial infection or reactivation of latent infection in several animal models, including non-human primates [3-8]. The use of TNF inhibitors as treatment for inflammatory diseases in humans has also confirmed that TNF is a major player in the protective immune response against Mtb [9-13]. However, TNF has numerous functions in the human immune response and sorting out which are the relevant mechanisms is difficult *in vivo.* TNF mediates cell death via inducing the caspase-mediated apoptotic pathway [14,15]. TNF activates the NF-κB signaling pathway in immune cells. When NF-κB is activated, inflammatory genes are induced that ultimately lead to activation of macrophages to efficiently kill bacteria [16-19], induction of macrophages to express TNF and chemokines [20], and inhibition of apoptosis [21,22].

The transcription factor NF-κB is a central inflammatory mediator that is essential for the induction of a variety of inflammatory genes in response to various pathogens and inflammatory cytokines, particularly TNF. In resting cells, NF-κB is bound to IκB proteins that hold it latent in cytoplasm. Cellular stimulation with TNF, for example, occurs when TNF binds and activates cell surface TNF receptor type 1 (TNFR1). This results in activation of IκB kinase (IKK) and IKK-mediated phosphorylation of IκB proteins that ultimately leads to ubiquitination and proteasome-mediated degradation of IκB. Free NF-κB then accumulates in the nucleus and mediates the transcription of target genes [23,24]. These genes include extracellular signaling molecules such as TNF and chemokines, intracellular proteins such as macrophage-activating molecules (referred to here as ACT) and inhibitor of apoptosis proteins (IAPs), as well as negative regulators of NF-κB such as IκBα and A20 [17,25,26]. The inhibitory impact of A20 on NF-κB results from its roles in attenuating TNFR1 activity and inhibiting IKK activation [27]. The regulation of NF-κB via multiple critical intracellular feedback mechanisms is important for the control of inflammation and immune activation [28-31]. Further, the structural characteristics of the inflammatory genes induced by NF-κB, particularly stability of their corresponding mRNA transcripts, control the dynamics of NF-κB mediated responses in cells [32]. However, the significance of these intracellular molecular mechanisms controlling the dynamics of TNF-induced NF-κB signaling in regulating the long-term immune response to Mtb infection is poorly characterized.

The key pathological feature of TB that arises as a result of the immune response is the formation of granulomas, aggregates of bacteria and immune cells within the lung. TB granulomas are varied in type based on their composition and function, but are

generally composed primarily of macrophages and lymphocytes, organized into a spherical structure (for review, see [33,34]). The classic caseous granuloma consists of a centrally necrotic area surrounded by infected, activated and resting macrophages, which are in turn surrounded by a smaller cuff of lymphocytes (T and B cells) [35-41]. A TB granuloma serves to focus the host immune response, contain infection and pathology, and provide a niche for Mtb to persist within the host. Thus, one can hypothesize that factors such as NF-κB that are critical to immunity against Mtb have significant effects on formation and function of different types of granulomas in the host [42,43]. These effects, however, have remained unknown. For example, it is unclear how the dynamics of NF-κB mediated responses (i.e. expression of chemokines, TNF and IAPs, and activation of macrophages) affect formation and function of a granuloma. A critical requirement for such studies is the integration of biological information across multiple biological scales (molecular, cellular, tissue and organ) [44].

We recently suggested via multi-scale computational modeling that TNF receptor (TNFR) dynamics, in particular the process of TNFR1 internalization, as well as the organization of immune cells within a granuloma critically control the TNF concentration gradients, bacterial load within a granuloma, and levels of inflammation in lung tissue [45,46] (see Chapters 2 and 3). Further, we identified, at the granuloma level, a synergy between TNF activities that contributes to control of infection [47]. TNF-mediated macrophage activation was shown to be a key mechanism for restricting bacterial growth and TNF-dependent apoptosis was indicated to be required for reducing inflammation in tissue. These studies have significantly improved our understanding of the role of TNF in TB granuloma formation and function. However, in order to use these data to improve

immunity to Mtb, we need to dissect further the molecular mechanisms that control these TNF activities within a granuloma. Understanding these mechanisms will lead us to approaches allowing us to manipulate TNF activities within a granuloma in favor of the host.

In this study, we modify our current multi-scale computational model to include molecular scale interactions and reactions involved within the TNF-induced NF-κB signaling pathway for each individual cell. Hence, the next-generation model links tissue scale outcome of granuloma formation to molecular scale processes that control dynamics of NF-κB signaling and thus the dynamics of the NF-κB mediated cell responses. We assess the sensitivity of the model identifying NF-κB-associated processes that influence infection outcome and inflammation at the granuloma scale. We show that dynamics of TNF-induced NF-κB signaling critically control bacterial load and inflammation levels in tissue. Further, activation of resting macrophages, in addition to infected macrophages, is required for a protective immune response, but must be optimally regulated by the immune system to prevent excessive inflammation. We also predict the impact of the dynamics (the extent and the timing) of various NF-κB mediated responses (i.e. expression of chemokines, TNF, IAPs, and activation of macrophages) on both formation and function of a granuloma. Finally, we ask the question whether manipulating the NF-κB signaling pathway can improve the outcome of a granuloma that is initially unable to control infection. Our analysis highlights the importance of NF-κB mediated response dynamics controlled by stability of their corresponding mRNAs as a target for infection control. These results can aid in the development of immunotherapeutic approaches to battle TB.

4.2 Methods

4.2.1 Multi-scale granuloma model

To address questions regarding TNF-regulated host immune responses to Mtb infection in the lung and the impact of NF-κB signaling dynamics on these responses, we developed a multi-scale computational model (Fig. 4.1) that describes processes over three biological length scales: tissue, cellular and molecular. Cellular and tissue scale dynamics are captured via probabilistic rules for interactions between immune cells and Mtb using a stochastic two-dimensional agent-based model (ABM). Single-cell level molecular scale processes include TNF/TNFR binding and trafficking events (defined here to include synthesis, internalization, recycling and degradation of ligand and receptors) as well as intracellular NF-κB signaling pathway interactions and reactions that are captured by nonlinear ordinary differential equations (ODEs). We briefly describe these models below and then describe our approach for linking them.

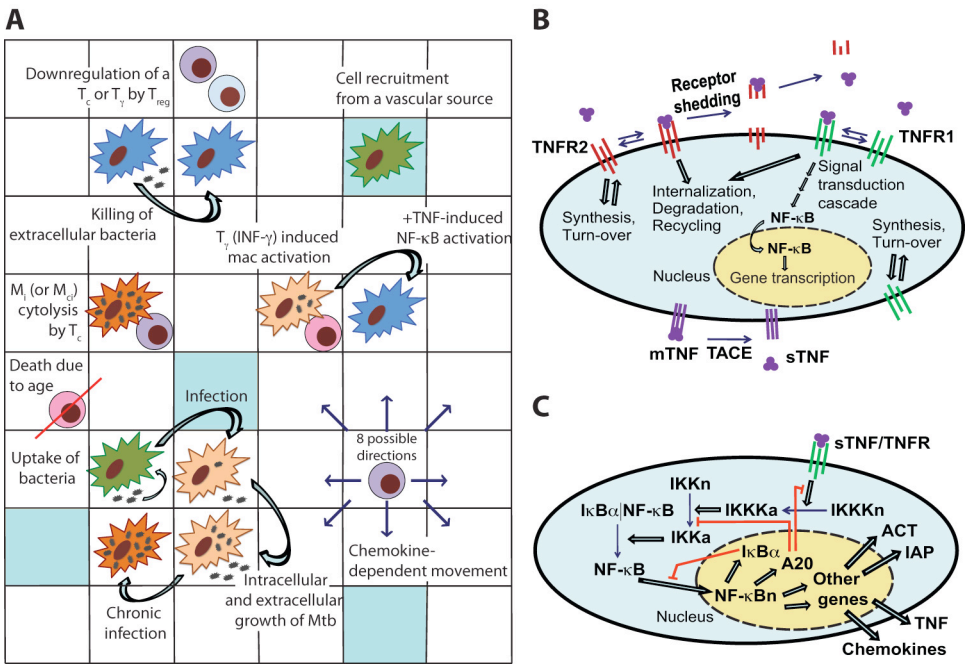

Fig. 4.1 Multi-scale computational model of granuloma formation in response to Mtb infection in the lung. (A) An overview of selected cell-level ABM rules based on known immunological activities and interactions (M_i: infected macrophage, M_{ci}: chronically infected macrophage, T_γ: pro-inflammatory IFN-γ producing T cell, T_c: cytotoxic T cell, T_{reg}: regulatory T cell). For a full description of all AMB rules, see Chapter 3 and [45]. (B) An overview of TNF/TNFR binding and trafficking interactions and reactions and the NF-κB signal transduction cascade at the level of individual cell. (C) Detailed description of the regulation of the TNF-induced NF-κB signaling pathway and NF-κB mediated responses for an individual macrophage.

The current ABM follows our previous models that capture cellular scale interactions leading to a tissue-level readout, namely granuloma formation in response to Mtb infection in primates [45,47,48]. The ABM has the following components: *agents* (immune cells, bacteria, chemokines and cytokines), the *environment* where agents reside (a two-dimensional grid representing a section of lung tissue), the probabilistic *rules* that govern the dynamics of agents, including movements, actions and interactions among agents and between agents and environment, and *time-scales* on which the rules are executed. Briefly, events described by probabilistic rules include: chemotactic movement and recruitment of immune cells from vascular sources to site of infection, intracellular and extracellular growth of Mtb, phagocytosis of bacteria by macrophages, cell death and

apoptosis, macrophage/T-cell interactions such as cytolytic functions of cytotoxic T cells (T_c) and IFN-γ-mediated activation of macrophages by pro-inflammatory T cells (T_γ), down-regulation of immune cells by regulatory T cells (T_{reg}), diffusion of chemokines and soluble TNF (sTNF), and caseation (Fig. 4.1A). A detailed description of the ABM structure and rules are presented in Chapter 3 and [45]. ABM parameters that reflect known biological activities are provided in Appendix C (Table C.1). We modified the most recent and complete version of the ABM [45] to facilitate its linking to an NF-κB signaling dynamics model. Major modifications in ABM rules are: NF-κB mediated macrophage activation, NF-κB mediated chemokine and TNF expression, and NF-κB-mediated inhibition of apoptosis. All of these activities are now controlled as part of the NF-κB signaling dynamics model.

The ODE model describing kinetic processes of TNF/TNFR binding and trafficking occurring in individual cells follows our previous models described in Chapters 2 and 3 [45,46] (Fig. 4.1B and Appendix C (Tables C.2, C.3)). We modified the reactions associated with TNF expression in this model to capture the linkage between this process and the NF-κB signaling pathway (see Appendix C (Table C.6)).

In order to capture the molecular mechanisms that control TNF-mediated responses at the single cell level, we first need to have a model describing intracellular NF-κB signaling pathway activation that follows TNFR activation due to TNF binding. Then, NF-κB activation must be linked to each of the NF-κB-mediated cell responses that include macrophage activation and expression of chemokines, TNF and inhibitor of apoptosis proteins. The single-cell level intracellular NF-κB signaling pathway interactions and reactions are captured by using the deterministic approximation of the

two-compartment NF-κB dynamics model presented by Tay *et al* [49]. This model combines the two-feedback NF-κB-IκBα-A20 regulatory module with the signal transduction cascade transmitting the signal from sTNF-bound TNFR1 receptors. TNFR1 activation results in an oscillatory NF-κB response that controls the dynamics of gene expression [50]. The model includes noise due to different levels of TNFRs and total NF-κB molecules across the cell population. This noise results from random assignment of initial values for TNFR densities and total NF-κB molecules to each single cell as described in [49].

In this study, we link the molecular scale NF-κB dynamics model described above to four major NF-κB-mediated cell responses in macrophages (Fig. 4.1C). These responses are: TNF expression, chemokine expression, macrophage activation, and inhibition of apoptosis. To do this, we incorporate NF-κB-mediated expression of genes corresponding to TNF, chemokines, a generic inhibitor of apoptosis protein (IAP), and a generic macrophage-activating molecule (ACT), translation of their mRNA transcripts, and secretion of translated TNF and chemokines into the single-cell level NF-κB dynamics model. The generic IAP represents a family of proteins that serve as inhibitors of apoptosis (e.g. cellular inhibitors of apoptosis, c-IAPs) via binding and inhibiting caspase activities [51]. The generic ACT represents various molecules (e.g. membrane trafficking molecules or lysosomal enzyme) that are induced by NF-κB and are required for activation of a macrophage to efficiently kill bacteria [17]. The reactions, parameters, and equations describing intracellular NF-κB signaling pathway processes and NF-κB-mediated responses for an individual cell are listed in Appendix C (Tables C.4, C.5, C.6).

4.2.2 Linking the single-cell molecular scale NF-κB signaling dynamics to the TNF/TNFR kinetic model and the cellular/tissue scale model

The activation of TNF-induced NF-κB signaling pathway requires sTNF binding to cell surface TNFR1. It is this process that links the TNF/TNFR kinetic model to the intracellular NF-κB signaling dynamics model. The activation of the NF-κB signaling pathway initiates four major cellular responses: induction of chemokine expression, TNF expression, macrophage activation (to efficiently kill bacteria), and inhibition of apoptosis. These responses serve as the link between the single-cell molecular scale NF-κB signaling dynamics model and the cellular/tissue scale model (Fig. 4.1). Secretion of chemokines and TNF by macrophages into extracellular spaces follows NF-κB-mediated expression of their genes and translation of their mRNA transcripts as described in the NF-κB signaling equations (see Appendix C (Tables C.4, C.6)). Recent studies on NF-κB activation and apoptosis have shown that these are processes with discrete nature at the single-cell level, with more cells responding to higher doses of stimuli and longer periods of stimulation [49,52]. Accordingly, we describe NF-κB-mediated activation of a macrophage as a Poisson process with a probability determined within each time-step (Δt), based on a Poisson rate parameter that is a function of the macrophage activation rate constant (k_{ACT}), intracellular concentration of ACT protein [ACT], and the ACT concentration threshold for macrophage activation (τ_{ACT}):

$$P_{activation} = \begin{cases} 0 & ; [ACT] < \tau_{ACT} \\ 1 - e^{-k_{ACT}([ACT]-\tau_{ACT})\Delta t} & ; [ACT] \geq \tau_{ACT} \end{cases} \quad (4.1)$$

Similarly, we model TNF-induced apoptosis for each individual cell by:

$$P_{apoptosis} = \begin{cases} 0 & ; [sTNF/TNFR1_i] < \tau_{apopt} \\ 1 - e^{-k_{apopt}([sTNF/TNFR1_i]-\tau_{apopt})\Delta t} & ; [sTNF/TNFR1_i] \geq \tau_{apopt} \end{cases} \quad (4.2)$$

We use a Poisson process with a probability computed as a function of the apoptosis rate constant (k_{apopt}), the concentration of internalized sTNF/TNFR1 complexes [sTNF/TNFR1$_i$], and the concentration threshold for internalized sTNF/TNFR1 (τ_{apopt}). The inhibitory impact of the NF-κB activation on macrophage apoptosis is captured by:

$$k_{apopt} = \frac{k_{IAP}}{k_{IAP} + [IAP]} k^0_{apopt} \tag{4.3}$$

The magnitude of k_{apopt} is a function of the intracellular concentration of IAP [IAP], the apoptosis inhibition coefficient (k_{IAP}), and the intrinsic TNF-induced apoptosis rate constant (k^0_{apopt}). Parameters introduced in Equations 4.1-3 are listed in Appendix C (Table C.5).

4.2.3 Computer simulations and model outputs

The multi-scale computational model is used to simulate the immune response to Mtb and granuloma formation in the lung for 200 days post-infection. Simulations are initiated following placement of one infected macrophage with one intracellular bacterium at the center of a grid representing a section of lung tissue (see Chapter 3 and [45] for details). Cell-cell interactions governed by ABM rules are updated within every ABM time-step (Δt = 10 min). Molecular scale processes, including TNF/TNFR dynamics and NF-κB signaling dynamics at the single-cell level, are updated within shorter time-steps (dt = 0.5 s).

We use several model outputs to track formation and function of a granuloma during the immune response to Mtb. Granuloma size and total number of macrophages and T cells in tissue are used as readouts to track granuloma formation. We also track total number of bacteria and total number of activated macrophages as readouts for

quantifying granuloma function. These outputs represent the ability of a granuloma to control infection and inflammation, respectively. Other outputs of interest include chemokine and TNF concentrations in tissue, and caseation area.

We previously showed that the efficacy of TNF in controlling Mtb infection is strongly affected by whether or not macrophages stimulated by TNF are infected [45]. To analyze how NF-κB signaling affects infected versus uninfected (resting) macrophages in a granuloma, we define *infected/resting cell ratios*, $R_{apoptosis}$ and $R_{activation}$, as follows. $R_{apoptosis}$ is defined as the ratio of the number of infected macrophages that undergo TNF-mediated apoptosis to the number of resting macrophages that undergo TNF-mediated apoptosis during a 200-day period post-infection. $R_{activation}$ is similarly defined as the number of infected macrophages that become activated (to efficiently kill bacteria) to the number of resting macrophages that become activated during a 200-day period post-infection.

4.2.4 Parameter estimation

We estimate ABM parameter values from literature data or by using uncertainty analysis as described in detail in [45,47,53]. Cell-specific TNFR densities and rate constants for TNF/TNFR processes are estimated based on experimental data from our group [46], as described in Chapter 2, and other groups as indicated in Appendix C (Table C.3). Intracellular NF-κB signaling parameters are as in Tay *et al* [49] (Appendix C (Table C.5)). Values of parameters used to describe TNF-induced apoptosis and NF-κB-mediated cell responses, including induction of expression of chemokines and TNF, macrophage activation and inhibition of apoptosis, are estimated via uncertainty analysis.

This is done by varying parameter values in ranges that are consistent with experimental and modeling data on time-scales of events associated with these responses [32,49,52,54,55]. We specify a baseline set of parameter values (containment baseline values as listed in Appendix C (Tables C.1, C.3 and C.5)) that robustly leads to control of infection in granulomas with organized structures as reported for humans and non-human primates.

4.2.5 Control experiments and model validation (virtual deletion and depletion studies)

Immunity to Mtb in humans and animal studies has been attributed to activities of a variety of factors, including specific immune cells (e.g. macrophages and T cells), cytokines (e.g. TNF and IFN-γ), chemokines (e.g. CCL2, CCL5, CXCL9/10/11), immune receptors (e.g. TNFR1), and signaling pathways (e.g. NF-κB). Our new multi-scale computational model (resulting from the incorporation of the single cell-level NF-κB signaling dynamics, as indicated in Fig. 4.1, into our previous generation model (Chapter 3) [45]) must retain its ability to reproduce experimental findings regarding the importance of these factors in control of infection. Hence, we first test whether our model is able to: (i) capture key features of granuloma formation and maintenance, and (ii) recapitulate different granuloma types as observed in humans and nonhuman primate models in response to Mtb infection [34,56]. To this aim, we take advantage of a number of useful and powerful tools to identify parameter changes that determine the infection outcome at the granuloma level. One approach is to perform virtual deletion and depletion experiments that mimic experimental gene knockout or molecule depletion

studies. Loss of activity is achieved by setting relevant parameters (e.g. probabilities or rate constants) to zero or raising relevant thresholds to an unattainable level. Virtual deletion refers to the loss of activity from the beginning of simulation (such as a gene knockout) and virtual depletion refers to the loss of activity after establishment of a granuloma. Specifically, we simulate gene knockouts of previously identified essential components of the Mtb immune response (e.g. TNF, TNFR1, IFN-γ and T cell knockouts). These simulation studies are used for testing the ability of the model to predict different infection outcomes under pathological conditions compatible with both experimental and previous modeling data on granuloma formation.

4.2.6 Infection outcomes at the granuloma level: containment, clearance, uncontrolled growth of bacteria, and uncontrolled inflammation

Our model is able to recapitulate different types of granuloma with different abilities to control infection and inflammation (Fig. 4.2). Using a baseline set of values for model parameters (Appendix C (Tables C.1, C.3, C.5), our model captures a state of equilibrium between the host and Mtb termed bacterial containment (Fig. 4.2A). This state represents control of infection for more than 200 days within a well-circumscribed granuloma containing stable bacteria numbers ($<10^3$ total bacteria). Simulated containment granulomas closely represent experimentally characterized solid granulomas [35-41] that are predominantly composed of uninfected macrophages surrounding a core of bacteria and infected and activated macrophages with T cells localized at the periphery. Varying values of important model parameters lead to other possibilities, including clearance of bacteria, uncontrolled growth of bacteria, or excessive inflammation.

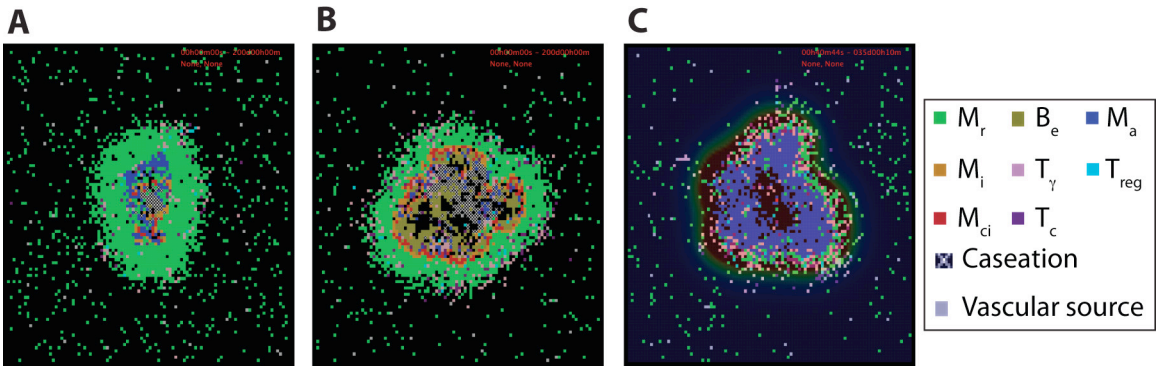

Fig. 4.2 Examples of control experiments on the multi-scale computational model of granuloma formation in response to Mtb infection. (A)-(C) Granuloma snapshots for a scenario of containment (200 days post-infection), a TNFR1 knockout ($TNFR1_{mac} = TNFR1_{Tcell} = 0$) scenario resulting in uncontrolled growth of bacteria 200 days post-infection, and a scenario of blocking TNFR1 internalization ($k_{int1} = 0$) resulting in excessive inflammation 5 weeks post-infection, respectively. All other model parameter values used for these experiments are listed in Appendix C (Tables C.1, C.3 and C.5). Cell types and status are shown by different color squares, as indicated in the lower right corner of the figure (M_r: resting macrophage, M_i: infected macrophage, M_{ci}: chronically infected macrophage, M_a: activated macrophage, B_e: extracellular bacteria, T_γ: pro-inflammatory IFN-γ producing T cell, T_c: cytotoxic T cell, T_{reg}: regulatory T cell). Caseation and vascular sources are also indicated.

Simulations of TNF or TNFR1 knockout (Fig. 4.2B), IFN-γ gene knockout, and deletion of T cells (data not shown), in agreement with experimental data and our previous modeling studies [2,45,47,48,57,58], lead to uncontrolled growth of Mtb and formation of granulomas with irregular structures that include very high numbers of extracellular bacteria, large numbers of infected macrophages and widespread caseation. In contrast, inhibition of TNFR1 internalization, a process critical to control of TNF concentration and apoptosis [45,46], leads to excessive inflammation by which we mean recruitment of a large number of immune cells in tissue, uncontrolled activation of macrophages and very high concentrations of TNF (Fig. 4.2C).

4.2.7 Sensitivity analysis

A second approach to identify important processes that determine infection outcome is to use sensitivity analysis [53]. We use sensitivity analysis to analyze the impact of

parameters describing events at different scales (molecular, cellular or tissue scales) on model outputs describing granuloma outcomes. Latin hypercube sampling (LHS) is an algorithm that allows multiple parameters to be varied and sampled simultaneously in a computationally efficient manner [59]. We use LHS sensitivity analysis as adapted for use in ABMs [60] to analyze the impact of NF-κB signaling-associated parameter values on model outputs. These outputs are, for example, bacteria numbers, macrophage and T cell numbers, chemokine and TNF concentrations in tissue, granuloma size and caseation area. The correlation of model outputs with each parameter is quantified via calculation of a partial rank correlation coefficient (PRCC). PRCC values vary between -1 (perfect negative correlation) and +1 (perfect positive correlation) and can be differentiated based on *p*-values derived from Student's *t* test. Here, we performed 700-sample LHS simulations for each parameter. Each sampled parameter set was run 4 times (to account for stochasticity) and averages of the outputs were used to calculate PRCC values. The choice of the number of simulations is determined by the desired significance level for the PRCC [59,60]. Here, 700 runs imply that PRCC values above +0.13 or below -0.13 are significantly different from zero ($p < 0.001$).

4.2.8 Programming and visualization

The model was implemented in C++. We use Qt, a C++ framework that runs our simulations on multiple platforms (Linux, Windows and Mac OS) with a graphical user interface (GUI). Through the GUI, one can visualize and track different aspects of the granuloma, including the structure and molecular concentration gradients, as the granuloma forms and is maintained. Simulations can be run with or without graphical

visualization. For more detailed description of the Qt framework applications in studying granuloma characteristics, see [61].

4.3 Results

4.3.1 Contribution of NF-κB signaling factors to control of TNF concentration, TNF activities and granuloma outcomes

We know from both experimental data and predictions from our previous modeling studies that TNF availability and activities (i.e. macrophage activation, induction of TNF and chemokine expression, regulation of immune cell recruitment and induction of apoptosis) within a granuloma are essential to control of infection [4,5,10,12,13,45,47]. The NF-κB signaling pathway activated as a result of TNF binding to TNFR1 on the membrane of immune cells is critical for regulation of these activities [25]. What are the NF-κB signaling-associated biochemical factors and intracellular processes that control TNF concentration and activities within a granuloma? We use the new model to predict the role of biochemical factors and interactions associated with the NF-κB signaling pathway that have not been experimentally characterized, or are difficult to characterize by current experimental methods.

We analyze the impact of TNF-mediated NF-κB signaling-associated parameters in six groups as defined in Appendix C (Table C.5): (1) concentration of intracellular signaling molecules (NF-κB, IκBα kinase (IKK), and IKK kinase (IKKK)), (2) processes associated with activation of the signal transduction cascade, (3) A20 and IκBα synthesis, (4) IκBα interactions, (5) NF-κB and IκBα transport between cytoplasm and nucleus, and (6) NF-κB-mediated cell responses (TNF and chemokine expression,

macrophage activation, inhibition of apoptosis). Notably, parameters identified to have strong correlations with bacterial levels within a granuloma, i.e. granuloma function, belong to groups 1-3 and group 6 (see Table 4.1 and Appendix C (Tables C.7, C.8)). Processes within groups 4 and 5, although essential for NF-κB activation, have a less significant impact on model outputs when they are varied within a similar range as other parameters. Within group 1, increasing the average number of NF-κB molecules per macrophage significantly enhances macrophage activation and thus reduces bacterial numbers within a granuloma. This is consistent with the published data on the role of NF-κB in activating macrophages to kill mycobacteria [17]. Similarly, IKKK activation (from group 2), a key process in NF-κB signaling cascade that occurs following TNF binding to TNFR1, strongly and negatively correlates with bacterial load. Among group 3 parameters, the rate of NF-κB binding at A20 and IκBα gene promoters as well as the rates of A20 and IκBα mRNA synthesis and translation positively correlate with bacterial levels. In contrast, increasing A20 and IκBα mRNA and protein degradation rates impairs granuloma's ability to control infection. These results highlight the important role that the NF-κB-IκBα-A20 feedback regulatory module plays in the regulation of the NF-κB-mediated cell responses [28], and thus in the regulation of granuloma function.

Table 4.1 NF-κB-associated model parameters significantly correlated with outputs of interest, i.e. bacterial numbers, granuloma size, caseation area and TNF concentration at day 200 post-infection. Detailed sensitivity analysis results are presented in Appendix C (Tables C.7, C.8).

NF-κB-associated parameter *	Parameter description † (parameter group number ‡)	Selected Model Outputs			
		Total number of bacteria	Granuloma size	Caseation	Average tissue concentration of sTNF
$NF\text{-}\kappa B_{tot}$	Average number of NF-κB molecules per cell (1)	−−		−	
k_a	IKKK activation rate (2)	−−			
k_i	IKKK inactivation rate (2)	+			
q_1	Rate of NF-κB binding at A20 and IκBα gene promoters (3)	+			
c_1	Inducible A20 and IκBα mRNA synthesis rate (3)	++		+	
c_3	A20 and IκBα mRNA degradation rate (3)	−−			
c_4	A20 and IκBα translation rate (3)	++			−−
c_5	A20 degradation rate (3)	−−			++
c_{1r}	Rate of NF-κB induced mRNA synthesis for chemokines, TNF, ACT and IAP (6)	−−	−−	−−	++
c_{3rchem}	Chemokine mRNA degradation rate (6)		−−	++	
c_{4chem}	Chemokine translation rate (6)			−−	
e_{3chem}	Chemokine secretion rate (6)		++	−	
c_{3rTNF}	TNF mRNA degradation rate (6)	++	++	++	
c_{4TNF}	TNF translation rate (6)	−−	−−	−−	++
c_{5TNF}	Intracellular TNF degradation rate (6)	++	++	++	
e_{3TNF}	TNF secretion rate (6)	−−	−−	−−	++
c_{4ACT}	ACT translation rate (6)	−−			
c_{5ACT}	ACT degradation rate (6)	++			
τ_{ACT}	ACT concentration threshold for macrophage activation (6)	++			
c_{5IAP}	IAP degradation rate (6)		−−	−−	−

* Only parameters with significant PRCC values are indicated. Significant positive and negative correlations are shown using + and - as follows: -/+: 0.001 < *p*-value < 0.01, --/++: *p*-value < 0.001.
† IKKK: IKK kinase, IKK: IκBα kinase, ACT: generic macrophage-activating molecule, IAP: inhibitor of apoptosis
‡ NF-κB signaling-associated parameters are categorized in six groups as defined in Appendix C (Table C.5): (1) concentration of intracellular signaling molecules (NF-κB, IκBα kinase (IKK), and IKK kinase (IKKK)), (2) processes associated with activation of the signal transduction cascade, (3) A20 and IκBα synthesis, (4) IκBα interactions, (5) NF-κB and IκBα transport between cytoplasm and nucleus, and (6) NF-κB-mediated cell responses.

Finally, group 6 comprises important parameters with strong effects on most model outcomes. Parameters that control either TNF expression or macrophage activation significantly influence granuloma function and thus bacterial load within a granuloma. In

contrast, parameters that only affect chemokine expression or apoptosis control granuloma size (formation) without exerting strong effects on bacterial load. This is consistent with our previous studies indicating that TNF-induced macrophage activation is a key mechanism for controlling bacterial growth [47]. The rate of NF-κB-dependent mRNA synthesis for chemokines, TNF, the generic macrophage-activating molecule (ACT), and the inhibitor of apoptosis (IAP) is an important parameter. It strongly and positively correlates with all TNF-induced cellular responses in tissue (i.e. apoptosis, TNF and chemokine expression, and macrophage activation) and negatively correlates with bacterial load, caseation and granuloma size. The stability of TNF mRNA, as well as TNF translation, degradation and secretion significantly control granuloma outcomes. Increasing the rates of degradation of TNF mRNA and intracellular TNF or reducing the rates of TNF translation and secretion enhance bacterial numbers, caseation and granuloma size. In addition, the ACT translation rate (negatively), and the ACT degradation rate as well as the ACT concentration threshold for macrophage activation (positively) correlate with bacterial load within a granuloma. Increasing the chemokine secretion rate or reducing the chemokine mRNA degradation rate elevates chemokine concentration in tissue, enhancing immune cell recruitment and granuloma growth. Overall, each of the above parameters identified as critical for formation and function of a granuloma represents a potential target for therapeutic modulation. Hence, we focus our next analysis on the potential effects of manipulation in each of these parameters.

4.3.2 Optimal regulation of the NF-κB signaling dynamics for control of infection without inducing excessive inflammation

The analysis above highlights various NF-κB signaling pathway-associated biochemical factors and intracellular interactions that show significant impacts on infection outcomes at all scales (molecular, cellular and tissue). How do these responses influence granuloma formation? Do manipulation of these mechanisms alter infection outcome at the granuloma level? The effects of manipulation of four important NF-κB-associated factors as identified by the sensitivity analysis on granuloma formation, total numbers of bacteria, sTNF concentration, and macrophage activation after Mtb infection are shown in Fig. 4.3. These factors are: (i) average number of NF-κB molecules per cell, $NF\text{-}\kappa B_{tot}$, (ii) IKKK inactivation rate constant, k_i, (iii) A20 and IκBα mRNA degradation rate constant, c_3, and (iv) TNF mRNA degradation rate constant, c_{3rTNF}.

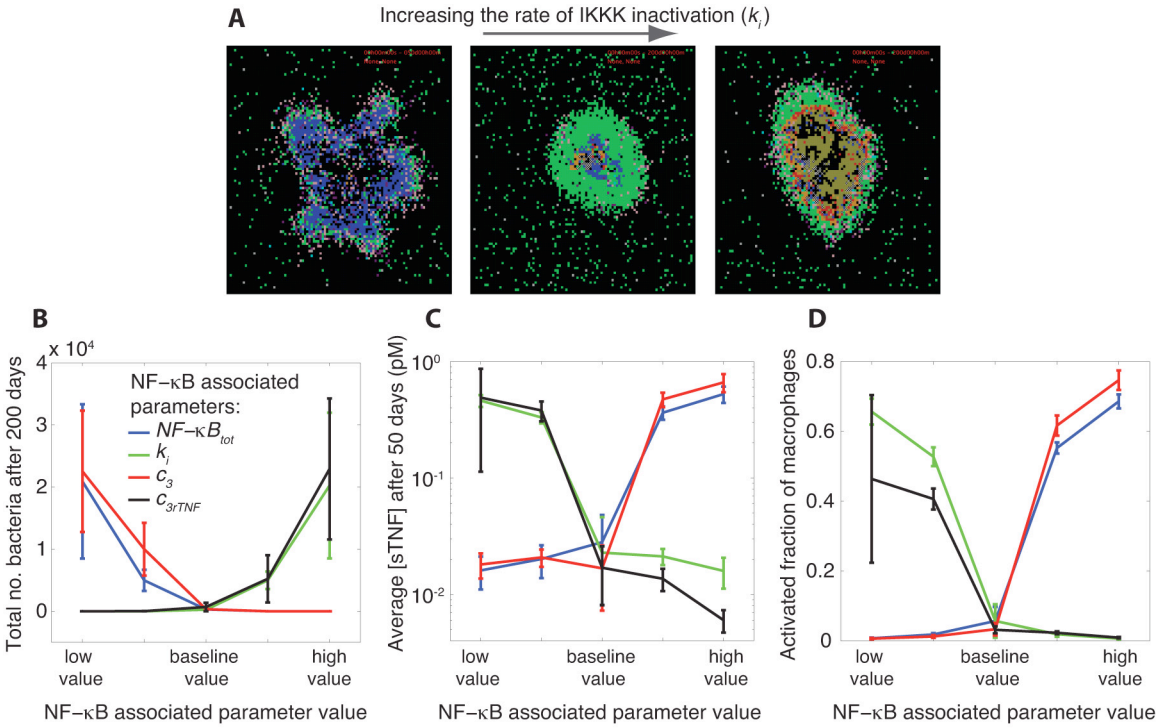

Fig. 4.3 NF-κB signaling dynamics control bacterial growth and inflammation level in tissue. (A) Granuloma snapshots for slow ($k_i = 3.2\times10^{-3}$ s^{-1}), moderate ($k_i = 10^{-2}$ s^{-1}), and rapid ($k_i = 3.2\times10^{-2}$ s^{-1}) rates of IKKK inactivation. Slow rates of IKKK inactivation lead to uncontrolled macrophage activation and excessive inflammation. A moderate value of k_i results in control of infection in a stable granuloma containing small numbers of bacteria. Rapid rates of IKKK inactivation lead to large numbers of bacteria and infected macrophages as well as widespread caseation. The colors representing cells of different type and status in granuloma snapshots are the same as those shown and defined in Fig. 4.2. (B)-(D) Simulation results showing the effects of four important parameters, as identified by sensitivity analysis, controlling NF-κB signaling dynamics on granuloma outcomes (total number of bacteria, tissue concentration of TNF, and macrophage activation). The parameters are: the average number of NF-κB molecules per cell ($NF-\kappa B_{tot}$), IKKK inactivation rate (k_i), A20 and IκBα mRNA degradation rate (c_3), and TNF mRNA degradation rate (c_{3rTNF}). In each simulation, only one of these parameters is varied. Moderate (baseline) values of these parameters lead to clearance or control of infection in stable granulomas with very low bacterial numbers, low levels of TNF and low levels of macrophage activation. Perturbing the NF-κB signaling dynamics by varying values of these parameters impair the balance toward either uncontrolled growth of bacteria or excessive inflammation (high TNF concentrations and high levels of macrophage activation) in tissue. The baseline value of each parameter is as reported in Appendix C (Table C.5) and is as follows: $NF-\kappa B_{tot} = 10^5$, $k_i = 10^{-2}$ s^{-1}, $c_3 = 7.5\times10^{-4}$ s^{-1}, $c_{3rTNF} = 3.8\times10^{-4}$ s^{-1}. The difference between the low value and high value presented in the figure is one order of magnitude.

The values of these parameters significantly determine the ability of a granuloma to control bacterial load. Small numbers of NF-κB molecules per cell, slow rates of A20 and IκBα mRNA degradation, rapid rates of IKKK inactivation, and rapid rates of TNF mRNA degradation all lead to uncontrolled growth of bacteria within a 200-day period

post-infection. These effects result from reduced rates of TNF-induced activation of macrophages, diminishing their ability to kill bacteria. Changing values of all of these parameters to moderate levels leads to containment of bacteria within a stable granuloma. Further increasing the values of parameters $NF\text{-}\kappa B_{tot}$ and c_3, or further reducing the values of parameters c_{3rTNF} and k_i from their containment-level values all reduce bacterial numbers and increase the chance of infection clearance. However, these clearance outcomes are generally accompanied by uncontrolled rates of macrophage activation and cell infiltration as well as very high concentrations of TNF in tissue that are markers of excessive inflammation and immunopathology. Overall, as depicted in Fig. 4.3B-D, moderate (containment baseline) values of $NF\text{-}\kappa B_{tot}$, k_i, c_3 and c_{3rTNF} (that can be found in Appendix C (Table C.5)) lead to control of infection in stable granulomas with very low bacteria numbers (and sometimes clearance), low levels of TNF and low levels of macrophage activation. Perturbing the NF-κB signaling dynamics by varying values of these parameters (i.e. rates these processes occur) impairs the balance toward either uncontrolled growth of bacteria or excessive inflammation in tissue. Hence, our model predicts that the optimal regulation of the TNF-mediated NF-κB signaling pathway is essential to controlling infection and inflammation in tissue. The balance between the NF-κB-mediated bacterial killing activities and the NF-κB-mediated inflammation results in an equilibrium state, i.e. containment of bacteria within a stable granuloma with minimal inflammation.

4.3.3 How do NF-κB signaling dynamics balance inflammation and bacterial killing?

As demonstrated above, several NF-κB-associated intracellular processes (summarized in Table 4.1 and Fig. 4.3) are identified to control granuloma function. How do these processes affect the balance of inflammation and bacterial killing activities within a granuloma? We previously showed that the impact of TNF on granuloma outcomes is strongly affected by whether or not macrophages stimulated by TNF are infected [45]. This motivates us to test whether there is a correlation between the effect of NF-κB signaling dynamics on granuloma function (as described in Fig. 4.3) and the infection status of macrophages stimulated by TNF during the immune response. Thus, we analyze the infection status of macrophages that become activated or undergo apoptosis after Mtb infection by computing infected/resting cell ratios, $R_{activation}$ and $R_{apoptosis}$, as defined in Methods. Our model predicts a very significant effect of important NF-κB-associated parameters on both $R_{activation}$ and $R_{apoptosis}$ (Fig. 4.4). At small numbers of NF-κB molecules per cell, slow rates of A20 and IκBα mRNA degradation, rapid rates of IKKK inactivation, and rapid rates of TNF mRNA degradation, infected macrophages are the main cells that become activated or undergo apoptosis as a result of TNF activities ($R_{activation}$ and $R_{apoptosis} >> 1$). However, with one order of magnitude increase in each of these parameters, resting macrophages become the main responders to TNF signaling ($R_{activation}$ and $R_{apoptosis} << 1$). Comparing these results with results from the previous section (Fig. 4.3), we observe a significant correlation between infected/resting cell ratios, $R_{activation}$ and $R_{apoptosis}$, and granuloma outcomes, bacterial load and inflammation. At large values of $R_{activation}$ and $R_{apoptosis}$ (values of 1-10 or greater), outcomes are

uncontrolled growth of Mtb. Small values of these ratios (smaller than ~0.1) correlate with excessive inflammation in tissue. These results suggest that a balance between the number of resting macrophages and infected macrophages responding to TNF signaling is required for control of infection and inflammation within a stable granuloma, and that such a balance is critically regulated by NF-κB signaling dynamics.

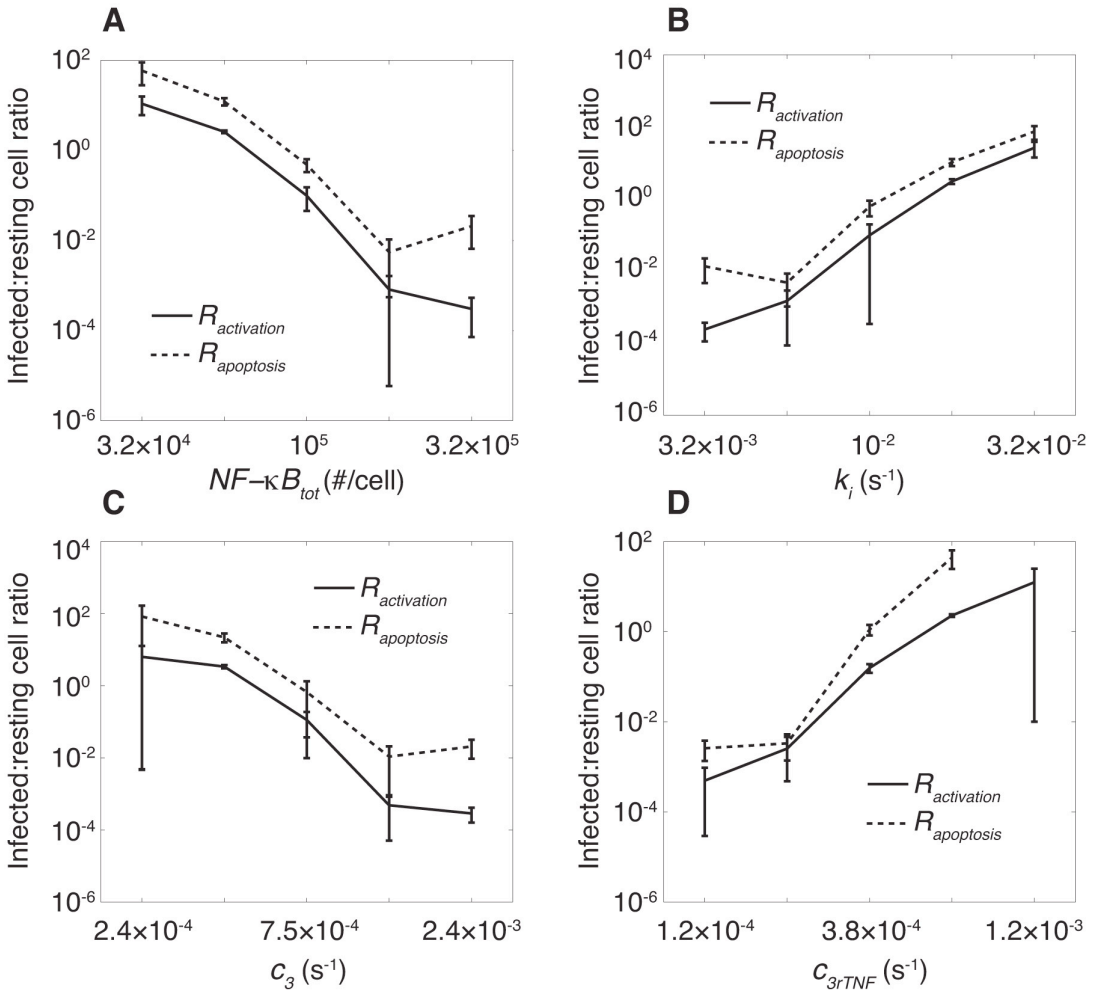

Fig. 4.4 The impact of important processes associated with the NF-κB signaling dynamics on granuloma outcomes is correlated with status of macrophages that undergo apoptosis or become activated by TNF. Simulation results show the effect of (A) the average number of NF-κB molecules per cell, $NF\text{-}\kappa B_{tot}$, (B) IKKK inactivation rate, k_i, (C) A20 and IκBα mRNA degradation rate, c_3, and (D) TNF mRNA degradation rate, c_{3rTNF} on infected/resting cell ratios $R_{apoptosis}$ and $R_{activation}$ within a 200 day period after Mtb infection.

4.3.4 The stability of mRNA transcripts controls bacterial load, inflammation and granuloma size by affecting the dynamics of NF-κB mediated responses

A key point of incorporating NF-κB signaling dynamics into our granuloma model is the ability to study the impact of the dynamics of NF-κB-mediated responses (i.e. macrophage activation, expression of chemokines, TNF, and inhibitors of apoptosis) on granuloma outcomes. These responses follow NF-κB oscillations [50]. The dynamics of these responses depend, to a large extent, on the stability of their corresponding mRNA transcripts [32]. Thus, we analyzed the effect of varying the stability of mRNA transcripts corresponding to macrophage activation (ACT), and expression of chemokines (CHEM), TNF, and inhibitors of apoptosis (IAP) on granuloma outcomes, bacterial load and inflammation level (represented by the activated fraction of macrophages). Varying the stability (half-life; $t_{1/2}$) of mRNA transcripts significantly influences the dynamics of the NF-κB-mediated responses (e.g. chemokine secretion) in an individual cell (Fig. 4.5A). Granuloma simulations show that the stability of mRNA transcripts for NF-κB-mediated responses, particularly ACT, TNF and CHEM, significantly control bacteria numbers and inflammation level in tissue (Fig. 4.5B, C). The impact of the IAP mRNA stability on these model outcomes is less significant.

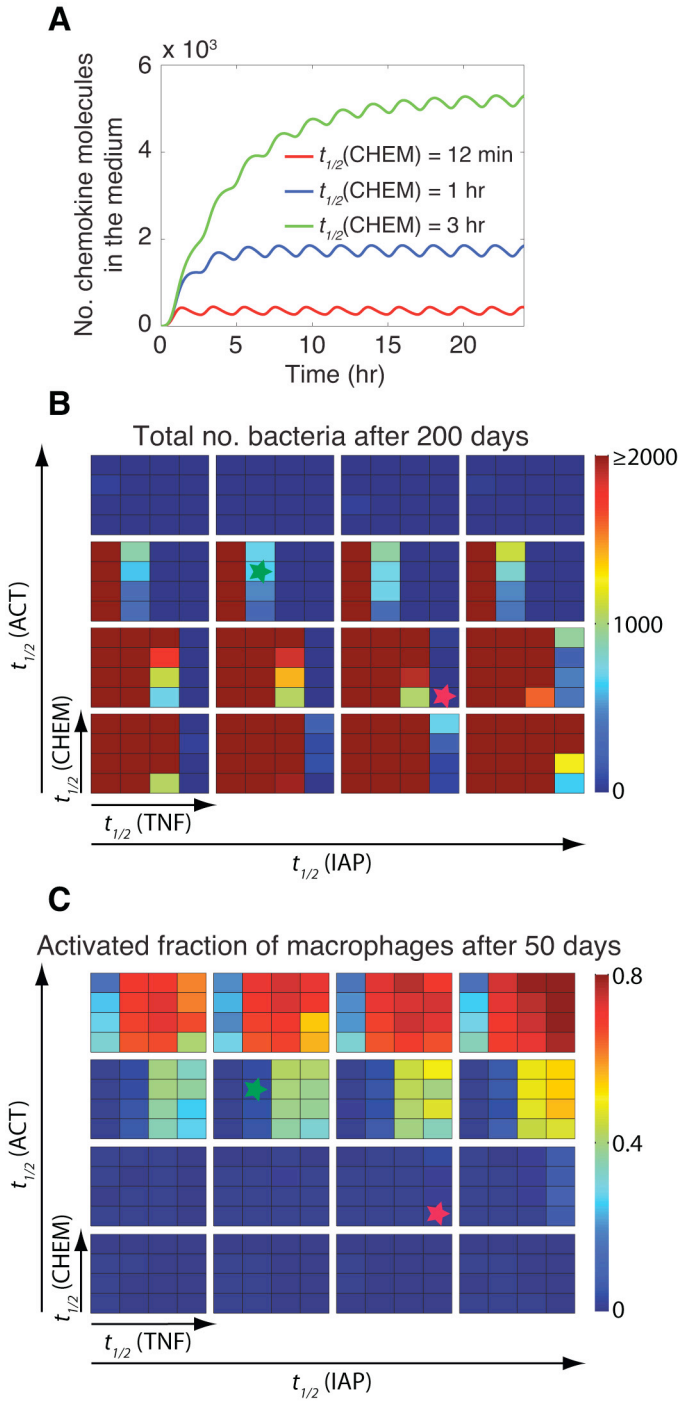

Fig. 4.5 The stability of mRNA transcripts controls bacterial load and inflammation by affecting the dynamics of NF-κB mediated responses. (A) The effect of the stability (half-life) of chemokine mRNA transcripts ($t_{1/2}$(CHEM)) on the dynamics of chemokine secretion by an individual cell. Simulated results are produced using the single-cell level NF-κB signaling dynamics model for continuous stimulation of a cell by 1 ng/ml TNF, with parameters and equations as described in Appendix C (Tables C.3, C.5 and C.6). A similar pattern of response can be observed when the effects of mRNA stability on the dynamics of other NF-κB-mediated responses (i.e. expression of ACT, IAP and TNF) are studied (data not shown). (B, C) Simulation results for the effect of the stability of mRNA transcripts corresponding to major NF-κB-mediated responses, including macrophage activation ($t_{1/2}$(ACT)), TNF expression ($t_{1/2}$(TNF)), chemokine expression ($t_{1/2}$(CHEM)) and inhibitor of apoptosis protein expression ($t_{1/2}$(IAP)), on bacteria numbers (B) and on the activated fraction of macrophages (C) 200 days post-infection. Small squares represent different values of $t_{1/2}$(CHEM) vertically and different values of $t_{1/2}$(TNF) horizontally. Large boxes represent different values of $t_{1/2}$(ACT) vertically and different values of $t_{1/2}$(IAP) horizontally. Four values of mRNA half-life were tested in simulations: 12 min, 30 min, 1 hr and 3 hr. Simulation results were averaged over 10 repetitions.

Our analysis shows that there are combinations of TNF, ACT, CHEM and IAP mRNA transcript half-lives that lead to distinct model outcomes such as control of infection within stable granulomas, clearance, uncontrolled growth of bacteria, or

excessive inflammation (see Fig. 4.2). For example, a containment outcome (as highlighted by green stars in Fig. 4.5B, C) may result from the following parameter combination: mRNA transcript half-life of 30 min for TNF, mRNA transcript half-life of 1 hr for ACT, mRNA transcript half-life of 1 hr for CHEM, and mRNA transcript half-life of 30 min for IAP. Increasing mRNA transcript stabilities for TNF and ACT from these values increases the chance of extensive inflammation in tissue, whereas reducing their values significantly enhance bacterial load. Increasing mRNA transcript stabilities for CHEM from the suggested value also slightly enhances bacterial load as well as granuloma size (data not shown). Further, our results suggest that there are combinations of mRNA stabilities for TNF-mediated responses that lead to clearance of Mtb without inducing excessive inflammation (see red stars in Fig. 4.5B, C as an example). This set of mRNA stability values significantly enhances the ability of granuloma to kill bacteria while limiting inflammation by controlling macrophage activation and apoptosis. Overall, these results suggest that the differential dynamics of NF-κB-mediated responses resulting from differential stabilities of their corresponding mRNA transcripts are essential to regulate granuloma's ability to control infection and inflammation.

4.3.5 The timing of NF-κB-induced macrophage activation is critical to controlling excessive inflammation

In the previous section, we showed that stability of mRNA transcripts associated with NF-κB-mediated inflammatory molecules significantly affects the immune response to Mtb. The stability of mRNA controls both the extent and the timing of NF-κB-mediated responses in individual cells [49]. However, it is not clear whether it is mostly the extent

of response, the timing of response, or both that influence granuloma outcomes. In other words, how important is the speed of responses of each individual macrophage to TNF signals in determining the overall function of a granuloma? To address this question, we analyzed the effect on granuloma outcomes of varying the stability of ACT, CHEM, TNF and IAP mRNA transcripts while maintaining the average extent of these responses at their containment baseline levels (determined in the previous section). To maintain the average extent of each response as its corresponding mRNA stability is varied, we simultaneously vary another parameter associated with a process downstream of mRNA translation. Parameters varied to adjust the extent of the four NF-κB mediated responses are: TNF secretion rate (e_{3TNF}), chemokine secretion rate (e_{3chem}), ACT concentration threshold for macrophage activation (τ_{ACT}), macrophage activation rate constant (k_{ACT}), and apoptosis inhibition constant (k_{IAP}). For example, we increase the chemokine mRNA half-life ($t_{1/2}$(CHEM)) and decrease the chemokine secretion rate (e_{3chem}) simultaneously to achieve the same average number of chemokine molecules secreted in tissue by an individual macrophage (Fig. 4.6A).

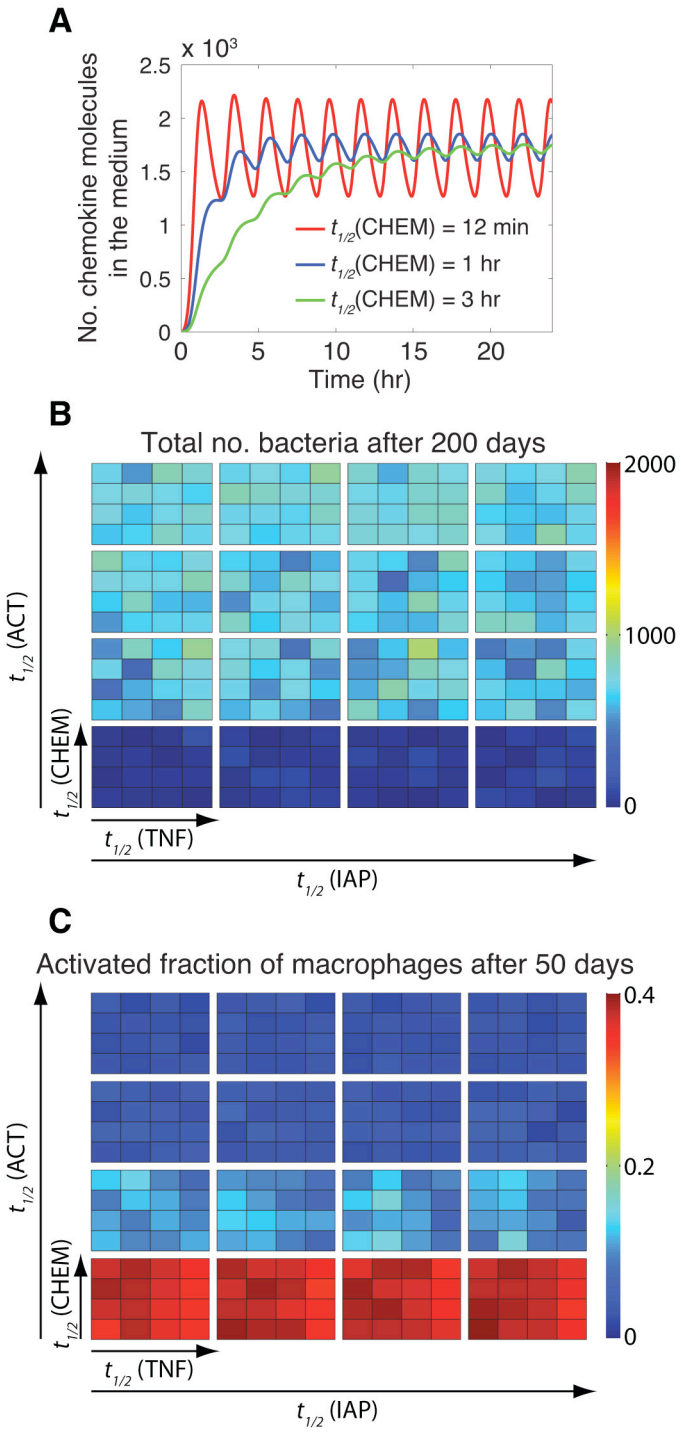

Fig. 4.6 The timing of NF-κB-induced macrophage activation is critical to control of inflammation. (A) Varying the chemokine mRNA half-life ($t_{1/2}$(CHEM): 12 min, 1 hr, and 3 hr, respectively) and the chemokine secretion rate (e_{3chem}: 7.65×10^{-5} s^{-1}, 1.39×10^{-5} s^{-1}, 4.52×10^{-6} s^{-1}, respectively) by an individual macrophage simultaneously leads to secretion of the same average number of chemokine molecules, but with distinct temporal patterns of chemokine secretion. Simulated results are produced using the single-cell level NF-κB signaling dynamics model for continuous stimulation of a cell by 1 ng/ml TNF, with parameters and equations as described in Appendix C (Tables C.3, C.5 and C.6). A similar pattern of response can be observed when the effects of mRNA stability on the timing of other NF-κB-mediated responses (i.e. expression of ACT, IAP and TNF) are studied (data not shown). (B, C) Simulation results for the effect of the timing of NF-κB-mediated responses, including macrophage activation (regulated by $t_{1/2}$(ACT)), TNF expression (regulated by $t_{1/2}$(TNF)), chemokine expression (regulated by $t_{1/2}$(CHEM)) and inhibitor of apoptosis protein expression (regulated by $t_{1/2}$(IAP)), on bacteria numbers (B) and on the activated fraction of macrophages (C) at 200 days post-infection. Small squares represent different values of $t_{1/2}$(CHEM) vertically and different values of $t_{1/2}$(TNF) horizontally. Large boxes represent different values of $t_{1/2}$(ACT) vertically and different values of $t_{1/2}$(IAP) horizontally. Four values of mRNA half-life were tested in simulations: 12 min, 30 min, 1 hr and 3hr. Simulation results were averaged over 10 repetitions.

Analysis of granuloma simulations indicates that among the four major NF-κB-mediated responses studied here (TNF, CHEM, ACT and IAP), only the timing of ACT

response, i.e. macrophage activation, is critical to control of inflammation in tissue as well as bacterial load within a granuloma (Fig. 4.6B, C). Early NF-κB-mediated activation of macrophages that occurs because of highly unstable ACT mRNA transcripts lead to uncontrolled activation of macrophages and excessive inflammation in tissue. This suggests that both extent and timing of NF-κB-mediated macrophage activation are critical to control of the immune response to Mtb.

4.3.6 Can manipulating TNF-mediated NF-κB signaling dynamics improve granuloma function?

Earlier in this study, we showed that optimal regulation of NF-κB signaling dynamics is critical to control of infection within a granuloma and control of inflammation in lung tissue. As such, impairing NF-κB activation leads to uncontrolled growth of bacteria that is in agreement with NF-κB knockout experimental studies [62]. The repression of NF-κB signaling in infected macrophages is also a mechanism that pathogenic mycobacteria use to enhance their survival and growth [17]. An important question is then: Can we manipulate TNF-mediated NF-κB signaling in a granuloma that is unable to control infection in order to improve its ability to kill bacteria? To test this hypothesis, we first simulate formation of a granuloma that is unable to control bacterial growth due to impaired NF-κB signaling (e.g. at high rates of IKKK inactivation, k_i) for 100 days. Then, we change one or more of the NF-κB-associated parameters to restore NF-κB activities within the granuloma and resume simulation for another 100 days. These simulations somehow represent treatment of an active TB granuloma with drugs targeting NF-κB-associated processes.

Our analysis, as depicted in Fig. 4.7, indicates that restoring normal NF-κB activities by decreasing k_i to its moderate values (Treatment I) enhances the ability of a granuloma to control bacteria. However, average bacteria levels for a 200-day granuloma after changing k_i are generally higher than bacteria levels resulting from simulating a containment scenario. A further decrease in the value of k_i (Treatment II) is more successful in killing bacteria. However, it leads to uncontrolled activation of macrophages and excessive inflammation in tissue. This suggests that targeting the process of IKKK inactivation alone is not sufficient for infection control at the granuloma scale. In another set of simulations (Treatment III), decreasing k_i to moderate values, together with manipulating stability of mRNA transcripts associated with NF-κB-mediated responses (based on results from Fig. 4.5) leads to better outcomes. Increasing the half-life of TNF mRNA transcripts to 3 hr, reducing the half-life of ACT mRNA transcripts to 30 min, and setting the IAP mRNA transcripts to 1 hr change the granuloma outcome with inducing efficient killing of bacteria within the granuloma without inducing excessive inflammation. Increasing TNF mRNA stability enhances the overall role of this pro-inflammatory cytokine in control of infection, while reducing ACT mRNA stability and setting IAP mRNA stability to 1 hr significantly contribute to limiting inflammation in tissue. Overall, this suggests that manipulating the dynamics of the NF-κB-mediated responses, particularly macrophage activation, TNF and IAP expression, can improve the function of a TB granuloma.

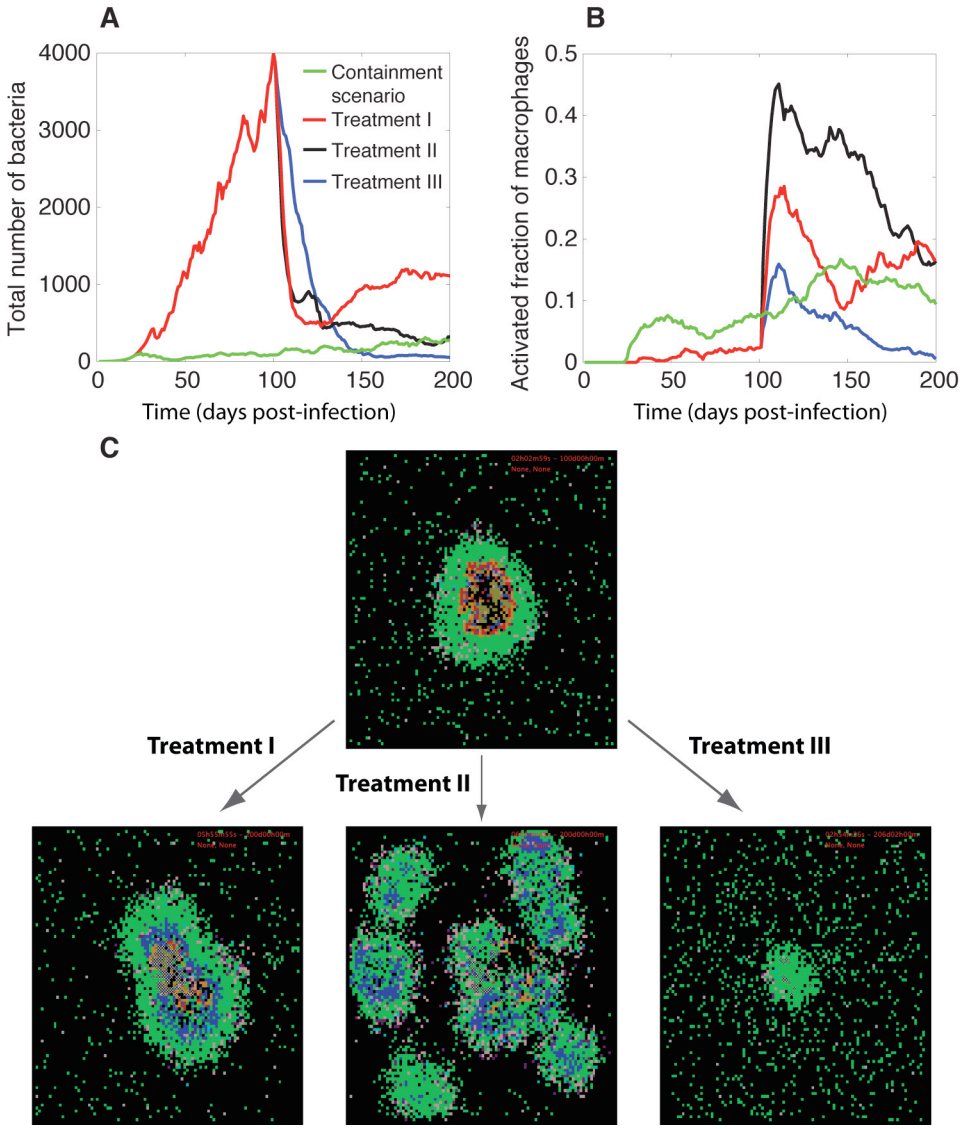

Fig. 4.7 Manipulation of TNF-mediated NF-κB signaling for improving granuloma function. Comparison of the dynamics of (A) bacteria growth, (B) activated fraction of macrophages, and (C) granuloma snapshots among three different treatment methods for enhancing NF-κB activities. In all treatments, we first simulate formation of a granuloma that is unable to control bacteria growth due to impaired NF-κB signaling at high rates of IKKK inactivation ($k_i = 3.16\times10^{-2}$ s^{-1}) for 100 days (All other parameter values are as listed in Appendix C (Tables C.1, C.3 and C.5)). Then, we change one or more of the NF-κB-associated parameters to restore NF-κB activities within the granuloma and resume simulation for another 100 days. Parameter changes in each treatment are as follows: Treatment I: $k_i = 1\times10^{-2}$ s^{-1}, Treatment II: $k_i = 3.16\times10^{-3}$ s^{-1}, Treatment III: $k_i = 1\times10^{-2}$ s^{-1}, $t_{1/2}$(TNF) = 3 hr, $t_{1/2}$(ACT) = 30 min, $t_{1/2}$(TNF) = 1 hr. Simulation results were averaged over 10 repetitions. The colors representing cells of different type and status in granuloma snapshots are the same as those shown and defined in Fig. 4.2.

4.4 Discussion

TNF affects the immune response to Mtb through several mechanisms, including induction of macrophage activation, induction of chemokine and cytokine expression, and apoptosis. Overall, these activities have made TNF a key factor for restricting bacterial growth in a granuloma [5,8]. This is confirmed by studies in humans, in which TNF neutralization leads to reactivation of latent TB due to a failure of the granuloma to control bacterial replication [63]. Importantly, these activities are regulated in part by the NF-κB signaling pathway. Hence, the TNF-induced NF-κB signaling pathway is central to the Mtb immune response, and one can hypothesize that regulation of intracellular NF-κB signaling dynamics is key to controlling Mtb infection. The important questions then, are how the molecular single-cell scale processes of the NF-κB signaling pathway influence the dynamics (i.e. the extent and the timing) of TNF activities within a granuloma, and how the dynamics of these activities control formation and function of a granuloma during the long-term immune response to Mtb? The experiments required to answer these questions are at present very difficult, as they invoke multiple biological scales in length and time. Thus, we suggest using a multi-scale systems biology approach. Our computational model links the dynamics of molecular scale TNF/TNFR interactions and the NF-κB signal transduction events that occur on second to minute time scales to cellular/tissue scale events that control the long-term immune response to Mtb. This approach can address critical questions necessary to understanding granulomas and contribute to the development and testing of strategies for prevention and treatment.

Immune responses induced by Mtb infection are myriad and complex, and it remains incompletely understood which responses are required for protection and which

contribute to pathology [57,64]. Indeed, there is significant overlap among protective and pathological responses. An important example, as dissected in this study, is TNF-induced NF-κB activation. Our model shows that NF-κB-mediated responses are critical for restricting bacterial growth in a granuloma. The model also shows that optimal regulation of NF-κB signaling dynamics is necessary for preventing pathological inflammation in tissue. In other words, the optimal outcome, particularly at the level of the granuloma, is achieved as a result of a balance between the NF-κB-mediated bacterial killing activities and the NF-κB-mediated inflammation. Such a balance is controlled by a combination of molecular scale biochemical processes identified in detail in this study such as IKKK activity, A20 and IκBα interactions, and stability of mRNA transcripts associated with NF-κB-mediated responses, particularly macrophage activation and TNF expression. Further, we find that these processes critically regulate whether resting macrophages or infected macrophages are the major targets for TNF signaling within a granuloma. Outcomes of uncontrolled growth of Mtb occur unless sufficient numbers of resting macrophages relative to infected macrophages become activated by TNF. On the other hand, excessive activation of resting macrophages leads to uncontrolled inflammation. These findings highlight the potential importance of NF-κB-associated processes as targets in future studies on TB examining approaches to control infection and pathology.

Another interesting finding from our study is that the stability of mRNA transcripts corresponding to NF-κB-mediated responses, particularly macrophage activation and expression of TNF and chemokines, significantly controls bacterial load in a granuloma, inflammation level in tissue, and granuloma size. This is due to the impact of mRNA stability on the kinetics of these responses [32]. We find that both the extent

and the timing of NF-κB-mediated macrophage activation are critical to control of the immune response to Mtb. However, the significance of the stability of TNF and chemokine mRNA transcripts is mostly due its effect on the extent of these responses. This is the first study, to our knowledge, that reveals the importance of the dynamics of various NF-κB-mediated responses on immunity to Mtb. Further, we show that manipulating the dynamics of these responses in a granuloma that is unable to control infection due to, for example, pathogen-induced inhibition of NF-κB activation can significantly improve granuloma function.

Finally, our approach is an initial step toward understanding the molecular targets at the level of intracellular signaling pathways for control of the tissue-scale outcomes of the immune response to Mtb, particularly granuloma formation. We anticipate that other factors, including crosstalk between signaling mediated by the Mtb bacteria and other cytokines through various types of receptors and different signaling pathways [65] in various types of cells, or the noise resulting from discrete regulation of TNFR activity and transcription regulation [66] will further influence these outcomes. Importantly, our multi-scale computational model provides a valuable platform for future studies using a systems approach to examine the impact of the dynamics of highly networked cellular signaling systems on tissue scale responses. Such studies may lead to novel therapeutic strategies that minimize non-specific or off-target side effects.

4.5 References

1. Russell DG, Barry CE,3rd, Flynn JL (2010) Tuberculosis: What we don't know can, and does, hurt us. Science 328: 852-856.

2. Flynn JL (2004) Immunology of tuberculosis and implications in vaccine development. Tuberculosis (Edinb) 84: 93-101.

3. Flynn JL, Goldstein MM, Chan J, Triebold KJ, Pfeffer K, et al. (1995) Tumor necrosis factor-alpha is required in the protective immune response against mycobacterium tuberculosis in mice. Immunity 2: 561-572.

4. Chakravarty SD, Zhu G, Tsai MC, Mohan VP, Marino S, et al. (2008) Tumor necrosis factor blockade in chronic murine tuberculosis enhances granulomatous inflammation and disorganizes granulomas in the lungs. Infect Immun 76: 916-926.

5. Lin PL, Myers A, Smith L, Bigbee C, Bigbee M, et al. (2010) Tumor necrosis factor neutralization results in disseminated disease in acute and latent mycobacterium tuberculosis infection with normal granuloma structure in a cynomolgus macaque model. Arthritis Rheum 62: 340-350.

6. Roach DR, Bean AG, Demangel C, France MP, Briscoe H, et al. (2002) TNF regulates chemokine induction essential for cell recruitment, granuloma formation, and clearance of mycobacterial infection. J Immunol 168: 4620-4627.

7. Bean AG, Roach DR, Briscoe H, France MP, Korner H, et al. (1999) Structural deficiencies in granuloma formation in TNF gene-targeted mice underlie the heightened susceptibility to aerosol mycobacterium tuberculosis infection, which is not compensated for by lymphotoxin. J Immunol 162: 3504-3511.

8. Clay H, Volkman HE, Ramakrishnan L (2008) Tumor necrosis factor signaling mediates resistance to mycobacteria by inhibiting bacterial growth and macrophage death. Immunity 29: 283-294.

9. Wallis RS, Broder M, Wong J, Lee A, Hoq L (2005) Reactivation of latent granulomatous infections by infliximab. Clin Infect Dis 41 Suppl 3: S194-8.

10. Keane J, Gershon S, Wise RP, Mirabile-Levens E, Kasznica J, et al. (2001) Tuberculosis associated with infliximab, a tumor necrosis factor alpha-neutralizing agent. N Engl J Med 345: 1098-1104.

11. Keane J (2005) TNF-blocking agents and tuberculosis: New drugs illuminate an old topic. Rheumatology (Oxford) 44: 714-720.

12. Winthrop KL (2006) Risk and prevention of tuberculosis and other serious opportunistic infections associated with the inhibition of tumor necrosis factor. Nat Clin Pract Rheumatol 2: 602-610.

13. Marino S, Sud D, Plessner H, Lin PL, Chan J, et al. (2007) Differences in reactivation of tuberculosis induced from anti-TNF treatments are based on bioavailability in granulomatous tissue. PLoS Comput Biol 3: 1909-1924.

14. Keane J, Shurtleff B, Kornfeld H (2002) TNF-dependent BALB/c murine macrophage apoptosis following mycobacterium tuberculosis infection inhibits bacillary growth in an IFN-gamma independent manner. Tuberculosis (Edinb) 82: 55-61.

15. Keane J, Balcewicz-Sablinska MK, Remold HG, Chupp GL, Meek BB, et al. (1997) Infection by mycobacterium tuberculosis promotes human alveolar macrophage apoptosis. Infect Immun 65: 298-304.

16. Harris J, Hope JC, Keane J (2008) Tumor necrosis factor blockers influence macrophage responses to mycobacterium tuberculosis. J Infect Dis 198: 1842-1850.

17. Gutierrez MG, Mishra BB, Jordao L, Elliott E, Anes E, et al. (2008) NF-kappa B activation controls phagolysosome fusion-mediated killing of mycobacteria by macrophages. J Immunol 181: 2651-2663.

18. Mosser DM, Edwards JP (2008) Exploring the full spectrum of macrophage activation. Nat Rev Immunol 8: 958-969.

19. Ray JC, Wang J, Chan J, Kirschner DE (2008) The timing of TNF and IFN-gamma signaling affects macrophage activation strategies during mycobacterium tuberculosis infection. J Theor Biol 252: 24-38.

20. Algood HM, Lin PL, Yankura D, Jones A, Chan J, et al. (2004) TNF influences chemokine expression of macrophages in vitro and that of CD11b+ cells in vivo during mycobacterium tuberculosis infection. J Immunol 172: 6846-6857.

21. Van Antwerp DJ, Martin SJ, Kafri T, Green DR, Verma IM (1996) Suppression of TNF-alpha-induced apoptosis by NF-kappaB. Science 274: 787-789.

22. Beg AA, Baltimore D (1996) An essential role for NF-kappaB in preventing TNF-alpha-induced cell death. Science 274: 782-784.

23. Hayden MS, Ghosh S (2008) Shared principles in NF-kappaB signaling. Cell 132: 344-362.

24. Baltimore D (2011) NF-kappaB is 25. Nat Immunol 12: 683-685.

25. Pahl HL (1999) Activators and target genes of Rel/NF-kappaB transcription factors. Oncogene 18: 6853-6866.

26. Hoffmann A, Baltimore D (2006) Circuitry of nuclear factor kappaB signaling. Immunol Rev 210: 171-186.

27. Wertz IE, O'Rourke KM, Zhou H, Eby M, Aravind L, et al. (2004) De-ubiquitination and ubiquitin ligase domains of A20 downregulate NF-kappaB signalling. Nature 430: 694-699.

28. Cheong R, Hoffmann A, Levchenko A (2008) Understanding NF-kappaB signaling via mathematical modeling. Mol Syst Biol 4: 192.

29. Cheong R, Bergmann A, Werner SL, Regal J, Hoffmann A, et al. (2006) Transient IkappaB kinase activity mediates temporal NF-kappaB dynamics in response to a wide range of tumor necrosis factor-alpha doses. J Biol Chem 281: 2945-2950.

30. Hoffmann A, Levchenko A, Scott ML, Baltimore D (2002) The IkappaB-NF-kappaB signaling module: Temporal control and selective gene activation. Science 298: 1241-1245.

31. Kearns JD, Hoffmann A (2009) Integrating computational and biochemical studies to explore mechanisms in NF-{kappa}B signaling. J Biol Chem 284: 5439-5443.

32. Hao S, Baltimore D (2009) The stability of mRNA influences the temporal order of the induction of genes encoding inflammatory molecules. Nat Immunol 10: 281-288.

33. Flynn JL & Klein E (2010) in *A color atlas of comparative pulmonary tuberculosis histopathology,* eds Leong J, Dartois V & Dick T (CRC Press, Taylor & Francis Publishers, Boca Raton), pp 83-106.

34. Flynn JL, Chan J, Lin PL (2011) Macrophages and control of granulomatous inflammation in tuberculosis. Mucosal Immunol 4: 271-278.

35. Algood HM, Chan J, Flynn JL (2003) Chemokines and tuberculosis. Cytokine Growth Factor Rev 14: 467-477.

36. Morel PA, Ta'asan S, Morel BF, Kirschner DE, Flynn JL (2006) New insights into mathematical modeling of the immune system. Immunol Res 36: 157-165.

37. Davis JM, Ramakrishnan L (2008) "The very pulse of the machine": The tuberculous granuloma in motion. Immunity 28: 146-148.

38. Tsai MC, Chakravarty S, Zhu G, Xu J, Tanaka K, et al. (2006) Characterization of the tuberculous granuloma in murine and human lungs: Cellular composition and relative tissue oxygen tension. Cell Microbiol 8: 218-232.

39. Ulrichs T, Kosmiadi GA, Trusov V, Jorg S, Pradl L, et al. (2004) Human tuberculous granulomas induce peripheral lymphoid follicle-like structures to orchestrate local host defence in the lung. J Pathol 204: 217-228.

40. Lin PL, Pawar S, Myers A, Pegu A, Fuhrman C, et al. (2006) Early events in mycobacterium tuberculosis infection in cynomolgus macaques. Infect Immun 74: 3790-3803.

41. Turner OC, Basaraba RJ, Frank AA & Orme IM (2003) in *Granulomatous infections and inflammations: cellular and molecular mechanisms,* ed Boros DL (ASM Press, Washington, D.C.), pp 65-84.

42. Barry CE,3rd, Boshoff HI, Dartois V, Dick T, Ehrt S, et al. (2009) The spectrum of latent tuberculosis: Rethinking the biology and intervention strategies. Nat Rev Microbiol 7: 845-855.

43. Kirschner DE, Young D, Flynn JL (2010) Tuberculosis: Global approaches to a global disease. Curr Opin Biotechnol 21: 524-531.

44. Marino S, Linderman JJ, Kirschner DE (2011) A multifaceted approach to modeling the immune response in tuberculosis. Wiley Interdiscip Rev Syst Biol Med 3: 479-489.

45. Fallahi-Sichani M, El-Kebir M, Marino S, Kirschner DE, Linderman JJ (2011) Multiscale computational modeling reveals a critical role for TNF-{alpha} receptor 1 dynamics in tuberculosis granuloma formation. J Immunol 186: 3472-3483.

46. Fallahi-Sichani M, Schaller MA, Kirschner DE, Kunkel SL, Linderman JJ (2010) Identification of key processes that control tumor necrosis factor availability in a tuberculosis granuloma. PLoS Comput Biol 6: e1000778.

47. Ray JC, Flynn JL, Kirschner DE (2009) Synergy between individual TNF-dependent functions determines granuloma performance for controlling mycobacterium tuberculosis infection. J Immunol 182: 3706-3717.

48. Segovia-Juarez JL, Ganguli S, Kirschner D (2004) Identifying control mechanisms of granuloma formation during M. tuberculosis infection using an agent-based model. J Theor Biol 231: 357-376.

49. Tay S, Hughey JJ, Lee TK, Lipniacki T, Quake SR, et al. (2010) Single-cell NF-kappaB dynamics reveal digital activation and analogue information processing. Nature 466: 267-271.

50. Nelson DE, Ihekwaba AE, Elliott M, Johnson JR, Gibney CA, et al. (2004) Oscillations in NF-kappaB signaling control the dynamics of gene expression. Science 306: 704-708.

51. Karin M, Lin A (2002) NF-kappaB at the crossroads of life and death. Nat Immunol 3: 221-227.

52. Albeck JG, Burke JM, Spencer SL, Lauffenburger DA, Sorger PK (2008) Modeling a snap-action, variable-delay switch controlling extrinsic cell death. PLoS Biol 6: 2831-2852.

53. Marino S, Hogue IB, Ray CJ, Kirschner DE (2008) A methodology for performing global uncertainty and sensitivity analysis in systems biology. J Theor Biol 254: 178-196.

54. Rangamani P, Sirovich L (2007) Survival and apoptotic pathways initiated by TNF-alpha: Modeling and predictions. Biotechnol Bioeng 97: 1216-1229.

55. Fotin-Mleczek M, Henkler F, Samel D, Reichwein M, Hausser A, et al. (2002) Apoptotic crosstalk of TNF receptors: TNF-R2-induces depletion of TRAF2 and IAP

proteins and accelerates TNF-R1-dependent activation of caspase-8. J Cell Sci 115: 2757-2770.

56. Lin PL, Rodgers M, Smith L, Bigbee M, Myers A, et al. (2009) Quantitative comparison of active and latent tuberculosis in the cynomolgus macaque model. Infect Immun 77: 4631-4642.

57. Lin PL, Flynn JL (2010) Understanding latent tuberculosis: A moving target. J Immunol 185: 15-22.

58. Lin PL, Plessner HL, Voitenok NN, Flynn JL (2007) Tumor necrosis factor and tuberculosis. J Investig Dermatol Symp Proc 12: 22-25.

59. Blower SM, Dowlatabadi H (1994) Sensitivity and uncertainty analysis of complex models of disease transmission: An HIV model, as an example. Int Stat Rev 62: 229-243.

60. Marino S, Hogue IB, Ray CJ, Kirschner DE (2008) A methodology for performing global uncertainty and sensitivity analysis in systems biology. J Theor Biol 254: 178-196.

61. Marino S, El-Kebir M, Kirschner D (2011) A hybrid multi-compartment model of granuloma formation and T cell priming in tuberculosis. J Theor Biol 280: 50-62.

62. Yamada H, Mizuno S, Reza-Gholizadeh M, Sugawara I (2001) Relative importance of NF-kappaB p50 in mycobacterial infection. Infect Immun 69: 7100-7105.

63. Iliopoulos A, Psathakis K, Aslanidis S, Skagias L, Sfikakis PP (2006) Tuberculosis and granuloma formation in patients receiving anti-TNF therapy. Int J Tuberc Lung Dis 10: 588-590.

64. Cooper AM (2009) Cell-mediated immune responses in tuberculosis. Annu Rev Immunol 27: 393-422.

65. Basak S, Hoffmann A (2008) Crosstalk via the NF-kappaB signaling system. Cytokine Growth Factor Rev 19: 187-197.

66. Lipniacki T, Puszynski K, Paszek P, Brasier AR, Kimmel M (2007) Single TNFalpha trimers mediating NF-kappaB activation: Stochastic robustness of NF-kappaB signaling. BMC Bioinformatics 8: 376.

Chapter 5

A multi-scale model with tunable resolution

5.1 Background

In previous chapters, we described a multi-scale modeling approach to understanding granuloma formation and function in lung during Mtb infection. We included molecular, cellular, and tissue scales, and temporal scales of minutes to years in the model. Our multi-scale approach allows us to integrate data from different types of experiments (e.g. immunohistochemistry, flow cytometry, and gene knockout studies) at various spatial and temporal scales. We incorporated information flow in both "bottom-up" (molecular events affecting cellular and tissue responses) and "top-down" (cellular and tissue scale events affecting molecular processes) directions to make predictions about how outcomes at one biological scale are affected by mechanisms occurring at another scale. This approach may help us in many ways to identify the mechanisms involved in Mtb-host dynamics. For example, the model in which TNF-TNF receptor interactions are presented [1], as described in Chapter 3, can help determine the role of these interactions in control of infection within a granuloma, or can identify potential immunological targets for immunotherapy.

An important question that arises is: How much detail does the model need to be sufficiently accurate in addressing our immunology questions, while remaining computationally feasible and tractable? Note that adding information from multiple biological scales and particularly different temporal scales significantly increases the

complexity of analysis and reduces the speed of computation. For example, the multi-scale model, including TNF/TNFR interactions, as described in Chapter 3, can simulate a 200-day granuloma using a 2.53 GHz CPU in 40 minutes. However, addition of the intracellular NF-κB signaling mechanisms to the model, as described in Chapter 4, increases the simulation time to 8 hours. Thus, it is important to use the model with an appropriate level of complexity to address questions of interest in a timely manner.

Our solution is to develop models that have *tunable resolution*, by which we mean the ability to fine-grain and coarse-grain model components at will [2]. Tunable resolution is an important tool that helps us find reasonable answers to our questions not only in science, but also in daily life, as quickly as possible. A general application of tunable resolution in daily life is, for example, using maps with different scales and details for different purposes. A city map that shows all street names and directions is useful when driving in town. However, such a map cannot provide useful information when we are interested in finding the distance between two cities located in two states far apart from each other. Similarly, computational models with tunable resolution can be used to address different types of questions from multiple biological scales in a computationally efficient manner. Tunable resolution can improve debugging, increase computational speed, and assist in analysis. For example, to answer questions about how the kinetics of binding of a particular cytokine (e.g. TNF) to its receptors on the cell membrane affects granuloma formation, our model needs to explicitly include molecular processes describing cytokine-receptor interactions. However, if we are interested in identifying the role of a different cytokine, or simulating a TNF knockout scenario, the model does not need extensive detail in TNF/TNF receptor interactions.

Tunable resolution can be achieved by replacing a sub-model consisting of several biologically-based equations (e.g. TNF/TNFR dynamics equations) or rules with a more phenomenological expression (e.g. a parameter, a function, or a simplified version of the sub-model approximating its overall effect on other sub-models). An example of implementing tunable resolution is the reduction of differential equation models, for example, by eliminating processes that are very fast (using pseudo steady-state approximation) or very slow (assuming constant) compared with the characteristic time-scale of interest. Some theoretical methods have been used to reduce these types of models (e.g. [3,4]). However, there is no standard method yet available for implementing tunable resolution, particularly when dealing with multiple linked models of different types (e.g. ODEs and ABMs).

We describe below the methods that we use to achieve tunable resolution for a multi-scale model that aims to capture the role of TNF in determining the outcomes of a granuloma forming in response to Mtb infection. We begin with a version of the granuloma model (with intermediate resolution) that includes an ABM describing cellular/tissue scale dynamics of the immune response to Mtb and ODEs describing molecular single-cell scale TNF/TNFR interactions. Then, we show how this model can be coarse-grained to a lower-resolution version that can be applied when the details of TNF/TNFR binding and interactions are not desired. We also demonstrate how the model can be fine-grained to a higher-resolution version that, in addition to TNF/TNFR interaction dynamics, includes details of the intracellular mechanisms that transmit the signal from TNF-bound TNFRs to the nucleus, where NF-κB activates expression of various genes corresponding to TNF-mediated responses. Fig. 5.1 displays an overview

of these resolutions and examples of questions that each resolution is appropriate to address. We also discuss the methods based on uncertainty and sensitivity analysis that are used to estimate parameter values and to assure that mutual parts of different resolutions of the model are compatible.

5.2 Tunable resolution for TNF/TNFR interactions

Our multi-scale model of the formation and functioning of a granuloma with TNF/TNFR dynamics (intermediate resolution) includes an ABM that captures cellular/tissue scale dynamics of the immune response to Mtb and nine ODEs that describe molecular single-cell scale TNF/TNFR binding and trafficking processes (defined here to include synthesis, internalization, recycling, and degradation of ligand and receptors [1]) (Chapter 3; Fig 5.1B). These processes significantly affect TNF concentration within a granuloma [1,5]. The ODEs describing these processes and thirty parameters associated with them are presented in Chapter 3 and are solved for each single cell (macrophage or T cell) on the grid, together with TNF diffusion and degradation equations within each time-step (dt = 6 s). These processes add a significant level of complexity to the model that ultimately increases the time required for running extensive simulations. However, we may desire to have a coarse-grain model that represents the overall effect of TNF/TNFR interactions on TNF concentration in tissue for cases in which every detail of TNF/TNFR binding and interactions are not of interest (Fig. 5.1A). In this section we describe our approach to capture the overall effect of single-cell scale TNF/TNFR interactions on TNF concentration within a granuloma without explicitly including all TNF/TNFR trafficking processes in the model.

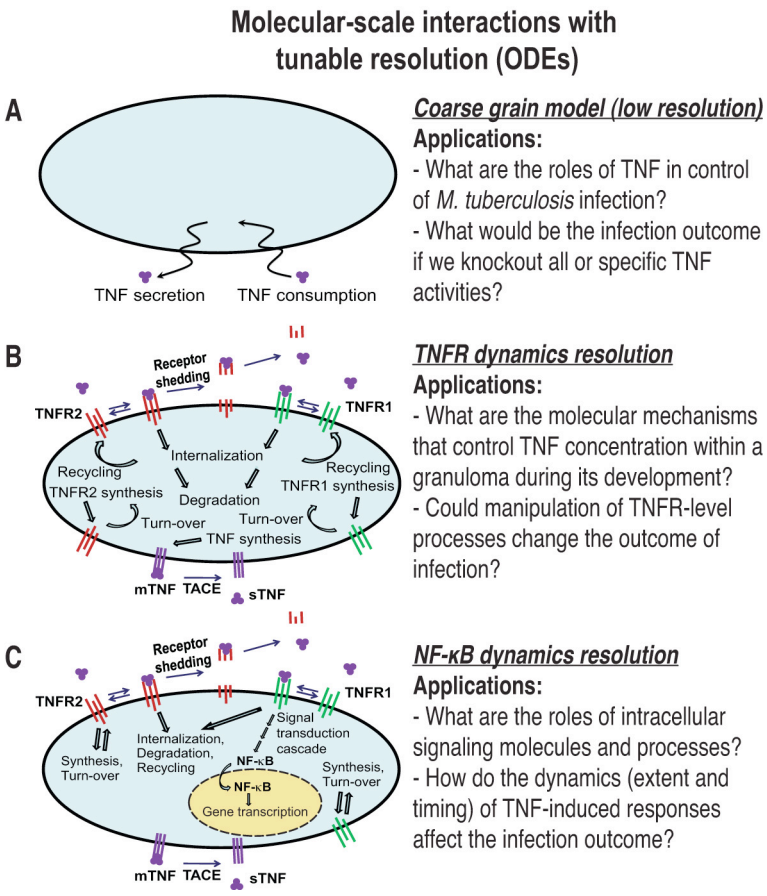

Fig. 5.1 An overview of the low-resolution, the intermediate-resolution (TNFR dynamics), and the high-resolution (NF-κB signaling dynamics) versions of the model, and examples of questions that each resolution is appropriate to address.

To do this, we only consider sTNF release (without consideration of mTNF synthesis) and apparent consumption of extracellular TNF (without explicit consideration of TNFR-associated processes such as reversible binding, internalization, degradation and recycling). Hence, all nine ODEs described above are replaced with the following equation that is solved for any micro-compartment containing a macrophage or a T cell on the grid,

$$\frac{d[sTNF]}{dt} = k'_{synth} - \left(\frac{[sTNF]}{[sTNF] + K_{d1}}\right) k_{consumption} \tag{5.1}$$

This equation describes the change of soluble TNF concentration [sTNF] within a micro-compartment containing an immune cell (macrophage or T cell), where k'_{synth} is the rate of sTNF secretion by the immune cell (#/cell.s), $k_{consumption}$ is the apparent rate constant for sTNF consumption (#/cell.s), and K_{d1} is TNFR1 affinity for sTNF (#/micro-compartment). Because apparent consumption of sTNF by immune cells is actually attributed to sTNF binding to TNFRs on the cell membrane, Equation 5.1 contains a factor $\frac{[sTNF]}{[sTNF]+K_{d1}}$ that represents the sTNF-bound fraction of TNFRs on the membrane of immune cells (using a pseudo steady-state approximation (give ref to a textbook?)). This factor imposes a maximum on the rate of consumption of sTNF by an immune cell. The value of $k_{consumption}$ is estimated via uncertainty analysis. However, knowing the rate constant for TNFR internalization and average numbers of cell surface TNFRs internalizing sTNF from the intermediate-resolution version of the model (Fig. 5.1B), it is possible to estimate a suitable range of values for this parameter on the order of $k_{\mathrm{int}1}[TNFR1]$, where $[TNFR1]$ is TNFR1 density on the cell membrane (#/cell), and k_{int1} is the TNFR1 internalization rate constant (s^{-1}). TNF diffusion and first-order degradation in the extracellular space are captured as in the original model (Fig 5.1B).

Comparison of the low-resolution model (that includes apparent consumption of TNF without explicit consideration of TNFR-associated processes; Fig. 5.1A) just described with a previous published model [6] that does not consider TNF consumption by immune cells at all shows that including this TNF consumption in the model is critical to achieving stable granulomas that are able to contain bacteria at low levels for a long period of time. Without cell-dependent consumption of TNF, TNF levels in tissue increase rapidly, leading to high levels of macrophage activation. This is because TNF

consumption by immune cells significantly contributes to localization of TNF at the core of granuloma where bacteria and infected macrophages are present. This effect is indeed similar to the effect of TNFR internalization on controlling the spatial range of TNF action within a granuloma (see Chapter 3 and [1] for details). Removal of immune cell-mediated sTNF consumption has an impact similar to removal of TNFR internalization on granuloma outcomes: it increases the chance of excessive inflammation in tissue.

In addition to controlling the available amount of TNF within a granuloma, TNF/TNFR interactions play an important role in determining TNF-mediated cellular responses. Activation of the two major TNF-induced signaling pathways, the caspase-mediated apoptotic pathway and the NF-κB pathway, in the model with intermediate resolution (Fig. 5.1B) is described at the level of sTNF/TNFR1 interactions [1]. Briefly, TNF-induced NF-κB activation for each individual macrophage is described as a Poisson process with a probability determined within each ABM time-step (Δt = 10 min), based on a Poisson rate parameter that is a function of the NF-κB activation rate constant ($k_{NF\text{-}\kappa B}$), the concentration of cell surface sTNF/TNFR1 complexes [sTNF/TNFR1], and the concentration threshold for cell surface sTNF/TNFR1 ($\tau_{NF\text{-}\kappa B}$):

$$P_{NF-\kappa B} = \begin{cases} 0 & ; [sTNF/TNFR1] < \tau_{NF-\kappa B} \\ 1 - e^{-k_{NF-\kappa B}([sTNF/TNFR1]-\tau_{NF-\kappa B})\Delta t} & ; [sTNF/TNFR1] \geq \tau_{NF-\kappa B} \end{cases} \quad (3.1)$$

An NF-κB-activated macrophage then secretes chemokines and TNF, and can become activated (after interaction with IFN-γ producing pro-inflammatory T cells) to efficiently kill bacteria. Similarly, we model TNF-induced apoptosis for each individual cell (macrophage and T cell) by:

$$P_{apopt} = \begin{cases} 0 & ; [sTNF/TNFR1_i] < \tau_{apopt} \\ 1 - e^{-k_{apopt}([sTNF/TNFR1_i]-\tau_{apopt})\Delta t} & ; [sTNF/TNFR1_i] \geq \tau_{apopt} \end{cases} \quad (3.2)$$

We use a Poisson process with a probability computed as a function of the apoptosis rate constant (k_{apopt}), the concentration of internalized sTNF/TNFR1 complexes [sTNF/TNFR1$_i$], and the concentration threshold for internalized sTNF/TNFR1 (τ_{apopt}).

When the model is coarse-grained to a lower resolution (Fig. 5.1A) in which TNF/TNFR interactions are not explicitly involved, it is critical to capture TNF-mediated cell responses (i.e. NF-κB activation and apoptosis) as functions of the amount of TNF available to immune cells. Thus, Equations 3.1, 3.2 that describe probabilities of TNF-induced NF-κB activation and apoptosis events as functions of the number of TNF-bound receptors are replaced with the following equations that only use available extracellular sTNF concentrations for probability computations.

$$P_{NF-\kappa B} = \begin{cases} 0 & ; \ \dfrac{[sTNF]}{[sTNF]+K_{d1}} < \tau'_{NF-\kappa B} \\ 1-e^{-k'_{NF-\kappa B}\left(\frac{[sTNF]}{[sTNF]+K_{d1}}-\tau'_{NF-\kappa B}\right)\Delta t} & ; \ \dfrac{[sTNF]}{[sTNF]+K_{d1}} \geq \tau'_{NF-\kappa B} \end{cases} \tag{5.2}$$

$$P_{apopt} = \begin{cases} 0 & ; \ \dfrac{[sTNF]}{[sTNF]+K_{d1}} < \tau'_{apopt} \\ 1-e^{-k'_{apopt}\left(\frac{[sTNF]}{[sTNF]+K_{d1}}-\tau'_{apopt}\right)\Delta t} & ; \ \dfrac{[sTNF]}{[sTNF]+K_{d1}} \geq \tau'_{apopt} \end{cases} \tag{5.3}$$

where $k'_{NF\text{-}\kappa B}$, k'_{apopt}, $\tau'_{NF\text{-}\kappa B}$ and τ'_{apopt} are modified rate constants and thresholds for TNF-induced NF-κB activation and apoptosis and their values are estimated via uncertainty analysis. Because TNF-induced responses (NF-κB activation and apoptosis) in immune cells actually result from sTNF binding to TNFRs on the cell membrane, TNF concentration thresholds ($\tau'_{NF\text{-}\kappa B}$ and τ'_{apopt}) in Equations 5.2, 5.3 are defined based on $\dfrac{[sTNF]}{[sTNF]+K_{d1}}$ that represents the sTNF-bound fraction of TNFRs on the membrane of immune cells (again using a pseudo steady-state approximation). Using a probabilistic

cell response with a probability computed as a function of TNF concentration, instead of a constant probability at all times, and also using the factor $\frac{[sTNF]}{[sTNF]+K_{d1}}$ (that represents sTNF-bound fraction of TNFRs on the cell membrane), instead of TNF concentration, as a base for determining the threshold for TNF-induced responses, are two major modifications that we implemented in the low-resolution model as compared with the previous generation model described in [6].

5.3 Tunable resolution for TNF-induced NF-κB activation

In Chapter 4, we described a higher-resolution model (Fig. 5.1C) that includes intracellular molecular mechanisms controlling TNF-induced NF-κB activation in a macrophage. Fine-graining of the model is implemented by replacing the discrete probabilistic NF-κB activation event described by Equation 3.1 by a set of nonlinear ODEs that determine NF-κB activities following TNF binding to cell surface TNFRs. NF-κB activities then dictate expression of genes associated with NF-κB mediated cell responses such as macrophage activation, apoptosis inhibition and chemokine and TNF expression via additional ODEs. Secretion of chemokines and TNF remains continuously regulated by ODEs, whereas macrophage activation is described as a Poisson process with a probability determined within each time-step (Δt), based on a Poisson rate parameter that is a function of the macrophage activation rate constant (k_{ACT}), intracellular concentration of a generic macrophage-activating protein [ACT], and the ACT concentration threshold for macrophage activation (τ_{ACT}):

$$P_{activation} = \begin{cases} 0 & ; [ACT] < \tau_{ACT} \\ 1 - e^{-k_{ACT}([ACT]-\tau_{ACT})\Delta t} & ; [ACT] \geq \tau_{ACT} \end{cases} \quad (4.1)$$

TNF-induced apoptosis for the high-resolution model is also described as a Poisson process similar to Equation 3.2. The inhibitory impact of the NF-κB activation on macrophage apoptosis is captured by:

$$k_{apopt} = \frac{k_{IAP}}{k_{IAP} + [IAP]} k^0_{apopt} \tag{4.3}$$

The magnitude of k_{apopt} is a function of the intracellular concentration of a generic inhibitor of apoptosis [IAP], the apoptosis inhibition coefficient (k_{IAP}), and the intrinsic TNF-induced apoptosis rate constant (k^0_{apopt}).

A comparison between the process of TNF-induced NF-κB activation in the intermediate resolution model and that in the higher resolution model indicates that fine-graining the model has two major effects on how TNF signaling is implemented. First, the fine-grained version of the model (Fig. 5.1C), unlike the one with the intermediate resolution (Fig. 5.1B), is able to capture the dynamics of TNF-induced responses, for example, oscillatory expression of chemokines. Further, fine-graining of the model has made different NF-κB mediated responses (TNF and chemokine expression, inhibition of apoptosis and macrophage activation) uncoupled. Thus, these processes are regulated by separate mechanisms (transcription and translation of distinct genes and mRNA transcripts).

5.4 Computer programming and algorithm

The tunable resolution multi-scale granuloma model was implemented in a single C++ program that uses Qt for running simulations with a graphical user interface (GUI) on multiple platforms (Linux, Windows and Mac OS). In the beginning of simulations, the

resolution of interest (low, intermediate, or high) is determined by the user. The model will then use essential adjustments to its rules as described above and shown in Fig. 5.2 depending on the selected resolution.

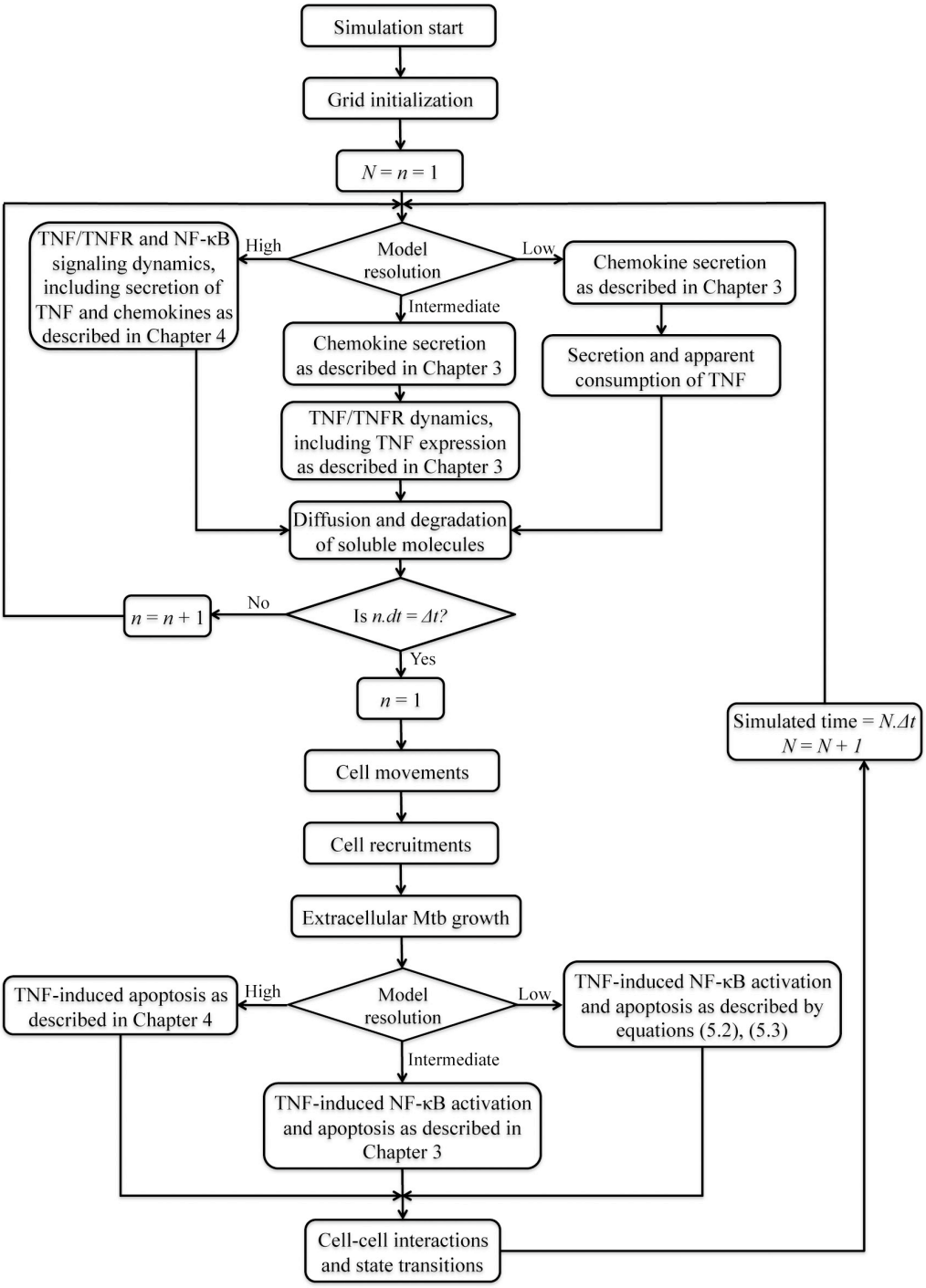

Fig. 5.2 An overview of the algorithm used in simulations of the tunable resolution multi-scale granuloma model. Rules and parameters for mutual ABM processes (e.g. cell movements and recruitments, and Mtb growth) are the same between different resolutions of the model.

5.5 Uncertainty and sensitivity analysis for estimating parameters and validating

When we coarse-grain or fine-grain a model component (e.g. TNF activity), parameters that do not belong to that component (e.g. diffusivity of chemokines in tissue) and their values will be shared between the two resolutions of the model. However, model parameters corresponding to the coarse-grained or fine-grained component become affected. In the case of coarse-graining, for example, a set of parameters that represent a group of mechanistic processes are usually replaced by a new and smaller group of parameters that somehow approximate the overall effect of those processes in the model in a simpler form. For example, we may assume that TNF/TNFR trafficking processes occurring at the surface and inside a cell control TNF concentration in extracellular spaces. Thus, for coarse-graining, we may consider the cell as a source for production and consumption of TNF (that can be represented by new parameters k'_{synth} and $k_{consumption}$ as shown in Equation 5.1) instead of capturing all TNF/TNFR interactions (i.e. synthesis, binding, internalization, recycling, degradation, etc). The question is then: How can we estimate values of the new parameters, TNF production rate (k'_{synth}) and the apparent TNF consumption rate constant ($k_{consumption}$) for a cell in our coarse-grain model? Our solution is to use uncertainty analysis to estimate the values of these coarse-grained parameters from ranges of parameter values such that they reproduce specific outcomes that can be used to calibrate the model. One important outcome used for calibration is containment: control of bacteria within a well-circumscribed granuloma containing stable and low bacterial levels (e.g. $<10^3$ total bacteria). We perform uncertainty analysis on the new coarse-grained parameters to identify values of these parameters that lead to containment outcomes. Note that uncertainty analysis on TNF-independent ABM

parameters (i.e. shared parameters between the two resolutions) was used before (as described in Chapter 3) to identify a containment baseline set of values for these parameters. Thus, we assume here that those parameter values are still appropriate to achieve containment. We perform uncertainty analysis by varying values of only the new parameters generated after coarse-graining, while maintaining values of TNF-independent parameters constant at their previously identified containment baseline level. Using this approach, we assure that by coarse-graining of TNF/TNFR interactions in the model we have not influenced functioning of TNF-independent processes.

In addition to estimating values of new parameters by uncertainty analysis, sensitivity analysis on shared parameters (e.g. chemokine secretion rate, chemokine degradation constant and TNF degradation constant in tissue) between the coarse-grain and fine-grain models can be performed. Comparing results of sensitivity analysis on these parameters indicates whether they have the same influence on model results at different levels of resolution, and thus can be used as a method for further validating the approach of coarse-graining. For example, sensitivity analysis results for the effects of TNF-independent and TNF/TNFR-associated parameters on the outputs of the high-resolution model (that includes NF-κB signaling dynamics) are shown in Table 5.1. We compare these results with results of sensitivity analysis on the intermediate-resolution model (Table 3.1). Although correlation of some parameters (e.g. TNF diffusivity) with model outputs is affected by model resolution, the overall effects of most of the important shared parameters on model outputs are similar between the two resolutions. In addition to sensitivity analysis, experimental data is also an important source for validation of the models at different resolutions.

Table 5.1. Model parameters significantly correlated with outputs of interest, bacterial numbers, granuloma size, caseation area and TNF concentration at day 200 post-infection when simulations are run at high resolution (with NF-κB signaling dynamics).

Selected model outputs	Important TNF-independent and cellular scale parameters [*†]	Important TNF/TNFR-associated molecular and linking parameters [*‡]
Total number of bacteria	α_{Bi} (+) T_{moveM} (--) $\tau_{recTgam}$ (+++) δ_{chem} (+)	D_{TNF} (+++) δ_{TNF} (+++) K_{d1} (+++) k_{int1} (+++) $TNFR1_{mac}$ (---) k_{on1} (---) τ_{apop} (++)
Granuloma size	α_{Bi} (+) M_{recr} (+) T_{moveM} (---) $P_{killMac}$ (-) $\tau_{recTgam}$ (+++)	D_{TNF} (+) k_{on1} (-)
Caseation	α_{Bi} (+++) M_{recr} (+) T_{moveM} (--) $\tau_{recTgam}$ (++)	$k_{synthMac}$ (--) δ_{TNF} (+++) K_{d1} (+++) k_{int1} (+++) $TNFR1_{mac}$ (---) k_{apop} (+++) D_{TNF} (+++) k_{on1} (---)
Average tissue concentration of sTNF	α_{Bi} (+) T_{moveM} (---) $\tau_{recTgam}$ (+++) $P_{killMac}$ (-)	δ_{TNF} (+++) K_{d1} (+++) $TNFR1_{mac}$ (---) D_{TNF} (+++) k_{on1} (---)

[*] Only parameters with significant PRCC values are indicated. Significant positive and negative correlations are shown using + and - as follows: -/+: 0.001 < p-value < 0.01, --/++: p-value < 0.001.

[†] TNF-independent and cellular scale parameter descriptions are as follows: α_{Bi} intracellular Mtb growth rate, T_{moveM} probability of T cell moving to a macrophage-containing location, $P_{killMac}$ probability of cytotoxic killing of an infected macrophage, M_{recr} probability of M_r recruitment, $\tau_{recTgam}$ TNF/chemokine concentration threshold for T_γ recruitment, δ_{chem} chemokine degradation rate constant.

[‡] TNF/TNFR associated parameter descriptions are as follows: D_{TNF} TNF TNF diffusivity in tissue, δ_{TNF} sTNF degradation rate constant, K_{d1} equilibrium dissociation constant of sTNF/TNFR1, k_{on1} sTNF/TNFR1 binding rate constant, k_{int1} TNFR1 internalization rate constant, $TNFR1_{mac}$ TNFR1 density on the surface of macrophages, k_{apop} rate constant for TNF-induced apoptosis in all cell types, τ_{apop} internalized sTNF/TNFR1 threshold for TNF-induced apoptosis.

5.6 Summary: general principles for coarse- or fine-graining the multi-scale model

As described earlier, the multi-scale granuloma model is composed of two major sub-models: (i) a stochastic agent-based model (ABM) that captures cellular and tissue scale dynamics via probabilistic rules for interactions between immune cells and Mtb that are implemented in a discrete manner within each ABM time-step, and (ii) an ordinary differential equation (ODE) model that describes single-cell level molecular scale

processes that, depending on the resolution of the model, includes synthesis and apparent consumption of TNF (low resolution), TNF/TNFR binding and trafficking dynamics (intermediate resolution), and intracellular NF-κB signaling dynamics (high resolution). These two sub-models are linked via TNF-induced cell responses: TNF-induced NF-κB-mediated macrophage activation, apoptosis inhibition, TNF and chemokine expression as well as TNF-induced apoptosis. We described earlier our approaches for tuning model resolution with respect to: (i) TNF/TNFR interactions, and (ii) NF-κB activation processes. We now review those approaches from a more general viewpoint that can be applied to other multi-scale models as well.

Our approach for coarse-graining or fine-graining of immunological processes within the multi-scale model depends on the sub-model to which those processes belong. We first begin with processes that are considered to be part of the ABM sub-model. Generally, the stochastic ABM is composed of cellular and tissue-scale rule events that are controlled by specific probabilities and thresholds. However, these events, in reality, are controlled by specific molecular mechanisms. For example, TNF-induced NF-κB activation is a process that occurs in the presence of sufficient amounts of TNF that stimulates activation of the NF-κB pathway in a macrophage, leading to various NF-κB mediated cell responses. Thus, it can be described, in a coarse-grain manner, as an ABM rule event with a discrete probability function (e.g. Equations 3.1, 5.2) that determines, in an ON/OFF manner, whether or not a macrophage is NF-κB-activated (and thus able to secrete chemokines and TNF, or to become activated). However, this process in reality is more complex, and involves molecular scale events such as TNF binding to cell surface TNFRs, activation of a cascade of kinases, and finally translocation of NF-κB into

nucleus, leading to expression of various inflammatory genes (see Chapter 4 for details). In order to fine-grain the model with respect to NF-κB activation, we need to include these molecular processes into the model. Including these processes requires addition of several NF-κB-associated molecular components (e.g. intracellular kinases, IκBα molecules, nuclear and cytoplasmic NF-κB, mRNAs, etc) to the model. These molecular components exist in relatively large numbers within each cell. This allows us to capture intracellular processes controlling NF-κB activation as continuous ODEs that describe the dynamics of concentration of each of these molecular components. Thus, a critical step in fine-graining the model with respect to NF-κB activation is transformation of the discrete probability function (Equation 3.1, 5.2) determining whether or not a macrophage is NF-κB-activated into a continuous set of ODEs that capture the dynamics of nuclear NF-κB concentration. In other words, the process of NF-κB activation, after fine-graining, becomes a part of the deterministic ODE model, as it does not contain stochastic and discrete components anymore. The dynamics of nuclear NF-κB concentration are then translated to TNF and chemokine expression as well as macrophage activation. This fine-graining approach can be applied to other components of the ABM as well. For example, pro-inflammatory T cell (T_γ)-mediated activation of a macrophage is controlled by a probability that is calculated as a function of the number of pro-inflammatory T cells surrounding the macrophage (see Chapter 3 for details). However, this process, in reality, is more complex and involves molecular scale events such as the expression of IFN-γ by T_γ cells, diffusion of IFN-γ in extracellular spaces, binding of IFN-γ to IFN-γ receptors on the surface of macrophage, and finally STAT-1 activation in the macrophage. One approach to fine-grain the model with respect to these

processes is to transform the discrete probability function determining whether or not a macrophage is activated by surrounding T_γ cells in an ON/OFF manner into a continuous set of ODEs that captures the dynamics of molecular-scale events lying between IFN-γ expression by T_γ cells and STAT-1 activation of a macrophage.

In addition to the above method, coarse-graining and fine-graining of processes can be performed within a single sub-model. For example, TNF/TNFR interactions are controlled by molecular processes that belong to the deterministic ODE sub-model. Coarse-graining of the model in this case, can be simply achieved by lumping several continuous processes (i.e. TNF and TNFR synthesis, binding and trafficking processes) into two simple, still continuous, processes (i.e. TNF synthesis and apparent consumption) that approximate the overall effect of TNF/TNFR interactions on TNF availability in extracellular spaces. In general, coarse-graining of a group of biological processes modeled as continuous equations can be performed by lumping or grouping of these processes into a smaller number of simpler equations representing the overall impact of the original processes. This can be done, for example, by using a pseudo-steady state approximation based on separation of time-scales of the model events.

5.7 References

1. Fallahi-Sichani M, El-Kebir M, Marino S, Kirschner DE, Linderman JJ (2011) Multiscale computational modeling reveals a critical role for TNF-{alpha} receptor 1 dynamics in tuberculosis granuloma formation. J Immunol 186: 3472-3483.

2. Marino S, Linderman JJ, Kirschner DE (2011) A multifaceted approach to modeling the immune response in tuberculosis. Wiley Interdiscip Rev Syst Biol Med 3: 479-489.

3. Maurya MR, Bornheimer SJ, Venkatasubramanian V, Subramaniam S (2005) Reduced-order modelling of biochemical networks: Application to the GTPase-cycle signalling module. Syst Biol (Stevenage) 152: 229-242.

4. Conzelmann H, Saez-Rodriguez J, Sauter T, Bullinger E, Allgower F, et al. (2004) Reduction of mathematical models of signal transduction networks: Simulation-based approach applied to EGF receptor signalling. Syst Biol (Stevenage) 1: 159-169.

5. Fallahi-Sichani M, Schaller MA, Kirschner DE, Kunkel SL, Linderman JJ (2010) Identification of key processes that control tumor necrosis factor availability in a tuberculosis granuloma. PLoS Comput Biol 6: e1000778.

6. Ray JC, Flynn JL, Kirschner DE (2009) Synergy between individual TNF-dependent functions determines granuloma performance for controlling mycobacterium tuberculosis infection. J Immunol 182: 3706-3717.

Chapter 6

Differential risk of tuberculosis reactivation among anti-TNF therapies is due to drug binding kinetics and permeability

6.1 Introduction

Mycobacterium tuberculosis (Mtb) is the causative agent of tuberculosis (TB) in humans. While TB is a global health problem with 2 billion people infected, most are in a latent state, controlling infection. The incidence of active TB is increased in patients with inflammatory conditions such as rheumatoid arthritis (RA) and psoriasis receiving treatment with tumor necrosis factor-α (TNF) inhibitors [1,2]. Mice, monkeys and zebrafish also exhibit impaired immunity during Mtb infection in the absence of TNF [3-5]. These observations support a central role for TNF in maintaining immunity to Mtb. However, these findings also represent a major challenge to anti-TNF therapy use for inflammatory diseases.

The key pathological feature that forms during the immune response to Mtb is a spherical collection of immune cells and bacteria termed a granuloma [6]; the collection of granulomas successfully limiting bacteria growth define a latent state of infection in the host. TNF plays an important role in regulating *granuloma function,* defined here as the ability of a granuloma to restrict bacterial growth [4,5,7-10]. TNF, a pleiotropic cytokine produced by infected and activated macrophages and pro-inflammatory T cells [3,11], has been shown to enhance macrophage activation [12], chemokine production by macrophages [13], and recruitment of immune cells during Mtb infection [14]. TNF can

also mediate cell death via inducing the caspase-mediated apoptotic pathway [15]. Neutralization of TNF can lead to uncontrolled growth of bacteria and reactivation of latent TB [4].

Excellent therapies that are currently licensed as TNF inhibitors are of two types: anti-TNF monoclonal antibodies (including infliximab, adalimumab and certolizumab) or soluble TNF receptor fusion proteins (etanercept) [16]. These drugs have been reported to be equally and highly effective in treatment of some (but not all) inflammatory diseases such as RA and psoriatic arthritis [17,18]. However, recent studies have shown the risk of TB reactivation posed by antibody-type drugs to be several-fold greater than for soluble TNF receptor-type drugs [19-21]. Several hypotheses based on differences in drug properties (reviewed in [16,22-26]) have been advanced to explain the observed differential risk of TB reactivation among anti-TNF therapies. However, no mechanisms have been definitively identified. For our study, we categorize these drug properties into four groups: (i) TNF *binding properties* (including affinity, binding/unbinding kinetics, stoichiometry, and ability to bind membrane-bound TNF (mTNF)), (ii) *permeability* (from blood vessels into lung tissue and penetration into the granuloma), (iii) *apoptotic and cytolytic activity* and (iv) *pharmacokinetic* (PK) characteristics.

Information on these four drug properties is available for clinically used TNF inhibitors [12,16,27]. TNF binding kinetics for etanercept, infliximab and adalimumab have been measured [28,29], and each binds both mTNF and soluble TNF (sTNF). Up to three molecules of antibody-type drugs can bind each TNF molecule, but etanercept binds TNF with a binding ratio of 1:1 [30]. TNF binding properties can influence TNF concentration in granulomatous tissue and affect immunity to Mtb [26,31]. A recent study

has provided evidence of decreased permeability of soluble TNF receptors in mouse granulomas compared with anti-TNF antibody [25]. Infliximab and adalimumab, but not etanercept and certolizumab, induce apoptosis in TNF-expressing cells [27,32-34]. This might be related to the ability of infliximab and adalimumab, and the inability of etanercept and certolizumab to cross-link mTNF [27]. Finally, PK data, including blood concentration-time profiles, are available for etanercept, infliximab and adalimumab as administered in RA and psoriasis patients [35]. It is not clear how these four drug properties, alone or in combination, contribute to observed differences in reactivation of TB induced by anti-TNF treatments and laboratory experiments needed to explore this *in vivo* are currently not feasible.

We recently used a systems biology approach to track formation and maintenance of a TB granuloma in lung tissue in space and time [7,8,36] (see Chapters 3 and 4). Our multi-scale computational model (described in Chapter 3) captures the dynamics of TNF/TNF receptor (TNFR) interactions that occur on second to minute time scales within the long-term cellular immune response to Mtb [8]. This model also provides detailed information regarding the spatial and temporal dynamics of TNF during development of a granuloma in lung tissue. Such information is essential to allow investigation of mechanisms by which TNF inhibitors interfere with granuloma function and thus immunity to Mtb. For the work herein, we incorporate TNF-neutralizing drugs and their relevant properties into the model described in Chapter 3 and indicated in Fig. 6.1, to predict those mechanisms. We identify functional and biochemical characteristics underlying the higher likelihood of TB reactivation that occurs for some TNF-

neutralizing drugs. We also determine immune factors that are central to infection control in a granuloma in the presence of TNF-neutralizing drugs.

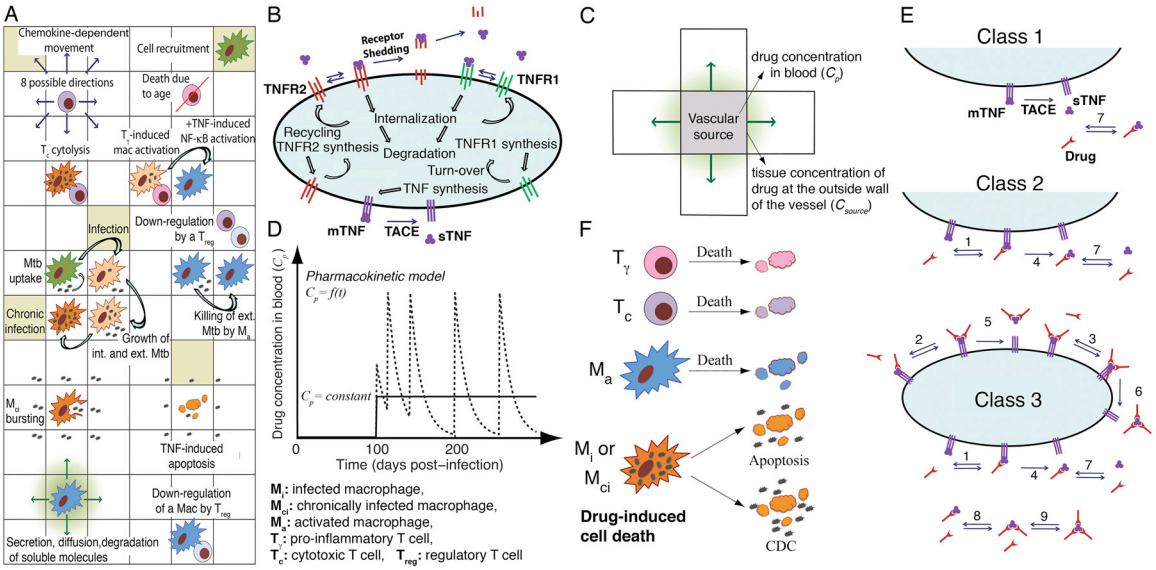

Fig. 6.1 Multi-scale model of the immune response to Mtb infection in the lung and TNF neutralization. Details are presented in Methods and Appendix D. (A) Selected cell-level ABM rules based on known immunological activities and interactions (M_i: infected macrophage, M_{ci}: chronically infected macrophage, M_a: activated macrophage, T_γ: pro-inflammatory IFN-γ producing T cell, T_c: cytotoxic T cell, T_{reg}: regulatory T cell). (B) Binding interactions and reactions controlling TNF/TNFR dynamics at the single-cell level. (C) Drug transport from a vascular source to the grid. Vascular permeability coefficient (k_c) determines the level of drug penetration from blood into lung tissue (relationship between C_p and C_{source}) as described in Appendix D. (D) Addition of TNF neutralizing drugs with either constant or varying blood concentrations (C_p), 100 days after Mtb infection. (E) Hypothetical classes of TNF inhibitors defined in this study based on TNF binding characteristics: Class 1 binds sTNF, but not mTNF, at a binding ratio of 1:1; Class 2 binds both sTNF and mTNF at a binding ratio of 1:1; Class 3 binds both sTNF and mTNF at a TNF/drug binding ratio of 1:3. Numbers represent reactions as listed in Appendix D (Table D.2). (F) The effect of drug-induced cell death in TNF-expressing cells.

6.2 Methods

6.2.1 Multi-scale granuloma model

We recently developed a multi-scale granuloma model that incorporates both cellular/tissue scale events (e.g. immune cell recruitment, movement and interactions) leading to granuloma formation and TNF/TNFR-associated molecular scale interactions that control TNF-mediated cell responses (e.g. apoptosis and NF-κB activation) [8] (see

Chapter 3). In this model, cellular and tissue scale dynamics are captured via a set of well-described interactions between immune cells and Mtb at the site of infection using stochastic simulations in the form of a two-dimensional (2-D) agent-based model (ABM) (Fig. 6.1A). Single-cell molecular scale processes that control TNF/TNFR binding and trafficking for each individual cell, as shown in Fig. 6.1B, are captured by a set of nonlinear ordinary differential equations (ODEs). The two scales are linked via TNF-induced cell responses (i.e. apoptosis and NF-κB activation) and are modeled as Poisson processes with rate parameters computed as functions of molecular concentrations from the ODE model. In addition to sTNF, mTNF has also been shown to contribute in part to control of Mtb infection in mice [37,38]. However, experimental data regarding molecular and cellular-level details of mTNF-mediated signaling and reverse signaling in Mtb immune responses (particularly in humans and non-human primates) are limited. Thus, at this time we only consider sTNF/TNFR-mediated signaling in the model. Details on rules, equations and parameters of the model are previously described [8] (see Chapter 3). Our baseline set of parameter values leads to stable control of infection (containment) in a granuloma (e.g. Fig. 6.3B).

6.2.2 Incorporation of TNF-neutralizing drugs (binding properties, permeability, apoptotic and cytolytic activity, and PK characteristics)

Using our model (described in Chapter 3) as a framework, we now study the impact that TNF-neutralizing drugs have on the immune response to Mtb. We incorporate drug by simulating its transport from vascular sources to the grid representing lung parenchyma as well as diffusion among micro-compartments (Fig. 6.1C, see details in Appendix D).

We assume drug concentrations in blood (C_p) are constant or vary with time based on available pharmacokinetic (PK) data on clinically used TNF inhibitors [35,39] (Fig. 6.1D, see details in Appendix D).

Once TNF inhibitors penetrate from blood into lung tissue, they bind TNF and thereby block TNF-mediated signaling in a granuloma. To analyze the effects of TNF-neutralizing drugs with various TNF binding properties, we define three hypothetical classes of TNF inhibitors (Fig. 6.1E). These classes are defined based on TNF binding characteristics reported for human TNF-neutralizing drugs and differ in their ability to bind mTNF and binding stoichiometry. A Class 1 TNF inhibitor is defined to bind sTNF, but not mTNF, at a binding ratio of 1:1; a Class 2 TNF inhibitor binds both sTNF and mTNF at a binding ratio of 1:1; and a Class 3 TNF inhibitor binds both sTNF and mTNF at a TNF/drug binding ratio of 1:3. The possibility of the higher binding ratio for a Class 3 TNF inhibitor results from the fact that both sTNF and mTNF are trimeric in their mature bioactive form. A Class 3 TNF inhibitor may have more than one binding site for TNF allowing formation of larger drug/TNF complexes. For simplicity, we do not model the formation of larger complexes. An sTNF molecule with either one, two or three drug molecules bound is neutralized and not able to bind TNFR1 or TNFR2. This assumption is consistent with experimental data indicating that only trimeric TNF is biologically active and that both monomeric TNF and artificially prepared dimeric TNF do not efficiently trigger signaling in cells [40,41].

Some TNF inhibitors are reported to induce apoptosis or complement-dependent cytotoxicity (CDC) in TNF-expressing cells. This results from drug binding to and cross-linking mTNF [42]. Based on descriptions presented for three classes of TNF inhibitors,

only a Class 3 TNF inhibitor has the potential to cross-link mTNF and mediate cell death. We describe drug-induced cell death for each individual TNF-expressing cell (including infected and activated macrophages and T cells) as a Poisson process as described in Appendix D. Drug-induced death events, apoptosis and CDC, occur with equal chances. The difference between the consequences of apoptosis and CDC is only significant if the target cell is an infected or a chronically infected macrophage. Cell lysis as a result of CDC leads to the release of intracellular bacteria to the environment similarly to death due to age or bursting of a chronically infected macrophage as described in [8]. However, drug-induced apoptosis, similarly to TNF- and Fas ligand-induced apoptosis, kills a fraction of intracellular bacteria [15,43,44] (Fig. 6.1F). Mtb may also cause caspase-independent cell death in infected macrophages or initiate bystander macrophage apoptosis in a TNF-independent manner [45,46]; it is not known how TNF inhibitors might affect these types of cell death and thus these events are not included in the current model.

To capture TB reactivation at the granuloma level, we first simulate the model in the absence of TNF inhibitors by using a baseline set of parameter values that leads to stable control of infection (containment) in a granuloma as previously described [8]. After 100 days, at which time a well-circumscribed granuloma with stable bacterial levels ($<10^3$ total bacteria) forms, the granuloma is exposed to a TNF-neutralizing drug. Further details of the modeling methods, parameter estimation, sensitivity analysis and computer visualization are presented in Appendix D. TNF neutralization reactions and parameters are presented in Appendix D (Tables D.1, D.2). Movies 1-7 can be found at http://malthus.micro.med.umich.edu/lab/movies/Multiscale/AntiTNFDrugs/.

6.3 Results

6.3.1 TNF binding properties, particularly binding to mTNF, are central to the neutralizing power of a drug

In all of our studies, unless otherwise noted, we use bacterial levels within the granuloma as a readout for quantifying granuloma function. We first compare the impact on bacterial levels for three classes of TNF inhibitors we define based on TNF binding properties, including stoichiometry and ability to bind mTNF versus sTNF (see Fig. 6.1E). Our results indicate that binding to mTNF, in addition to sTNF, is critical to impairing granuloma function. This follows from a comparison of simulations showing total numbers of bacteria in a granuloma for Class 1 drugs that only bind sTNF (Fig. 6.2A) with drugs of Class 2 and 3 that are able to bind both sTNF and mTNF (Fig. 6.2B, C). The cell membrane provides a scaffold on which TNF at high concentrations is available for neutralization before it is released as a result of TNF-α converting enzyme (TACE) activity and diluted in extracellular spaces. Thus, binding to mTNF enhances the TNF-neutralizing power of drugs.

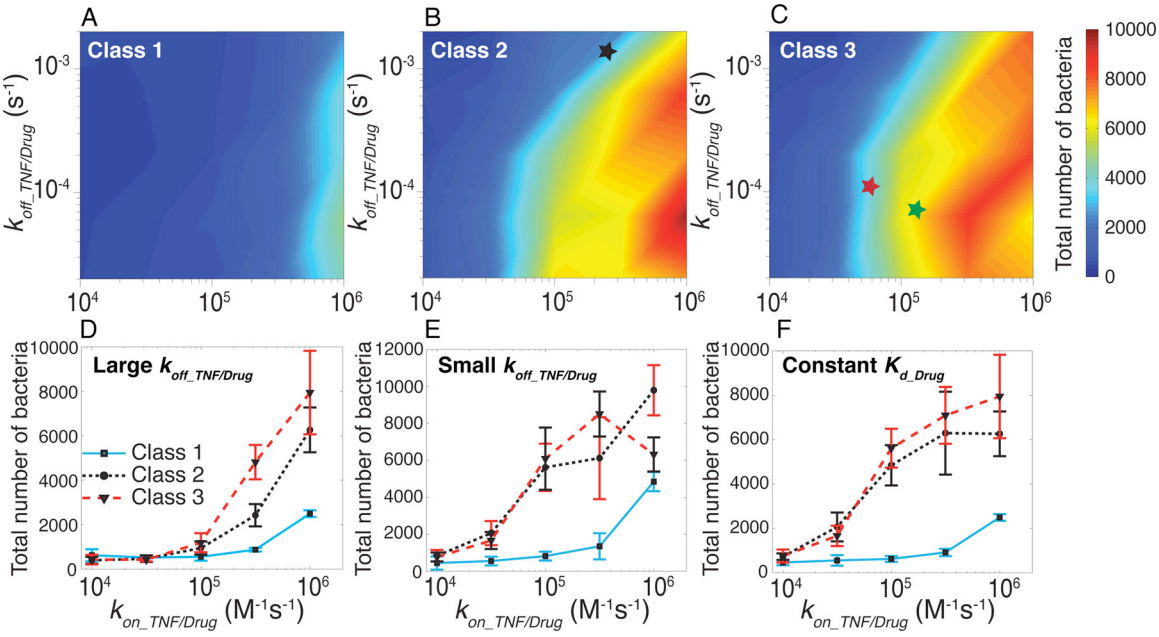

Fig. 6.2 Effect of TNF/drug binding characteristics on bacterial levels within a granuloma 100 days after anti-TNF treatment. (A)-(C) Effect of variations of TNF/drug binding ($k_{on\_TNF/Drug}$) and unbinding rate constants ($k_{off\_TNF/Drug}$) on bacterial levels in a granuloma after treatment with TNF inhibitors of Class 1, 2 and 3, respectively. The black, red and green stars locate TNF inhibitors with TNF binding kinetics similar to etanercept, infliximab and adalimumab, respectively. (D), (E) Effect of variation of TNF/drug binding rate constant ($k_{on\_TNF/Drug}$) on bacterial levels in a granuloma at large and small unbinding rate constants (large: $k_{off\_TNF/Drug} = 2\times10^{-3}$ s^{-1}, small: $k_{off\_TNF/Drug} = 6.3\times10^{-5}$ s^{-1}), respectively. (F) Effect of variation of TNF/drug binding rate constant ($k_{on\_TNF/Drug}$) on bacterial levels in a granuloma at a constant drug affinity for TNF ($K_{d\_Drug} = k_{off\_TNF/Drug} / k_{on\_TNF/Drug} = 2\times10^{-9}$ M). Simulations are run with drug blood concentrations of $C_p = 1.25\times10^{-8}$ M and vascular permeability coefficient of $k_c = 1.1\times10^{-7}$ cm/s representing an approximately 50% drug permeability in tissue.

We also test the impact of affinity and TNF binding kinetics on granuloma function. For Class 1 and 2 drugs, increasing affinity for TNF (by increasing TNF/drug binding rate constant ($k_{on\_TNF/Drug}$) at a constant TNF/drug unbinding rate constant ($k_{off\_TNF/Drug}$)) leads to more efficient neutralization of TNF and higher bacterial levels in a granuloma (Fig. 6.2D, E). However, behavior of a Class 3 drug is more complex. As detailed in Methods, an sTNF molecule with one, two or three drug molecules bound is considered neutralized and unable to trigger TNF-mediated cell responses. Increasing binding rate constants for large values of unbinding rate constant enhances the neutralizing power of a Class 3 drug as compared with a Class 2 drug (Fig. 6.2D).

However, at very high affinities (large values of binding rate constant and small values of unbinding rate constant), particularly if drug concentration in tissue is not sufficiently high, multivalent binding of a Class 3 drug to TNF can limit drug availability for binding to free (unbound) TNF (similar to other physical situations involving multivalent binding [47]). This can reduce the neutralizing power of a Class 3 drug as compared with a Class 2 drug of the same affinity (Fig. 6.2E).

Furthermore, at a constant, moderate affinity for TNF ($K_{d\_Drug} = 2\times10^{-9}$ M), drugs with greater binding rate constants can more efficiently neutralize TNF, resulting in higher bacterial levels (Fig. 6.2F). This is because drugs compete with cell surface TNFRs for binding to sTNF and thus a drug with a greater binding rate constant can neutralize larger amounts of sTNF. Larger values of binding rate constant for Class 2 and 3 drugs also favor mTNF neutralization before it is released as sTNF and diluted in extracellular spaces.

Considering only differences in TNF binding properties, and assuming similar constant blood concentrations and vascular permeability coefficients, we can predict bacterial levels in granulomas treated individually with etanercept (Class 2), infliximab (Class 3) or adalimumab (Class 3) (see stars in Fig. 6.2B, C). Higher bacterial levels are predicted to occur for treatments with infliximab and particularly adalimumab in comparison with etanercept, suggesting that the TNF binding properties of these drugs contribute to the observed clinical differences in TB reactivation rates.

6.3.2 Differences in both blood drug concentrations and permeabilities into lung tissue can explain differential rates of TB reactivation

We next assess the role of blood drug concentrations and drug permeability into lung tissue in determining bacterial levels in a granuloma. For blood drug concentrations, we use drug-specific data on the average blood concentrations of etanercept, infliximab and adalimumab that correspond to drug doses administered in RA patients [35] (see Appendix D (Table D.1)). At all values of vascular permeability coefficient k_c within the range of 10^{-9}-10^{-6} cm/s, both infliximab and adalimumab treatments lead to statistically significantly higher bacterial levels compared with etanercept (Fig. 6.3A). This is consistent with data indicating a higher risk of TB reactivation from antibody-type drugs as compared with the TNF receptor fusion protein [20,21].

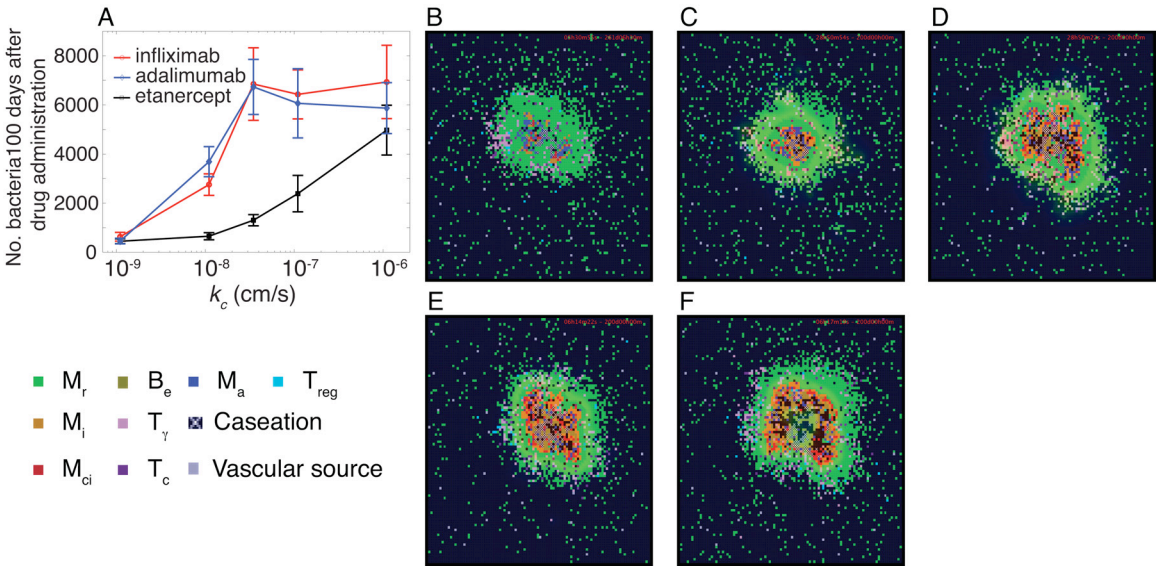

Fig. 6.3 Comparison of effects of etanercept, infliximab and adalimumab on bacterial numbers and granuloma snapshots at different blood concentrations and vascular permeability coefficients (k_c). (A) Effect of permeability coefficient variations on bacterial numbers within a granuloma for infliximab, etanercept, and adalimumab. Results are shown for drug-specific blood concentrations, corresponding to doses administered in RA patients (see Appendix D (Table D.1)). Vascular permeability coefficients of 10^{-9}-10^{-6} cm/s correspond to approximately 1%-90% drug permeability levels from blood into tissue. (B) Granuloma snapshot for a scenario of containment in the absence of TNF inhibitor. (C), (D) Granuloma snapshots 200 days post-infection for 100 day etanercept treatment for $k_c = 1.1\times10^{-8}$ cm/s and $k_c = 1.1\times10^{-7}$ cm/s, respectively. (E), (F) Granuloma snapshots 200 days post-infection for 100 day infliximab treatment for $k_c = 1.1\times10^{-8}$ cm/s and $k_c = 1.1\times10^{-7}$ cm/s, respectively. Cell types and status are shown by different color squares, as indicated in the bottom left corner of the figure (M_r: resting macrophage, M_i: infected macrophage, M_{ci}: chronically infected macrophage, M_a: activated macrophage, B_e: extracellular bacteria, T_γ: pro-inflammatory IFN-γ producing T cell, T_c: cytotoxic T cell, T_{reg}: regulatory T cell). Caseation and vascular sources are also indicated.

Tissue/blood concentration ratios for most antibodies are reported to be in the range of 0.1-0.5 [48], corresponding to vascular permeability coefficients of approximately 10^{-8}-10^{-7} cm/s. Our simulations predict that this range for vascular permeability is sufficient for infliximab (and also adalimumab), but not for etanercept, to exert their maximal effect on TNF neutralization in lung at reported blood concentrations of these drugs (Fig. 6.3A-F and Movies 1-5). For example, at small permeability coefficients ($k_c = 1.1\times10^{-8}$ cm/s) that lead to only 10% permeability of etanercept into

tissue, the amount of available TNF in a granuloma is still sufficient to maintain bacterial levels within the range observed in the absence of drug (Fig. 6.3A, C). However, this same level of drug permeability can result in approximately five to nine-fold increase in bacterial levels in the case of infliximab and adalimumab (Fig. 6.3A, E). This prediction supports data suggesting that different permeabilities of TNF inhibitors into lung tissue and TB lesions contribute to differential effects on exacerbation or reactivation of TB [25,26].

6.3.3 Infliximab-induced apoptosis and cytolysis are not key factors for impairing granuloma function

Antibody-type drugs such as adalimumab and infliximab can cross-link mTNF, leading to cell death via apoptosis or complement-dependent cytolysis (CDC) [27,32]. We test the impact of drug-induced cell death on immunity to Mtb by comparing simulation results for infliximab with and without its ability to induce apoptosis and CDC (Fig. 6.4). Fig. 6.4A shows that the ability of infliximab to induce cell death does *not* have a strong effect on controlling bacterial levels in a granuloma. Over a wide range of values governing induction of apoptosis or CDC (i.e. τ_{death_Drug}, threshold for induction of apoptosis or CDC) and at both low and high drug permeabilities, bacterial numbers remain similar to those when drug is present but its apoptotic and cytolytic capabilities are removed. To clarify the mechanism behind this finding, we identify immune cell types and states that are influenced by drug-induced mTNF-mediated cell death.

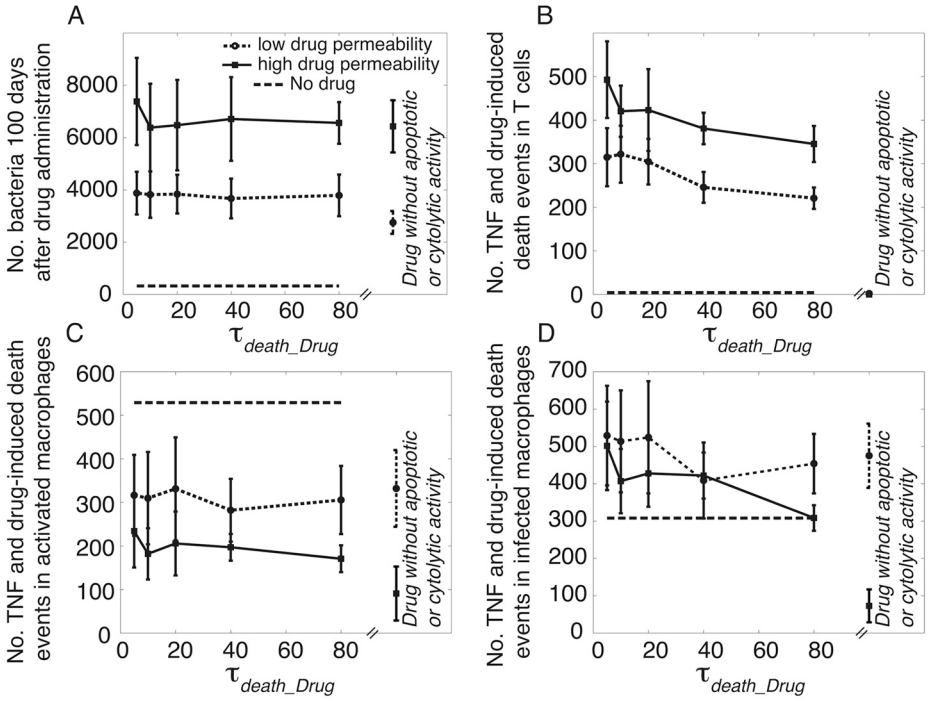

Fig. 6.4 Effect of infliximab-induced cell death as a result of binding to mTNF on a granuloma at 100 days after anti-TNF treatment. (A) Bacterial levels within a granuloma controlling infection in the absence of infliximab and in the presence of infliximab with low and high vascular permeabilities (low: $k_c = 1.1\times10^{-8}$ cm/s, high: $k_c = 1.1\times10^{-7}$ cm/s) with or without apoptotic and cytolytic activities and at different concentration thresholds for drug-induced cell death ($\tau_{death\text{-}Drug}$). (B)-(D) Levels of TNF and drug-induced cell death for T cells, activated macrophages (M_a) and infected and chronically infected macrophages (M_i and M_{ci}), respectively. Cell death numbers does not include death events induced by factors other than TNF and drug. Infliximab's ability to induce apoptosis and cytolysis significantly contributes, at low and high drug permeabilities, to death of T cells, and only at high permeabilities to death of activated and infected macrophages. At low drug permeabilities, there is no statistically significant difference between activated and infected macrophage death with or without apoptotic and cytolytic activities of the drug.

Most T cell death is due to infliximab, and in particular the apoptotic and cytolytic activity of the drug, than to TNF (Fig. 6.4B). However, infliximab's ability to induce apoptosis and cytolysis contributes only slightly, at high permeabilities, to death of activated macrophages (Fig. 6.4C). Activated macrophage and T cell loss have negative effects on granuloma function, as they contribute to bacteria killing. However, we also see a statistically significant increase (at high drug permeabilities) in infected and chronically infected macrophage death (Fig. 6.4D) when the drug is given cytolytic and

apoptotic ability. When infected and chronically infected macrophages are killed, a fraction of intracellular Mtb may also be killed, a positive effect on granuloma function that compensates for a loss of T cells and activated macrophages. Thus, our predictions do not support hypotheses that assign a key role to apoptotic and cytolytic activities of antibody-type TNF-neutralizing drugs in determining their ability to reactivate TB, although we do confirm a significant reduction in T cell levels as a result of anti-TNF antibody (e.g. infliximab) treatments reported in literature [32,49]. This finding does not dismiss the importance of T cells as key immune cells in immunity to Mtb. However, it suggests that a TNF inhibitor that has TNF binding properties and the same blood concentration as infliximab can impair granuloma function *independent* of its apoptotic and cytolytic activities.

6.3.4 Pharmacokinetic fluctuations in blood concentration of infliximab do not significantly alter granuloma function

Using our model, we can assess the impact of PK fluctuations in blood concentrations of drugs. We follow the PK model for RA patients presented by St Clair *et al* [39] as the blood concentration-time profile for infliximab following intravenous administration (see Appendix D for details on drug transport from blood into tissue). As shown in Figures 6.5A and 6.5B, fluctuations of approximately two orders of magnitude in blood concentrations of infliximab result in significant fluctuations in the average drug concentration in a granuloma. As expected, smaller vascular permeabilities lead to smaller concentrations of infliximab in lung tissue as well as smaller peak-trough ratios of infliximab concentration in a granuloma. At low permeabilities, fluctuations in the

blood concentration of infliximab can lead to fluctuations in the number of bacteria in a granuloma (Fig. 6.5C). At high permeabilities, the concentration of infliximab in a granuloma is above a threshold that leads to uncontrolled growth of Mtb and thus fluctuations in blood concentration have no significant effect on bacterial levels (Movies 6, 7). In addition to blood concentration fluctuations, we also analyze the influence of infliximab half-life in granulomatous tissue on granuloma outcomes. Our analysis shows comparable bacterial numbers among simulations using different values of tissue half-life of the drug within the range of 4-12 days (Fig. 6.5D). Overall, our model suggests that PK fluctuations in blood concentration and half-life of infliximab in granulomatous tissue are not major factors in TB reactivation, as the effect of infliximab on granuloma function may persist at a longer time-scale, enhancing bacterial replication. This finding highlights the importance of biological half-life of infliximab, rather than serum half-life, in driving TB reactivation.

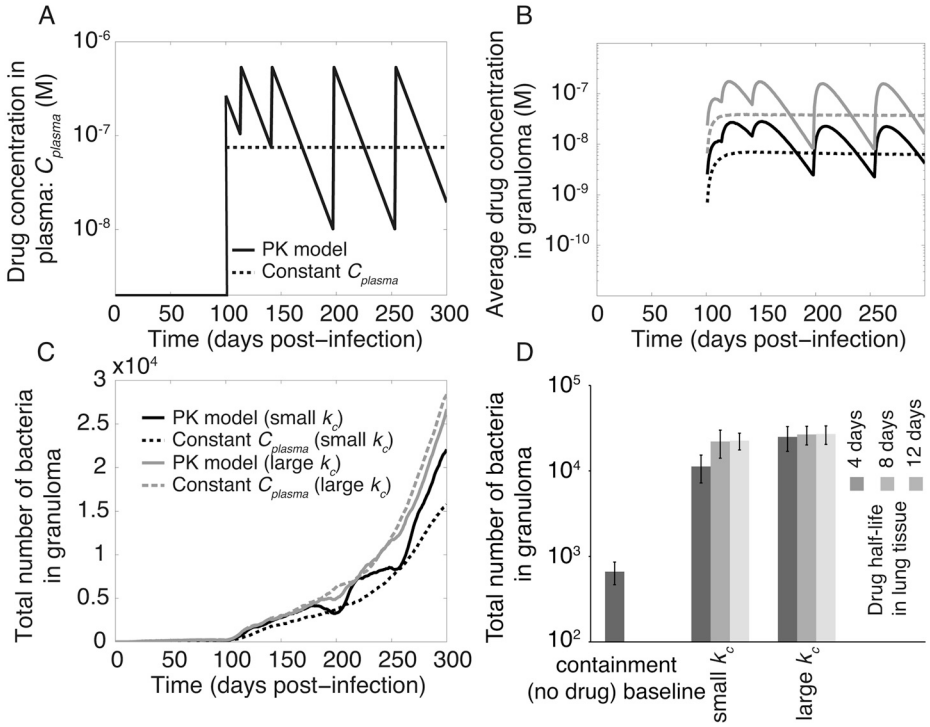

Fig. 6.5 Effect of pharmacokinetic (PK) fluctuations in the blood concentration of infliximab and variation of tissue half-life of infliximab on free drug concentration and bacterial levels within a granuloma. (A) The mono-exponential PK model with a first order elimination for blood concentration of infliximab in RA patients at a 3 mg/kg dose level as presented by [39]**, compared with an estimated steady state concentration. (B) Dynamics of the average free infliximab concentration within a granuloma following anti-TNF treatment for different values of permeability coefficient (small $k_c = 1.1\times10^{-8}$ cm/s, large $k_c = 1.1\times10^{-7}$ cm/s). (C) Dynamics of bacteria numbers within a granuloma following anti-TNF treatment. (D) Bacterial levels within a granuloma in the absence of infliximab (containment baseline) and in the presence of infliximab at low and high vascular permeabilities (small $k_c = 1.1\times10^{-8}$ cm/s, large $k_c = 1.1\times10^{-7}$ cm/s) and different tissue half-lives (half-life of 4 days: $k_{deg\_Drug} = 2\times10^{-6}$ s^{-1}, half-life of 8 days: $k_{deg\_Drug} = 1\times10^{-6}$ s^{-1}, half-life of 12 days: $k_{deg\_Drug} = 5.35\times10^{-5}$ s^{-1}) 300 days post-infection. Anti-TNF treatments are initiated at day 100 post-infection.**

6.3.5 Immune factors that affect granuloma function in the presence of TNF inhibitors

We perform sensitivity analysis on our model to identify host and bacterial factors that most influence different granuloma functional outcomes, including bacterial levels, amount of caseation, granuloma size, and TNF concentrations in tissue in the presence of two TNF inhibitors, infliximab and etanercept (Fig. 6.6). Of the cellular/tissue scale processes we explored (see previous work in Chapter 3 and [8]), mechanisms that most

influence granuloma outcomes for both drugs are: chemokine degradation, a chemokine concentration threshold for recruitment of IFN-γ producing T cells, T cells' ability to migrate through a dense macrophage network surrounding bacteria and infected macrophages at the core of a granuloma, and the intracellular growth rate of bacteria (see Fig. 6.6 and Appendix D (Tables D.3, D.4) for correlation coefficients and *p*-values) . However, our analysis predicts that TNF-associated parameters (operating at the molecular scale) that significantly influence granuloma outcomes differ between the drugs. For example, apoptosis and macrophage TACE activity are important mechanisms operating during infliximab treatment. This follows from the impact that these processes have on infliximab-induced apoptosis of infected macrophages, a process that can aid bacterial killing. TNF-induced NF-κB activation is an important determinant of granuloma function during etanercept treatment in which TNF concentration in a granuloma, in contrast to infliximab treatment, is still high enough to activate macrophages.

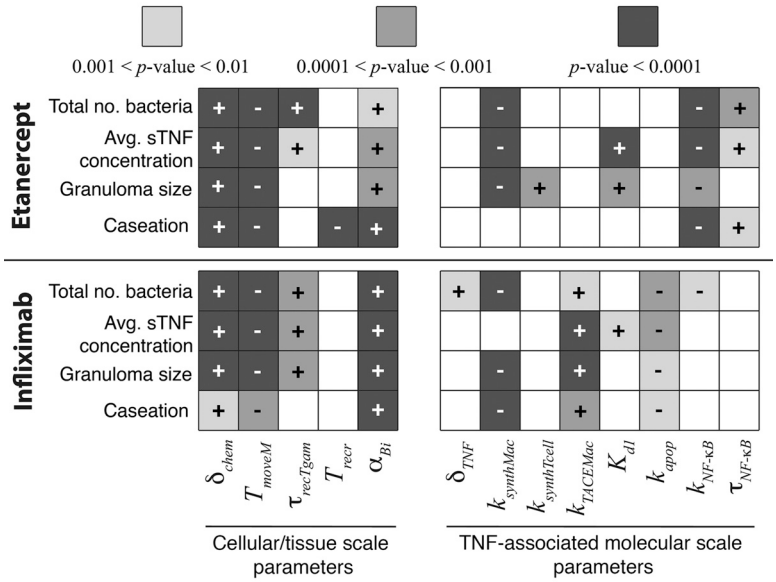

Fig. 6.6 Sensitivity analysis results for the effect of cellular/tissue scale and TNF-associated molecular scale parameters on model outcomes in the presence of TNF-neutralizing drugs: etanercept and infliximab. Important cellular/tissue scale parameters are identified to be: chemokine degradation rate constant δ_{chem}, probability of T cell moving onto a macrophage-containing location T_{moveM}, TNF/chemokine concentration threshold for T_γ recruitment $\tau_{recTgam}$, probability of T cell recruitment T_{recr}, and intracellular Mtb growth rate α_{Bi}. Important TNF-associated parameters include: sTNF degradation rate constant δ_{TNF}, mTNF synthesis rate for macrophages $k_{synthMac}$, mTNF synthesis rate for T cells $k_{synthTcell}$, TACE activity rate constant for macrophages $k_{TACEMac}$, equilibrium dissociation constant of sTNF/TNFR1 K_{d1}, apoptosis rate constant k_{apop}, rate constant for TNF-induced NF-κB activation in macrophages $k_{NF\kappa B}$, and cell surface sTNF/TNFR1 threshold for TNF-induced NF-κB activation $\tau_{NF\kappa B}$. +/- signs show positive/negative correlations. Color intensities show the significance of correlations based on *p*-values. Significant correlation coefficient values are shown in Appendix D (Tables D.3, D.4). White squares show non-significant correlations.

6.4 Discussion

A major complication of anti-TNF immunotherapy is an increased risk of granulomatous disease, particularly the reactivation of latent TB. The risk of TB reactivation in patients receiving monoclonal antibodies (e.g. infliximab and adalimumab) is higher compared to soluble TNF receptor fusion protein (etanercept) [19]. Several hypotheses based on structural and functional differences among TNF inhibitors (reviewed in [16,22-26]) have been suggested to explain this observation. There are conflicting data, however, regarding the significance of drug characteristics in determining risk of TB reactivation. For

example, it has been suggested that high peak blood levels of infliximab might account for its increased risk of infection compared with etanercept [16,35]. However, adalimumab treatment with peak blood levels comparable to etanercept also leads to an increased risk of TB [35]. Further, the differential ability to induce CDC in key immune cells (e.g. T cells) as a result of drug binding to mTNF has been suggested to explain differential risks of TB reactivation by infliximab and etanercept [49]. Certolizumab, which has only one TNF-binding region and no Fc region, similar to etanercept, is unable to cross-link mTNF and does not activate complement, yet significantly increases the risk of TB [19]. The experiments required to fully evaluate these various hypotheses, i.e. a comprehensive experimental analysis of the effect of each of these drug characteristics, alone and in combination, on the immune response to Mtb, are at present very difficult. Indeed, some of the controversy about reactivation mechanisms may stem from different animal systems within which these data were generated. To begin to address these challenges, we use a systems biology approach. Our computational model links dynamics of molecular scale drug/TNF/TNFR interactions that occur on second to minute time scales to cellular/tissue scale events that control the long-term immune response to Mtb at the level of a granuloma. Computational models can be used together with experiments as tools to unravel important mechanisms underlying drug-induced TB reactivation at the granuloma scale.

We find that the ability of a drug to bind mTNF is a main factor impairing the ability of the granuloma to control bacteria load. Drug binding to mTNF has already been suggested to be important for inducing TB reactivation. However, this suggestion has been motivated by a hypothesis that drug binding to mTNF induces cytotoxicity in key

immune cells (e.g. T cells), impairing immunity to Mtb [49]. Although our model confirms the importance of T cells as key immune cells in immunity to Mtb [7,8,36], it predicts that a drug capable of binding to mTNF, even if unable to induce cell death, is generally much more able to induce reactivation of TB compared with a drug that only binds sTNF. This finding may have implications for development of drugs that block sTNF for therapy of inflammatory diseases. Further, the ability of a TNF inhibitor to induce TB reactivation not only depends on the affinity of a drug for TNF, but also on the TNF/drug binding kinetics.

We used published data on TNF binding properties for three commonly used TNF inhibitors to predict their impact on granuloma function. Our findings suggest that TNF/drug binding kinetics are sufficient to explain why adalimumab is more potent than etanercept in TB reactivation. Regarding TNF binding/unbinding kinetics, infliximab leads to *slightly* higher bacterial numbers than etanercept. This suggests that factors in addition to TNF/drug binding kinetics must account for the significant increase in risk of TB induced by infliximab. Our simulations, consistent with some experimental data [25], suggest that blood concentrations and vascular permeabilities of infliximab and etanercept are those critical factors. Our work does not support hypotheses that consider apoptotic and cytolytic activities or large fluctuations in blood concentration of infliximab as the most important factors in driving TB reactivation by this drug.

These findings might be tested using non-human primate models of TB; non-human primates show immune responses more similar to humans than mouse models [4,50]. Design of novel agents that neutralize sTNF but have no effect on mTNF may reveal the importance of mTNF binding in determining drugs' abilities to induce TB

reactivation. Further, if anti-TNF antibodies are engineered in order to modulate their TNF binding kinetics and apoptotic activities, we should be able to verify our model predictions about the relative importance of these factors in determining the outcome of infection. To test the importance of pharmacokinetic fluctuations, TNF neutralization experiments could be performed under different dosing regimens that lead to the same average blood concentrations and outcomes then can be compared.

Finally, our approach enables us to determine both TNF-independent cellular/tissue scale events and TNF-associated molecular scale processes that significantly influence granuloma function during treatment with anti-TNF drugs. These processes can be studied as potential targets for therapy and control of TB reactivation induced by anti-TNF treatments. Our key findings also suggest characteristics of suitable anti-TNF drugs for treatment of inflammatory diseases. Further, our multi-scale computational model can be used as a template for studying the effects of other immunomodulatory drugs, as it enables us to combine PK analysis with drug/target interactions at the molecular scale that manifest as cellular/tissue scale responses.

6.5 References

1. Wallis RS, Broder M, Wong J, Lee A, Hoq L (2005) Reactivation of latent granulomatous infections by infliximab. Clin Infect Dis 41 Suppl 3: S194-8.

2. Winthrop KL (2006) Risk and prevention of tuberculosis and other serious opportunistic infections associated with the inhibition of tumor necrosis factor. Nat Clin Pract Rheumatol 2: 602-610.

3. Flynn JL, Goldstein MM, Chan J, Triebold KJ, Pfeffer K, et al. (1995) Tumor necrosis factor-alpha is required in the protective immune response against mycobacterium tuberculosis in mice. Immunity 2: 561-572.

4. Lin PL, Myers A, Smith L, Bigbee C, Bigbee M, et al. (2010) Tumor necrosis factor neutralization results in disseminated disease in acute and latent mycobacterium tuberculosis infection with normal granuloma structure in a cynomolgus macaque model. Arthritis Rheum 62: 340-350.

5. Clay H, Volkman HE, Ramakrishnan L (2008) Tumor necrosis factor signaling mediates resistance to mycobacteria by inhibiting bacterial growth and macrophage death. Immunity 29: 283-294.

6. Tsai MC, Chakravarty S, Zhu G, Xu J, Tanaka K, et al. (2006) Characterization of the tuberculous granuloma in murine and human lungs: Cellular composition and relative tissue oxygen tension. Cell Microbiol 8: 218-232.

7. Ray JC, Flynn JL, Kirschner DE (2009) Synergy between individual TNF-dependent functions determines granuloma performance for controlling mycobacterium tuberculosis infection. J Immunol 182: 3706-3717.

8. Fallahi-Sichani M, El-Kebir M, Marino S, Kirschner DE, Linderman JJ (2011) Multiscale computational modeling reveals a critical role for TNF-{alpha} receptor 1 dynamics in tuberculosis granuloma formation. J Immunol 186: 3472-3483.

9. Barry CE,3rd, Boshoff HI, Dartois V, Dick T, Ehrt S, et al. (2009) The spectrum of latent tuberculosis: Rethinking the biology and intervention strategies. Nat Rev Microbiol 7: 845-855.

10. Lin PL, Flynn JL (2010) Understanding latent tuberculosis: A moving target. J Immunol 185: 15-22.

11. Saunders BM, Briscoe H, Britton WJ (2004) T cell-derived tumour necrosis factor is essential, but not sufficient, for protection against mycobacterium tuberculosis infection. Clin Exp Immunol 137: 279-287.

12. Harris J, Hope JC, Keane J (2008) Tumor necrosis factor blockers influence macrophage responses to mycobacterium tuberculosis. J Infect Dis 198: 1842-1850.

13. Algood HM, Lin PL, Yankura D, Jones A, Chan J, et al. (2004) TNF influences chemokine expression of macrophages in vitro and that of CD11b+ cells in vivo during mycobacterium tuberculosis infection. J Immunol 172: 6846-6857.

14. Zhou Z, Connell MC, MacEwan DJ (2007) TNFR1-induced NF-kappaB, but not ERK, p38MAPK or JNK activation, mediates TNF-induced ICAM-1 and VCAM-1 expression on endothelial cells. Cell Signal 19: 1238-1248.

15. Keane J, Balcewicz-Sablinska MK, Remold HG, Chupp GL, Meek BB, et al. (1997) Infection by mycobacterium tuberculosis promotes human alveolar macrophage apoptosis. Infect Immun 65: 298-304.

16. Wallis RS (2008) Tumour necrosis factor antagonists: Structure, function, and tuberculosis risks. Lancet Infect Dis 8: 601-611.

17. Hochberg MC, Tracy JK, Hawkins-Holt M, Flores RH (2003) Comparison of the efficacy of the tumour necrosis factor alpha blocking agents adalimumab, etanercept, and infliximab when added to methotrexate in patients with active rheumatoid arthritis. Ann Rheum Dis 62 Suppl 2: ii13-6.

18. Gladman DD (2008) Adalimumab, etanercept and infliximab are equally effective treatments for patients with psoriatic arthritis. Nat Clin Pract Rheumatol 4: 510-511.

19. Wallis RS (2009) Infectious complications of tumor necrosis factor blockade. Curr Opin Infect Dis 22: 403-409.

20. Wallis RS, Broder MS, Wong JY, Hanson ME, Beenhouwer DO (2004) Granulomatous infectious diseases associated with tumor necrosis factor antagonists. Clin Infect Dis 38: 1261-1265.

21. Tubach F, Salmon D, Ravaud P, Allanore Y, Goupille P, et al. (2009) Risk of tuberculosis is higher with anti-tumor necrosis factor monoclonal antibody therapy than with soluble tumor necrosis factor receptor therapy: The three-year prospective french research axed on tolerance of biotherapies registry. Arthritis Rheum 60: 1884-1894.

22. Ehlers S (2005) Tumor necrosis factor and its blockade in granulomatous infections: Differential modes of action of infliximab and etanercept?. Clin Infect Dis 41 Suppl 3: S199-203.

23. Taylor PC (2010) Pharmacology of TNF blockade in rheumatoid arthritis and other chronic inflammatory diseases. Curr Opin Pharmacol 10: 308-315.

24. Furst DE, Wallis R, Broder M, Beenhouwer DO (2006) Tumor necrosis factor antagonists: Different kinetics and/or mechanisms of action may explain differences in the risk for developing granulomatous infection. Semin Arthritis Rheum 36: 159-167.

25. Plessner HL, Lin PL, Kohno T, Louie JS, Kirschner D, et al. (2007) Neutralization of tumor necrosis factor (TNF) by antibody but not TNF receptor fusion molecule exacerbates chronic murine tuberculosis. J Infect Dis 195: 1643-1650.

26. Marino S, Sud D, Plessner H, Lin PL, Chan J, et al. (2007) Differences in reactivation of tuberculosis induced from anti-TNF treatments are based on bioavailability in granulomatous tissue. PLoS Comput Biol 3: 1909-1924.

27. Tracey D, Klareskog L, Sasso EH, Salfeld JG, Tak PP (2008) Tumor necrosis factor antagonist mechanisms of action: A comprehensive review. Pharmacol Ther 117: 244-279.

28. Kim MS, Lee SH, Song MY, Yoo TH, Lee BK, et al. (2007) Comparative analyses of complex formation and binding sites between human tumor necrosis factor-alpha and its three antagonists elucidate their different neutralizing mechanisms. J Mol Biol 374: 1374-1388.

29. Song MY, Park SK, Kim CS, Yoo TH, Kim B, et al. (2008) Characterization of a novel anti-human TNF-alpha murine monoclonal antibody with high binding affinity and neutralizing activity. Exp Mol Med 40: 35-42.

30. Scallon B, Cai A, Solowski N, Rosenberg A, Song XY, et al. (2002) Binding and functional comparisons of two types of tumor necrosis factor antagonists. J Pharmacol Exp Ther 301: 418-426.

31. Fallahi-Sichani M, Schaller MA, Kirschner DE, Kunkel SL, Linderman JJ (2010) Identification of key processes that control tumor necrosis factor availability in a tuberculosis granuloma. PLoS Comput Biol 6: e1000778.

32. Mitoma H, Horiuchi T, Tsukamoto H, Tamimoto Y, Kimoto Y, et al. (2008) Mechanisms for cytotoxic effects of anti-tumor necrosis factor agents on transmembrane tumor necrosis factor alpha-expressing cells: Comparison among infliximab, etanercept, and adalimumab. Arthritis Rheum 58: 1248-1257.

33. Fossati G, Nesbitt AM (2005) Effect of the anti-TNF agents, adalimumab, etanercept, infliximab, and certolizumab pegol (CDP870) on the induction of apoptosis in activated peripheral blood lymphocytes and monocytes. Am J Gastroenterol 100: S298-S299.

34. Fossati G, Nesbitt AM (2005) In vitro complement-dependent cytotoxicity and antibody-dependent cellular cytotoxicity by the anti-TNF agents adalimumab, etanercept, infliximab, and certolizumab pegol (CDP870). Am J Gastroenterol 100: S299.

35. Nestorov I (2005) Clinical pharmacokinetics of TNF antagonists: How do they differ?. Semin Arthritis Rheum 34: 12-18.

36. Segovia-Juarez JL, Ganguli S, Kirschner D (2004) Identifying control mechanisms of granuloma formation during M. tuberculosis infection using an agent-based model. J Theor Biol 231: 357-376.

37. Saunders BM, Tran S, Ruuls S, Sedgwick JD, Briscoe H, et al. (2005) Transmembrane TNF is sufficient to initiate cell migration and granuloma formation and provide acute, but not long-term, control of mycobacterium tuberculosis infection. J Immunol 174: 4852-4859.

38. Olleros ML, Guler R, Vesin D, Parapanov R, Marchal G, et al. (2005) Contribution of transmembrane tumor necrosis factor to host defense against mycobacterium bovis bacillus calmette-guerin and mycobacterium tuberculosis infections. Am J Pathol 166: 1109-1120.

39. St Clair EW, Wagner CL, Fasanmade AA, Wang B, Schaible T, et al. (2002) The relationship of serum infliximab concentrations to clinical improvement in rheumatoid arthritis: Results from ATTRACT, a multicenter, randomized, double-blind, placebo-controlled trial. Arthritis Rheum 46: 1451-1459.

40. Menart V, Gaberc-Porekar V, Jevsevar S, Pernus M, Meager A, et al. (2000) Early events in TNFa-p55 receptor interations--experiments with TNF dimers. Pflugers Arch 439: R113-5.

41. Corti A, Fassina G, Marcucci F, Barbanti E, Cassani G (1992) Oligomeric tumour necrosis factor alpha slowly converts into inactive forms at bioactive levels. Biochem J 284 (Pt 3): 905-910.

42. Dinarello CA (2005) Differences between anti-tumor necrosis factor-alpha monoclonal antibodies and soluble TNF receptors in host defense impairment. J Rheumatol Suppl 74: 40-47.

43. Keane J, Remold HG, Kornfeld H (2000) Virulent mycobacterium tuberculosis strains evade apoptosis of infected alveolar macrophages. J Immunol 164: 2016-2020.

44. Oddo M, Renno T, Attinger A, Bakker T, MacDonald HR, et al. (1998) Fas ligand-induced apoptosis of infected human macrophages reduces the viability of intracellular mycobacterium tuberculosis. J Immunol 160: 5448-5454.

45. O'Sullivan MP, O'Leary S, Kelly DM, Keane J (2007) A caspase-independent pathway mediates macrophage cell death in response to mycobacterium tuberculosis infection. Infect Immun 75: 1984-1993.

46. Kelly DM, ten Bokum AM, O'Leary SM, O'Sullivan MP, Keane J (2008) Bystander macrophage apoptosis after mycobacterium tuberculosis H37Ra infection. Infect Immun 76: 351-360.

47. Lauffenburger D, Linderman JJ (1993) Receptors: models for binding, trafficking, and signaling. New York: Oxford University Press.

48. Lobo ED, Hansen RJ, Balthasar JP (2004) Antibody pharmacokinetics and pharmacodynamics. J Pharm Sci 93: 2645-2668.

49. Bruns H, Meinken C, Schauenberg P, Harter G, Kern P, et al. (2009) Anti-TNF immunotherapy reduces CD8+ T cell-mediated antimicrobial activity against mycobacterium tuberculosis in humans. J Clin Invest 119: 1167-1177.

50. Lin PL, Rodgers M, Smith L, Bigbee M, Myers A, et al. (2009) Quantitative comparison of active and latent tuberculosis in the cynomolgus macaque model. Infect Immun 77: 4631-4642.

Chapter 7

Lipid raft-mediated regulation of G-protein coupled receptor signaling by ligands which influence receptor dimerization: A computational study

7.1 Introduction

G-protein coupled receptors (GPCRs) play an important role in signal transduction and are encoded by more than 1000 genes in the human genome [1]. It is estimated that more than 50% of pharmaceuticals target GPCRs, leading to initiation or blockage of a signaling cascade that results in a cell response [2]. When stimulated by their specific ligands, GPCRs activate heterotrimeric G-proteins on the cell membrane, inducing GDP-GTP exchange and formation of the GTP-bound Gα-subunit and release of the Gβγ-dimer. These G-protein subunits then activate specific secondary effectors, leading to distinct biological functions. The ligand-bound GPCR can be desensitized by a mechanism which involves receptor phosphorylation by G-protein receptor kinase (GRK) and internalization of the receptor followed by either recycling or degradation [3]. Much research is underway to determine the mechanisms by which GPCR signaling is regulated. Here we focus on understanding factors that influence GPCR organization on the cell membrane and how such organization can influence GPCR signaling.

Two mechanisms that affect receptor organization on the cell membrane have been proposed. First, many GPCRs have been shown to form homo- and/or hetero-dimers/oligomers on the cell membrane [1, 4], although the role of such dimer/oligomer

formation in GPCR signaling is unclear [5-9]. Using a computational model, we recently demonstrated that reversible dimerization of receptors under the diffusion-limited conditions typical of membrane-localized reactions can influence receptor organization [10]. Depending on the values of the dimerization and monomerization rate constants, receptors can be organized in different ways on the two-dimensional surface of the cell. The monomer regime is observed when the rate of receptor monomerization is much greater than the dimerization rate. In the dimer regime, the rate of dimerization is much greater than the monomerization rate. However, when both receptor dimerization and monomerization are fast, "partner switching", i.e. alternating of bonds between neighboring receptors, occurs quickly, leading to the formation of oligomer-like clusters of receptors on the cell membrane (oligomer regime) (Appendix E (Fig. E.1)). Some GPCRs undergo ligand-induced dimerization, while ligand stimulation has either no effect or decreases the level of dimerization in others [4, 11]. Therefore, dimerization-mediated organization of receptors can be affected differently by ligand stimulation.

As a second mechanism of receptor organization, many GPCRs become localized in membrane microdomains, including lipid rafts and caveolae. Lipid rafts are regions of elevated cholesterol and glycosphingolipid content, greater order, and less fluidity within cell membrane [12]. Caveolae are lipid rafts with flask-shaped structures and are distinguished from flat-shaped lipid rafts by the presence of the cholesterol-binding protein caveolin [12]. It has been reported that membrane proteins with at least one transmembrane domain or with a hydrophobic modification are enriched in lipid rafts [13]. Lipid raft-associated proteins diffuse more slowly inside lipid rafts than in non-raft regions, probably due to the tight packing of lipids which leads to a higher local viscous

drag on raft proteins [14]. In the simplest model proposed for the role of lipid rafts in GPCR signaling, lipid rafts are viewed as signaling platforms that facilitate interaction of different molecules involved in a specific signaling pathway with a higher density [15]. Compartmentalization of signaling molecules may lead to an increase in activation because of an increased collision frequency between the species [16]. This model may also enhance the specificity of signaling (i.e. reduce crosstalk) when localization of receptors is restricted to a particular class of rafts or when some receptor species are excluded from domains containing other receptor species, although the data on this point are not conclusive [17].

Although dimerization and lipid raft-localization have individually been identified as mechanisms that influence GPCR organization on the cell membrane, some reports have also indicated that localization of membrane proteins in lipid rafts can be affected by their dimerization [18, 19]. This suggests that these two mechanisms of receptor localization must be considered together to understand GPCR localization on the cell surface. We developed a computational model describing GPCR organization on the cell membrane and G-protein activation by ligand-bound receptors. We use our model to answer the following questions: Is GPCR localization in microdomains influenced by dimerization? Why do some GPCRs move into lipid rafts following ligand binding [20-22] while others move out of lipid rafts [23, 24] or are not affected [23]? How does GPCR localization in microdomains affect signaling? Why does lipid raft disruption amplify G-protein signaling in some cells but attenuate it in others [24, 25]? Our results suggest that lipid rafts and GPCR dimerization together provide a mechanism by which the cell can regulate G-protein signaling.

7.2 Methods

To describe GPCR organization on the cell membrane due to dimerization and lipid raft partitioning and the effect of that organization on GPCR signaling, two separate models were used (Fig. 7.1). First, a kinetic Monte Carlo (MC) model was developed to determine the effect of a ligand-induced change in the dimerization status of receptors on localization within low-diffusivity microdomains (lipid rafts) on the cell surface and to estimate the time-scale and level of receptor clustering and declustering. An MC framework allows examination of the roles of stochastic effects and partner switching in receptor organization and quantification of non-homogeneous receptor distributions in membrane microdomains. Second, an ordinary differential equation (ODE) model based on the collision coupling model [26, 27] was developed for studying the effect of receptor localization within lipid rafts on downstream signaling events. Linking this simple model to the MC model allows us to study and analyze G-protein activation while incorporating the effects of receptor organization; continuing to use the MC method for the activation part of the problem adds substantial computational time and complicates the sensitivity analysis without significant benefit. MC and ODE models and their inputs and outputs are linked as depicted in Fig. 7.1.

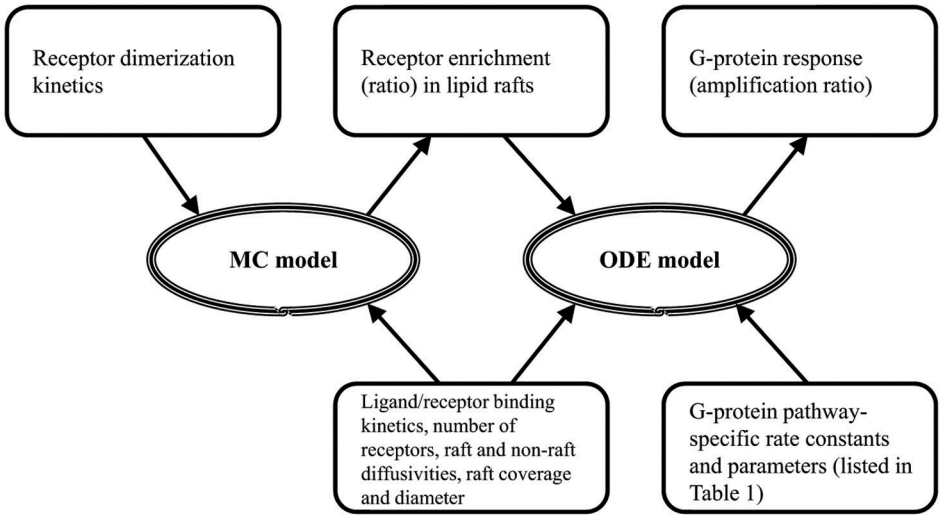

Fig. 7.1 Schematic showing the relationship between the Monte Carlo (MC) model of receptor dimerization and localization and the ordinary differential equation (ODE) model of G-protein signaling. Input parameters are shown by arrows pointing toward the models. Model outputs are shown by arrows pointing away from the models.

7.2.1 Monte Carlo model for receptor dimerization and localization

A two-dimensional lattice was used to represent the cell membrane and cell surface molecules. Simulations were run on a 700 by 700 triangular lattice with periodic boundary conditions and a lattice spacing of 0.5 nm. To simulate lipid rafts, we assigned low diffusivity regions with uniform distribution and defined surface area (2-30% of the cell membrane) as raft regions on the lattice. The diameter of simulated lipid rafts was varied from 20-50 nm in different simulations. The range of parameters for raft coverage and diameter is consistent with a variety of experimental data [13, 14, 28-31].

The lattice contained receptor molecules simulated as hexagons with a diameter of 5 nm, the approximate diameter of a single GPCR (Fig. 7.2A). Receptor movement and dimerization was simulated using the algorithm presented by Woolf and Linderman [10]. Briefly, receptors were chosen at random to dimerize with a neighbor, dissociate from a dimerized pair, or diffuse in the plane of the membrane. If the chosen action was a

dimerization event, the receptor was first tested to be a monomer. Then, a random neighboring receptor within the "interaction radius" of 5 lattice spacings (2.5 nm) was chosen as a binding partner. If the binding partner was also a monomer, dimerization was allowed with probability P_{dimer}. If the chosen action was a monomerization event and the receptor was part of a dimer, then monomerization was allowed with probability P_{mono}. The probabilities of these reactions are derived from the intrinsic reaction rate constants (k_{dimer}, k_{mono}). For a diffusion event, receptors moved a single lattice space in a random direction with a probability calculated from the translational diffusion coefficient, D, of the protein on the cell membrane. As a result of these diffusion rules, individual receptors move with approximately the same diffusion coefficient regardless of their dimerization state, which is consistent with theoretical findings that show the diffusion is only a weak function of particle radius [32].

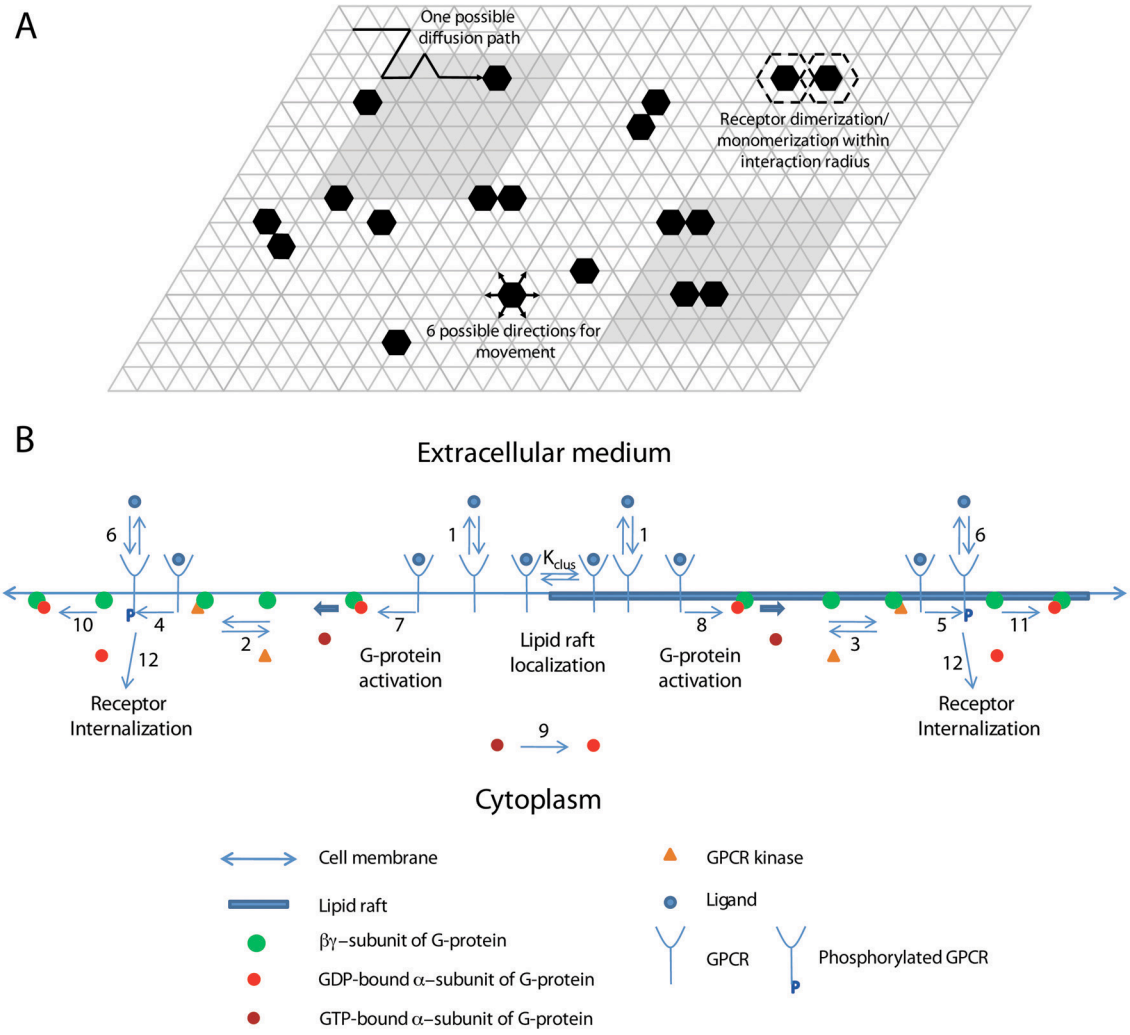

Fig. 7.2 Schematic representation of the structure of the model: (A) the Monte Carlo model of receptor dimerization and localization and a section of the lattice simulating the cell membrane, and (B) the ODE model of G-protein coupled receptor signaling. Black hexagons and gray squares in (A) represent receptors and lipid rafts, respectively. One lattice spacing here is equivalent to 10 real simulation lattice spacings. The ODE model shown in (B) includes ligand binding, ligand-induced lipid raft partitioning of receptors, G-protein activation by receptor-ligand complex, receptor phosphorylation by GPCR kinase, and receptor internalization. Numbers represent model reactions as listed in Table 7.2. Clustering equilibrium constant K_{clus} is determined by MC simulations and characterizes receptor enrichment in lipid rafts.

In order to study the effect of ligand binding, simulations were run to equilibrium for unligated receptors with specified probabilities of dimerization and monomerization. Ligand at a particular concentration was then added. Receptor/ligand association and dissociation reaction probabilities were calculated based on ligand concentration,

receptor/ligand association and dissociation rate constants [33]. Ligand-bound receptors were assumed to participate in dimerization and monomerization reactions with different probabilities from unligated receptors. A more detailed description of the MC simulation procedure is presented in Appendix E.

To express the level of receptor localization in lipid rafts, we defined the "*enrichment ratio*" as the ratio of the equilibrated number of receptors in lipid rafts over the number of receptors in lipid rafts when receptors are randomly distributed on the cell surface. The enrichment ratio was measured in 1000 simulation runs for each set of parameters and averaged.

Parameter values used in the simulations are listed in Table 7.1. The intrinsic rate constant for receptor dimerization, k_{dimer}, describes binding that occurs *after* diffusion has brought two receptors close together. In previous work, we estimated the value of k_{dimer} to be on the order of 105 s^{-1} by using the GPCR rotational diffusion coefficient of 2.7×10^5 s^{-1} [32]; a similar value of 10^4 s^{-1} has been used for dimerization of the epidermal growth factor receptor [34, 35]. Although our MC simulations account for diffusion explicitly by allowing receptors to move among lattice sites, one can also estimate a rate constant k_+ for the transport (via diffusion) of one receptor to another (from $k_+ = 2\pi D/\ln(b/s)$ where D is the translational diffusion coefficient of receptors in the cell membrane, b is one-half the mean distance between receptors, and s is the encounter radius between two monomeric receptors [26]) of 10^3-10^5 s^{-1}. k_+ is thus likely less than or of the same order as k_{dimer}, suggesting a diffusion-limited or partially diffusion-controlled reaction in the membrane [26] for which MC simulations are well-suited. Values for the intrinsic monomerization rate constant (k_{mono}) similar to k_{dimer} are used, consistent with other work

[34]. Diffusivity (D) was assumed to be in the range of 10^{-10}-10^{-9} cm^2/s for non-raft regions and 10^{-12}-10^{-11} cm^2/s for low-diffusivity raft regions on the cell surface. These values are consistent with the lower and upper limits of cell membrane diffusivity for membrane receptors [26, 36, 37]. The simulation time step was chosen such that the probability of the most likely event was ~20%. Simulations were run with 100-1000 particles corresponding to a surface coverage of 1.8-18%. This range of receptor density is consistent with the density of GPCRs that form homo- and hetero-dimers on the membrane of different cell lines used in G-protein signaling experiments [38].

Table 7.1 Model parameter values

MC model

Parameter	Definition	Value	Reference
k_{dimer} (s^{-1}) *	Receptor dimerization rate constant	10^3-10^7	[10, 34]
k_{mono} (s^{-1})	Receptor monomerization rate constant	10^3-10^7	[10, 34]
k_f ($M^{-1}s^{-1}$)	Ligand/receptor association rate constant	10^8	[26, 52]
k_r (s^{-1})	Ligand/receptor dissociation rate constant	1	[52]
D_{raft} (cm^2/s)	Membrane diffusivity in the raft region	10^{-12}-10^{-11}	[14, 26, 36, 37]
$D_{non\text{-}raft}$ (cm^2/s)	Membrane diffusivity in the non-raft region	10^{-10}-10^{-9}	[14, 26, 36, 37]
R (%)	Lipid raft coverage	2-30	[13, 14, 28, 30, 31]
d (nm)	Lipid raft diameter	20-50	[13, 14, 28, 30, 31]

ODE model

Parameter	Definition	Value †	Reference
k_f ($M^{-1}s^{-1}$)	Ligand/receptor association rate constant	10^7-10^8 (10^8)	[26, 52]
k_r (s^{-1})	Ligand/receptor dissociation rate constant	0.1-1 (1)	[52]
k_f' ($M^{-1}s^{-1}$)	Ligand/phosphorylated receptor association rate constant	10^6-10^9 (10^8)	[52]
k_r' (s^{-1})	Ligand/phosphorylated receptor dissociation rate constant	0.001-0.005 (0.002)	[52]
k_{on} ($M^{-1}s^{-1}$)	Receptor/kinase association rate constant	10^9-10^{11} (10^{11})	[52]
k_{off} (s^{-1})	Receptor/kinase dissociation rate constant	10-100 (25)	[52]
k_{int} (s^{-1})	Receptor internalization rate constant	10^{-4}-10^{-1} (10^{-2})	[52, 74]
k_{rec} ($M^{-1}s^{-1}$)	G-protein recombination rate constant	6×10^9-6×10^{11} (1.6×10^{10})	[52]
k_{hyd} (s^{-1})	GTP hydrolysis rate constant	0.02-30	[70, 75-77]
R_{tot} (#/cell)	Total number of cell surface receptors	5×10^4-5×10^5 (2.5×10^5)	[52]
G_{tot} (#/cell)	Total number of G-proteins	10^4-10^5 (7.5×10^4)	[52]
$[L]/K_d$	Scaled ligand concentration	0.1-10	
RK_{tot} (M)	Total concentration of GPCR kinase	1.5×10^{-9}-3×10^{-9} (3×10^{-9})	[52]
r	Relative G-protein density	0.02-0.8	
$D_{non\text{-}raft}$ (cm^2/s)	Membrane diffusivity in the non-raft region	10^{-10}-10^{-9} (10^{-10})	
k_c, k_c' ($M^{-1}s^{-1}$)	G-protein activation rate constant	Computed from Equation (1)	
K_{clus}	Clustering equilibrium constant	Found from MC simulation	
k_p, k_p' ($M^{-1}s^{-1}$)	Receptor phosphorylation rate constant	Computed similarly to k_c and k_c'	
$D_{non\text{-}raft}/D_{raft}$	Ratio of non-raft diffusivity to lipid raft diffusivity	10	

* k_{dimer} is an intrinsic rate constant, meaning that it describes the rate at which binding takes place after diffusion has brought the proteins within reaction range.

† Ranges of parameters shown for the first 15 parameters (all independent) are used for sensitivity analysis. Values in parentheses are used to generate model results shown in Fig. 7.6-8.

7.2.2 ODE Model for GPCR signaling

Our model for GPCR signaling incorporates ligand binding, lipid raft partitioning of receptors due to ligand binding (i.e. the enrichment ratio as determined by the MC model), G-protein activation by receptor-ligand complexes (both within and outside of lipid rafts), receptor phosphorylation by GPCR kinase, and receptor internalization as

shown in Fig. 7.2B. G-proteins were assumed to be highly enriched in membrane microdomains (lipid rafts and caveolae) and did not translocate into/out of them during the time course of simulation. This assumption is based on a variety of experiments showing (more than 10-fold) enrichment of G-proteins in membrane microdomains and preferential interaction of G-proteins with microdomain-specific proteins such as caveolin [13, 39-44]. Phosphorylated receptors were considered to be desensitized. The reactions and equations to describe the ODE model are listed in Table 7.2. Definitions and values of parameters are given in Table 7.1. The ligand concentration, [L], was assumed to remain constant (no depletion). Equations were solved numerically using MATLAB 7.5 (The MathWorks, Natick, MA).

Table 7.2 Description of the reaction species, reactions and equations of the ODE model

Reaction species

L	Ligand	G_{clus}	Trimeric G-protein in the raft region
R	G-protein coupled receptor	$(\beta\gamma)_{clus}$	βγ-subunit of G-protein in the raft region
LR	Ligand/receptor complex	RK	GPCR kinase
LR_{scat}	Ligand/receptor complex in the non-raft region	$LR\text{-}P$	Phosphorylated ligand-bound receptor
LR_{clus}	Ligand/receptor complex in the raft region	$R\text{-}P$	Phosphorylated receptor
G_{scat}	Trimeric G-protein in the non-raft region	LR_i	Internalized ligand-bound receptor
$\alpha\text{-}GTP$	GTP-bound (active) α-subunit of G-protein	$\alpha\text{-}GDP$	GDP-bound α-subunit of G-protein
$(\beta\gamma)_{scat}$	βγ-subunit of G-protein in the non-raft region		

ODE model reactions and flux expressions

1	$L + R \leftrightarrow LR$ $v_1 = k_f[L][R] - k_r[LR]$	7	$[LR_{scat}]$: $G_{scat} \rightarrow \alpha\text{-}GTP + \beta\gamma_{scat}$ $v_7 = k_c[LR_{scat}][G_{scat}]$
2	$\beta\gamma_{scat} + RK \leftrightarrow \beta\gamma\text{-}RK_{scat}$ $v_2 = k_{on}[\beta\gamma_{scat}][RK] - k_{off}[\beta\gamma - RK_{scat}]$	8	$[LR_{clus}]$: $G_{clus} \rightarrow \alpha\text{-}GTP + \beta\gamma_{clus}$ $v_8 = k_c'[LR_{clus}][G_{clus}]$
3	$\beta\gamma_{clus} + RK \leftrightarrow \beta\gamma\text{-}RK_{clus}$ $v_3 = k_{on}[\beta\gamma_{clus}][RK] - k_{off}[\beta\gamma - RK_{clus}]$	9	$\alpha\text{-}GTP \rightarrow \alpha\text{-}GDP$ $v_9 = k_{hyd}[\alpha - GTP]$
4	$[\beta\gamma\text{-}RK_{scat}]$: $LR_{scat} \rightarrow LR\text{-}P_{scat}$ $v_4 = k_p[LR_{scat}][\beta\gamma - RK_{scat}]$	10	$\alpha\text{-}GDP + \beta\gamma_{scat} \rightarrow G_{scat}$ $v_{10} = k_{rec}[\alpha - GDP][\beta\gamma_{scat}]$
5	$[\beta\gamma\text{-}RK_{clus}]$: $LR_{clus} \rightarrow LR\text{-}P_{clus}$ $v_5 = k_p'[LR_{clus}][\beta\gamma - RK_{clus}]$	11	$\alpha\text{-}GDP + \beta\gamma_{clus} \rightarrow G_{clus}$ $v_{11} = k_{rec}[\alpha - GDP][\beta\gamma_{clus}]$
6	$L + R\text{-}P \leftrightarrow LR\text{-}P$ $v_6 = k_f'[L][R-P] - k_r'[LR-P]$	12	$LR\text{-}P \rightarrow LR_i$ $v_{12} = k_{\text{int}}[LR-P]$

ODE model equations

$$\frac{d[R]}{dt} = -v_1$$

$$\frac{d[LR]}{dt} = v_1 - v_4 - v_5$$

$$\frac{d[\beta\gamma - RK_{scat}]}{dt} = v_2$$

$$\frac{d[LR-P]}{dt} = v_4 + v_5 + v_6 - v_{12}$$

$$\frac{d[R-P]}{dt} = -v_6$$

$$[LR_{scat}] = (1/(1+K_{clus}))[LR]$$

$$\frac{d[G_{scat}]}{dt} = -v_7 + v_{10}$$

$$\frac{d[\alpha - GTP]}{dt} = v_7 + v_8 - v_9$$

$$\frac{d[\alpha - GDP]}{dt} = v_9 - v_{10} - v_{11}$$

$$\frac{d[LR_i]}{dt} = v_{12}$$

$$\frac{d[RK]}{dt} = -v_2 - v_3$$

$$[LR_{clus}] = (K_{clus}/(1+K_{clus}))[LR]$$

$$\frac{d[\beta\gamma_{clus}]}{dt} = -v_3 + v_8 - v_{11}$$

$$\frac{d[G_{clus}]}{dt} = -v_8 + v_{11}$$

$$[LR-P] = [LR-P_{scat}] + [LR-P_{clus}]$$

$$\frac{d[\beta\gamma - RK_{clus}]}{dt} = v_3$$

$$\frac{d[\beta\gamma_{scat}]}{dt} = -v_2 + v_7 - v_{10}$$

G-protein activation and receptor phosphorylation were assumed to be diffusion-limited reactions in the membrane [45]. The rate constants for diffusion-limited activation of G-protein by receptor/ligand complex were estimated separately for the non-raft and raft regions using [26]:

$$k_c = \frac{2\pi D}{\ln(b/s)}, \quad \text{where } b = \sqrt{\frac{A}{\pi[G(t)]}} \tag{7.1}$$

where D is the diffusion coefficient, b is half of the mean separation distance between reactants, s is the encounter radius, A is the surface area of the raft or non-raft region, and $[G(t)]$ is the time-dependent inactive G-protein concentration ($[G_{clus}(t)]$ in the raft and $[G_{scat}(t)]$ in the non-raft region as defined in Table 7.2). This estimation is based on the assumption that reactants are well-mixed on the surface of the raft or non-raft regions, while they have different concentrations in each region. If the reactants are locally enriched or depleted in one area, the well-mixed assumption may not be realistic and can be more accurately determined by MC simulations [16, 46]. However, these estimations are similar for the situations described here. The rate constant for receptor phosphorylation was similarly estimated for the raft and non-raft regions. We assumed the total surface area of a cell and the encounter radius, s, to be 1000 μm^2 and 10 nm respectively. The surface area of the raft and non-raft regions was determined from the raft diameter and the total raft coverage.

The distribution of G-proteins may influence the way in which lipid rafts contribute to GPCR signaling. In order to express the pattern of G-protein distribution on the cell membrane (which is not varied over the time course of one simulation), relative G-protein density (r) was defined as the ratio of number of (active and inactive) G-proteins in lipid rafts over the total number of G-proteins in the membrane ($G_{clus}|_{t=0} = r \times G_{tot}$ and $G_{scat}|_{t=0} = (1-r) \times G_{tot}$). Thus, r determines the available amount of G-protein for signaling in the raft and non-raft regions. Further, to understand how receptor localization within lipid rafts influences G-protein signaling, the maximum level of G-protein activation was measured as the response in different simulations. This level was used to produce dose-response curves. We defined the "*amplification ratio*" as the ratio of the

maximum level of G-protein activation in the presence of lipid rafts to that in the absence of lipid rafts. Amplification ratio values of more than one show that the presence of lipid rafts leads to signal amplification. Amplification ratio values of less than one show that G-protein signal is attenuated by lipid rafts.

7.2.3 Sensitivity Analysis

Parameter sensitivity of the MC model output (enrichment ratio) was explored by changing input parameters within the ranges specified in Table 7.1. To identify parameters that significantly influence the outcome of lipid raft-mediated G-protein signaling (signal amplification or attenuation, as calculated by the ODE model), we used Latin hypercube sampling (LHS) [47] to sample values of 15 parameters from the ranges listed in Table 7.1. A logarithmic distribution was used for ligand concentration and uniform distributions were used for other parameters. Simulations sampled each parameter 1000 times, producing 1000 solutions to the model equations. To determine the correlation between parameter values and the model outcome, amplification ratio, partial rank correlation coefficient (PRCC) values were calculated. PRCC values vary between -1 (perfect negative correlation) and 1 (perfect positive correlation) and can be differentiated based on *p*-values derived from Student's *t* test. Fisher's *z* test was performed to assess if two PRCC values are significantly different from each other [48].

7.3 Results and Discussion

7.3.1 Receptor localization within lipid rafts can be controlled by dimerization

To understand whether localization of membrane receptors into low-diffusivity microdomains (lipid rafts) on the cell surface is influenced by receptor dimerization, MC simulations were run for different values of the rate constants for receptor dimerization and monomerization, assuming diffusion of particles is reduced in specified regions (lipid rafts) on the lattice. When simulations were run with a small value of the ratio k_{dimer}/k_{mono}, the monomer regime was observed, driving the equilibrium toward translocation of receptors into lipid rafts (Fig. 7.3A). This is consistent with a recent model describing motion of monomeric particles on a cell membrane including low-diffusivity lipid rafts [49, 50]. When the ratio k_{dimer}/k_{mono} was large, the dimer regime was observed, and receptors still translocated into lipid rafts (Fig. 7.3B). Particles (either dimeric or monomeric receptors) in the dimer or monomer regimes move almost independently on the surface. Existence of low-diffusivity regions on such a surface can limit particle movements, leading to crowding of receptors in these regions.

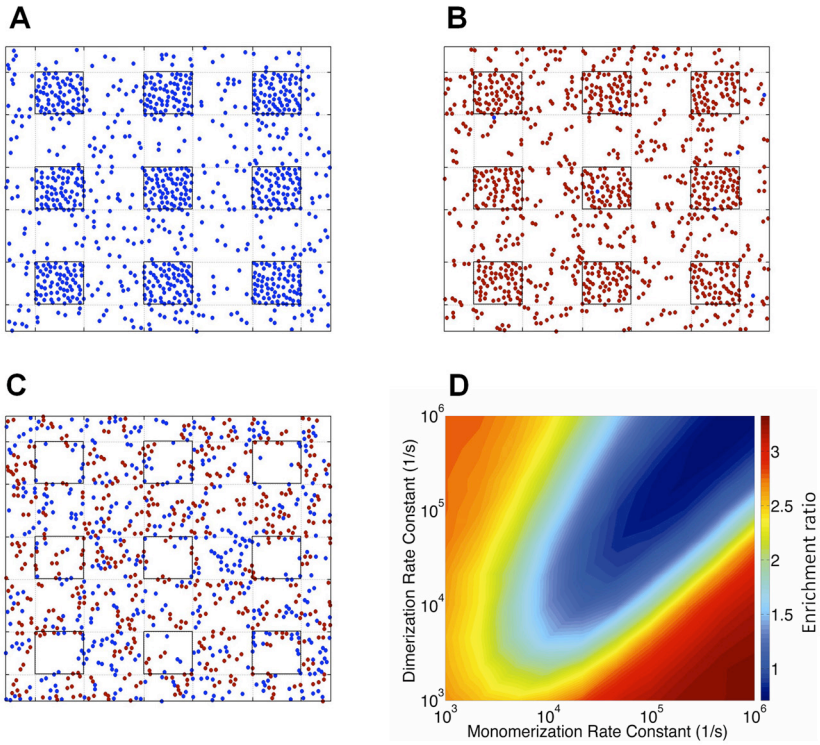

Fig. 7.3 Model-generated organization (snapshots) of receptors diffusing on a cell membrane with low-diffusivity microdomains (lipid rafts): (A) monomer regime ($k_{mono} = 10^6$ s^{-1}, $k_{dimer} = 10^3$ s^{-1}), (B) dimer regime ($k_{mono} = 10^3$ s^{-1}, $k_{dimer} = 10^6$ s^{-1}), and (C) oligomer regime ($k_{mono} = 10^6$ s^{-1}, $k_{dimer} = 10^6$ s^{-1}). Lipid raft regions are shown as nine small squares. Monomers and dimers are shown with blue and brown dots respectively. (D) The predicted enrichment ratio varies with k_{mono} and k_{dimer}. Diffusion coefficients in lipid raft and non-raft regions for A-D were set to 10^{-12} and 10^{-10} cm^2/s respectively. Simulation results with other values of diffusivity are shown in Fig. E.3 in Appendix E. Simulations were run to equilibrium with receptor density of 18%. In this set of simulations, rafts make up 20% of the simulated membrane and the raft diameter is 50 nm.

Between the two extremes (very large and very small values of the ratio k_{dimer}/k_{mono}), receptors on the cell surface are ordered in oligomer-like structures via the partner switching mechanism (recall Fig. E.1 in Appendix E). Interestingly, the equilibrium lipid raft concentration of receptors in the oligomer regime is lower than in the monomer and dimer regimes (Fig. 7.3C). In the oligomer regime, movements of particles can be affected by interactions which are due to the fast dimerization and monomerization reactions. This leads to the formation of oligomer-like structures of receptors which can move together. To test this, an average interaction time was defined

as the time two randomly selected interacting particles (either dimer or monomer) spent at a distance of not longer than the previously defined interaction radius from each other, normalized to the time that all particles move on average one lattice spacing. The average interaction time was measured for different regimes in different simulations, and for the oligomer regime was shown to be up to 4 times greater than the monomer or dimer regimes, depending on diffusion conditions, receptor concentration and the rates of receptor dimerization and monomerization (Appendix E (Fig. E.2)). This suggests that receptors in a cluster in the oligomer regime move together on the cell surface. Larger clusters are formed in more diffusion-limited conditions [10]. When the cell surface is composed of two distinct regions, one with lower diffusivity (raft region) and one with higher diffusivity (non-raft region), small receptor clusters formed in the high-diffusivity region may enter the low-diffusivity region. Similarly, larger receptor clusters formed in the low-diffusivity region may enter the high-diffusivity region. At equilibrium, this leads to a lower receptor concentration in the low-diffusivity region (Figure 7.3C). Thus dimerization status influences the localization of GPCRs in lipid rafts.

7.3.2 Enrichment of receptors in lipid rafts depends on receptor dimerization kinetics and membrane diffusivity

Receptor enrichment in lipid rafts (as defined in Methods) was chosen as a simple metric to study the combined effects of low-diffusivity lipid rafts and receptor dimerization on organization of receptors on the cell membrane. Fig. 7.3D shows the simulation results for variation of the enrichment ratio with dimerization and monomerization rate constants given different values of diffusivity in lipid rafts and non-raft regions of the cell

membrane. The minimum enrichment ratio is observed when dimerization and monomerization rates are both large compared to the rate of diffusion and have the similar order of magnitudes (oligomer regime, Fig 7.3C). However, when $k_{dimer} >> k_{mono}$ (dimer regime, Fig. 7.3B) or $k_{dimer} << k_{mono}$ (monomer regime, Fig. 7.3A), receptors instead tend to translocate into lipid rafts. Significantly, we predict that the enrichment ratio is a ligand-dependent parameter based on experimental data showing that dimerization status of many GPCRs can be altered by the presence or absence of ligands [4, 11].

Diffusivity of receptors in the raft and non-raft regions also influences the organization of receptors. Comparison of Fig. 7.3D with Fig. E.3 in Appendix E shows that as the difference between diffusivities of lipid rafts and non-raft regions is increased, the difference between the maximum and minimum values of enrichment ratio increases. Furthermore, lower values of diffusivity for raft and non-raft regions favor the raft-leaving of receptors with lower values of dimerization and monomerization rate constants. For example, using a value of 10^{-10} cm^2/s for $D_{non\text{-}raft}$ is sufficient for observing receptor partitioning phenomena in the oligomer regime with an order of magnitude smaller values of k_{dimer} and k_{mono} ($< 10^4$ s^{-1}) compared with the case of $D_{non\text{-}raft} = 10^{-9}$ cm^2/s (compare Fig. 7.3D with Fig. E.3 in Appendix E). Thus partitioning of GPCRs into lipid rafts depends on both dimerization and diffusion rates.

7.3.3 Enrichment of receptors in lipid rafts depends weakly on raft diameter, modestly on total raft area and strongly on the number of receptors

Cell-specific parameters such as raft diameter, raft area, and receptor number may also influence receptor organization. We next examined the effect of the size of a single raft and total lipid raft area on the membrane organization of receptors. Fig. 7.4 indicates simulation results for the range of dimerization-mediated enrichment of receptors in lipid rafts for two distinct numbers of receptors on the cell membrane. Enrichment of receptors in lipid rafts depends weakly on raft diameter. However, total raft area significantly influences the range of dimerization-mediated receptor enrichment in lipid rafts. Fig. 7.4 shows that increasing the area of cell membrane covered by lipid rafts limits the range of variation of enrichment ratio with dimerization and monomerization rate constants. Dependency of receptor enrichment on lipid raft characteristics has a clear biological relevance. Partitioning of receptors with small non-caveolae rafts with a small cell surface coverage and their localization with larger caveolae that occupy 4-35% of the cell membrane area are expected to have different consequences [51].

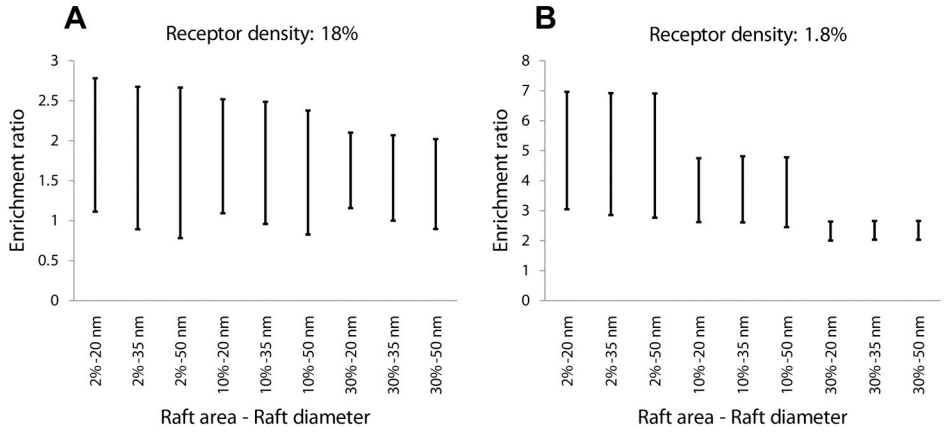

Fig. 7.4 Predicted variation in the enrichment ratio with k_{mono} and k_{dimer} as a function of the total area (as a percentage of the cell membrane area) and diameter of lipid rafts. Results are shown for receptor densities of (A) 18% and (B) 1.8% of the cell surface area. For each pair of raft diameter and raft coverage, k_{mono} and k_{dimer} are varied from 10^4 to 10^7 s^{-1} so as to include monomer, dimer and oligomer regimes. Diffusion coefficients in lipid raft and non-raft regions are 10^{-11} cm^2/s and 10^{-10} cm^2/s respectively.

Decreasing the total number of receptors on the cell membrane leads to a higher enrichment ratio in low-diffusivity raft regions (Fig. 7.4). With fewer receptors, interactions between particles are reduced, leading to the behavior seen for independent particles, i.e. translocation into low diffusivity regions. Thus cell-specific parameters (raft diameter and number, receptor number, diffusivities) as well as ligand-dependent parameters (ability of GPCR to dimerize when bound, or not, by ligand) control GPCR organization or partitioning into lipid raft regions.

7.3.4 Ligand-induced dimerization-mediated partitioning of receptors with lipid rafts is rapid

Dimerization-mediated partitioning of GPCRs into lipid rafts will only be relevant to determining G-protein activation if it occurs quickly. The simulations presented thus far have examined only steady state behavior. To determine how rapidly the effect of ligand-induced changes in dimerization kinetics can result in receptor re-organization on the

membrane, MC simulations were run for different concentrations of ligand, receptor/ligand binding kinetics, and dimerization kinetics. Simulation results indicated that ligand-induced receptor re-organization is rapid compared with ligand binding. One scenario is shown in Fig. 7.5; here rate constants were set such that ligand binding reduced the rate of receptor dimerization and led to an increase in the number of receptors (due to a shift from the oligomer regime to the monomer regime) in lipid rafts. For the simulation shown, lipid raft partitioning of receptors due to ligand binding is rapid, occurring approximately 0.1 s following ligand binding. Thus receptor re-organization occurs quickly enough to be relevant to signaling.

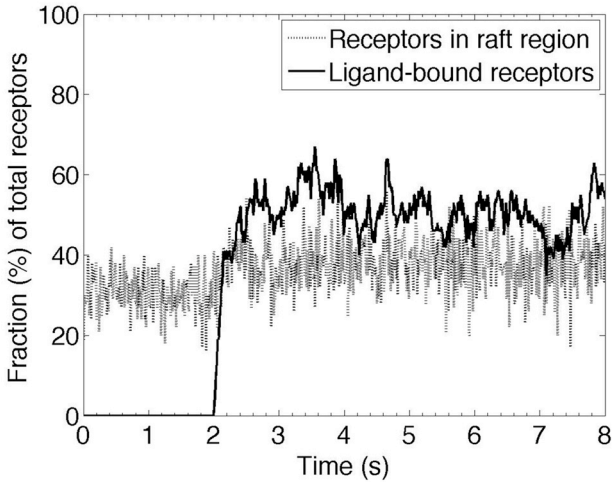

Fig. 7.5 Rapid ligand-induced localization of receptors within lipid rafts due to a ligand-induced change in dimerization kinetics of receptors. Simulation was initiated with randomly distributed receptors on the membrane. Receptors were allowed to equilibrate between monomer and dimer states in the absence of ligand with $k_{mono} = 10^6$ s^{-1} and $k_{dimer} = 10^6$ s^{-1}. Ligand with concentration $[L] = K_d = k_r/k_f$ was then added and simulations continued until a steady state was reached; $k_f = 10^8$ M^{-1}s^{-1} and $k_r = 1$ s^{-1}. Ligand-bound receptors were assumed to have the same monomerization rate constant as the unligated state but k_{dimer} was decreased to 10^4 s^{-1}. Simulations were run on a membrane including lipid rafts with total area of 10% and diameter of 20 nm. Diffusion coefficients in lipid raft and non-raft regions were 10^{-11} cm^2/s and 10^{-10} cm^2/s respectively.

Because receptor re-organization is rapid compared with ligand binding, in later modeling (below) we simply assume that receptor enrichment in lipid rafts following ligand binding can be predicted from the MC model based on the equilibrated

concentration of receptors in the raft region. The alternative approach of fitting the MC simulation results to receptor clustering and declustering reactions and using the estimated rate constants for receptor clustering and declustering in the ODE model gave nearly identical results (data not shown).

7.3.5 G-protein signaling may be amplified or attenuated by lipid rafts

In order to study the effect lipid rafts have on G-protein signaling, predicted values for receptor enrichment in lipid rafts (determined in the MC model) were used in an ODE model for G-protein signaling (Fig. 7.1, 7.2). Sensitivity analysis (see Methods) was used to identify parameters that quantitatively and qualitatively affect the level of G-protein signaling resulting from GPCR binding.

Two regimes of signaling behavior were identified in the model. In the first regime, lipid rafts enhance G-protein signaling. The G-protein activation as a function of time for a specific value of receptor enrichment (enrichment ratio = 4.5) and several different values of the G-protein density in lipid rafts that are 35 nm in diameter and cover 2% of the plasma membrane is shown in Fig. 7.6A. The time course and the level of predicted response are qualitatively consistent with a variety of G-protein signaling experimental and modeling data such as [52, 53], suggesting that our model captures the essential features of GPCR signaling. When receptors are clustered into these relatively small and sparsely distributed lipid rafts following ligand stimulation, increasing the relative density r of G-protein in lipid rafts leads to an increase in the maximum level of response. The highest value of relative G-protein density shown ($r = 0.8$) is consistent with experimental data on G-protein enrichment in lipid rafts [13]. Note that the diffusion

of GPCRs was assumed to be slower in lipid rafts compared to the non-raft region. This has a negative effect on the rate of diffusion-limited G-protein activation by activated ligand-bound receptors in lipid rafts. However, high levels of G-protein enrichment and receptor localization in lipid rafts provide a high density of reactants which can result in signal amplification compared with G-protein signaling without lipid rafts.

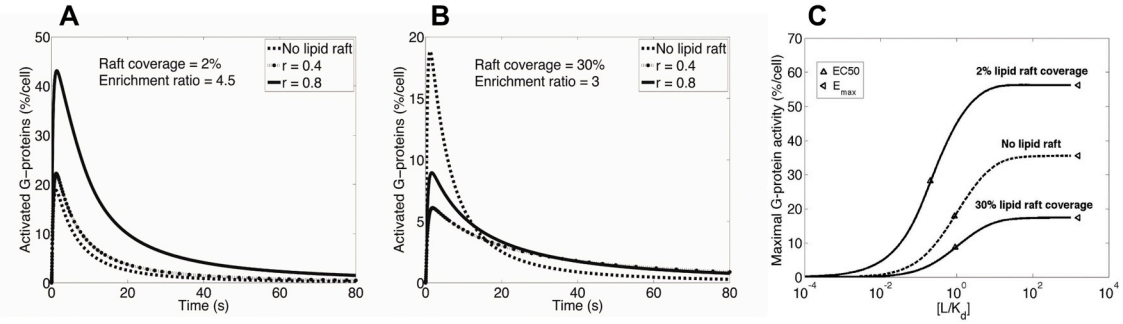

Fig. 7.6 Simulation results for G-protein activation as a function of time at (A) 2% and (B) 30% raft coverage for changing values of *r*, the relative G-protein density in lipid rafts, (C) Simulation results for maximal G-protein activity as a function of scaled ligand concentration for different values of raft coverage. Lines marked "no lipid raft" show the predicted level of G-protein activation in the absence of lipid rafts assuming random distribution of G-proteins on the cell membrane. Although G-protein signaling is attenuated at 30% raft coverage, the rate of termination of the response is smaller compared with no lipid raft condition. This occurs due to reduced rate of (Gβγ-dependent) diffusion-limited phosphorylation (and thus desensitization) of receptors. Magnitudes of the commonly measured pharmacological parameters maximal effect, Emax, and half maximal effective concentration, EC_{50}, are marked in (C). Parameter values are as listed in Table 7.1 with $k_{hyd} = 10\ s^{-1}$ and $[L] = K_d$ in (A) and (B).

In the second regime, lipid rafts attenuate G-protein signaling. This occurs at larger values of lipid raft coverage (Fig. 7.6B). Scatter plots for the effect of G-protein enrichment in lipid rafts (relative G-protein density) on the model outcome, signal amplification ratio, at three levels of lipid raft coverage are indicated in Appendix E (Fig. E.4). These plots (and also Fig. 7.6A, B) show that the amplification ratio significantly depends on lipid raft coverage. As described earlier, the diameter of a single raft and total lipid raft coverage can significantly affect dimerization-mediated localization of receptors in lipid rafts. Further, lipid raft coverage influences lipid raft-mediated G-protein

signaling by controlling the density of membrane signaling molecules in the raft region. As such, signal attenuation (amplification ratio < 1) is the general consequence of the presence of lipid rafts at higher levels of coverage (10 or 30%), where the negative effect of low diffusivity in lipid raft dominates G-protein signaling. However, 2% lipid raft coverage provides a sufficient level of receptor and G-protein enrichment in lipid rafts to amplify G-protein signaling (amplification ratio > 1). In addition, G-protein enrichment in lipid rafts is positively correlated with amplification ratio and this correlation is significantly stronger for 2% lipid raft coverage than 10 or 30% coverage (via Fisher's *z* test).

Experimental studies on the role of lipid rafts in GPCR signal transduction are done indirectly by examining the effect of disruption of lipid rafts by cholesterol depletion using agents such as methyl-β-cyclodextrin on GPCR signaling. Cholesterol depletion generally impairs G-protein mediated signaling, indicating that the presence of lipid rafts enhances G-protein signaling [22, 54, 55]. This effect can be explained by the first regime of signaling behavior in our model. However, in some systems disruption of lipid rafts has a positive effect on GPCR signaling, indicating that G-protein signaling may also be diminished by lipid rafts as explained by the second regime [24, 25, 56, 57]. The effect of lipid raft disruption experiments on the G-protein response can be tracked by comparing the dose-response curves displayed in Fig. 7.6C (and also curves in Fig. 7.6A, B) in the case of no lipid rafts with those in the presence of lipid rafts.

Although the general effect of lipid raft disruption on G-protein signaling (change in the level of response) has been assessed via the experiments referenced above, the significance of different physical processes represented in our model in lipid raft-

mediated G-protein signaling has not been studied. There are other parameters (besides raft coverage) that also affect amplification ratio. Table 7.3 indicates the rank order of PRCC values for model parameters at three levels of lipid raft coverage. Amplification ratio was shown to be influenced by a variety of cell-specific parameters that most importantly include G-protein enrichment in lipid rafts (relative G-protein density, r), GTP hydrolysis rate constant (k_{hyd}), diffusivity ($D_{non\text{-}raft}$), total number of cell surface receptors (R_{tot}) and G-proteins (G_{tot}), as well as ligand concentration (L). Although the parameters that were highly correlated did not differ much between 10% and 30% lipid raft coverage, a significantly distinct pattern of correlation was observed for 2% lipid raft coverage. Ligand concentration, total number of cell surface receptors and diffusivity in non-raft region are parameters that negatively correlate with amplification ratio in G-protein signaling at 2% lipid raft coverage but positively correlate with amplification ratio at higher levels of lipid raft coverage. On the other hand, decreasing the GTP hydrolysis rate constant (k_{hyd}) reduces amplification ratio when lipid rafts cover 2% of the cell membrane but increases amplification ratio when lipid rafts cover 10 or 30% of the cell membrane. Indeed, the four parameters mentioned above all act to strengthen the effect of the presence of lipid rafts on G-protein signaling, so that greater k_{hyd}, for example, induces greater amplification when lipid rafts lead to signal amplification (2% lipid raft coverage), but intensifies signal attenuation when lipid rafts attenuate G-protein signaling (10 or 30% lipid raft coverage).

Table 7.3 Parameters significantly correlated with amplification ratio

2% lipid raft coverage		10% lipid raft coverage		30% lipid raft coverage	
r	0.89	k_{hyd}	-0.65	k_{hyd}	-0.76
G_{tot}	0.59	$D_{non\text{-}raft}$	0.63	$D_{non\text{-}raft}$	0.75
$[L]$	-0.20	r	0.48	r	0.63
k_{hyd}	0.20	R_{tot}	0.46	R_{tot}	0.63
k_{on}	0.20	G_{tot}	0.40	$[L]$	0.48
R_{tot}	-0.19	$[L]$	0.37	k_r	-0.34
k_{rec}	-0.16	k_{on}	0.29	G_{tot}	0.31
$D_{non\text{-}raft}$	-0.12	k_{off}	-0.22	k_{on}	0.19
		k_r	-0.17		
		k_{rec}	-0.12		

PRCC values of model parameters are listed in rank order of correlation. Parameters with significant PRCC values ($p < 0.001$) are listed.

The correlation of GTP hydrolysis rate constant k_{hyd} with amplification ratio suggests a role for RGS proteins in lipid raft-mediated G-protein signaling. RGS proteins enhance GTP hydrolysis, thus reducing the concentration of activated G-protein. However, such enhancement exerts differential effects in the raft and non-raft regions of the membrane. Greater enrichment of reactants in lipid rafts at 2% coverage leads to more rapid re-activation of G-protein following GTP hydrolysis compared with that in the non-raft region or when reactants are randomly distributed on the membrane due to lipid raft disruption. In other words, receptor and G-protein enrichment in lipid rafts but not in the non-raft region compensates for G-protein deactivation by RGS, leading to a larger signal amplification ratio overall. However, at 10 or 30% lipid raft coverage, re-activation of G-proteins in the raft region following GTP hydrolysis is not sufficiently rapid (and is even slower than the non-raft region) to compensate for G-protein deactivation in the presence of RGS. This explains the negative correlation of k_{hyd} with amplification ratio at 10 and 30% lipid raft coverage (see Table 7.3).

7.3.6 Dimerization can act as a tool for regulating GPCR signaling

Taken together, the results presented above demonstrate that dimerization may act to enrich or deplete the number of GPCRs in lipid rafts, and that lipid rafts may serve to either amplify or attenuate G-protein signaling. The effect of ligand-induced receptor dimerization on G-protein signaling is summarized in Fig. 7.7, which includes results from both the MC and the ODE model. The maximum level of G-protein activation (as described by the amplification ratio) depends on receptor enrichment in lipid rafts (enrichment ratio) and receptor enrichment itself can be regulated by ligand-dependent receptor dimerization kinetics. The greatest receptor enrichment in lipid rafts is observed in the monomer regime (when $k_{dimer} << k_{mono}$). Increasing the dimerization rate constant without changing the monomerization rate constant results in a shift from the monomer regime to the oligomer regime. This moves receptors out of lipid rafts, leading to a lower level of response. However, a further increase in the dimerization rate constant to values larger than the monomerization rate constant ($k_{dimer} >> k_{mono}$) shifts receptors to the dimer regime, leading to a greater enrichment in lipid rafts and thus a higher level of response. This pattern is qualitatively similar for G-protein enriched lipid raft-mediated signaling at small and large lipid raft coverage (data not shown). These results indicate that receptor clustering could be used as a tool for regulating GPCR signaling, particularly in the context of G-protein distribution which can also be regulated, for example via priming [58].

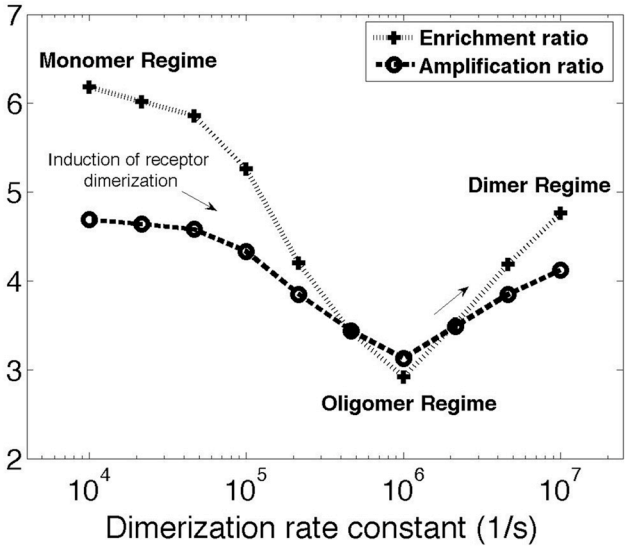

Fig. 7.7 Regulation of the G-protein response by dimerization-mediated enrichment of receptors in lipid rafts. Combination of the results of the Monte Carlo and the ordinary differential equation models are indicated for the effect of ligand-induced receptor dimerization on lipid raft-mediated G-protein signaling at 2% raft coverage. Monomerization rate constant was maintained constant (k_{mono} = 6.7×10^5 s^{-1}). Results are shown for ligand concentration: [L] = 0.1K_d, k_{hyd} = 30 s^{-1}. Membrane diffusivities in the raft and non-raft regions are the same as Fig. 7.6A. Other parameter values are as listed in Table 7.1. The qualitative aspects of this plot are similar for large values of lipid raft coverage, except that the amplification ratio values are less than one.

7.3.7 Modeling results are consistent with unexplained experimental data on receptor distribution and lipid raft-mediated GPCR signaling

We now compare our modeling results with experimental data, beginning first with the predictions of the MC model. As summarized most clearly in Fig. 7.7, in different GPCR systems ligand-induced receptor dimerization can exert opposite effects on the level of receptor enrichment in lipid rafts, depending in large part on the regime (monomer, oligomer and dimer) of unligated receptors. Our finding that a ligand-induced change in dimerization kinetics can cause translocation of receptors into or out of lipid rafts is consistent with unexplained experimental data on GPCRs. For example, δ-opioid receptors have been shown to exist as dimers on the membrane of CHO cells [59], and a majority (approximately 70%) of the receptors on CHO cell membranes are located in

lipid rafts [24]. This is consistent with our model results showing that receptors in the dimer regime translocate into lipid rafts. Further, the level of dimerization is agonist-dependent; increasing concentrations of etorphine reduce the level of receptor dimerization [59]. Etorphine treatment has been shown to move more than 20% of raft-associated receptors out of lipid rafts [24], consistent with our modeling results for shifting from the dimer regime to the oligomer regime. In contrast to etorphine, naloxone, an inverse agonist for δ-opioid receptors, does not affect receptor dimerization [59] and thus our model does not indicate any significant changes in distribution of receptors relative to lipid rafts, consistent with experimental observations [24, 59].

As a second example, although ligand binding has been found to induce dimerization of both β2-adrenergic receptors on Sf9 cells and bradykinin B2 receptors on PC-12 cells [60, 61], it has distinct effects on receptor localization with lipid rafts. While ligand binding causes translocation of the β2-adrenergic receptors out of lipid rafts, it leads to bradykinin B2 receptor clustering in lipid rafts [12]. Our modeling indicates that unligated β2-adrenergic receptors on Sf9 cells are in the monomer regime, while unligated bradykinin B2 receptors on PC-12 cells are in the oligomer regime. In these examples, then, our (MC) model offers explanations for apparently contradictory data on receptor localization from several GPCR systems.

Next, we address the ability of our combined (MC + ODE) model to explain signaling data. Both signal amplification and attenuation have been reported as the effect of lipid rafts on different GPCR signaling systems. This is consistent with our combined (MC + ODE) model results for the influence of lipid raft coverage on the level of G-protein response (Appendix E (Fig. E.4)). For example, disruption of cell membrane lipid

rafts attenuates the δ-opioid receptor-mediated signaling in brain neuronal cells, while enhances it in non-neuronal CHO cells [25]. Neurons in the brain have been demonstrated to be devoid of caveolae, but CHO cell line is a caveolae-rich cell line [24, 25, 62]. Non-caveolae rafts with their small size and cell surface coverage amplify G-protein signaling in neuronal cells, while caveolae with their relatively larger size and membrane coverage may attenuate it in CHO cells.

Recently, a FRET microscopy technique was used to reveal that functional neurokinin 1 receptors expressed in HEK293 cells are monomeric, concentrate in microdomains representing only 0.8-2.5% of the total cell surface area and do not dimerize upon agonist binding [30]. These observations are consistent with results of our MC model showing receptors in the monomer regime reside in lipid rafts. Moreover, our modeling indicates that receptor localization within G-protein enriched lipid rafts with small coverage (~2%) leads to signal amplification, consistent with experimental data on neurokinin 1 receptor signaling in HEK293 cells [63].

Maximal effect (E_{max}) and half maximal effective concentration (EC_{50}) are commonly measured to compare the signaling efficacies of different ligands as well as potency of the ligands under different conditions. We calculated and compared E_{max} and EC_{50} for our model in the presence and absence of lipid rafts (Fig. 7.6C). Both maximal effect and ligand potency increase (over the case of no lipid rafts) when lipid rafts at 2% coverage amplify the G-protein response. On the other hand, when lipid rafts at 30% coverage are compared to the case of no lipid rafts, although maximal effect decreases, EC_{50} is not significantly affected. In agreement with Fig. 7.6C, disruption of lipid rafts (via cholesterol depletion) in systems with small (e.g. 2%) raft coverage has been

observed to be accompanied by a decrease in both maximal effect (E_{max}) and potency of the agonist [24, 63]. Further, cholesterol depletion has been shown to increase the maximal effect without significantly changing ligand potency when lipid raft disruption increases the level of G-protein response that occurs (based on our model) at a high (e.g. 30%) raft coverage [24, 57, 64].

7.3.8 Modeling results can be tested via particular experimental protocols on GPCR signaling systems

Further experiments are required to rigorously test our model. Bioluminescence resonance energy transfer (BRET) and fluorescence resonance energy transfer (FRET) techniques have been used to provide quantitative information on either dimerization status or lateral distribution of receptors (e.g. lipid raft partitioning) in living cells or lipid vesicles [30, 65-67], but the correlation between the two has not yet been studied. Similar experiments that simultaneously examine both dimerization status and receptor distribution following dimerization-inducing/inhibiting treatments (e.g. ligand addition) in multiple GPCR systems are needed and could be compared with results of the MC model (Fig. 7.3 and 7.7).

In addition, our sensitivity analysis findings (Table 7.3) can be used to describe a paradigm to design experiments for testing our G-protein signaling model. The amount of lipid raft coverage, total number of cell surface receptors, GTP hydrolysis rate constant and ligand concentration were shown to affect the amplification ratio. Simulation results for a few experimental protocols based on these findings are described in Fig. 7.8. As noted earlier, distinct results are expected for experiments on membranes with small and

great lipid raft coverage. For example, when lipid rafts amplify G-protein signaling (i.e. lipid rafts cover ~2% of the cell membrane), increasing k_{hyd} (via RGS overexpression) and decreasing R_{tot} (via receptor blockage) intensify signal amplification, while decreasing k_{hyd} (via RGS inhibition) and increasing R_{tot} (via receptor overexpression) are expected to decrease the amplification ratio. On the other hand, when the presence of lipid rafts leads to signal attenuation (i.e. lipid rafts cover 10-30% of the cell membrane), opposite effects are expected for similar variations in k_{hyd} and R_{tot}. As a result, both RGS inhibition and receptor overexpression are expected to neutralize the effect of lipid rafts on the level of response and thus diminish the influence of lipid raft disruption on G-protein signaling.

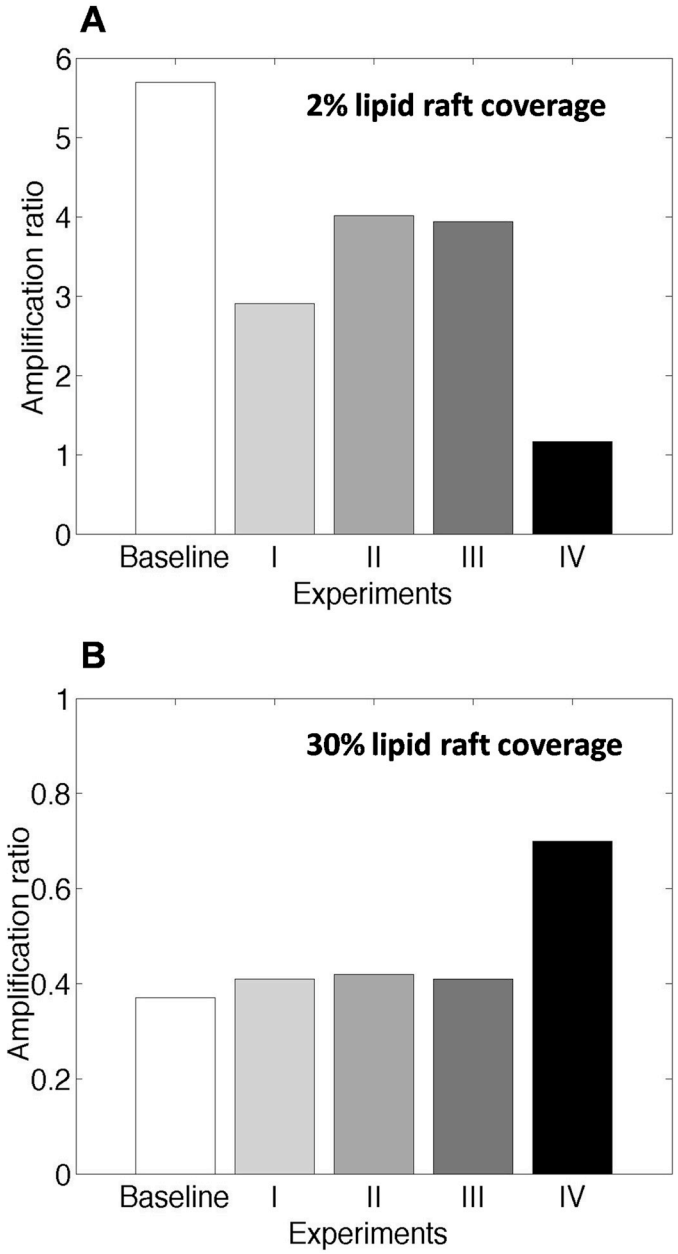

Fig. 7.8: Simulation results for proposed experimental protocols for (A) amplification of G-protein signaling in the presence of lipid rafts with 2% coverage, and (B) attenuation of G-protein signaling in the presence of lipid rafts with 30% coverage. Baseline experiments are performed using k_{hyd} = 10 s^{-1}, R_{tot} = 50,000 #/cell and $[L] = 0.1K_d$. The effects of a change in a single parameter are shown by experiments I-III (experiment I: k_{hyd} = 1 s^{-1}, experiment II: R_{tot} = 250,000 #/cell and experiment III: $[L] = K_d$). The effect of a simultaneous change in all three parameters is shown by experiment IV (k_{hyd} = 1 s^{-1}, R_{tot} = 250,000 #/cell and $[L] = K_d$). The greatest enrichment ratio for ligand-bound receptors predicted by MC model was used in each simulation. Other parameter values are as listed in Table 7.1.

7.4 Conclusions

We developed a kinetic model that quantitatively describes the effects of receptor dimerization and low diffusivity regions (lipid rafts) on GPCR organization and signaling. Although no direct experimental evidence yet exists for specific testing of results, our modeling demonstrates how ligands with particular dimerization-inducing or inhibiting characteristics may alter GPCR organization on the cell surface and in turn affect the level of G-protein activation. Depending on the unligated and ligated receptor dimerization and monomerization rate constants, ligand binding may quickly move receptors into or out of lipid rafts. Such re-organization of receptors may then enhance or diminish the GPCR-mediated response. Receptor phosphorylation can also be affected by the organization of GPCRs on the membrane as well (see Appendix E (Fig. E.5)). Thus receptor dimerization and lipid rafts may work together to provide a flexible platform for controlling both the extent and dynamics of GPCR signaling. A potentially powerful option for drug design for GPCR-associated diseases would be to tailor ligands to control receptor dimerization on the cell membrane in order to regulate G-protein signaling.

Our theoretical framework must be further validated in the context of experimental studies such as described in the text and Fig. 7.8. However, our model already allows us to understand and connect individual observations in the literature on the role of receptor dimerization and lipid rafts in G-protein signaling. For example, we can provide explanations for experimental observations, including how various ligands differently re-organize δ-opioid receptors on the cell membrane [24], how dimerization-inducing ligands have distinct effects on localization of β2-adrenergic receptors and

bradykinin B2 receptors relative to lipid rafts [12], and how lipid raft disruption amplifies G-protein signaling in a cell type but attenuates it in another type [24, 25].

Finally, we anticipate that other factors, including receptor hetero-dimerization, preferential interactions of GPCRs with particular membrane lipids, lipid raft dynamics and actin cytoskeleton re-arrangements, receptor cross-talk and G-protein independent pathways such as β-arrestin binding to receptors further increase the possible range of outcomes of this signaling system [52, 68-73].

7.5 References

1. George SR, O'Dowd BF, Lee SP. (2002) G-protein-coupled receptor oligomerization and its potential for drug discovery. Nat Rev Drug Discov 1(10): 808-820.

2. Sautel M, Milligan G. (2000) Molecular manipulation of G-protein-coupled receptors: A new avenue into drug discovery. Curr Med Chem 7(9): 889-896.

3. Baker A, Sauliere A, Dumas F, Millot C, Mazeres S, et al. (2007) Functional membrane diffusion of G-protein coupled receptors. Eur Biophys J 36(8): 849-860.

4. Rios CD, Jordan BA, Gomes I, Devi LA. (2001) G-protein-coupled receptor dimerization: Modulation of receptor function. Pharmacol Ther 92(2-3): 71-87.

5. Whorton MR, Bokoch MP, Rasmussen SG, Huang B, Zare RN, et al. (2007) A monomeric G protein-coupled receptor isolated in a high-density lipoprotein particle efficiently activates its G protein. Proc Natl Acad Sci U S A 104(18): 7682-7687.

6. Whorton MR, Jastrzebska B, Park PS, Fotiadis D, Engel A, et al. (2008) Efficient coupling of transducin to monomeric rhodopsin in a phospholipid bilayer. J Biol Chem 283(7): 4387-4394.

7. Chabre M, le Maire M. (2005) Monomeric G-protein-coupled receptor as a functional unit. Biochemistry 44(27): 9395-9403.

8. Fotiadis D, Liang Y, Filipek S, Saperstein DA, Engel A, et al. (2003) Atomic-force microscopy: Rhodopsin dimers in native disc membranes. Nature 421(6919): 127-128.

9. Botelho AV, Huber T, Sakmar TP, Brown MF. (2006) Curvature and hydrophobic forces drive oligomerization and modulate activity of rhodopsin in membranes. Biophys J 91(12): 4464-4477.

10. Woolf PJ, Linderman JJ. (2003) Self organization of membrane proteins via dimerization. Biophys Chem 104(1): 217-227.

11. Gomes I, Jordan BA, Gupta A, Rios C, Trapaidze N, et al. (2001) G protein coupled receptor dimerization: Implications in modulating receptor function. J Mol Med 79(5-6): 226-242.

12. Pike LJ. (2003) Lipid rafts: Bringing order to chaos. J Lipid Res 44(4): 655-667.

13. Foster LJ, De Hoog CL, Mann M. (2003) Unbiased quantitative proteomics of lipid rafts reveals high specificity for signaling factors. Proc Natl Acad Sci U S A 100(10): 5813-5818.

14. Pralle A, Keller P, Florin EL, Simons K, Horber JK. (2000) Sphingolipid-cholesterol rafts diffuse as small entities in the plasma membrane of mammalian cells. J Cell Biol 148(5): 997-1008.

15. Simons K, Toomre D. (2000) Lipid rafts and signal transduction. Nat Rev Mol Cell Biol 1(1): 31-39.

16. Shea LD, Linderman JJ. (1998) Compartmentalization of receptors and enzymes affects activation for a collision coupling mechanism. J Theor Biol 191(3): 249-258.

17. Brinkerhoff CJ, Traynor JR, Linderman JJ. (2008) Collision coupling, crosstalk, and compartmentalization in G-protein coupled receptor systems: Can a single model explain disparate results? J Theor Biol 255: 278-286.

18. Cunningham O, Andolfo A, Santovito ML, Iuzzolino L, Blasi F, et al. (2003) Dimerization controls the lipid raft partitioning of uPAR/CD87 and regulates its biological functions. EMBO J 22(22): 5994-6003.

19. Savi P, Zachayus JL, Delesque-Touchard N, Labouret C, Herve C, et al. (2006) The active metabolite of clopidogrel disrupts P2Y12 receptor oligomers and partitions them out of lipid rafts. Proc Natl Acad Sci U S A 103(29): 11069-11074.

20. Feron O, Smith TW, Michel T, Kelly RA. (1997) Dynamic targeting of the agonist-stimulated m2 muscarinic acetylcholine receptor to caveolae in cardiac myocytes. J Biol Chem 272(28): 17744-17748.

21. Ishizaka N, Griendling KK, Lassegue B, Alexander RW. (1998) Angiotensin II type 1 receptor: Relationship with caveolae and caveolin after initial agonist stimulation. Hypertension 32(3): 459-466.

22. Xue M, Vines CM, Buranda T, Cimino DF, Bennett TA, et al. (2004) N-formyl peptide receptors cluster in an active raft-associated state prior to phosphorylation. J Biol Chem 279(43): 45175-45184.

23. Rybin VO, Xu X, Lisanti MP, Steinberg SF. (2000) Differential targeting of beta -adrenergic receptor subtypes and adenylyl cyclase to cardiomyocyte caveolae. A mechanism to functionally regulate the cAMP signaling pathway. J Biol Chem 275(52): 41447-41457.

24. Huang P, Xu W, Yoon SI, Chen C, Chong PL, et al. (2007) Cholesterol reduction by methyl-beta-cyclodextrin attenuates the delta opioid receptor-mediated signaling in neuronal cells but enhances it in non-neuronal cells. Biochem Pharmacol 73(4): 534-549.

25. Huang P, Xu W, Yoon SI, Chen C, Chong PL, et al. (2007) Agonist treatment did not affect association of mu opioid receptors with lipid rafts and cholesterol

reduction had opposite effects on the receptor-mediated signaling in rat brain and CHO cells. Brain Res 1184: 46-56.

26. Lauffenburger D, Linderman JJ. (1993) Receptors: Models for binding, trafficking, and signaling. New York: Oxford University Press.

27. Linderman JJ. (2009) Modeling of G-protein-coupled receptor signaling pathways. J Biol Chem 284(9): 5427-5431.

28. Sharma P, Varma R, Sarasij RC, Ira, Gousset K, et al. (2004) Nanoscale organization of multiple GPI-anchored proteins in living cell membranes. Cell 116(4): 577-589.

29. Smith SM, Lei Y, Liu J, Cahill ME, Hagen GM, et al. (2006) Luteinizing hormone receptors translocate to plasma membrane microdomains after binding of human chorionic gonadotropin. Endocrinology 147(4): 1789-1795.

30. Meyer BH, Segura JM, Martinez KL, Hovius R, George N, et al. (2006) FRET imaging reveals that functional neurokinin-1 receptors are monomeric and reside in membrane microdomains of live cells. Proc Natl Acad Sci U S A 103(7): 2138-2143.

31. Schroeder F, Gallegos AM, Atshaves BP, Storey SM, McIntosh AL, et al. (2001) Recent advances in membrane microdomains: Rafts, caveolae, and intracellular cholesterol trafficking. Exp Biol Med (Maywood) 226(10): 873-890.

32. Saffman PG, Delbruck M. (1975) Brownian motion in biological membranes. Proc Natl Acad Sci U S A 72(8): 3111-3113.

33. Mahama PA, Linderman JJ. (1994) A monte carlo study of the dynamics of G-protein activation. Biophys J 67(3): 1345-1357.

34. Mayawala K, Vlachos DG, Edwards JS. (2006) Spatial modeling of dimerization reaction dynamics in the plasma membrane: Monte carlo vs. continuum differential equations. Biophys Chem 121(3): 194-208.

35. Hsieh MY, Yang S, Raymond-Stinz MA, Steinberg S, Vlachos DG, et al. (2008) Stochastic simulations of ErbB homo and heterodimerisation: Potential impacts of receptor conformational state and spatial segregation. IET Syst Biol 2(5): 256-272.

36. Gennis RB. (1989) Biomembranes: Molecular structure and function. New York: Springer-Verlag.

37. Kusumi A, Sako Y, Yamamoto M. (1993) Confined lateral diffusion of membrane receptors as studied by single particle tracking (nanovid microscopy). effects of calcium-induced differentiation in cultured epithelial cells. Biophys J 65(5): 2021-2040.

38. Claasen B, Axmann M, Meinecke R, Meyer B. (2005) Direct observation of ligand binding to membrane proteins in living cells by a saturation transfer double difference (STDD) NMR spectroscopy method shows a significantly higher affinity of integrin alpha(IIb)beta3 in native platelets than in liposomes. J Am Chem Soc 127(3): 916-919.

39. Oh P, Schnitzer JE. (2001) Segregation of heterotrimeric G proteins in cell surface microdomains. G(q) binds caveolin to concentrate in caveolae, whereas G(i) and G(s) target lipid rafts by default. Mol Biol Cell 12(3): 685-698.

40. Smart EJ, Ying YS, Mineo C, Anderson RG. (1995) A detergent-free method for purifying caveolae membrane from tissue culture cells. Proc Natl Acad Sci U S A 92(22): 10104-10108.

41. Seno K, Kishimoto M, Abe M, Higuchi Y, Mieda M, et al. (2001) Light- and guanosine 5'-3-O-(thio)triphosphate-sensitive localization of a G protein and its effector on detergent-resistant membrane rafts in rod photoreceptor outer segments. J Biol Chem 276(24): 20813-20816.

42. Ostasov P, Bourova L, Hejnova L, Novotny J, Svoboda P. (2007) Disruption of the plasma membrane integrity by cholesterol depletion impairs effectiveness of TRH receptor-mediated signal transduction via G(q)/G(11)alpha proteins. J Recept Signal Transduct Res 27(5-6): 335-352.

43. Huang C, Hepler JR, Chen LT, Gilman AG, Anderson RG, et al. (1997) Organization of G proteins and adenylyl cyclase at the plasma membrane. Mol Biol Cell 8(12): 2365-2378.

44. Li S, Okamoto T, Chun M, Sargiacomo M, Casanova JE, et al. (1995) Evidence for a regulated interaction between heterotrimeric G proteins and caveolin. J Biol Chem 270(26): 15693-15701.

45. Brinkerhoff CJ, Choi JS, Linderman JJ. (2008) Diffusion-limited reactions in G-protein activation: Unexpected consequences of antagonist and agonist competition. J Theor Biol 251(4): 561-569.

46. Shea LD, Omann GM, Linderman JJ. (1997) Calculation of diffusion-limited kinetics for the reactions in collision coupling and receptor cross-linking. Biophys J 73(6): 2949-2959.

47. Blower SM, Dowlatabadi H. (1994) Sensitivity and uncertainty analysis of complex models of disease transmission: An HIV model, as an example. Int Stat Rev 62(2): 229-243.

48. Marino S, Hogue IB, Ray CJ, Kirschner DE. (2008) A methodology for performing global uncertainty and sensitivity analysis in systems biology. J Theor Biol 254(1):

178-196.

49. Nicolau DV,Jr, Burrage K, Parton RG, Hancock JF. (2006) Identifying optimal lipid raft characteristics required to promote nanoscale protein-protein interactions on the plasma membrane. Mol Cell Biol 26(1): 313-323.

50. Nicolau DV,Jr, Hancock JF, Burrage K. (2007) Sources of anomalous diffusion on cell membranes: A monte carlo study. Biophys J 92(6): 1975-1987.

51. Parton RG. (2003) Caveolae--from ultrastructure to molecular mechanisms. Nat Rev Mol Cell Biol 4(2): 162-167.

52. Maurya MR, Subramaniam S. (2007) A kinetic model for calcium dynamics in RAW 264.7 cells: 1. mechanisms, parameters, and subpopulational variability. Biophys J 93(3): 709-728.

53. Yi TM, Kitano H, Simon MI. (2003) A quantitative characterization of the yeast heterotrimeric G protein cycle. Proc Natl Acad Sci U S A 100(19): 10764-10769.

54. Jiao X, Zhang N, Xu X, Oppenheim JJ, Jin T. (2005) Ligand-induced partitioning of human CXCR1 chemokine receptors with lipid raft microenvironments facilitates G-protein-dependent signaling. Mol Cell Biol 25(13): 5752-5762.

55. Sitrin RG, Emery SL, Sassanella TM, Blackwood RA, Petty HR. (2006) Selective localization of recognition complexes for leukotriene B4 and formyl-met-leu-phe within lipid raft microdomains of human polymorphonuclear neutrophils. J Immunol 177(11): 8177-8184.

56. Xiang Y, Rybin VO, Steinberg SF, Kobilka B. (2002) Caveolar localization dictates physiologic signaling of beta 2-adrenoceptors in neonatal cardiac myocytes. J Biol Chem 277(37): 34280-34286.

57. Pontier SM, Percherancier Y, Galandrin S, Breit A, Gales C, et al. (2008) Cholesterol-dependent separation of the beta2-adrenergic receptor from its partners determines signaling efficacy: Insight into nanoscale organization of signal transduction. J Biol Chem 283(36): 24659-24672.

58. Keil ML, Solomon NL, Lodhi IJ, Stone KC, Jesaitis AJ, et al. (2003) Priming-induced localization of G(ialpha2) in high density membrane microdomains. Biochem Biophys Res Commun 301(4): 862-872.

59. Cvejic S, Devi LA. (1997) Dimerization of the delta opioid receptor: Implication for a role in receptor internalization. The Journal of Biological Chemistry 272(43): 26959.

60. Hebert TE, Moffett S, Morello JP, Loisel TP, Bichet DG, et al. (1996) A peptide derived from a beta2-adrenergic receptor transmembrane domain inhibits both receptor dimerization and activation. J Biol Chem 271(27): 16384-16392.

61. AbdAlla S, Zaki E, Lother H, Quitterer U. (1999) Involvement of the amino terminus of the B(2) receptor in agonist-induced receptor dimerization. J Biol Chem 274(37): 26079-26084.

62. Cameron PL, Ruffin JW, Bollag R, Rasmussen H, Cameron RS. (1997) Identification of caveolin and caveolin-related proteins in the brain. J Neurosci 17(24): 9520-9535.

63. Monastyrskaya K, Hostettler A, Buergi S, Draeger A. (2005) The NK1 receptor localizes to the plasma membrane microdomains, and its activation is dependent on lipid raft integrity. J Biol Chem 280(8): 7135-7146.

64. Xu W, Yoon SI, Huang P, Wang Y, Chen C, et al. (2006) Localization of the kappa opioid receptor in lipid rafts. J Pharmacol Exp Ther 317(3): 1295-1306.

65. Ayoub MA, Couturier C, Lucas-Meunier E, Angers S, Fossier P, et al. (2002) Monitoring of ligand-independent dimerization and ligand-induced conformational changes of melatonin receptors in living cells by bioluminescence resonance energy transfer. J Biol Chem 277(24): 21522-21528.

66. Mercier JF, Salahpour A, Angers S, Breit A, Bouvier M. (2002) Quantitative assessment of beta 1- and beta 2-adrenergic receptor homo- and heterodimerization by bioluminescence resonance energy transfer. J Biol Chem 277(47): 44925-44931.

67. Harding PJ, Attrill H, Boehringer J, Ross S, Wadhams GH, et al. (2009) Constitutive dimerization of the G-protein coupled receptor, neurotensin receptor 1, reconstituted into phospholipid bilayers. Biophys J 96(3): 964-973.

68. Milligan G. (2004) G protein-coupled receptor dimerization: Function and ligand pharmacology. Mol Pharmacol 66(1): 1-7.

69. Woolf PJ, Linderman JJ. (2004) An algebra of dimerization and its implications for G-protein coupled receptor signaling. J Theor Biol 229(2): 157-168.

70. Turcotte M, Tang W, Ross EM. (2008) Coordinate regulation of G protein signaling via dynamic interactions of receptor and GAP. PLoS Comput Biol 4(8): e1000148.

71. Flaherty P, Radhakrishnan ML, Dinh T, Rebres RA, Roach TI, et al. (2008) A dual receptor crosstalk model of G-protein-coupled signal transduction. PLoS Comput Biol 4(9): e1000185.

72. Manes S, Viola A. (2006) Lipid rafts in lymphocyte activation and migration. Mol Membr Biol 23(1): 59-69.

73. Chini B, Parenti M. (2004) G-protein coupled receptors in lipid rafts and caveolae: How, when and why do they go there? J Mol Endocrinol 32(2): 325-338.

74. Riccobene TA, Omann GM, Linderman JJ. (1999) Modeling activation and desensitization of G-protein coupled receptors provides insight into ligand efficacy. J Theor Biol 200(2): 207-222.

75. Mukhopadhyay S, Ross EM. (1999) Rapid GTP binding and hydrolysis by G(q) promoted by receptor and GTPase-activating proteins. Proc Natl Acad Sci U S A 96(17): 9539-9544.

76. Zhong H, Wade SM, Woolf PJ, Linderman JJ, Traynor JR, et al. (2003) A spatial focusing model for G protein signals. regulator of G protein signaling (RGS) protien-mediated kinetic scaffolding. J Biol Chem 278(9): 7278-7284.

77. Kinzer-Ursem TL, Linderman JJ. (2007) Both ligand- and cell-specific parameters control ligand agonism in a kinetic model of g protein-coupled receptor signaling. PLoS Comput Biol 3(1): e6.

Chapter 8

Conclusions and future directions

8.1 Summary

Despite years of scientific research and efforts by world health organizations, tuberculosis (TB) remains a global health problem and is responsible for ~2 million deaths per year. Of great concern is that TB persists as a latent infection in ~2 billion humans worldwide, providing a reservoir of potential disease and contagion. Drug-susceptible TB can be treated only with a lengthy regimen that is fraught with compliance and drug toxicity issues. Drug-resistant TB, on the other hand, is a major problem worldwide and development of new drugs and strategies is essential to prevent further spread of these strains. Single drug therapy is not permitted in the treatment of active TB in humans because drug resistance can arise and the standard of care must be adhered to. It is difficult to evaluate the effects of new TB drugs or strategies in human clinical trials. Thus, there is a critical need for novel approaches and platforms for testing and optimizing new therapies for TB.

The granuloma is where the central battle in TB plays out. The function of granuloma is believed to reflect success or failure of the host to contain infection. Systems biology approaches presented in this work have generated predictions and novel hypotheses regarding cellular and molecular mechanisms influencing granuloma formation and function over a time period of days to years. As noted in previous chapters, the primary goal of this work is to link processes at multiple biological scales involved

within the immune response to Mtb via dynamical computational modeling. The payoff to establishing such a linkage lies in bridging studies of therapeutic targets at the molecular and cellular scales to the effects of modulation of these targets at the tissue, organ, and whole organism levels. To this end, we have identified various extracellular, intracellular, or cell membrane-associated processes as targets that determine the concentration of TNF, the extent and timing of TNF activities within a granuloma during the long-term immune response to Mtb, and thus the outcome of infection at the level of a granuloma. These outcomes include containment, clearance, uncontrolled growth of bacteria, or excessive inflammation in tissue. We have also studied whether modulation of these targets can improve the function of granuloma towards lower bacteria numbers and lower kevels of inflammation. These studies are critical to our understanding of disease mechanisms as well as identifying efficient immunotherapeutic approaches to battle TB.

In this final chapter, I will briefly summarize the key findings from each phase of my research. I will then use these findings to make recommendations for future studies toward understanding the immune response to Mtb infection. Specifically, I will address the application of new multi-scale systems biology approaches towards identification of both host and bacterial factors that determine the outcome of infection, and the application of these approaches to identify mechanisms of TB reactivation due to, for example, HIV co-infection or anti-TNF therapy.

8.2 Key findings by aim

8.2.1 Aim 1

We calculated the TNF concentration in a granuloma using a differential equation model that considers a simple representation of the spatial structure of a granuloma at steady state. We used a simple experimental system for granuloma formation in mice to measure critical model parameters. The formation of granulomas was induced in mice following injection of Sepharose beads covalently coupled to *Mycobacterium* purified protein derivative (PPD) antigen. Our experiments indicated that macrophages and dendritic cells (DCs) are the major TNF-producing immune cells within a granuloma. Further, DCs, macrophages and B cells are found to be the major TNFR-expressing cells. Our simulations (as described in Chapter 2) suggest that there is a TNF concentration gradient in granulomas, such that the highest concentration occurs at the center of a granuloma [1]. This gradient results from the emergence of a specific organization of immune cells within a granuloma (i.e. concentration of infected macrophages at the core and concentration of lymphocytes at the periphery of the granuloma) and the processes of TNF/TNFR binding and intracellular trafficking. What might the impact of this gradient be? The gradient could allow the spatial coordination of TNF-induced biological activities (i.e. activation of NF-κB and apoptotic signaling pathways) within a granuloma. Higher concentrations of TNF in the center of granuloma can induce caspase-mediated apoptotic pathway that favors antigen cross-presentation as well as the elimination of pathogen inside infected macrophages. However, very low levels of TNF at the periphery of the granuloma, although unable to induce apoptosis, are sufficient to turn on the NF-

κB signaling pathway that favors cell survival and expression of pro-inflammatory genes in T cells.

8.2.2 Aim 2

We developed a multi-scale computational model that describes the immune response to Mtb in lung over three biological length scales: tissue, cellular and molecular. Using this model, we predicted the impact of TNF-associated molecular scale processes on the outcome of infection in a single granuloma. We first analyzed the effect of TNFR dynamics as described in Chapter 3. Our simulations indicated a key role for TNFR1 internalization in control of the local TNF concentration and regulation of TNF activities during granuloma development [2]. Further, our results demonstrated that TNF-induced TNFR1 internalization plays an important role in preventing excessive inflammation in tissue. Removal of the process of TNFR1 internalization leads to uncontrollably high tissue concentrations of TNF and very high rates of macrophage activation. TNFR1 internalization kinetics are also predicted to have a significant impact on bacterial numbers within a granuloma [2]. Increasing the rate of receptor internalization reduces the rate of bacterial clearance. Overall, our results suggest the novel hypothesis that TNFR1 internalization kinetics play an important role in balancing inflammation and bacterial killing within a granuloma. This finding can be considered in future studies investigating approaches to control and therapy of TB, as a number of methods have already been proposed to control the rate of TNFR1 internalization *in vitro* [3-5].

Further, we used the model to identify NF-κB-associated processes that influence infection outcome and inflammation at the granuloma scale (see Chapter 4). We showed

that the dynamics of the TNF-induced NF-κB signaling critically control bacterial load and inflammation level in tissue. Activation of resting macrophages, in addition to infected macrophages, is required for a protective immune response but must be accurately regulated to prevent excessive inflammation. We also showed that the stability of mRNA transcripts corresponding to NF-κB-mediated responses, particularly macrophage activation and expression of TNF and chemokines, controls bacterial load in a granuloma, inflammation level in tissue, and granuloma size. Our model suggests that both the extent and the timing of NF-κB-mediated macrophage activation, but only the extent of chemokine and TNF synthesis, are critical to control of the immune response to Mtb. Our analysis elucidates intracellular NF-κB associated signaling molecules and processes involved in immunity to Mtb that may be new targets for disease control.

8.2.3 Aim 3

We used the multi-scale computational model of TB granuloma (as described in Chapter 6) to identify functional and biochemical characteristics underlying the higher likelihood of TB reactivation that occurs for some TNF-neutralizing drugs. Our model-based analyses lead to novel and interesting hypotheses regarding drug-induced TB reactivation at the granuloma scale. First, we found that the ability of a drug to bind membrane-bound TNF (mTNF) is a major factor impairing granuloma function, leading to TB reactivation. This is because the cell membrane provides a scaffold on which TNF at a high concentration is available for neutralization before it is released as soluble TNF (sTNF) and diluted in extracellular spaces. Second, our results suggest that differences in blood concentrations of drugs, TNF/drug binding and unbinding kinetics and the level of drug

permeability into lung tissue can dramatically affect the likelihood of reactivation. In fact, we found that these factors result in different rates of TB reactivation between antibody-type drugs (e.g. infliximab) and TNF receptor fusion proteins (etanercept). Finally, although there are differences in drug abilities to induce apoptosis or cytolysis in TNF-expressing key immune cells (e.g. infected and activated macrophages and T cells), our analysis suggested that these activities are not as important as other factors in driving TB reactivation. These findings suggest characteristics of suitable anti-TNF drugs for treatment of inflammatory diseases while balancing high risks of TB reactivation.

8.2.4 Modeling of the impact of receptor organization on the cell membrane on receptor signaling

Using a combination of stochastic (Monte Carlo) and deterministic modeling, we proposed a novel mechanism for lipid raft partitioning of G-protein coupled receptors (GPCRs) based on reversible dimerization of receptors and then demonstrate that such localization can affect GPCR signaling. Modeling results are consistent with a variety of experimental data indicating that lipid rafts have a role in amplification or attenuation of G-protein signaling. Our work suggests a new mechanism by which dimerization-inducing or inhibiting characteristics of ligands can influence GPCR signaling by controlling receptor organization on the cell membrane.

8.3 Future directions

8.3.1 Identification of bacterial factors that influence granuloma function

One important factor that limits control of TB is the remarkably long period of antibiotic treatment necessary to eradicate the pathogen. Although there are antibiotics that rapidly

kill Mtb *in vitro*, in humans these agents require 6-24 months of treatment to be effective. Incomplete treatment is not only ineffective but also may increase the risk of development of drug-resistant strains of bacteria [6]. The reason that antibiotics are less effective against Mtb *in vivo* remain unclear. One potential hypothesis that could be tested using a combination of experimental and computational methods is that the slow replication and low metabolic rate of bacteria in the host environment produces an antibiotic-tolerant state [7]. A recent study has determined a signal transduction pathway in Mtb that is triggered by various growth-limiting stresses and slows bacterial growth by redirecting cellular carbon fluxes away from the central metabolic pathways and towards storage [8]. Adoption of a quiescent antibiotic-tolerant state by Mtb within the host limits our ability to treat TB.

In this work, I focused my research on identifying host factors (in particular, TNF-associated processes) that affect granuloma formation and function in the lung during immune responses to Mtb. However, development of effective strategies for treatment of TB requires attention to mechanisms that both enhance host immunity to Mtb and enhance bacterial sensitivity to antibiotic treatments. To this aim, I suggest incorporation of known signaling and metabolic pathways that regulate Mtb growth into the multi-scale granuloma model. The triacylglycerol (TAG) pathway triggered by stresses such as hypoxic conditions in tissue, for example, has been shown to play an important role in inhibiting Mtb growth by affecting tricarboxylic acid (TCA) flux [8]. Analysis of these pathways in the context of granuloma development during Mtb infection will reveal how bacterial and host factors communicate, and how they are affected by each other. Further analyses of the dynamics of immune response which is

controlled simultaneously by the dynamics of bacterial and host factors may lead to identification of novel molecular targets as well as critical time-points during Mtb infection for triggering each of the targets to most efficiently control the infection.

8.3.2 Identification of critical intracellular signaling pathways that control pro- and anti-inflammatory responses during the immune response to Mtb

The immune responses induced by Mtb infection are myriad and complex, and even now it remains incompletely understood which responses are required for protection and which contribute to pathology [9,10]. In truth, there is significant overlap among protective and pathologic responses, with the best outcome achieved by a balance of pro-inflammatory and anti-inflammatory responses, particularly at the level of the granuloma. A significant amount of literature exists exploring the identity of factors (including different types of immune cells, cytokines, and chemokines) involved within pro- and anti-inflammatory responses during Mtb infection [9-11]. However, there is limited understanding of how the complex inflammatory cell signaling network (that controls cellular responses to a variety of factors such as antigens, cytokines, growth factors and many drugs) is affected by Mtb infection in various immune cells (e.g. macrophages and T cells) during the immune response to Mtb. Systematic study of cell signaling networks increasingly involves high-throughput proteomics and transcriptional profiling with the aim of assembling large-scale interaction networks [12]. However, functional analysis of these networks is essential to understand how cells respond to complex sets of signaling factors from the environment, and to understand dysfunctional signaling mechanisms in diseased cells or infected cells as well as to understand mechanisms of complex drug

actions [13]. Recently, protein signaling networks inferred from large-scale biochemical data have elucidated profound differences in inflammatory signaling (e.g. NF-κB-dependent secretion of chemokines and cytokines) between primary human hepatocytes and liver cancer cell lines, indicating potential mechanisms by which cancer cells down-regulate inflammatory responses to avoid immune editing [14]. This highlights the importance of studying signaling network differences in understanding disease mechanisms as well as identifying therapeutic targets.

In the context of Mtb infection, a recent study has also indicated that pathogenic mycobacteria repress NF-κB signaling in infected macrophages and use this mechanism to enhance their survival and growth in macrophages [11]. Based on this observation and other studies, one can hypothesize that pathological environmental factors (such as infection with Mtb) can induce major functional differences in inflammatory signaling network topology in immune cells. Uncovering these differences can reveal important insights into disease mechanisms and our understanding of efficient and selective immunotherapeutic targets for TB. Thus, I suggest exposing healthy macrophages and T cells, infected macrophages, and macrophages or T cells activated with mycobacteria and/or mycobacterial antigens to a variety of biochemical factors with either inflammation-inducing or -inhibiting characteristics in the presence and absence of a variety of drugs (e.g. small molecule kinase inhibitors), and then measuring the levels or states of modification of intracellular proteins associated with different signaling pathways, secreted cytokines and chemokines, membrane receptors, and apoptosis/necrosis. This will yield a large set of data based on which inflammatory signaling networks associated with pathogen effects can be inferred by using, for

example, multi-linear regression analysis. A comparison between data inferred from healthy (resting), infected, and activated immune cells will lead to understanding of mechanisms that Mtb uses to enhance its survival in the host, as well as mechanisms that host uses to control bacterial growth.

8.3.3 Application of systems pharmacology approaches to develop therapeutic strategies to improve granuloma function

Using the multi-scale granuloma model and extensive sensitivity analysis techniques, we have identified and will continue to identify candidate mechanisms at different biological scales that could be considered in future studies as therapeutic targets for TB. These mechanisms (as shown in examples presented in Chapters 3, 4) include inhibiting/activating specific types of immune cells and/or their specific functions, inhibiting/inducing cell-type-specific expression of particular cytokines and/or cytokine receptors, or inhibiting/activating specific intracellular signaling pathways in a cell-type-specific fashion. Although identification of these mechanisms is a significant first step toward selection of primary drug candidates, it is important to characterize conditions under which novel suggested drug candidates would exert an optimal effect with respect to efficacy and safety of treatment. In order to suggest efficient treatment strategies, it is critical to characterize the time-dependent effects of these drugs on disease progression by studying the dynamics of drug responses as a function of the temporal and spatial dynamics of drug exposure. The multi-scale granuloma model developed in this research provides a platform for developing and optimizing therapeutic strategies that could then be tested in animal models. Similar to the incorporation of TNF-neutralizing drugs into

the granuloma model, as described in Chapter 6, I suggest combining the multi-scale model with Pharmacokinetic-Pharmacodynamic (PK-PD) models describing drug uptake and distribution (pharmacokinetics) in lung tissue and in single cells (in the case of intracellular targets) as well as multiple downstream responses evoked over different time-scales (pharmacodynamics). These models allow us to study and predict biological effects of drugs on granuloma function and to characterize pharmacological conditions under which these drugs have their optimal therapeutic effects.

For example, our analysis in Chapter 4 shows that manipulating the dynamics of the NF-κB-mediated responses by controlling the rate of degradation of mRNAs corresponding to these responses can be used as a strategy to improve granuloma function and to inhibit bacteria growth. A recent experimental study has also indicated that efficient degradation of CCR2 mRNA in monocytes by using therapeutic RNA silencing (by using siRNAs formulated into lipid nanoparticles) in mice prevents monocyte accumulation in sites of inflammation and attenuates disease progression in different disease models such as mouse atherosclerosis, myocardial infarction, and cancer [15]. Incorporation of mechanism-based PK-PD models into the multi-scale granuloma model can help us identify and optimize similar strategies for treatment of TB that could be tested in animal models.

8.3.4. Identification of TB reactivation mechanisms by HIV co-infection

One-third of the world's population is estimated to be latently infected with Mtb. However, latent infection may reactivate to active disease (reactivation TB), with an average 10% per lifetime frequency. One important reason for TB reactivation is known

to be impaired immunity due to, for example, human immunodeficiency virus (HIV) co-infection. In fact, reactivation TB is a major source of morbidity and mortality among HIV-infected individuals. Of the 9.4 million individuals with new cases of active TB each year, approximately 15% are HIV-positive [16]. Further, while most opportunistic infections occur when CD4 T cell numbers are at low levels, TB occurs throughout the entire spectrum of HIV disease, even when this group of T cells are well-preserved and stable in HIV-infected persons [17-19]. This is clearly an important observation, and research into factors underlying reactivation in HIV-infected persons may reveal unknown mechanisms and strategies for control of Mtb infection and for preventing TB reactivation. However, an important barrier against progress of research in this area is the lack of appropriate animal models combining latent TB and HIV infection. In a recent study, cynomolgus macaques have been used, for the first time, as animal models of latent TB for investigation of immunologic and microbiologic responses to simian immunodeficiency virus (SIV) co-infection [20]. All latently infected animals in this study developed reactivation TB following SIV infection, with a variable time to reactivation. Data presented in this study suggest that the extent of early peripheral T cell depletion, but not virus load, is associated with reactivation of latent TB in monkey models infected with SIV. Although this study marks a significant step in understanding the relationships between Mtb and HIV infection, using monkey models for investigating TB has limitations that are described in detail in Chapter 1. Thus, I suggest combining the computational granuloma model for Mtb infection (as described in Chapters 3, 4) with excellent modeling studies performed on HIV infection [21,22] to develop a tractable multi-disease computational model of reactivation TB in HIV-co-infected hosts. Such a

model can become a useful tool to complement investigations on interactions between Mtb and HIV, and on immunologic events that lead to reactivation of latent TB or exacerbation of primary infection. This model, in particular, can also be used to test various hypotheses presented about how HIV exacerbates TB pathology through the manipulation of granulomas [23].

8.3.5 Experimental verification of mechanisms suggested by modeling studies for TB reactivation due to anti-TNF therapy

In chapter 5, we described an approach to dissect the effect of TNF-neutralizing drugs on the ability of a granuloma to control infection. Our findings do not support hypotheses that assign a key role to apoptotic and cytolytic activities of antibody-type TNF-neutralizing drugs in determining their ability to reactivate TB, although we did confirm a significant reduction in T cell levels as a result of anti-TNF antibody (e.g. infliximab) treatments reported in literature [24,25]. To verify the results of our modeling studies, I suggest designing experiments to neutralize TNF in non-human primate models of TB, without inducing apoptosis or cytolysis in their immune cells. One possible approach could be to use RNA silencing techniques to inhibit expression of TNF protein during the immune response. Using this technique will help us neutralize TNF activities, without inducing cell death because of drug binding to membrane-bound TNF. Therapeutic siRNA silencing has already been used *in vivo* to control inflammation in various mouse disease models by formulating siRNAs against CCR2 mRNA into lipid nanoparticles and dynamic FMT-CT imaging of siRNA bio-distribution within mouse body [15]. Using this approach, we would be able to control the dose of siRNA to neutralize TNF activities at

desired levels. We would then be able to compare granuloma outcomes between siRNA-silenced models with models in which TNF has been neutralized by using anti-TNF antibodies or TNF receptors. Comparison of these results will help us better understand mechanisms underlying TB reactivation after anti-TNF therapy.

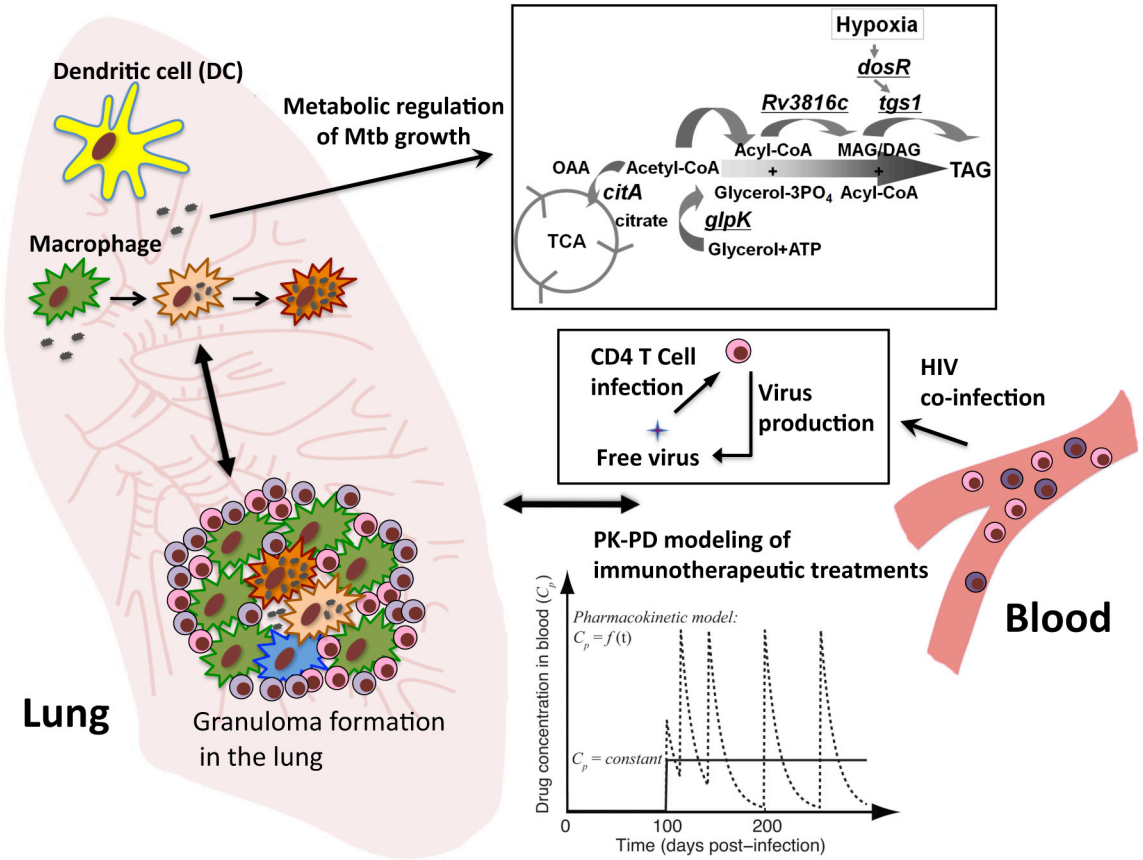

Fig. 8.1 Potential directions for research on the immune response to Mtb infection. The image showing triacylglycerol (TAG) biosynthetic pathway of Mtb and its relationship to tricarboxylic acid (TCA) cycle is taken from [8]**.**

Fig. 8.1 summarizes suggested future directions for research on the immune response to Mtb infection. Overall, systems biology approaches, particularly those focused on the granuloma, can be very useful in identifying new vaccines or therapeutic strategies for TB. For example, combining immune modulation ("immunomodulation") with

antibiotics is a potential strategy for enhancing treatment of TB [26,27]. A computational platform such as described in this work could allow for development of various strategies that could then be tested in animal models.

8.4 References

1. Fallahi-Sichani M, Schaller MA, Kirschner DE, Kunkel SL, Linderman JJ (2010) Identification of key processes that control tumor necrosis factor availability in a tuberculosis granuloma. PLoS Comput Biol 6: e1000778.

2. Fallahi-Sichani M, El-Kebir M, Marino S, Kirschner DE, Linderman JJ (2011) Multiscale computational modeling reveals a critical role for TNF-{alpha} receptor 1 dynamics in tuberculosis granuloma formation. J Immunol 186: 3472-3483.

3. Schutze S, Machleidt T, Adam D, Schwandner R, Wiegmann K, et al. (1999) Inhibition of receptor internalization by monodansylcadaverine selectively blocks p55 tumor necrosis factor receptor death domain signaling. J Biol Chem 274: 10203-10212.

4. Schneider-Brachert W, Tchikov V, Merkel O, Jakob M, Hallas C, et al. (2006) Inhibition of TNF receptor 1 internalization by adenovirus 14.7K as a novel immune escape mechanism. J Clin Invest 116: 2901-2913.

5. Neumeyer J, Hallas C, Merkel O, Winoto-Morbach S, Jakob M, et al. (2006) TNF-receptor I defective in internalization allows for cell death through activation of neutral sphingomyelinase. Exp Cell Res 312: 2142-2153.

6. Salomon JA, Lloyd-Smith JO, Getz WM, Resch S, Sanchez MS, et al. (2006) Prospects for advancing tuberculosis control efforts through novel therapies. PLoS Med 3: e273.

7. Mitchison DA (2006) Clinical development of anti-tuberculosis drugs. Journal of Antimicrobial Chemotherapy 58: 494-495.

8. Baek SH, Li AH, Sassetti CM (2011) Metabolic regulation of mycobacterial growth and antibiotic sensitivity. PLoS Biol 9: e1001065.

9. Lin PL, Flynn JL (2010) Understanding latent tuberculosis: A moving target. J Immunol 185: 15-22.

10. Cooper AM (2009) Cell-mediated immune responses in tuberculosis. Annu Rev Immunol 27: 393-422.

11. Gutierrez MG, Mishra BB, Jordao L, Elliott E, Anes E, et al. (2008) NF-kappa B activation controls phagolysosome fusion-mediated killing of mycobacteria by macrophages. J Immunol 181: 2651-2663.

12. Pieroni E, de la Fuente van Bentem,S., Mancosu G, Capobianco E, Hirt H, et al. (2008) Protein networking: Insights into global functional organization of proteomes. Proteomics 8: 799-816.

13. Sachs K, Perez O, Pe'er D, Lauffenburger DA, Nolan GP (2005) Causal protein-signaling networks derived from multiparameter single-cell data. Science 308: 523-529.

14. Alexopoulos LG, Saez-Rodriguez J, Cosgrove BD, Lauffenburger DA, Sorger PK (2010) Networks inferred from biochemical data reveal profound differences in toll-like receptor and inflammatory signaling between normal and transformed hepatocytes. Mol Cell Proteomics 9: 1849-1865.

15. Leuschner F, Dutta P, Gorbatov R, Novobrantseva TI, Donahoe JS, et al. (2011) Therapeutic siRNA silencing in inflammatory monocytes in mice. Nat Biotechnol 29: 1005-1010.

16. Harrington M (2010) From HIV to tuberculosis and back again: A tale of activism in 2 pandemics. Clin Infect Dis 50 Suppl 3: S260-6.

17. Post FA, Wood R, Pillay GP (1995) Pulmonary tuberculosis in HIV infection: Radiographic appearance is related to CD4+ T-lymphocyte count. Tubercle Lung Dis 76: 518-521.

18. Mukadi Y, Perriëns JH, St Louis ME, Brown C, Ryder RW, et al. (1993) Spectrum of immunodeficiency in HIV-1-infected patients with pulmonary tuberculosis in zaire. The Lancet 342: 143-146.

19. Hanson DL, Chu SY, Farizo KM, Ward JW (1995) Distribution of CD4+ T lymphocytes at diagnosis of acquired immunodeficiency syndrome-defining and other human immunodeficiency virus-related illnesses. the adult and adolescent spectrum of HIV disease project group. Arch Intern Med 155: 1537-1542.

20. Diedrich CR, Mattila JT, Klein E, Janssen C, Phuah J, et al. (2010) Reactivation of latent tuberculosis in cynomolgus macaques infected with SIV is associated with early peripheral T cell depletion and not virus load. PLoS One 5: e9611.

21. Perelson AS, Nelson PW (1999) Mathematical analysis of HIV-I: Dynamics in vivo. SIAM Rev 41: pp. 3-44.

22. Kirschner D (1999) Dynamics of co-infection with M. tuberculosis and HIV-1. Theor Popul Biol 55: 94-109.

23. Diedrich CR, Flynn JL (2011) HIV-1/mycobacterium tuberculosis coinfection immunology: How does HIV-1 exacerbate tuberculosis?. Infect Immun 79: 1407-1417.

24. Bruns H, Meinken C, Schauenberg P, Harter G, Kern P, et al. (2009) Anti-TNF immunotherapy reduces CD8+ T cell-mediated antimicrobial activity against mycobacterium tuberculosis in humans. J Clin Invest 119: 1167-1177.

25. Mitoma H, Horiuchi T, Tsukamoto H, Tamimoto Y, Kimoto Y, et al. (2008) Mechanisms for cytotoxic effects of anti-tumor necrosis factor agents on transmembrane tumor necrosis factor alpha-expressing cells: Comparison among infliximab, etanercept, and adalimumab. Arthritis Rheum 58: 1248-1257.

26. Kirschner DE, Webb GF (1998) Immunotherapy of HIV-1 infection. J Biol Systems 6: 71-83.

27. Kirschner D, Panetta JC (1998) Modeling immunotherapy of the tumor-immune interaction. J Math Biol 37: 235-252.

Appendix A

Supplementary information for Chapter 2

A.1 Simulation results for the spatial profiles of different forms of TNF in the model

Sample simulation results from the granuloma model for two sets of parameter values are presented in Fig. A.2. This figure displays the spatial profiles of extracellular (free and shed TNFR2-bound) and cell-associated (membrane and internalized TNFR1- and TNFR2-bound) sTNF concentrations at steady state. The model predicts that the average free sTNF concentration in the granuloma (depending on parameter values) lies within the range of 10^{-12}-10^{-10} M (~100-10,000 pg/ml). In the particular simulation indicated in Fig. A.2 (A, B), TNF is mostly produced at the inner compartment of granuloma and diffuses outward ($k_{synth\_in} > k_{synth\_out}$), binding to TNF receptors with identical densities on all cells ($R_{1\_in} = R_{1\_out} = R_{2\_in} = R_{2\_out}$). For the set of parameter values considered here, the average sTNF-bound fraction of cell surface TNFR1 molecules in the inner and outer compartments are 0.66 and 0.07 and the average internalized fraction of TNFR1 molecules in the inner and outer compartments are 0.88 and 0.34, respectively. For a second simulation shown in Fig. A.2 (C, D), TNF is homogeneously expressed in the whole granuloma ($k_{synth\_in} = k_{synth\_out}$), while binding to cell surface TNFR1 with the same compartment densities and TNFR2 with a higher density in the outer compartment ($R_{1\_in} = R_{1\_out} = R_{2\_in} < R_{2\_out}$). The average sTNF-bound fraction of cell surface TNFR1 molecules in the inner and outer compartments are 0.27 and 0.15 and the average internalized fraction of TNFR1 molecules in the inner and outer compartments are 0.76

and 0.62, respectively. These simulation results show that differential densities of TNFRs and the rate of TNF synthesis in granuloma compartments significantly influence the concentration profile of different forms of TNF in the granuloma.

Table A.1 Parameters defined or modified based on incorporation of different cell types in the granuloma model.

Parameter	Parameter description	Value
f_B, f_{CD4}, f_{CD8}, f_{Mac}, f_{mDC}, f_{pDC}	Cell fractions of B cells, CD4 and CD8 T cells, macrophages, mDCs and pDCs in granuloma*	Measured herein
k_B, k_{CD4}, k_{CD8}, k_{Mac}, k_{mDC}, k_{pDC}	Rate of mTNF synthesis by B cells, CD4 and CD8 T cells, macrophages, mDCs and pDCs in granuloma	Measured herein
R_{1_B}, R_{1_CD4}, R_{1_CD8}, R_{1_Mac}, R_{1_mDC}, R_{1_pDC}	TNFR1 density in B cells, CD4 and CD8 T cells, macrophages, mDCs and pDCs in granuloma	Measured herein
R_{2_B}, R_{2_CD4}, R_{2_CD8}, R_{2_Mac}, R_{2_mDC}, R_{2_pDC}	TNFR2 density in B cells, CD4 and CD8 T cells, macrophages, mDCs and pDCs in granuloma	Measured herein
V_1 (l)	Mean volume of a macrophage or dendritic cell†	1×10^{-12}
V_2 (l)	Mean volume of a lymphocyte†	3×10^{-13}
l_g	Lymphocyte fraction in the whole granuloma	$f_B + f_{CD4} + f_{CD8}$
s	Separation index	Varied from 0 to 1
l_o	Lymphocyte fraction in the outer compartment	$s(1-l_g)+l_g$
f_1	Fraction of granuloma cells that compose macrophages and DCs in the inner compartment	$[1-\frac{l_g(1-l_o)}{1-l_g}](1-l_g)$
f_2	Fraction of granuloma cells that compose lymphocytes in the inner compartment	$l_g(1-l_o)$
f_3	Fraction of granuloma cells that compose macrophages and DCs in the outer compartment	$l_g(1-l_o)$
f_4	Fraction of granuloma cells that compose lymphocytes in the outer compartment	$l_o l_g$
V_{in} (l)	Mean cell volume in the inner compartment	$\frac{f_1V_1+f_2V_2}{f_1+f_2}$
V_{out} (l)	Mean cell volume in the outer compartment	$\frac{f_3V_1+f_4V_2}{f_3+f_4}$
ρ_{in} (cell/l)	Mean cell number density in the inner compartment	$\frac{1-\phi}{V_{in}}$
ρ_{out} (cell/l)	Mean cell number density in the outer compartment	$\frac{1-\phi}{V_{out}}$
r_{core} (μm)	Radius of the inner compartment	$[(r_g^3-r_{bead}^3)\frac{f_1V_1+f_2V_2}{(1-l_g)V_1+l_gV_2}+r_{bead}^3]^{\frac{1}{3}}$

* Cell fraction values measured in PPD bead granulomas were normalized before using in the mathematical model such that the sum of cell fractions was unity.

† Average volumes of mouse macrophages and lymphocytes were calculated based on data from [1-3]

Table A.2 Parameter sets used to generate curves on Fig. 2.3.

Simulation run	Parameter values*
1	$k_{synth\_in} = 0.5$, $k_{synth\_out} = 0.0$, $R_{1\_in} = 1000$, $R_{2\_in} = 1000$, $R_{1\_out} = 1000$, $R_{2\_out} = 1000$, $f = 0.4$
2	$k_{synth\_in} = 0.3$, $k_{synth\_out} = 0.1$, $R_{1\_in} = 1000$, $R_{2\_in} = 1000$, $R_{1\_out} = 1000$, $R_{2\_out} = 1000$, $f = 0.4$
3	$k_{synth\_in} = 0.5$, $k_{synth\_out} = 0.1$, $R_{1\_in} = 4000$, $R_{2\_in} = 1000$, $R_{1\_out} = 1000$, $R_{2\_out} = 1000$, $f = 0.6$
4	$k_{synth\_in} = 0.1$, $k_{synth\_out} = 0.1$, $R_{1\_in} = 4000$, $R_{2\_in} = 1000$, $R_{1\_out} = 1000$, $R_{2\_out} = 1000$, $f = 0.4$, $k_{int1} = 5\times10^{-4}$
5	$k_{synth\_in} = 0.2$, $k_{synth\_out} = 0.0$, $R_{1\_in} = 1000$, $R_{2\_in} = 1000$, $R_{1\_out} = 1000$, $R_{2\_out} = 1000$, $f = 0.7$
6	$k_{synth\_in} = 0.1$, $k_{synth\_out} = 0.1$, $R_{1\_in} = 1000$, $R_{2\_in} = 1000$, $R_{1\_out} = 1000$, $R_{2\_out} = 1000$, $f = 0.4$, $K_{d1} = 1\times10^{-12}$, $k_{int1} = 5\times10^{-4}$
7	$k_{synth\_in} = 0.1$, $k_{synth\_out} = 0.1$, $R_{1\_in} = 1000$, $R_{2\_in} = 5000$, $R_{1\_out} = 500$, $R_{2\_out} = 1000$, $f = 0.4$, $K_{d1} = 1\times10^{-12}$

* Parameter definitions and their units are as defined in Table 3. Parameters unspecified in each run (including D_1, D_2, ϕ, d_G, ρ, r_g, r_m, r_{bead}, r_{core}, k_{TACE}, k_{deg}, K_{d1}, K_{d2}, k_{on1}, k_{on2}, k_{int1}, k_{int2}, k_{shed}, k_{rec1}, k_{rec2}, k_{t1}, k_{t2}, k_{deg1}, and k_{deg2}) have the same values as indicated in parentheses in Table 2.3.

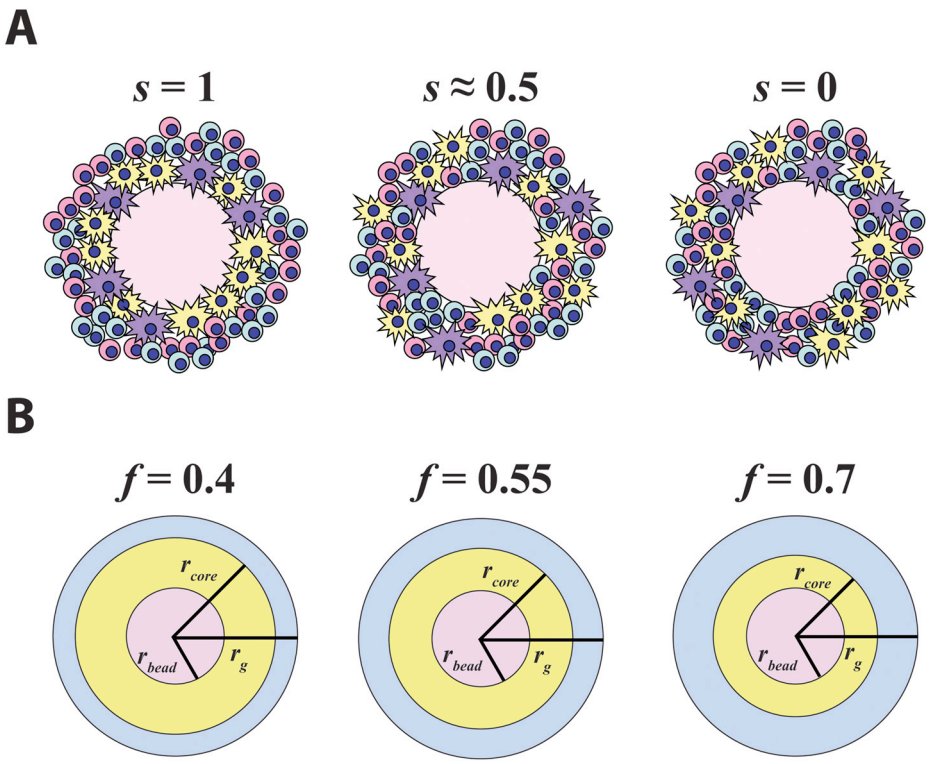

Fig. A.1 A schematic representation of parameters *s* and *f* used in the two-compartment model of PPD-bead granuloma. (A) Parameter *s* (separation index) is defined as indicated in Equation (2.5) to present the level of separation between different cell types in the granuloma model (other than sensitivity analysis) when all cell types are present. A separation index (*s*) of 0 is equivalent to a totally mixed cellular organization. Increasing *s* leads to an increase in the level of separation in the cellular organization as *s* = 1 represents a cellular organization in which macrophages and DCs are separate from but surrounded by lymphocytes. (B) Parameter *f* is defined as the fraction of cellular granuloma in the outer compartment and is only used when distinct cell types are not considered in the model (e.g. in sensitivity analysis). Increasing *f* results in a decrease in r_{core} while r_{bead} and r_g are maintained constant.

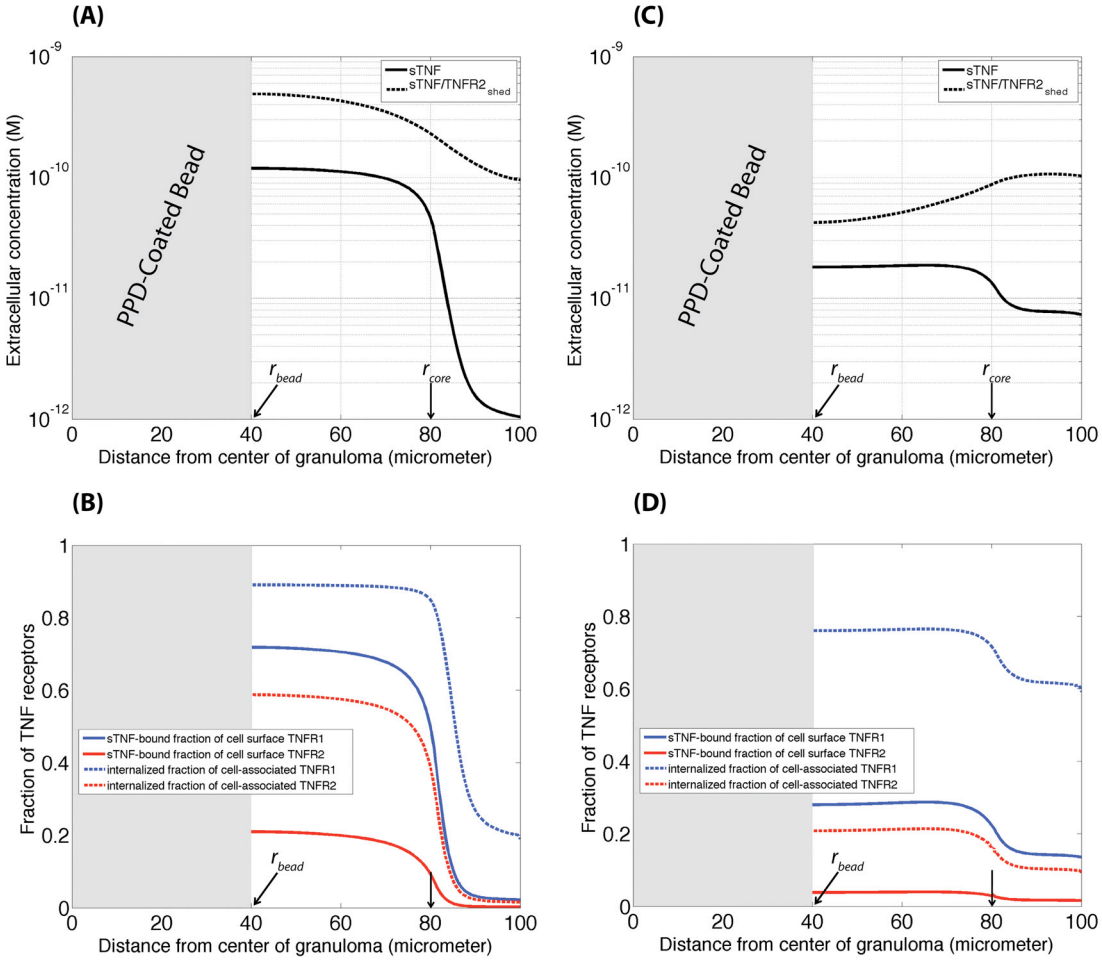

Fig. A.2 Simulation results for the steady-state concentration profiles of the model species, including sTNF, sTNF/TNFR2$_{shed}$, sTNF-bound and internalized TNFRs in a granuloma for two sets of parameter values: (A), (B) k_{synth_in} = 1 #/cell.s, k_{synth_out} = 0.01 #/cell.s, $R_{1\_in} = R_{2\_in} = R_{1\_out} = R_{2\_out}$ = 2000 #/cell. (C), (D) $k_{synth\_in} = k_{synth\_out}$ = 0.1 #/cell.s, $R_{1\_in} = R_{2\_in} = R_{1\_out}$ = 500 #/cell, R_{2_out} = 5000 #/cell. For both simulations, s = 1 and f = 0.5. Other parameter values are as listed in Table 2.2. Arrows indicate radius of the bead (r_{bead}) and radius at which the two compartments are separated (r_{core}).

A.2 References

1. Morgan A, Talbot RJ (1992) Effects of inhaled alpha-emitting actinides on mouse alveolar macrophages. Environ Health Perspect 97: 177-184.

2. Westermann J, Ehlers EM, Exton MS, Kaiser M, Bode U (2001) Migration of naive, effector and memory T cells: Implications for the regulation of immune responses. Immunol Rev 184: 20-37.

3. Eurelings M, Notermans NC, Wokke JH, Bosboom WM, Van den Berg LH (2002) Sural nerve T cells in demyelinating polyneuropathy associated with monoclonal gammopathy. Acta Neuropathol 103: 107-114.

Appendix B

Supplementary information for Chapter 3

The overall structure of the multi-scale agent-based model for the immune response to Mtb infection in the lung (as described in Chapter 3) as well as the detailed description of processes at each scale, including the stochastic cellular/tissue scale ABM and the deterministic ODE model of TNF/TNFR associated molecular processes, are presented. Fig. 3.1 in the main text of Chapter 3 indicates how these models exist separately and how they are linked. All parameter definitions and values are listed in Tables B.1, B.2 and B.5.

B.1 Overall structure of the multi-scale ABM

The multi-scale ABM was developed based on four considerations: an environment, agents (immune cells), ABM rules that govern the agents and their interactions, and the time-step (Δt) used to update events. The environment represents a two-dimensional section of lung parenchyma as a 100 × 100 square lattice that simulates an area of 2 mm × 2 mm. Each grid micro-compartment is thus scaled to the approximate size of a single human macrophage, 20 μm in diameter. Discrete agents (macrophages and T cells) are recruited from specific micro-compartments on the lattice that represent vascular sources. Cells move on the lattice and interact with each other and the environment based on the ABM rules that are defined based on known biological activities. Due to the size

difference between macrophages and T cells, up to two T cells are permitted to enter the same micro-compartment (with probability T_{moveT}). A T cell may also move into the same micro-compartment as a macrophage (with probability T_{moveM}). This model of cell spacing is a compromise between a realistic spatial representation and computational tractability and is consistent with observations on macrophage and T cell dynamics during development of mycobacterial granulomas that show granuloma-associated T cells squeeze through cell junctions created by a dense macrophage network [1].

Extracellular Mtb and soluble molecules, including chemokines (CCL2, CCL5 and CXCL9/10/11), soluble TNF (sTNF) and shed TNFR2 are simulated as continuous entities that can reside anywhere on the lattice. Extracellular Mtb grow in each micro-compartment. Soluble molecules diffuse among micro-compartments. Caseation represents inflammation of and damage to the lung parenchyma from macrophage cell death. In the ABM, caseation is defined to occur when a specific number (N_{caseum}) of infected or activated macrophages die in a micro-compartment. When a micro-compartment becomes caseated, any T cell present in the micro-compartment is killed and no further cells are permitted to enter the micro-compartment.

There are two major types of discrete agents in the model, macrophages and T cells. Macrophages are either resting (M_r, uninfected), infected (M_i; have taken up Mtb), chronically infected (M_{ci}; are unable to clear their intracellular Mtb due to a high number of bacterial load), or activated (M_a; can effectively kill bacteria). Three distinct T cell classes based on their functions are modeled. The T_γ class represents CD4 and CD8 pro-inflammatory T cells; T_c class represents cytotoxic T cells (CTLs); and T_{reg} class represents regulatory T cells.

Cell-cell interactions are governed by ABM rules that are updated within every ABM time-step (Δt = 10 min) and will be discussed in the next section. Single-cell molecular scale processes, including diffusion of soluble molecules on the lattice, secretion of chemokines from individual cells and TNF/TNFR dynamics at the single-cell level, that generally occur in shorter time-scales compared to cellular interactions, are updated within shorter time-steps (dt = 6 s). Thus, each molecular event is updated 100 times within each ABM time-step, the time in which each cellular scale event is updated once. The overall algorithm of the simulation takes the form outlined indicated in Fig. B.1 and will be presented in detail in the following sections.

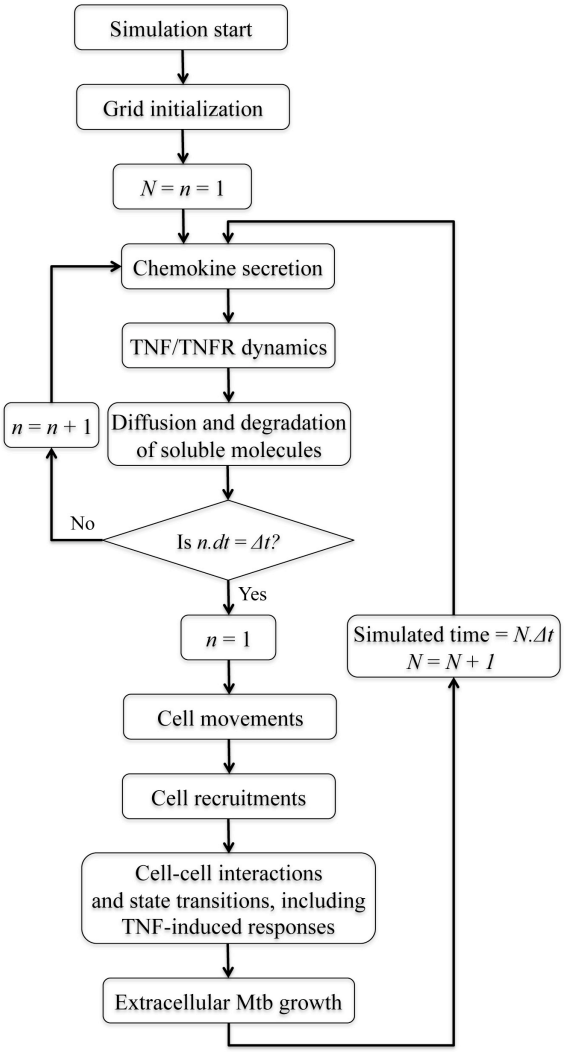

Fig. B.1 The overall outline of the multi-scale granuloma simulations.

B.2 Grid initialization

A 100 × 100 two-dimensional grid is created. Periodic boundary conditions for cell movement and Dirichlet boundary conditions (zero outside grid perimeter) for molecular diffusion is used. N_{source} = 50 vascular source locations are distributed on the grid. 49 of the vascular sources are randomly distributed in 7 × 7 approximately equally sized partitions on the grid. One other micro-compartment is randomly selected from the whole grid as the last vascular source. Initial resting macrophages that represent resident alveolar macrophages are randomly placed on the grid. One infected macrophage with

one intracellular Mtb is placed at the center of the grid. This is consistent with estimations of the minimum infection dose of Mtb that range from a single bacterium upward [2].

B.3 Cellular/tissue scale ABM rules

Cells move, become recruited to the site of infection and respond to local conditions depending on their type and state according to rules that represent known biological activities *in vivo*. ABM rules that govern cell behaviors and interactions are as follows. Because the main goal of this study is to investigate the role of TNF availability and kinetics of TNF-associated molecular scale processes on the outcome of Mtb infection, we discuss TNF-independent chemokine-related processes (such as chemokine secretion, diffusion and degradation) in addition to cellular scale immunological details of the ABM in this section.

B.3.1 Cell movements

i) Macrophages:

Macrophages may stay in place or move in 8 possible directions on the grid based on CCL2 and CCL5 chemokine concentrations in their Moore neighborhood, the nine micro-compartments around the cell location including the micro-compartment occupied by the cell. Speed of movement only depends on the state of macrophages with the highest speed for M_r and the smallest speed (zero) for M_{ci}. The differences among macrophage speeds are shown in the model by time intervals in which each macrophage attempts once to move (t_{moveMr}, t_{moveMi}, t_{moveMa}). There are minimum and maximum (saturating)

concentration thresholds (τ_{chem} and s_{chem}) for the effect of each chemokine on the cell movement. Chemokine concentrations below τ_{chem} or above s_{chem} do not have any effect on direction of movement. For simplicity we assume similar threshold values for all chemokines and cell types. Movement is random if chemokine concentrations in the Moore neighborhood are below τ_{chem} or above s_{chem}. Otherwise, CCL2 and CCL5 concentrations in the Moore neighborhood determine a linear probability distribution for movement. We assume a bias for macrophage movement to the micro-compartment with the highest chemokine concentration. Hence, the highest chemokine concentration in the Moore neighborhood is multiplied by a factor 1.5 before calculation of movement probabilities. Movement is blocked by a caseous micro-compartment or macrophage presence and if blocked, no extra attempt for moving is made.

ii) T cells:

T cell movements are updated in time intervals of length t_{MoveT} that is determined by the speed of T cell migration *in vivo*. Movement of T_γ cells depends on CCL2, CCL5 and CXCL9/10/11 concentrations in the Moore neighborhood. T_c cells move based on CCL5 and CXCL9/10/11 concentrations and T_{reg} cells move based on CCL5 concentrations. The details of T cell chemotactic movements are similar to what was described for macrophages. T cell movement is blocked by caseation. However, T cell movement to a micro-compartment that contains one macrophage or one T cell is possible with reduced probabilities, T_{moveM} and T_{moveT}, respectively.

B.3.2 Cell recruitments

i) Macrophages:

Resting macrophages are recruited every time-step from vascular sources based on available TNF and chemokine concentrations in each vascular source, provided that the vascular source is not caseated nor blocked by a macrophage or two T cells. For a macrophage to be recruited from a vascular source, the following condition must be met. If ω_{recTNF}.[sTNF] + $\omega_{recCCL2}$.[CCL2] + $\omega_{recCCL5}$.[CCL5] > τ_{recMac}, M_r recruitment occurs with a probability M_{recr}; where [sTNF], [CCL2] and [CCL5] are the numbers of sTNF, CCL2 and CCL5 molecules in the vascular source micro-compartment, respectively.

ii) T cells:

Recruitment of T cells begins after a delay (t_{delay}) that represents the time required for activation of the adaptive immune response following Mtb infection. T cell recruitment occurs for all vascular sources at every time-step with a probability T_{recr}. If T cell recruitment is allowed, then T cells of each class are recruited based on TNF and chemokine concentrations in each vascular source as described below, provided that the vascular source is not caseated or blocked by two T cells or one macrophage and another T cell. For a T_γ to be recruited, the following condition must be met. If ω_{recTNF}.[sTNF] + $\omega_{recCCL2}$.[CCL2] + $\omega_{recCCL5}$.[CCL5] + $\omega_{recCXCL9/10/11}$.[CXCL9/10/11] > $\tau_{recTgam}$, T_γ recruitment is permitted with a probability $T_{recTgam}$. Otherwise, T_c recruitment can occur. If ω_{recTNF}.[sTNF] + $\omega_{recCCL5}$.[CCL5] + $\omega_{recCXCL9/10/11}$.[CXCL9/10/11] > $\tau_{recTcyt}$, T_c recruitment is permitted with a probability $T_{recTcyt}$. Otherwise, T_{reg} recruitment can occur. If ω_{recTNF}.[sTNF] + $\omega_{recCCL5}$.[CCL5] > $\tau_{recTreg}$, T_{reg} recruitment is permitted with a probability $T_{recTreg}$.

B.3.3 Cell-cell interactions and state transitions

All cell-cell interactions and state transitions described below are updated every time-step for all cells.

i) Cell death due to age:

All macrophages that are initially distributed or recruited on the grid are assigned a lifespan selected from a uniform distribution between zero and max_{ageMac}. T cells are also assigned a lifespan randomly distributed between zero and $max_{ageTcell}$. M_a has a shortened lifespan of $max_{ageActive}$. At death, M_r and T cells are removed from the grid. At death, M_i and M_{ci} are removed from the grid and intracellular Mtb from dead cells are dispersed uniformly in the Moore neighborhood including the micro-compartment originally occupied by the cell. M_a death contributes to caseation of the micro-compartment.

ii) ABM rules for M_r:

There is a chance of STAT-1 activation in a time-step as a result of interaction between a M_r and IFN-γ producing T_γ cells with a probability ($n_{Tgam}.P_{STAT1}$); where, n_{Tgam} is the number of T_γ cells surrounding the M_r in the Moore neighborhood including the micro-compartment occupied by the M_r.

M_r is able to uptake or to kill extracellular Mtb that reside in the same micro-compartment. If the number of extracellular Mtb (B_{ext}) ≤ N_{rk}, M_r kills them. Otherwise, it either kills N_{rk} of the extracellular Mtb with probability P_k or becomes infected (M_i) after uptake of N_{rk} of the extracellular Mtb as its initial intracellular Mtb.

If both STAT1 and NF-κB are activated in a M_r and it is not already down-regulated by a T_{reg}, it becomes activated (M_a). If the remaining lifespan of such an activated macrophage is greater than $max_{ageActive}$, it will be shortened to $max_{ageActive}$.

iii) ABM rules for Mi:

Intracellular Mtb (B_{int}) replicate in M_i every time-step according to the following equation:

$$B_{\text{int}}(t + \Delta t) = (1 + \alpha_{Bi})B_{\text{int}}(t) \quad \text{(B.1)}$$

M_i is able to uptake but not kill extracellular bacteria from its micro-compartment with a probability ($P_{uptakeMi}$) that is computed as a function of B_{int} as follows:

$$P_{uptakeMi} = (N_c - B_{\text{int}})/100 \quad \text{(B.2)}$$

M_i takes up N_{rk} of extracellular bacteria if $B_{ext} > N_{rk}$. Otherwise, it takes up all extracellular bacteria that are available in the micro-compartment. If the number of intracellular Mtb (B_{int}) exceeds a threshold N_c, the M_i becomes chronically infected (M_{ci}).

There is a chance of STAT-1 activation in a time-step as a result of interaction between a M_i and IFN-γ producing T_γ cells with a probability ($n_{Tgam}.P_{STAT1}$) where, n_{Tgam} is the number of T_γ cells surrounding the M_i in the Moore neighborhood (including the micro-compartment occupied by the M_i). If both STAT1 and NF-κB are activated in a M_i and it is not already down-regulated by a T_{reg}, it becomes activated (M_a). If the remaining lifespan of such an activated macrophage is greater than $max_{ageActive}$, it will be shortened to $max_{ageActive}$.

iv) ABM rules for M_{ci}:

Intracellular Mtb (B_{int}) replicate in M_{ci} every time-step according to Equation 1. If the number of intracellular Mtb exceeds a threshold (N_{burst}), M_{ci} bursts and its intracellular Mtb are evenly distributed to the Moore neighborhood surrounding the M_{ci} (including the micro-compartment occupied by the cell). M_{ci} bursting contributes to caseation of the micro-compartment.

v) ABM rules for M_a:

M_a is capable of effectively killing extracellular Mtb. Each time-step, M_a kills N_{ak} of the extracellular Mtb in its micro-compartment.

vi) ABM rules for T_c:

If T_c is not already down-regulated by a T_{reg} and there is a M_i or M_{ci} present in the same micro-compartment as T_c, there is a chance of perforin/granulysin-mediated killing of M_i or M_{ci} with probability $P_{cytKill}$. M_i killing by a T_c kills all intracellular Mtb and contributes to caseation of the micro-compartment. In the case of M_{ci} killing, the intracellular Mtb are killed with probability $P_{cytKillClean}$. Otherwise, the intracellular Mtb will be uniformly distributed in the Moore neighborhood (including the micro-compartment occupied by the cell). M_{ci} killing by T_c also contributes to caseation of the micro-compartment.

vii) ABM rules for T_γ:

If T_γ is not already down-regulated by a T_{reg} and there is a M_i or M_{ci} present in the same micro-compartment as T_γ, there is a chance of Fas/FasL-induced apoptosis of M_i or M_{ci} with probability $P_{apop/Fas}$. As a result of apoptosis, half of the intracellular Mtb in M_i or M_{ci} will be killed and the other half will be equally distributed in the Moore neighborhood (including the micro-compartment occupied by the cell).

viii) ABM rules for T_{reg}:

Regulatory T cells suppress or down-regulate the action of T cells and macrophages through poorly understood mechanisms that may occur by cell contact, secretion of immunosuppressive cytokines or both [3,4]. T_{reg} here down-regulates all cells (macrophages, T_c and T_γ) in its Moore neighborhood including its own micro-compartment. Down-regulated states last for t_{regMac}, $t_{regTgam}$ and $t_{regTcyt}$ for macrophages,

T_c and T_γ cells, respectively. Consequences of T_{reg} down-regulation for each cell type is explained in sections that describe ABM rules for that cell type.

B.3.4 Extracellular Mtb growth

Growth of extracellular Mtb (B_{ext}) in all micro-compartments is calculated based on the following equation:

$$B_{ext}(t+\Delta t) = B_{ext}(t) + \alpha_{Be} B_{ext}(t)\left[1 - \frac{B_{ext}(t)}{1.1K_{be}}\right] \quad \text{(B.3)}$$

B.3.5 Chemokine secretion

M_i, M_{ci}, M_a, NF-κB activated M_r and NF-κB activated M_i are able to secrete chemokines, provided that they are not down-regulated by T_{reg}. The rates of chemokine secretion for different cell types are as follows. M_{ci}, M_a and NF-κB activated M_i are able to secrete chemokines with full secretion rates (r_{CCL2}, r_{CCL5} and r_{CXCL9}) as listed in Supplementary Table S1. NF-κB activated M_r and M_i cells that are not NF-κB activated secrete chemokines with half-full secretion rates ($0.5 \times r_{CCL2}$, $0.5 \times r_{CCL5}$ and $0.5 \times r_{CXCL9}$). Caseated micro-compartments also secrete attractants that attract immune cells. For simplicity, we use quarter-full rates of chemokine secretion to simulate the effect of such attractants ($0.25 \times r_{CCL2}$, $0.25 \times r_{CCL5}$ and $0.25 \times r_{CXCL9}$). Chemokine secretions to the micro-compartments on the grid are updated in time intervals of dt. Secretion of TNF will be discussed in TNF/TNFR dynamics section.

B.3.6 Diffusion and degradation

The equation for diffusion and degradation of chemokines and other soluble molecules, including sTNF and shed TNFR2, can be implemented numerically on the grid by using an iterative finite-difference method. This form of this equation in two dimensions is as follows:

$$\frac{\partial C}{\partial t} = D\left(\frac{\partial^2 C}{\partial x^2} + \frac{\partial^2 C}{\partial y^2}\right) - \delta C \qquad \text{(B.4)}$$

where C is the concentration of diffusing molecule that changes with time (t) in the x and y directions, D is the diffusion coefficient for the molecule in the diffusion environment, and δ is the degradation rate constant. Rewriting this equation using a finite difference approximation for discrete-time discrete-space diffusion on our grid gives:

$$C_{i,j}(t+dt) = (1-\delta dt)C_{i,j}(t) + \frac{\lambda}{4}\{C_{i-1,j}(t) + C_{i+1,j}(t) + C_{i,j-1}(t) + C_{i,j+1}(t) - 4C_{i,j}(t)\} \qquad \text{(B.5)}$$

where $C_{i,j}(t)$ is the concentration of the diffusing molecule in the micro-compartment (i,j) at time t and λ is determined as a function of D, diffusion time-step (dt = 6 s), and lattice spacing through which diffusion occurs (dx = 20 μm):

$$\lambda = \frac{4Ddt}{(dx)^2} \qquad \text{(B.6)}$$

Solution to Equation B.5 is stable if $\lambda < 1$. Thus, dt and dx must be picked accordingly.

B.3.7 Extensions and updates to the ABM rules described by Ray *et al*

In the previous sub-sections we presented the ABM rules describing cellular/tissue scale activities and interactions. As mentioned earlier, this model was first developed by Segovia-Juarez *et al* [5] and later extended by Ray *et al* [6]. The differences and

extensions of the cellular/tissue scale ABM used in this study compared with the ABM by Ray *et al* are as follows:

i) T_γ cells used to have two different active states. These two states have been merged, as they were not significantly different and introduced unnecessary complexity to the model.

ii) In order to have more realistic down-regulatory mechanisms in the model, T_c cells and macrophages according to the published data reviewed in [7], in addition to T_γ cells, can be down-regulated by T_{reg} cells. When down-regulated, T_c cells lose their cytotoxic capabilities for a fixed period of time $t_{regTcyt}$. Following macrophage down-regulation, STAT1 is deactivated and the macrophage does nothing but moves for a fixed period of time t_{regMac}.

iii) The extracellular bacteria threshold for NF-κB activation, B_{actM}, has been extended to consider the Moore neighborhood, rather than the local micro-compartment.

iv) We assume that a fully activated macrophage can only secrete TNF and chemokines at the maximal rate. Thus, resting macrophages that have been NF-κB activated but have not been STAT-1 activated now secrete TNF and chemokines at half rate compared with activated macrophages.

v) We did not consider possibility of Mtb uptake by infected macrophages in our previous model. Infected macrophages now have the ability to uptake additional extracellular bacteria; the probability of extracellular Mtb uptake is inversely proportional to the number of intracellular Mtb that reside in the macrophage.

vi) TNF-induced NF-κB activation and apoptosis were previously modeled as events that occurred with probabilities of 100% and 4% (approximated via uncertainty analysis) for

extracellular TNF concentrations above specific thresholds. Here, we have revised TNF-induced cell responses as will be discussed in detail in later sections.

vii) We have revised the user interface for performing our modeling studies so that we can easily visualize and track different aspects of the granuloma, including the structure and molecular concentration gradients, as it forms and is maintained. In order to satisfy the cross-platform requirement, we make use of the Qt framework. Qt is a C++ framework for developing cross-platform applications with a graphical user interface (GUI).

B.4 ODEs that govern molecular scale TNF/TNFR dynamics

The binding interactions and reactions controlling TNF/TNFR dynamics at the single-cell level regardless of the cell type are schematically illustrated in the main text (Fig. 3.1B). TNF is first synthesized by TNF-producing cells (M_i, M_{ci}, M_a, NF-κB activated M_r, T_γ and T_c), if not down-regulated by T_{reg} cells, as a membrane-bound precursor form (mTNF) that can then be processed and released as a soluble form (sTNF) into extracellular spaces. This processing occurs via a cell-associated metalloproteinase called TACE. Two types of TNF receptors (TNFR1 and TNFR2) are synthesized and expressed on the cell surface as free receptors. Soluble TNF (sTNF) reversibly binds to TNFRs on the cell membrane. sTNF-bound cell surface TNFR1 internalizes and sTNF-bound cell surface TNFR2 may undergo internalization or shedding into extracellular spaces [8]. Internalized receptors may degrade or recycle to the cell membrane where they can re-bind to sTNF [9]. Ligand-free TNFRs also turn over (internalize) [9,10]. Intact sTNF may dissociate from the shed sTNF/TNFR2 complex in the extracellular space [11]. We

modeled these molecular processes based on mass action kinetics as shown in Table B.5; model equations are listed in Table B.4; definitions and values of the rate constants are given in Table B.2. Note that the rates of mTNF synthesis and release from the cell membrane and TNFR synthesis (k_{Synth}, $k_{TACE,}$ V_{r1} and V_{r2}) are cell type/state-specific as indicated in Table B.2, but other rate constant values are common between all cells. Note that this ODE model was presented previously [12] and is described here for completeness.

In the multi-scale model described in this work, the rates of mTNF synthesis for different cell types are as follows. M_{ci}, M_a and NF-κB activated M_i are able to synthesize mTNF with a full rate ($k_{synth} = k_{synthMac}$) as shown in Table B.2. NF-κB activated M_r and NF-κB deactivated M_i express mTNF with a half-full rate ($k_{synth} = 0.5 \times k_{synthMac}$). T_γ cells and T_c cells express mTNF with rates $k_{synthTcell}$ and $0.1 \times k_{synthTcell}$, respectively. T_{reg}-down-regulated cells do not express TNF. TACE activity is also assumed to be cell type-dependent as shown in Table B.2.

TNF/TNFR dynamics model ODEs are solved for each individual cell on the grid in combination with TNF diffusion and degradation equations using the time-step *dt*. Soluble molecules in the model (sTNF and sTNF/$TNFR2_{shed}$) are expressed as volumetric concentration units (e.g. M), whereas cell-associated species are expressed as # of molecules per cell. Thus, when a membrane-bound molecule releases to the extracellular space (i.e. the micro-compartment occupied by the cell), or when a soluble molecule binds to the cell membrane, a scaling factor (ρ/N_{av}) is required as indicated in Supplementary Table S4, where ρ is the cell density in the micro-compartment and can be computed as $(dx)^{-3}$ assuming that each micro-compartment is a cube of side *dx*.

B.5 NF-κB activation and apoptosis

TNF-induced NF-κB activation and TNF-induced apoptosis are modeled, as described in the main text, as Poisson processes with rate parameters computed as functions of molecular concentrations from the ODE model. NF-κB activation is checked once for all M_r and M_i within each ABM time-step (Δt). NF-κB pathway can also be activated in M_r or M_i if the number of extracellular bacteria (B_{ext}) in the Moore neighborhood micro-compartments exceeds a threshold (B_{actM}). TNF-induced apoptosis is checked once for all cells on the grid within each time-step (Δt). If the apoptotic cell is a M_i or M_{ci}, half of the intracellular Mtb in M_i or M_{ci} will be killed as a result of apoptosis and the other half will be equally distributed in the Moore neighborhood including the micro-compartment occupied by the cell.

Table B.1 TNF-independent and cellular/tissue scale parameters, definitions and values estimated from literature as described in [6], or approximated via uncertainty analysis as described in Chapter 3 Methods. Further descriptions of parameters, if needed, are presented in Appendix B.

Parameter	Parameter description	Value*
N_{source}	Number of vascular sources	50
N_{caseum}	Number of qualified cell deaths required for caseation	7
D_{chem} (cm^2/s)	Diffusion coefficient of chemokines	10^{-8}-10^{-7} (5.2×10^{-8})
δ_{chem} (s^{-1})	Chemokine degradation rate constant	10^{-4}-10^{-3} (4.58×10^{-4})
τ_{chem} (molecules)	Minimum chemokine concentration threshold	1-10 (2)
s_{chem} (molecules)	Saturating chemokine concentration threshold	10^{3}-10^{4} (2000)
M_{init}	Initial number of resident macrophages	105
max_{ageMac} (day)	Maximum lifespan of macrophages	100
$max_{ageActive}$ (day)	Maximum lifespan of an active macrophage	10
t_{regMac} (hours)	Macrophage inactivity time after down-regulation by T_{reg}	12
t_{moveMr} (min)	Time interval for M_r movement	20
t_{moveMa} (hour)	Time interval for M_a movement	7.8
t_{moveMi} (hour)	Time interval for Mi movement	24
r_{CCL2} (molecules per 10 min)	Full secretion rate of CCL2	35.5
r_{CCL5} (molecules per 10 min)	Full secretion rate of CCL5	35.5
r_{CXCL9} (molecules per 10 min)	Full secretion rate of CXCL9/10/11	71
ω_{recTNF}	Effect of TNF on cell recruitment	1
$\omega_{recCCL2}$	Effect of CCL2 on cell recruitment	0.0507
$\omega_{recCCL5}$	Effect of CCL5 on cell recruitment	0.0507
$\omega_{recCXCL9/10/11}$	Effect of CXCL9 on cell recruitment	0.0254
N_{rk}	Number of extracellular Mtb engulfed by M_r or M_i	1
P_k	Probability of M_r killing bacteria	0.01-0.1 (0.015)
B_{actM}	Number of extracellular Mtb activating NF-κB in a mac	50-150 (110)
N_c	Number of intracellular Mtb for $M_i \rightarrow M_{ci}$ transition	10
N_{burst}	Number of intracellular Mtb that leads to M_{ci} bursting	20-30 (20)
P_{STAT1}	Probability of STAT-1 activation in M_r or M_i	0.001-0.1 (0.085)
N_{ak}	Number of extracellular Mtb killed by M_a each time-step	10
τ_{recMac}	TNF/chemokine threshold for M_r recruitment	0.01-0.1 (0.023)
M_{recr}	Probability of M_r recruitment	0.01-0.1 (0.04)
$max_{ageTcell}$ (day)	Maximum lifespan of T cells	3
t_{delay} (day)	T cell recruitment delay	20
T_{moveM}	Probability of T cell moving to a mac-containing location	0.001-0.1 (0.014)
T_{moveT}	Probability of T cell moving to a T cell-containing location	0.001-0.1 (0.08)
T_{recr}	Probability of T cell recruitment	0.05-0.5 (0.15)
$t_{regTgam}$ (min)	T_γ inactivity time after down-regulation by T_{reg}	100
$P_{apop/Fas}$	Probability of Fas/FasL apoptosis by T_γ	0.01-0.1 (0.06)
$\tau_{recTgam}$	TNF/chemokine threshold for T_γ recruitment	0.1-1.0 (0.4)
$T_{recTgam}$	Probability of T_γ recruitment	0.54
$t_{regTcyt}$ (min)	T_c inactivity time after down-regulation by T_{reg}	100
$\tau_{recTcyt}$	TNF/chemokine threshold for T_c recruitment	0.1-1.0 (0.4)
$T_{recTcyt}$	Probability of T_c recruitment	0.36
$P_{cytKill}$	Probability of T_c killing M_i or M_{ci}	0.02 0.2 (0.12)
$P_{cytKillClean}$	Probability of T_c killing all intracellular Mtb by killing M_{ci}	0.75
$\tau_{recTreg}$	TNF/chemokine threshold for T_{reg} recruitment	0.01-0.1 (0.05)
$T_{recTreg}$	Probability of T_{reg} recruitment	0.1
α_{Bi} (per 10 min)	Intracellular Mtb growth rate	2×10^{-4}-2×10^{-3} (1.4×10^{-3})
α_{Be} (per 10 min)	Extracellular Mtb growth rate	10^{-4}-10^{-3} (7×10^{-4})
K_{be}	Capacity of a micro-compartment for extracellular Mtb	200

* Parameters used for sensitivity analysis are indicated by their ranges of values. Values in parentheses are used to generate containment baseline.

Table B.2 Molecular/single-cell scale TNF/TNFR parameters, definitions and values estimated from literature

Parameter	Parameter description	Value*	Reference
$k_{synthMac}$ (#/cell.s)	Full synthesis rate of mTNF for macrophages	10^{-1}-1 (0.21)	[12]
$k_{synthTcell}$ (#/cell.s)	Full synthesis rate of mTNF for T cells	10^{-2}-10^{-1} (0.021)	[13]
$TNFR1_{mac}$ (#/cell)	TNFR1 density on the surface of macrophages	500-5000 (1100-1900) †	[12,14-16]
$TNFR1_{Tcell}$ (#/cell)	TNFR1 density on the surface of T cells	500-5000 (400-1200) †	[12,14-16]
$TNFR2_{mac}$ (#/cell)	TNFR2 density on the surface of macrophages	500-5000 (400-800) †	[12,14-16]
$TNFR2_{Tcell}$ (#/cell)	TNFR2 density on the surface of T cells	500-5000 (600-800) †	[12,14-16]
D_1 (cm^2/s) ‡	Diffusion coefficient of sTNF	10^{-8}-10^{-7} (5.2×10^{-8})	[17,18]
D_2 (cm^2/s) ‡	Diffusion coefficient of shed TNF/TNFR2 complex	10^{-8}-10^{-7} (3.2×10^{-8})	[17,18]
k_{TACE_Mac} (s^{-1})	Rate constant for TNF release by TACE activity on a macrophage	10^{-4}-10^{-3} (4.4×10^{-4})	[12,19-21]
k_{TACE_Tcell} (s^{-1})	Rate constant for TNF release by TACE activity on a T cell	10^{-5}-10^{-4} (4.4×10^{-5})	
δ_{TNF} (s^{-1})	sTNF degradation rate constant	10^{-4}-10^{-3} (4.58×10^{-4})	[22]
K_{d1} (M)	Equilibrium dissociation constant of sTNF/TNFR1	10^{-12}-10^{-10} (1.9×10^{-11})	[14,23]
K_{d2} (M)	Equilibrium dissociation constant of sTNF/TNFR2	10^{-10}-10^{-9} (4.2×10^{-10})	[14,23,24]
k_{on1} ($M^{-1}s^{-1}$)	sTNF/TNFR1 association rate constant	10^7-10^8 (2.8×10^7)	[23]
k_{on2} ($M^{-1}s^{-1}$)	sTNF/TNFR2 association rate constant	10^7-10^8 (3.5×10^7)	[23]
k_{off1} (s^{-1})	sTNF/TNFR1 dissociation rate constant	$k_{on1}\times K_{d1}$	
k_{off2} (s^{-1})	sTNF/TNFR2 dissociation rate constant	$k_{on2}\times K_{d2}$	
k_{int1} (s^{-1})	TNFR1 internalization rate constant	1.5×10^{-4}-1.5×10^{-3} (7.7×10^{-4})	[8,23]
k_{int2} (s^{-1})	TNFR2 internalization rate constant	3.9×10^{-4}-5×10^{-4} (4.6×10^{-4})	[24]
k_{shed} (s^{-1})	TNFR2 shedding rate constant	3.9×10^{-4}-1.5×10^{-3} (5×10^{-4})	[8,20]
k_{rec1} (s^{-1})	TNFR1 recycling rate constant	8.8×10^{-5}-5.5×10^{-4} (1.8×10^{-5})	[9,10]
k_{rec2} (s^{-1})	TNFR2 recycling rate constant	8.8×10^{-5}-5.5×10^{-4} (1.8×10^{-5})	[9,10]
k_{t1} (s^{-1})	TNFR1 turn-over rate constant	3×10^{-4}-5×10^{-4} (3.8×10^{-4})	[9,10]
k_{t2} (s^{-1})	TNFR2 turn-over rate constant	3×10^{-4}-5×10^{-4} (3.8×10^{-4})	[9,10]
k_{deg1} (s^{-1})	TNFR1 degradation rate constant	10^{-5}-10^{-4} (5×10^{-5})	[9,10,14,25]
k_{deg2} (s^{-1})	TNFR2 degradation rate constant	10^{-5}-10^{-4} (5×10^{-5})	[9,10,14,25]
V_{r1_mac} (#/cell.s)	Cell surface TNFR1 synthesis rate constant for macrophages	$k_{t1}\times TNFR1_{mac}$	
V_{r1_Tcell} (#/cell.s)	Cell surface TNFR1 synthesis rate constant for T cells	$k_{t1}\times TNFR1_{Tcell}$	
V_{r2_mac} (#/cell.s)	Cell surface TNFR2 synthesis rate constant for macrophages	$k_{t2}\times TNF21_{mac}$	
V_{r2_Tcell} (#/cell.s)	Cell surface TNFR2 synthesis rate constant for T cells	$k_{t2}\times TNF21_{Tcell}$	

* Ranges of parameter values used for sensitivity analysis are indicated out of parentheses. Values in parentheses are used to generate baseline model results.

† Baseline model values for TNFR densities on each recruited individual cell was randomly chosen from the range shown in parentheses.

‡ Diffusion coefficients of the soluble species in granuloma were estimated in line with estimates for diffusible factors of similar molecular weight in tumors [17,18].

Table B.3 Definition of reaction species, reactions describing TNF/TNFR processes and their rates (v_i).

Reaction species			
mTNF	Membrane-bound TNF	*sTNF/TNFR2*	sTNF/TNFR2 complex on the membrane
sTNF	Extracellular soluble TNF	$sTNF/TNFR1_i$	Internalized sTNF/TNFR1 complex
TNFR1	Cell surface TNF receptor 1	$sTNF/TNFR2_i$	Internalized sTNF/TNFR2 complex
TNFR2	Cell surface TNF receptor 2	$sTNF/TNFR2_{shed}$	Shed sTNF/TNFR2 complex
sTNF/TNFR1	sTNF/TNFR1 complex on the membrane		

Model reactions			
1	*mTNF synthesis* $v_1 = k_{Synth}$	9	*TNFR2 synthesis* $v_9 = V_{r2}$
2	$mTNF \rightarrow sTNF$ $v_2 = k_{TACE}[mTNF]$	10	$TNFR1 \rightarrow TNFR1_i$ $v_{10} = k_{i1}[TNFR1]$
3	$sTNF + TNFR1 \leftrightarrow sTNF/TNFR1$ $v_3 = k_{on1}[sTNF][TNFR1] - k_{off1}[sTNF/TNFR1]$	11	$TNFR2 \rightarrow TNFR2_i$ $v_{11} = k_{i2}[TNFR2]$
4	$sTNF + TNFR2 \leftrightarrow sTNF/TNFR2$ $v_4 = k_{on2}[sTNF][TNFR2] - k_{off2}[sTNF/TNFR2]$	12	$sTNF/TNFR1_i \rightarrow degradation$ $v_{12} = k_{deg1}[sTNF/TNFR1_i]$
5	$sTNF/TNFR1 \rightarrow sTNF/TNFR1_i$ $v_5 = k_{int1}[sTNF/TNFR1]$	13	$sTNF/TNFR2_i \rightarrow degradation$ $v_{13} = k_{deg2}[sTNF/TNFR2_i]$
6	$sTNF/TNFR2 \rightarrow sTNF/TNFR2_i$ $v_6 = k_{int2}[sTNF/TNFR2]$	14	$sTNF/TNFR1_i \rightarrow TNFR1$ $v_{14} = k_{rec1}[sTNF/TNFR1_i]$
7	$sTNF/TNFR2 \rightarrow sTNF/TNFR2_{shed}$ $v_7 = k_{shed}[sTNF/TNFR2]$	15	$sTNF/TNFR2_i \rightarrow TNFR2$ $v_{15} = k_{rec2}[sTNF/TNFR2_i]$
8	*TNFR1 synthesis* $v_8 = V_{r1}$	16	$sTNF/TNFR2_{shed} \rightarrow sTNF + TNFR2_{shed}$ $v_{16} = k_{off2}[sTNF/TNFR2_{shed}]$

Table B.4 Differential equations describing TNF/TNFR processes.

$$\frac{d[mTNF]}{dt} = v_1 - v_2$$

$$\frac{d[sTNF]}{dt} = (\frac{\rho}{N_{av}})(v_2 - v_3 - v_4) + v_{16}$$

$$\frac{d[TNFR1]}{dt} = v_8 - v_3 - v_{10} + v_{14}$$

$$\frac{d[TNFR2]}{dt} = v_9 - v_4 - v_{11} + v_{15}$$

$$\frac{d[sTNF/TNFR1]}{dt} = v_3 - v_5$$

$$\frac{d[sTNF/TNFR2]}{dt} = v_4 - v_6 - v_7$$

$$\frac{d[sTNF/TNFR1_i]}{dt} = v_5 - v_{12} - v_{14}$$

$$\frac{d[sTNF/TNFR2_i]}{dt} = v_6 - v_{13} - v_{15}$$

$$\frac{d[sTNF/TNFR2_{shed}]}{dt} = (\frac{\rho}{N_{av}})v_7 - v_{16}$$

Table B.5 Linking parameters used to calculate the probability of TNF-induced cell responses, definitions and values estimated in this study

Parameter	Parameter description	Value*
$k_{NF\text{-}\kappa B}$ ((#/cell)$^{-1}$s^{-1})	Rate constant for TNF-induced NF-κB activation in macrophages	10^{-8}-10^{-7} (3.97×10^{-8})
k_{apopt} ((#/cell)$^{-1}$s^{-1})	Rate constant for TNF-induced apoptosis in all cell types	5×10^{-10}-5×10^{-9} (1.33×10^{-9})
$\tau_{NF\text{-}\kappa B}$ (#/cell)	Cell surface sTNF/TNFR1 threshold for TNF-induced NF-κB activation	5-50 (26)
τ_{apopt} (#/cell)	Internalized sTNF/TNFR1 threshold for TNF-induced apoptosis	50-500 (300)

* Ranges of parameter values used for sensitivity analysis are indicated. Values in parentheses are used to generate baseline model results.

Table B.6 LHS sensitivity analysis results for the effect of TNF-independent and cellular scale parameters on model outputs at day 200 post-infection. Parameter definitions are presented in Table B.1.

	D_{chem}	δ_{chem}	τ_{chem}	P_{STAT1}	M_{recr}	T_{moveM}	T_{recr}	$P_{apop/Fas}$	$\tau_{recTgam}$	α_{Bi}	α_{Be}
TNF function-related outputs											
$(\text{No. apoptosis})_{\text{Macs}}$	-	+	+		++	---	---	-	+++	+++	
$(\text{No. apoptosis})_{\text{Mr}}$	-	+			+++	---	---		+++	+++	
$(\text{No. apoptosis})_{\text{Mi \& Mci}}$	--	++	+	-	+	---	---		+++	+++	
$(\text{No. apoptosis})_{\text{Ma}}$					+++	---	---	-	+++	+++	
$(\text{No. apoptosis})_{\text{T cells}}$	-	++				---	---	-	++	+++	
$(\text{No. NF}\kappa\text{B activation})_{\text{Mr}}$		+			+++	---	---		+++	+++	
$(\text{No. NF}\kappa\text{B activation})_{\text{Mi}}$	-	++	+	-	+	---	---		+++	+++	
Cellular-level outputs											
B_{int} (intracellular Mtb)		+++	+	-		---	---		+++	+++	
B_{ext} (extracellular Mtb)	---	+++		---		---	---		+++	+++	++
B_{tot}	---	+++		---		---	---		+++	+++	+
Total Macrophages			+		+++	---	-		+++	+++	
M_r			+		+++	--			+++	++	
M_i		+++	++	-		---	---		+++	+++	
M_{ci}		+++		--		---	---		+++	+++	
M_a		+	+			---	---		+++	+++	
Total T cells			+			---		-	+++	+++	
T_γ	+		+			---		-	+++	+++	
T_c	+		+			---		-	+++	+++	
T_{reg}			+			---			+++	+++	
Tissue-level outputs											
Caseation		++	+	-	+++	---	---		+++	+++	
Granuloma size				-	++	---	---	-	+++	+++	
Tissue concentrations											
$[\text{sTNF}]_{\text{avg}}$		+++	+	-		---	---		+++	+++	
$[\text{Chemokines}]_{\text{avg}}$			+			---	---		+++	+++	

Only parameters with significant PRCC values are indicated. Significant positive and negative correlations are shown using +/- as follows:

-/+, $0.001 < p\text{-value} < 0.01$

--/++, $0.0001 < p\text{-value} < 0.001$

---/+++, $p\text{-value} < 0.0001$

Table B.7 LHS sensitivity analysis results for the effect of TNF/TNFR-associated molecular and linking parameters on model outputs at day 200 post-infection. Parameter definitions are presented in Tables B.2 and B.5.

	D_1	δ_{TNF}	$k_{synthMac}$	K_{d1}	k_{int1}	k_{rec1}	$TNFR1_{mac}$	k_{apop}	τ_{apop}	$k_{NF\kappa B}$	$\tau_{NF\kappa B}$
TNF function-related outputs											
(No. apoptosis)$_{Macs}$	+	---	+++	-		---		++	---		
(No. apoptosis)$_{Mr}$	+++	---	+++	-		---		+	---		
(No. apoptosis)$_{Mi\ \&\ Mci}$			---	---	+++	---		+++	---	---	
(No. apoptosis)$_{Ma}$		---	+++	-		---		+	-		
(No. apoptosis)$_{T\ cells}$			+++			--			--		
(No. NFκB activation)$_{Mr}$	+++	--	+++		---	+++		-		+++	---
(No. NFκB activation)$_{Mi}$	-		---	-		+					
Cellular-level outputs											
B_{int} (intracellular Mtb)		++	---		+		-			---	++
B_{ext} (extracellular Mtb)		++	---		+		-			---	++
B_{tot}		++	---	+	+		-			---	++
Total Macrophages		+++	---	+			---			---	++
M_r		++	---	+	+		---			---	++
M_i		+	---		+		-			---	+
M_{ci}		+	---		+		-			---	++
M_a			---							---	
Total T cells		+	---	+			-			---	+
T_γ		+	---	+			-			---	+
T_c		+	---	+			-			---	+
T_{reg}		+	---	+	+		-			---	+
Tissue-level outputs											
Caseation		+++	---	+++	+	+++	---	-		---	++
Granuloma size		+++	---	++	+		--			---	+++
Tissue concentrations											
$[sTNF]_{avg}$			---	+			-			---	+
$[Chemokines]_{avg}$		+	---	+			-			---	+

Only parameters with significant PRCC values are indicated. Significant positive and negative correlations are shown using +/- as follows:

-/+, $0.001 < p\text{-value} < 0.01$

--/++, $0.0001 < p\text{-value} < 0.001$

---/+++, $p\text{-value} < 0.0001$

B.6 References

1. Egen JG, Rothfuchs AG, Feng CG, Winter N, Sher A, et al. (2008) Macrophage and T cell dynamics during the development and disintegration of mycobacterial granulomas. Immunity 28: 271-284.

2. Russell DG, Barry CE,3rd, Flynn JL (2010) Tuberculosis: What we don't know can, and does, hurt us. Science 328: 852-856.

3. Baatar D, Olkhanud P, Sumitomo K, Taub D, Gress R, et al. (2007) Human peripheral blood T regulatory cells (tregs), functionally primed CCR4+ tregs and unprimed CCR4- tregs, regulate effector T cells using FasL. J Immunol 178: 4891-4900.

4. Thornton AM, Shevach EM (1998) CD4+CD25+ immunoregulatory T cells suppress polyclonal T cell activation in vitro by inhibiting interleukin 2 production. J Exp Med 188: 287-296.

5. Segovia-Juarez JL, Ganguli S, Kirschner D (2004) Identifying control mechanisms of granuloma formation during M. tuberculosis infection using an agent-based model. J Theor Biol 231: 357-376.

6. Ray JC, Flynn JL, Kirschner DE (2009) Synergy between individual TNF-dependent functions determines granuloma performance for controlling mycobacterium tuberculosis infection. J Immunol 182: 3706-3717.

7. Sakaguchi S, Miyara M, Costantino CM, Hafler DA (2010) FOXP3+ regulatory T cells in the human immune system. Nat Rev Immunol 10: 490-500.

8. Higuchi M, Aggarwal BB (1994) TNF induces internalization of the p60 receptor and shedding of the p80 receptor. J Immunol 152: 3550-3558.

9. Bajzer Z, Myers AC, Vuk-Pavlovic S (1989) Binding, internalization, and intracellular processing of proteins interacting with recycling receptors. A kinetic analysis. J Biol Chem 264: 13623-13631.

10. Vuk-Pavlovic S, Kovach JS (1989) Recycling of tumor necrosis factor-alpha receptor in MCF-7 cells. FASEB J 3: 2633-2640.

11. Aderka D, Engelmann H, Maor Y, Brakebusch C, Wallach D (1992) Stabilization of the bioactivity of tumor necrosis factor by its soluble receptors. J Exp Med 175: 323-329.

12. Fallahi-Sichani M, Schaller MA, Kirschner DE, Kunkel SL, Linderman JJ (2010) Identification of key processes that control tumor necrosis factor availability in a tuberculosis granuloma. PLoS Comput Biol 6: e1000778.

13. Marino S, Sud D, Plessner H, Lin PL, Chan J, et al. (2007) Differences in reactivation of tuberculosis induced from anti-TNF treatments are based on bioavailability in granulomatous tissue. PLoS Comput Biol 3: 1909-1924.

14. Imamura K, Spriggs D, Kufe D (1987) Expression of tumor necrosis factor receptors on human monocytes and internalization of receptor bound ligand. J Immunol 139: 2989-2992.

15. Pocsik E, Mihalik R, Ali-Osman F, Aggarwal BB (1994) Cell density-dependent regulation of cell surface expression of two types of human tumor necrosis factor receptors and its effect on cellular response. J Cell Biochem 54: 453-464.

16. van Riemsdijk-Van Overbeeke IC, Baan CC, Knoop CJ, Loonen EH, Zietse R, et al. (2001) Quantitative flow cytometry shows activation of the TNF-alpha system but not of the IL-2 system at the single cell level in renal replacement therapy. Nephrol Dial Transplant 16: 1430-1435.

17. Nugent LJ, Jain RK (1984) Extravascular diffusion in normal and neoplastic tissues. Cancer Res 44: 238-244.

18. Pluen A, Boucher Y, Ramanujan S, McKee TD, Gohongi T, et al. (2001) Role of tumor-host interactions in interstitial diffusion of macromolecules: Cranial vs. subcutaneous tumors. Proc Natl Acad Sci U S A 98: 4628-4633.

19. Newton RC, Solomon KA, Covington MB, Decicco CP, Haley PJ, et al. (2001) Biology of TACE inhibition. Ann Rheum Dis 60 Suppl 3: iii25-32.

20. Crowe PD, Walter BN, Mohler KM, Otten-Evans C, Black RA, et al. (1995) A metalloprotease inhibitor blocks shedding of the 80-kD TNF receptor and TNF processing in T lymphocytes. J Exp Med 181: 1205-1210.

21. Solomon KA, Covington MB, DeCicco CP, Newton RC (1997) The fate of pro-TNF-alpha following inhibition of metalloprotease-dependent processing to soluble TNF-alpha in human monocytes. J Immunol 159: 4524-4531.

22. Cheong R, Bergmann A, Werner SL, Regal J, Hoffmann A, et al. (2006) Transient IkappaB kinase activity mediates temporal NF-kappaB dynamics in response to a wide range of tumor necrosis factor-alpha doses. J Biol Chem 281: 2945-2950.

23. Grell M, Wajant H, Zimmermann G, Scheurich P (1998) The type 1 receptor (CD120a) is the high-affinity receptor for soluble tumor necrosis factor. Proc Natl Acad Sci U S A 95: 570-575.

24. Pennica D, Lam VT, Mize NK, Weber RF, Lewis M, et al. (1992) Biochemical properties of the 75-kDa tumor necrosis factor receptor. characterization of ligand binding, internalization, and receptor phosphorylation. J Biol Chem 267: 21172-21178.

25. Tsujimoto M, Yip YK, Vilcek J (1985) Tumor necrosis factor: Specific binding and internalization in sensitive and resistant cells. Proc Natl Acad Sci U S A 82: 7626-7630.

Appendix C

Supplementary information for Chapter 4

C.1 Supplementary tables

Supplementary information for Chapter 4 includes: ABM parameter description and estimated values (Table C.1), TNF/TNFR dynamics model equations and parameters (Table C.2, C.3), NF-κB dynamics model equations and parameters (Table C.4-6), and LHS sensitivity analysis results (Table C.7, C.8).

Table C.1 TNF-independent and cellular/tissue scale parameters, definitions and values estimated from literature or approximated via uncertainty analysis as described in [1,2].

Parameter	Parameter description	Value*
N_{source}	Number of vascular sources	50
N_{caseum}	Number of qualified cell deaths required for caseation	10
D_{chem} (cm^2/s)	Diffusion coefficient of chemokines	10^{-8}-10^{-7} (5.2×10^{-8})
δ_{chem} (s^{-1})	Chemokine degradation rate constant	10^{-4}-10^{-3} (4.58×10^{-4})
τ_{chem} (molecules)	Minimum chemokine concentration threshold	1-10 (2)
s_{chem} (molecules)	Saturating chemokine concentration threshold	10^3-10^4 (2000)
M_{init}	Initial number of resident macrophages	105
max_{ageMac} (day)	Maximum lifespan of macrophages	100
$max_{ageActive}$ (day)	Maximum lifespan of an active macrophage	10
t_{regMac} (hours)	Macrophage inactivity time after down-regulation by T_{reg}	12
t_{moveMr} (min)	Time interval for M_r movement	20
t_{moveMa} (hour)	Time interval for M_a movement	7.8
t_{moveMi} (hour)	Time interval for Mi movement	24
ω_{recTNF}	Effect of TNF on cell recruitment	1
$\omega_{recCCL2}$	Effect of CCL2 on cell recruitment	0.0507
$\omega_{recCCL5}$	Effect of CCL5 on cell recruitment	0.0507
$\omega_{recCXCL9/10/11}$	Effect of CXCL9 on cell recruitment	0.0254
N_{rk}	Number of extracellular Mtb engulfed by M_r or M_i	1
P_k	Probability of M_r killing bacteria	0.01-0.1 (0.015)
B_{actM}	Number of extracellular Mtb activating a macrophage	50-150 (110)
N_c	Number of intracellular Mtb for $M_i \rightarrow M_{ci}$ transition	10
N_{burst}	Number of intracellular Mtb that leads to M_{ci} bursting	20-30 (20)
P_{STAT1}	Probability of STAT-1 activation in M_r or M_i	0.001-0.1 (0.085)
N_{ak}	Number of extracellular Mtb killed by M_a each time-step	10
τ_{recMac}	TNF/chemokine threshold for M_r recruitment	0.01-0.1 (0.023)
M_{recr}	Probability of M_r recruitment	0.01-0.1 (0.04)
$max_{ageTcell}$ (day)	Maximum lifespan of T cells	3
t_{delay} (day)	T cell recruitment delay	20
T_{moveM}	Probability of T cell moving to a mac-containing location	0.001-0.1 (0.014)
T_{moveT}	Probability of T cell moving to a T cell-containing location	0.001-0.1 (0.08)
T_{recr}	Probability of T cell recruitment	0.05-0.5 (0.15)
$t_{regTgam}$ (min)	T_γ inactivity time after down-regulation by T_{reg}	100
$P_{apop/Fas}$	Probability of Fas/FasL apoptosis by T_γ	0.01-0.1 (0.06)
$\tau_{recTgam}$	TNF/chemokine threshold for T_γ recruitment	0.1-1.0 (0.4)
$T_{recTgam}$	Probability of T_γ recruitment	0.54
$t_{regTcyt}$ (min)	T_c inactivity time after down-regulation by T_{reg}	100
$\tau_{recTcyt}$	TNF/chemokine threshold for T_c recruitment	0.1-1.0 (0.4)
$T_{recTcyt}$	Probability of T_c recruitment	0.36
$P_{cytKill}$	Probability of T_c killing M_i or M_{ci}	0.02 0.2 (0.12)
$P_{cytKillClean}$	Probability of T_c killing all intracellular Mtb by killing M_{ci}	0.75
$\tau_{recTreg}$	TNF/chemokine threshold for T_{reg} recruitment	0.01-0.1 (0.05)
$T_{recTreg}$	Probability of T_{reg} recruitment	0.1
α_{Bi} (per 10 min)	Intracellular Mtb growth rate	2×10^{-4}-2×10^{-3} (1.5×10^{-3})
α_{Be} (per 10 min)	Extracellular Mtb growth rate	10^{-4}-10^{-3} (7×10^{-4})
K_{be}	Capacity of a micro-compartment for extracellular Mtb	200

* Parameters used for sensitivity analysis are indicated by their ranges of values. Values in parentheses are used to generate containment baseline.

Table C.2 Definition of reaction species, reactions describing TNF/TNFR processes and their rates (v_i).

Reaction species			
mTNF	Membrane-bound TNF	*sTNF/TNFR2*	sTNF/TNFR2 complex on the membrane
sTNF	Extracellular soluble TNF	$sTNF/TNFR1_i$	Internalized sTNF/TNFR1 complex
TNFR1	Cell surface TNF receptor 1	$sTNF/TNFR2_i$	Internalized sTNF/TNFR2 complex
TNFR2	Cell surface TNF receptor 2	$sTNF/TNFR2_{shed}$	Shed sTNF/TNFR2 complex
sTNF/TNFR1	sTNF/TNFR1 complex on the membrane	TNF_i	Intracellular translated TNF

Model reactions			
1	*mTNF expression* (*T cells*): $v_1 = k_{synthTcell}$ (*Macrophages*): $v_1 = e_{eTNF}[TNF_i]$	9	*TNFR2 synthesis* $v_9 = V_{r2}$
2	$mTNF \rightarrow sTNF$ $v_2 = k_{TACE}[mTNF]$	10	$TNFR1 \rightarrow TNFR1_i$ $v_{10} = k_{r1}[TNFR1]$
3	$sTNF + TNFR1 \leftrightarrow sTNF/TNFR1$ $v_3 = k_{on1}[sTNF][TNFR1] - k_{off1}[sTNF/TNFR1]$	11	$TNFR2 \rightarrow TNFR2_i$ $v_{11} = k_{r2}[TNFR2]$
4	$sTNF + TNFR2 \leftrightarrow sTNF/TNFR2$ $v_4 = k_{on2}[sTNF][TNFR2] - k_{off2}[sTNF/TNFR2]$	12	$sTNF/TNFR1_i \rightarrow degradation$ $v_{12} = k_{deg1}[sTNF/TNFR1_i]$
5	$sTNF/TNFR1 \rightarrow sTNF/TNFR1_i$ $v_5 = k_{int1}[sTNF/TNFR1]$	13	$sTNF/TNFR2_i \rightarrow degradation$ $v_{13} = k_{deg2}[sTNF/TNFR2_i]$
6	$sTNF/TNFR2 \rightarrow sTNF/TNFR2_i$ $v_6 = k_{int2}[sTNF/TNFR2]$	14	$sTNF/TNFR1_i \rightarrow TNFR1$ $v_{14} = k_{rec1}[sTNF/TNFR1_i]$
7	$sTNF/TNFR2 \rightarrow sTNF/TNFR2_{shed}$ $v_7 = k_{shed}[sTNF/TNFR2]$	15	$sTNF/TNFR2_i \rightarrow TNFR2$ $v_{15} = k_{rec2}[sTNF/TNFR2_i]$
8	*TNFR1 synthesis* $v_8 = V_{r1}$	16	$sTNF/TNFR2_{shed} \rightarrow sTNF + TNFR2_{shed}$ $v_{16} = k_{off2}[sTNF/TNFR2_{shed}]$

Table C.3 Molecular/single-cell scale TNF/TNFR parameters, definitions and values estimated from literature

Parameter	Parameter description	Value*	Reference
$k_{synthTcell}$ (#/cell.s)	Full synthesis rate of mTNF for T cells	10^{-2}-10^{-1} (0.021)	[3]
$TNFR1_{mac}$ (#/cell)	TNFR1 density on the surface of macrophages	500-5000 (1100-1900) †	[4-7]
$TNFR1_{Tcell}$ (#/cell)	TNFR1 density on the surface of T cells	500-5000 (400-1200) †	[4-7]
$TNFR2_{mac}$ (#/cell)	TNFR2 density on the surface of macrophages	500-5000 (400-800) †	[4-7]
$TNFR2_{Tcell}$ (#/cell)	TNFR2 density on the surface of T cells	500-5000 (600-800) †	[4-7]
D_1 (cm^2/s) ‡	Diffusion coefficient of sTNF	10^{-8}-10^{-7} (5.2×10^{-8})	[8,9]
D_2 (cm^2/s) ‡	Diffusion coefficient of shed TNF/TNFR2 complex	10^{-8}-10^{-7} (3.2×10^{-8})	[8,9]
k_{TACE_Mac} (s^{-1})	Rate constant for TNF release by TACE activity on a macrophage	10^{-4}-10^{-3} (4.4×10^{-4})	[4,10-12]
k_{TACE_Tcell} (s^{-1})	Rate constant for TNF release by TACE activity on a T cell	10^{-5}-10^{-4} (4.4×10^{-5})	
δ_{TNF} (s^{-1})	sTNF degradation rate constant	10^{-4}-10^{-3} (4.58×10^{-4})	[13]
K_{d1} (M)	Equilibrium dissociation constant of sTNF/TNFR1	10^{-12}-10^{-10} (1.9×10^{-11})	[5,14]
K_{d2} (M)	Equilibrium dissociation constant of sTNF/TNFR2	10^{-10}-10^{-9} (4.2×10^{-10})	[5,14,15]
k_{on1} ($M^{-1}s^{-1}$)	sTNF/TNFR1 association rate constant	10^7-10^8 (2.8×10^7)	[14]
k_{on2} ($M^{-1}s^{-1}$)	sTNF/TNFR2 association rate constant	10^7-10^8 (3.5×10^7)	[14]
k_{off1} (s^{-1})	sTNF/TNFR1 dissociation rate constant	$k_{on1}\times K_{d1}$	
k_{off2} (s^{-1})	sTNF/TNFR2 dissociation rate constant	$k_{on2}\times K_{d2}$	
k_{int1} (s^{-1})	TNFR1 internalization rate constant	1.5×10^{-4}-1.5×10^{-3} (7.7×10^{-4})	[14,16]
k_{int2} (s^{-1})	TNFR2 internalization rate constant	3.9×10^{-4}-5×10^{-4} (4.6×10^{-4})	[15]
k_{shed} (s^{-1})	TNFR2 shedding rate constant	3.9×10^{-4}-1.5×10^{-3} (5×10^{-4})	[12,16]
k_{rec1} (s^{-1})	TNFR1 recycling rate constant	8.8×10^{-5}-5.5×10^{-4} (1.8×10^{-5})	[17,18]
k_{rec2} (s^{-1})	TNFR2 recycling rate constant	8.8×10^{-5}-5.5×10^{-4} (1.8×10^{-5})	[17,18]
k_{t1} (s^{-1})	TNFR1 turn-over rate constant	3×10^{-4}-5×10^{-4} (3.8×10^{-4})	[17,18]
k_{t2} (s^{-1})	TNFR2 turn-over rate constant	3×10^{-4}-5×10^{-4} (3.8×10^{-4})	[17,18]
k_{deg1} (s^{-1})	TNFR1 degradation rate constant	10^{-5}-10^{-4} (5×10^{-5})	[5,17-19]
k_{deg2} (s^{-1})	TNFR2 degradation rate constant	10^{-5}-10^{-4} (5×10^{-5})	[5,17-19]
V_{r1_mac} (#/cell.s)	Cell surface TNFR1 synthesis rate constant for macrophages	$k_{t1}\times TNFR1_{mac}$	
V_{r1_Tcell} (#/cell.s)	Cell surface TNFR1 synthesis rate constant for T cells	$k_{t1}\times TNFR1_{Tcell}$	
V_{r2_mac} (#/cell.s)	Cell surface TNFR2 synthesis rate constant for macrophages	$k_{t2}\times TNF21_{mac}$	
V_{r2_Tcell} (#/cell.s)	Cell surface TNFR2 synthesis rate constant for T cells	$k_{t2}\times TNF21_{Tcell}$	

* Ranges of parameter values used for sensitivity analysis are indicated out of parentheses. Values in parentheses are used to generate baseline model results.

† Baseline model values for TNFR densities on each recruited individual cell was randomly chosen from the range shown in parentheses.

‡ Diffusion coefficients of the soluble species in granuloma were estimated in line with estimates for diffusible factors of similar molecular weight in tumors [8,9].

Table C.4 Definition of reaction species, reactions describing NF-κB signaling and response associated processes in macrophages and their rates (v_i).

Reaction species

sTNF/TNFR1	sTNF/TNFR1 complex on the membrane	*NFkB*	Cytoplasmic NF-κB
IKKn	Neutral form of IKK kinase	$NFkB_n$	Nuclear NF-κB
IKKa	Active form of IKK	*A20*	Translated A20
IKKi	Inactive form of IKK	$A20_t$	A20 transcript
IKKii	Inactive intermediate form of IKK	G_{A20}	State of A20 gene
K_{NN}	Total number of IKK molecules (assumed constant in time)	G_{IkB}	State of IκBα gene
IKKKa	Active form of IKKK	G_R	State of genes corresponding to NF-κB mediated responses
IKKKn	Neutral form of IKKK	$chem_i$	Intracellular translated chemokines
K_N	Total number of IKKK molecules (assumed to be constant in time)	$chem_t$	Chemokine transcript
IkB	Cytoplasmic IκBα	TNF_i	Intracellular translated TNF
IkB_n	Nuclear IκBα	TNF_t	TNF transcript
IkB_t	IκBα transcript	*ACT*	Generic macrophage-activating molecule
IkB_p	Phosphorylated cytoplasmic IκBα	ACT_t	ACT transcript
NFkB|IkB	Cytoplasmic IκBα|NF-κB complex	*IAP*	Inhibitor of apoptosis protein
$NFkB\|IkB_p$	Phosphorylated cytoplasmic IκBα in complex with NF-κB	IAP_t	IAP transcript
$NFkB\|IkB_n$	Nuclear IκBα|NF-κB complex		

Model reactions

17	*IKKK kinase activation and activity attenuation by A20* $v_{17} = k_a[sTNF/TNFR1].([K_N]-[IKKKa]).\frac{k_{A20}}{k_{A20}+[A20]}$	42	*Transport of NF-κB|IκBα complex out of nucleus* $v_{42} = e_{2a}[NFkB\|IkB_n]$
18	*Spontaneous inactivation of IKKKa* $v_{18} = k_i[IKKKa]$	43	*A20 gene activation due to NF-κB binding* $v_{43} = q_1[NFkB_n](2-[G_{A20}])$
19	*IKKii→IKKn* $v_{19} = k_4([K_{NN}]-[IKKn]-[IKKa]-[IKKi])$	44	*A20 gene inactivation due to removal of NF-κB molecules by IκBα* $v_{44} = q_2[IkB_n][G_{A20}]$
20	*IKKn→IKKa mediated by IKKKa phosphorylation at two sites* $v_{20} = k_1[IKKKa]^2[IKKn]$	45	*IκBα gene activation due to NF-κB binding* $v_{45} = q_1[NFkB_n](2-[G_{IkB}])$
21	*IKKa → IKKi mediated by A20* $v_{21} = k_3[IKKa].\frac{k_2+[A20]}{k_2}$	46	*IκBα gene inactivation due to removal of NF-κB molecules by IκBα* $v_{46} = q_2[IkB_n][G_{IkB}]$
22	*IKKi → IKKii* $v_{22} = k_4[IKKi]$	47	*NF-κB mediated response gene activation due to NF-κB binding* $v_{47} = q_{1r}[NFkB_n](2-[G_R])$
23	*IκBα phosphorylation by IKKa* $v_{23} = a_2[IKKa][IkB]$	48	*NF-κB mediated response gene inactivation due to spontaneous removal of NF-κB molecules* $v_{48} = q_{2rr}[G_R]$
24	*Degradation of phosphorylated IκBα* $v_{24} = t_p[IkB_p]$	49	*NF-κB mediated response gene inactivation due to removal of NF-κB molecules by IκBα* $v_{49} = q_{2r}[IkB_n][G_R]$
25	*Phosphorylation of IκBα in complex with NF-κB by IKKa* $v_{25} = a_3[IKKa][NFkB\|IkB]$	50	*Constitutive transcription of TNF and chemokines* $v_{50} = c_{1rrchemTNF}$
26	*Degradation of phosphorylated IκBα in complex with NF-κB* $v_{26} = t_p[NFkB\|IkB_p]$	51	*NF-κB dependent transcription of chemokines and TNF* $v_{51} = c_{1r}[G_R]$

Table C.4 (continued)

27	*Liberation of free NF-κB due to degradation of IκBα in their complex* $v_{27} = c_{6a}[NFkB \mid IkB]$	52	*Chemokine mRNA degradation* $v_{52} = c_{3rchem}[chem_t]$
28	*Formation of NF-κB and IκBα complex* $v_{28} = a_1[NFkB][IkB]$	53	*Chemokine translation* $v_{53} = c_{4chem}[chem_t]$
29	*Transport of free cytoplasmic NF-κB to nucleus* $v_{29} = i_1[NFkB]$	54	*Intracellular chemokine degradation* $v_{54} = c_{5chem}[chem_i]$
30	*Association of nuclear NF-κB with nuclear IκBα* $v_{30} = a_1 k_v[IkB_n][NFkB_n]$	55	*Chemokine secretion* $v_{55} = e_{3chem}[chem_i]$
31	*A20 translation* $v_{31} = c_4[A20_t]$	56	*TNF mRNA degradation* $v_{56} = c_{3rTNF}[TNF_t]$
32	*Constitutive degradation of A20* $v_{32} = c_5[A20]$	57	*TNF translation* $v_{57} = c_{4TNF}[TNF_t]$
33	*NF-κB inducible transcription of A20* $v_{33} = c_1[G_{A20}]$	58	*Intracellular TNF degradation* $v_{58} = c_{5TNF}[TNF_i]$
34	*Degradation of A20 transcript* $v_{34} = c_3[A20_t]$	59	*Constitutive transcription of ACT* $v_{59} = c_{1rrACT}$
35	*IκBα translation* $v_{35} = c_4[IkB_t]$	60	*ACT mRNA degradation* $v_{60} = c_{3rACT}[ACT_t]$
36	*Constitutive degradation of IκBα* $v_{36} = c_{5a}[IkB]$	61	*ACT translation* $v_{61} = c_{4ACT}[ACT_t]$
37	*Transport of IκBα into nucleus* $v_{37} = i_{1a}[IkB]$	62	*ACT degradation* $v_{62} = c_{5ACT}[ACT]$
38	*Transport of IκBα out of nucleus* $v_{38} = e_{1a}[IkB_n]$	63	*Constitutive transcription of IAP* $v_{63} = c_{1rrIAP}$
39	*NF-κB inducible transcription of IκBα* $v_{39} = c_1[G_{IkB}]$	64	*IAP mRNA degradation* $v_{64} = c_{3rIAP}[IAP_t]$
40	*Degradation of IκBα transcript* $v_{40} = c_3[IkB_t]$	65	*IAP translation* $v_{65} = c_{4IAP}[IAP_t]$
41	*Association of NF-κB with IκBα in cytoplasm* $v_{41} = a_1[IkB][NFkB]$	66	*IAP degradation* $v_{66} = c_{5IAP}[IAP]$

Table C.5 Molecular/single-cell scale NF-κB signaling associated parameters, definitions and values from [20], or approximated via uncertainty analysis.

Parameter	Parameter description	Value*
(1) Concentration of intracellular signaling molecules		
K_N (#/cell)	Number of IKKK molecules	3.16×10^{4}-3.16×10^{5} (10^{5})
K_{NN} (#/cell)	Number of IKK molecules	6.32×10^{4}-6.32×10^{5} (2×10^{5})
$NF\text{-}\kappa B_{tot}$ (#/cell)	Average number of NF-κB molecules	3.16×10^{4}-3.16×10^{5} (10^{5})
(2) Activation of the signal transduction cascade		
k_a (s^{-1})	IKKK activation rate	6.32×10^{-7}-6.32×10^{-6} (2×10^{-6})
k_i (s^{-1})	IKKK inactivation rate	3.16×10^{-3}-3.16×10^{-2} (10^{-2})
k_1 (s^{-1})	IKKn activation rate	1.9×10^{-10}-1.9×10^{-9} (6×10^{-10})
k_{A20} (#/cell)	Michaelis coefficient in TNFR1 activity attenuation	3.16×10^{4}-3.16×10^{5} (10^{5})
k_2 (#/cell)	Michaelis coefficient in IKKa inactivation	3.16×10^{3}-3.16×10^{4} (10^{4})
k_3 (s^{-1})	IKKn inactivation rate	6.32×10^{-4}-6.32×10^{-3} (2×10^{-3})
k_4 (s^{-1})	IKKi→IKKii and IKKii→IKKn transformation	3.16×10^{-4}-3.16×10^{-3} (10^{-3})
(3) A20 and IκBα synthesis		
q_1 (s^{-1})	NF-κB binding at A20 and IκBα gene promoters	1.26×10^{-7}-1.26×10^{-6} (4×10^{-7})
q_2 (s^{-1})	IκBα inducible NF-κB detaching from A20 and IκBα genes	3.16×10^{-7}-3.16×10^{-6} (10^{-6})
c_1 (s^{-1})	Inducible A20 and IκBα mRNA synthesis	3.16×10^{-2}-3.16×10^{-1} (10^{-1})
c_3 (s^{-1})	A20 and IκBα mRNA degradation	2.37×10^{-4}-2.37×10^{-3} (7.5×10^{-4})
c_4 (s^{-1})	A20 and IκBα translation	1.58×10^{-1}-1.58 (5×10^{-1})
c_5 (s^{-1})	A20 degradation rate	1.58×10^{-4}-1.58×10^{-3} (5×10^{-4})
(4) IκBα interactions		
a_1 (s^{-1})	IκBα-NF-κB association	1.58×10^{-7}-1.58×10^{-6} (5×10^{-7})
a_2 (s^{-1})	IκBα phosphorylation	3.16×10^{-8}-3.16×10^{-7} (10^{-7})
a_3 (s^{-1})	IκBα phosphorylation in IκBα|NF-κB complexes	1.58×10^{-7}-1.58×10^{-6} (5×10^{-7})
t_p (s^{-1})	Degradation of phosphorylated IκBα	3.16×10^{-3}-3.16×10^{-2} (10^{-2})
c_{5a} (s^{-1})	Spontaneous IκBα degradation	3.16×10^{-5}-3.16×10^{-4} (10^{-4})
c_{6a} (s^{-1})	Spontaneous IκBα degradation in IκBα|NF-κB complexes	6.32×10^{-6}-6.32×10^{-5} (2×10^{-5})
(5) NF-κB and IκBα transport between cytoplasm and nucleus		
i_1 (s^{-1})	NF-κB nuclear import	3.16×10^{-3}-3.16×10^{-2} (10^{-2})
e_{2a} (s^{-1})	IκBα|NF-κB nuclear export	1.58×10^{-2}-1.58×10^{-1} (5×10^{-2})
i_{1a} (s^{-1})	IκBα nuclear import	6.32×10^{-4}-6.32×10^{-3} (2×10^{-3})
e_{1a} (s^{-1})	IκBα nuclear export	1.58×10^{-3}-1.58×10^{-2} (5×10^{-3})
k_v	Ratio of cytoplasmic to nuclear volume for a macrophage	5
(6) NF-κB-mediated cell responses and apoptosis		
q_{1r} (s^{-1})	NF-κB binding at response gene promoters	3.16×10^{-8}-3.16×10^{-7} (10^{-7})
q_{2r} (s^{-1})	IκBα inducible NF-κB detaching from response gene promoters	3.16×10^{-8}-3.16×10^{-7} (10^{-7})
q_{2rr} (s^{-1})	Spontaneous NF-κB detaching from response gene promoters	3.16×10^{-4}-3.16×10^{-3} (10^{-3})
c_{1r} (s^{-1})	Inducible response mRNA synthesis	0 (only resting macrophage), 1.58×10^{-2}-1.58×10^{-1} (5×10^{-2})
$c_{1rrchemTNF}$ (s^{-1})	Constitutive transcription rate for chemokines and TNF	0 (resting macrophage), 0.5× c_{1r} (infected macrophage), c_{1r} (activated or chronically-infected macrophage)
c_{3rchem} (s^{-1})	Chemokine mRNA degradation rate	6.1×10^{-5}-6.1×10^{-4} (1.92×10^{-4})
c_{4chem} (s^{-1})	Chemokine translation rate	1.42×10^{-1}-1.42 (4.5×10^{-1})
c_{5chem} (s^{-1})	Intracellular chemokine degradation rate	1.58×10^{-5}-1.58×10^{-4} (5×10^{-4})
e_{3chem} (s^{-1})	Chemokine secretion rate	4.4×10^{-6}-4.4×10^{-5} (1.39×10^{-5})
c_{3rTNF} (s^{-1})	TNF mRNA degradation rate	1.2×10^{-4}-1.2×10^{-3} (3.8×10^{-4})
c_{4TNF} (s^{-1})	TNF translation rate	4.74×10^{-2}-4.74×10^{-1} (1.5×10^{-1})
c_{5TNF} (s^{-1})	Intracellular TNF degradation rate	1.58×10^{-4}-1.58×10^{-3} (5×10^{-4})
e_{3TNF} (s^{-1})	TNF secretion rate	7.87×10^{-7}-7.87×10^{-6} (2.5×10^{-6})
c_{1rrACT} (s^{-1})	ACT mRNA constitutive synthesis rate	3.16×10^{-4}-3.16×10^{-3} (1×10^{-3})
c_{3rACT} (s^{-1})	ACT mRNA degradation rate	6.1×10^{-5}-6.1×10^{-4} (1.92×10^{-4})
c_{4ACT} (s^{-1})	ACT translation rate	1.58×10^{-1}-1.58 (5×10^{-1})

Table C.5 (continued)

c_{5ACT} (s^{-1})	ACT degradation rate	1.58×10^{-4}-1.58×10^{-3} (5×10^{-4})
τ_{ACT} (#/cell)	ACT concentration threshold for macrophage activation	8-80 (25)
k_{ACT} ((#/cell)$^{-1}s^{-1}$)	Macrophage activation rate constant	1.46×10^{-6}-1.46×10^{-5} (7.7×10^{-6})
c_{1rrIAP} (s^{-1})	IAP mRNA constitutive synthesis rate	3.16×10^{-4}-3.16×10^{-3} (1×10^{-3})
c_{3rIAP} (s^{-1})	IAP mRNA degradation rate	6.1×10^{-5}-6.1×10^{-4} (1.92×10^{-4})
c_{4IAP} (s^{-1})	IAP translation rate	1.58×10^{-1}-1.58 (5×10^{-1})
c_{5IAP} (s^{-1})	IAP degradation rate	1.58×10^{-4}-1.58×10^{-3} (5×10^{-4})
k_{IAP} (#/cell)	Apoptosis inhibition coefficient	1.22×10^{1}-1.22×10^{2} (3.86×10^{1})
k^0_{apopt}((#/cell)$^{-1}s^{-1}$)	Intrinsic TNF-induced apoptosis rate constant	4.2×10^{-10}-4.2×10^{-9} (1.33×10^{-9})
τ_{apopt} (#/cell)	Internalized sTNF/TNFR1 threshold for TNF-induced apoptosis	50-500 (300)

* Parameters used for sensitivity analysis are indicated by their ranges of values. Values in parentheses are used to generate containment baseline.

† Baseline model values for intracellular $NF\text{-}\kappa B_{tot}$ on each recruited individual macrophage was randomly based on a log-normal distribution as described in [20].

Table C.6 Differential equations describing molecular single-cell scale TNF/TNFR and NF-κB signaling and response associated processes.

$$\frac{d[mTNF]}{dt} = v_1 - v_2$$

$$\frac{d[sTNF]}{dt} = (\frac{\rho}{N_{av}})(v_2 - v_3 - v_4) + v_{16}$$

$$\frac{d[TNFR1]}{dt} = v_8 - v_3 - v_{10} + v_{14}$$

$$\frac{d[TNFR2]}{dt} = v_9 - v_4 - v_{11} + v_{15}$$

$$\frac{d[sTNF/TNFR1]}{dt} = v_3 - v_5$$

$$\frac{d[sTNF/TNFR2]}{dt} = v_4 - v_6 - v_7$$

$$\frac{d[sTNF/TNFR1_i]}{dt} = v_5 - v_{12} - v_{14}$$

$$\frac{d[sTNF/TNFR2_i]}{dt} = v_6 - v_{13} - v_{15}$$

$$\frac{d[sTNF/TNFR2_{shed}]}{dt} = (\frac{\rho}{N_{av}})v_7 - v_{16}$$

$$\frac{d[IKKKa]}{dt} = v_{17} - v_{18}$$

$$\frac{d[IKKn]}{dt} = v_{19} - v_{20}$$

$$\frac{d[IKKa]}{dt} = v_{20} - v_{21}$$

$$\frac{d[IKKi]}{dt} = v_{21} - v_{22}$$

$$\frac{d[IkB_p]}{dt} = v_{23} - v_{24}$$

$$\frac{d[NFkB|IkB_p]}{dt} = v_{25} - v_{26}$$

$$\frac{d[NFkB]}{dt} = v_{27} - v_{28} + v_{26} - v_{29}$$

$$\frac{d[NFkB_n]}{dt} = v_{29} - v_{30}$$

$$\frac{d[A20]}{dt} = v_{31} - v_{32}$$

$$\frac{d[A20_t]}{dt} = v_{33} - v_{34}$$

$$\frac{d[IkB]}{dt} = v_{23} - v_{28} + v_{35} - v_{36} - v_{37} + v_{38}$$

$$\frac{d[IkB_n]}{dt} = -v_{30} + v_{37} - v_{38}$$

$$\frac{d[IkB_t]}{dt} = v_{39} - v_{40}$$

$$\frac{d[NFkB|IkB]}{dt} = v_{41} - v_{27} - v_{25} + v_{42}$$

$$\frac{d[NFkB|IkB_n]}{dt} = v_{30} - v_{42}$$

$$\frac{d[G_{A20}]}{dt} = v_{43} - v_{44}$$

$$\frac{d[G_{IkB}]}{dt} = v_{45} - v_{46}$$

$$\frac{d[G_R]}{dt} = v_{47} - v_{48} - v_{49}$$

$$\frac{d[chem_t]}{dt} = v_{50} + v_{51} - v_{52}$$

$$\frac{d[chem_i]}{dt} = v_{53} - v_{54} - v_{55}$$

$$\frac{d[TNF_t]}{dt} = v_{50} + v_{51} - v_{56}$$

$$\frac{d[TNF_i]}{dt} = v_{57} - v_{58} - v_1$$

$$\frac{d[ACT_t]}{dt} = v_{59} + v_{51} - v_{60}$$

$$\frac{d[ACT]}{dt} = v_{61} - v_{62}$$

$$\frac{d[IAP_t]}{dt} = v_{63} + v_{51} - v_{64}$$

$$\frac{d[IAP]}{dt} = v_{65} - v_{66}$$

Table C.7 LHS sensitivity analysis results for the effect of important NF-κB-associated model parameters (groups 1-3) on model outputs at day 200 post-infection. Parameter definitions are presented in Table C.5.

	$NF\text{-}\kappa B_{tot}$	k_a	k_i	q_1	c_1	c_3	c_4	c_5
TNF function-related outputs								
$(\text{No. apoptosis})_{\text{Macs}}$								
$(\text{No. apoptosis})_{\text{Mr}}$								
$(\text{No. apoptosis})_{\text{Mi \& Mci}}$						--		
$(\text{No. apoptosis})_{\text{Ma}}$							-	+
$(\text{No. apoptosis})_{\text{T cells}}$	+						--	++
$(\text{No. activation})_{\text{Mr}}$	++	++				++	--	++
$(\text{No. activation})_{\text{Mi}}$							-	
Cellular-level outputs								
B_{int} (intracellular Mtb)	--	---	+	+	+	---	++	--
B_{ext} (extracellular Mtb)	--	---		+	++	---	++	--
B_{tot}	--	---	+	+	++	---	++	--
Total Macrophages								
M_r	---	---	+++	++	+++	---	+++	---
M_i and M_{ci}	--	---	+	+	+	---	++	--
M_a	+	+				++	--	++
Total T cells	+	+						+
T_γ		+					-	+
T_c	+	+					-	+
T_{reg}	+	++				+		++
Tissue-level outputs								
Caseation	-				+			
Granuloma size								
Tissue concentrations								
$[\text{sTNF}]_{\text{avg}}$							--	++
$[\text{Chemokines}]_{\text{avg}}$						--	-	+

Only parameters with significant PRCC values are indicated. Significant positive and negative correlations are shown using +/- as follows:
-/+, $0.001 < p\text{-value} < 0.01$
--/++, $0.0001 < p\text{-value} < 0.001$
---/+++, $p\text{-value} < 0.0001$

Table C.8 LHS sensitivity analysis results for the effect of important NF-κB-associated model parameters (group 6) on model outputs at day 200 post-infection. Parameter definitions are presented in Table C.5.

	c_{1r}	c_{3rchem}	c_{4chem}	e_{3chem}	c_{3rTNF}	c_{4TNF}	c_{5TNF}	e_{3TNF}	c_{4ACT}	c_{5ACT}	τ_{ACT}	c_{5IAP}
TNF function-related outputs												
$(\text{No. apoptosis})_{\text{Macs}}$	+++				--	+++	---	+++				
$(\text{No. apoptosis})_{\text{Mr}}$	+++				---	+++	---	+++				
$(\text{No. apoptosis})_{\text{Mi \& Mci}}$					--	++	---	+++	---	+++	+++	
$(\text{No. apoptosis})_{\text{Ma}}$	+++					+++		+++	++	--	-	
$(\text{No. apoptosis})_{\text{T cells}}$	+++				--	+++	---	+++	+			
$(\text{No. activation})_{\text{Mr}}$	+++				+				+++	---	---	
$(\text{No. activation})_{\text{Mi}}$	+++				++		++	-	+++	---	---	
Cellular-level outputs												
B_{int} (intracellular Mtb)	---				++	---	++	--	---	+++	+++	
B_{ext} (extracellular Mtb)	---				++	--	++	--	---	+++	+++	
B_{tot}	---				++	---	++	--	---	+++	+++	
Total Macrophages		---	++	+++	+++	---	+++	---				-
M_r	---	--	+	+++	+++	---	+++	---	---	+++	+++	
M_i and M_{ci}	---				++	---	++	--	---	+++	+++	
M_a	+++				+++	--	+++	---	+++	---	---	
Total T cells	+++			++	+++	--	+++	---	+++	---	---	
T_γ	+++			++	+++	--	+++	---	+++	---	---	
T_c	+++			++	+++	--	+++	---	+++	---	---	
T_{reg}	+++			+	+++	--	+++	---	+++	---	---	
Tissue-level outputs												
Caseation	---	+++	--	-	+++	---	+++	---				---
Granuloma size	---	--		+++	+++	---	+++	---				--
Tissue concentrations												
$[\text{sTNF}]_{\text{avg}}$	+++					++		++				-
$[\text{Chemokines}]_{\text{avg}}$	+++	---	+++	+++	+++	---	+++	---				--

Only parameters with significant PRCC values are indicated. Significant positive and negative correlations are shown using +/- as follows:

-/+, $0.001 < p\text{-value} < 0.01$

--/++, $0.0001 < p\text{-value} < 0.001$

---/+++, $p\text{-value} < 0.0001$

C.2 References

1. Ray JC, Flynn JL, Kirschner DE (2009) Synergy between individual TNF-dependent functions determines granuloma performance for controlling mycobacterium tuberculosis infection. J Immunol 182: 3706-3717.

2. Fallahi-Sichani M, El-Kebir M, Marino S, Kirschner DE, Linderman JJ (2011) Multiscale computational modeling reveals a critical role for TNF-{alpha} receptor 1 dynamics in tuberculosis granuloma formation. J Immunol 186: 3472-3483.

3. Marino S, Sud D, Plessner H, Lin PL, Chan J, et al. (2007) Differences in reactivation of tuberculosis induced from anti-TNF treatments are based on bioavailability in granulomatous tissue. PLoS Comput Biol 3: 1909-1924.

4. Fallahi-Sichani M, Schaller MA, Kirschner DE, Kunkel SL, Linderman JJ (2010) Identification of key processes that control tumor necrosis factor availability in a tuberculosis granuloma. PLoS Comput Biol 6: e1000778.

5. Imamura K, Spriggs D, Kufe D (1987) Expression of tumor necrosis factor receptors on human monocytes and internalization of receptor bound ligand. J Immunol 139: 2989-2992.

6. Pocsik E, Mihalik R, Ali-Osman F, Aggarwal BB (1994) Cell density-dependent regulation of cell surface expression of two types of human tumor necrosis factor receptors and its effect on cellular response. J Cell Biochem 54: 453-464.

7. van Riemsdijk-Van Overbeeke IC, Baan CC, Knoop CJ, Loonen EH, Zietse R, et al. (2001) Quantitative flow cytometry shows activation of the TNF-alpha system but not of the IL-2 system at the single cell level in renal replacement therapy. Nephrol Dial Transplant 16: 1430-1435.

8. Nugent LJ, Jain RK (1984) Extravascular diffusion in normal and neoplastic tissues. Cancer Res 44: 238-244.

9. Pluen A, Boucher Y, Ramanujan S, McKee TD, Gohongi T, et al. (2001) Role of tumor-host interactions in interstitial diffusion of macromolecules: Cranial vs. subcutaneous tumors. Proc Natl Acad Sci U S A 98: 4628-4633.

10. Newton RC, Solomon KA, Covington MB, Decicco CP, Haley PJ, et al. (2001) Biology of TACE inhibition. Ann Rheum Dis 60 Suppl 3: iii25-32.

11. Solomon KA, Covington MB, DeCicco CP, Newton RC (1997) The fate of pro-TNF-alpha following inhibition of metalloprotease-dependent processing to soluble TNF-alpha in human monocytes. J Immunol 159: 4524-4531.

12. Crowe PD, Walter BN, Mohler KM, Otten-Evans C, Black RA, et al. (1995) A metalloprotease inhibitor blocks shedding of the 80-kD TNF receptor and TNF processing in T lymphocytes. J Exp Med 181: 1205-1210.

13. Cheong R, Bergmann A, Werner SL, Regal J, Hoffmann A, et al. (2006) Transient IkappaB kinase activity mediates temporal NF-kappaB dynamics in response to a wide range of tumor necrosis factor-alpha doses. J Biol Chem 281: 2945-2950.

14. Grell M, Wajant H, Zimmermann G, Scheurich P (1998) The type 1 receptor (CD120a) is the high-affinity receptor for soluble tumor necrosis factor. Proc Natl Acad Sci U S A 95: 570-575.

15. Pennica D, Lam VT, Mize NK, Weber RF, Lewis M, et al. (1992) Biochemical properties of the 75-kDa tumor necrosis factor receptor. characterization of ligand binding, internalization, and receptor phosphorylation. J Biol Chem 267: 21172-21178.

16. Higuchi M, Aggarwal BB (1994) TNF induces internalization of the p60 receptor and shedding of the p80 receptor. J Immunol 152: 3550-3558.

17. Vuk-Pavlovic S, Kovach JS (1989) Recycling of tumor necrosis factor-alpha receptor in MCF-7 cells. FASEB J 3: 2633-2640.

18. Bajzer Z, Myers AC, Vuk-Pavlovic S (1989) Binding, internalization, and intracellular processing of proteins interacting with recycling receptors. A kinetic analysis. J Biol Chem 264: 13623-13631.

19. Tsujimoto M, Yip YK, Vilcek J (1985) Tumor necrosis factor: Specific binding and internalization in sensitive and resistant cells. Proc Natl Acad Sci U S A 82: 7626-7630.

20. Tay S, Hughey JJ, Lee TK, Lipniacki T, Quake SR, et al. (2010) Single-cell NF-kappaB dynamics reveal digital activation and analogue information processing. Nature 466: 267-271.

Appendix D

Supplementary information for Chapter 6

D.1 Drug transport from the blood into the lung tissue

To study the effect of TNF inhibitors on the immune response to Mtb, we first run the base model described in Chapter 3 in the absence of TNF inhibitors by using a baseline set of parameter values that leads to stable control of infection (containment) in a granuloma as described in Chapter 3 and [1]. After 100 days, at which time a well-circumscribed granuloma with stable bacterial levels ($<10^3$ total bacteria) forms, the granuloma is exposed to a TNF-neutralizing drug that enters the grid representing lung parenchyma via vascular sources, and diffuses among micro-compartments. The flux of a drug from a blood vessel into the tissue is related to the vascular permeability coefficient of the drug (k_c) and the drug gradient across the vessel wall by:

$$-D_{drug}\frac{\partial[Drug]}{\partial r}\Big|_{r=0} = k_c(C_p - [Drug]_{r=0}) \tag{D.1}$$

where C_p is the concentration of the drug in blood, [*Drug*] is the concentration of the drug in tissue that is a function of time and distance from the vessel (r), $[Drug]_{r=0}$ is the concentration of the drug at the outside wall of the vessel, and D_{drug} is drug diffusion coefficient in tissue. Using this equation and rearranging it for discrete-space flux on the 2-D grid gives:

$$C_{source} = C_{i,j} = \frac{\frac{1}{4}D_{drug}\{C_{i-1,j} + C_{i+1,j} + C_{i,j-1} + C_{i,j+1}\} + C_p k_c dx}{D_{drug} + k_c dx} \tag{D.2}$$

where $C_{source} = C_{i,j}$ represents the drug concentration at the outside wall of the vascular source located at the micro-compartment (i,j) and $dx = 20$ μm is the lattice spacing through which diffusion occurs. Equation D.2 implies that at very large vascular permeabilities ($k_c \rightarrow \infty$), $C_{i,j}$ tends to blood concentration of the drug (C_p). However, a zero permeability coefficient ($k_c = 0$) leads to $C_{i,j} = (1/4)\{C_{i-1,j} + C_{i+1,j} + C_{i,j-1} + C_{i,j+1}\}$ meaning that the drug flux from the blood vessel into the tissue becomes zero. Drug diffusion among micro-compartments on the grid with periodic boundary conditions occurs as described in Chapter 3 and [1].

TNF-neutralizing drugs differ in their dosing regimens and pharmacokinetic properties, including route of administration (intravenous versus subcutaneous), drug half-lives in plasma and the blood concentration peak-trough ratios. Etanercept and adalimumab are, for example, administered in frequent (weekly or bi-weekly) small subcutaneous doses that rapidly lead to smooth and uniform concentration-time profiles at steady state [2]. This is consistent with assuming a constant blood concentration (C_p = constant) for these drugs in our model. However, infliximab is dosed every eight weeks in relatively large intravenous boluses that result in wide fluctuations in blood concentration of the drug [2,3]. To study the effect of these fluctuations on the function of a granuloma, we also simulate infliximab-mediated TNF neutralization in which blood concentration of infliximab follows a pharmacokinetic model ($C_p = f(t)$) presented by St Clair *et al* [4].

D.2 Neutralization of TNF by TNF inhibitors

Once TNF inhibitors penetrate from blood into the lung tissue, they can bind TNF and thus block TNF-mediated signaling in a granuloma. To analyze the effects of TNF-neutralizing drugs with various TNF binding properties, including TNF/drug association and dissociation kinetics, stoichiometry of binding as well as drug ability to bind mTNF versus sTNF on immunity to Mtb, we define three hypothetical classes of TNF inhibitors (Fig. 6.1C). These classes are defined based on TNF binding characteristics reported for human TNF-neutralizing drugs (including infliximab, adalimumab, etanercept and certolizumab) as described in Methods in the main text. An sTNF molecule with either one, two or three drug molecules bound is neutralized and not able to bind TNFR1 or TNFR2. This assumption is consistent with experimental data indicating that only trimeric TNF is biologically active and that both monomeric TNF and artificially prepared dimeric TNF do not efficiently trigger signaling in cells [5,6]. TNF/drug interactions for different classes of TNF inhibitors are modeled based on mass action kinetics. The reactions and equations are listed in Table D.2. These equations are solved in combination with TNF/TNFR kinetic equations from the base model presented in Chapter 3.

D.3 TNF inhibitors with apoptotic and cytolytic activities

Some TNF inhibitors are reported to induce apoptosis or complement-dependent cytotoxicity (CDC) in TNF-expressing cells. This results from drug binding to mTNF and cross-linking of mTNF [7,8]. Based on descriptions presented for three classes of TNF

inhibitors, only a Class 3 TNF inhibitor has the potential to cross-link mTNF and mediate cell death.

We describe drug-induced cell death for each individual TNF-expressing cell (including infected, chronically infected and activated macrophages and T cells), as a Poisson process with a probability determined within each time-step (Δt), based on a Poisson rate parameter that is a function of the drug-induced death rate constant (k_{apopt}), the concentration of mTNF molecules that are bound to more than one drug molecule [mTNF/(drug)$_{>1}$], and the concentration threshold for [mTNF/(drug)$_{>1}$] for inducing apoptosis or CDC ($\tau_{death\text{-}Drug}$):

$$P_{death-Drug} = \begin{cases} 0 & ; [mTNF/(drug)_{>1}] < \tau_{death-Drug} \\ 1 - e^{-k_{apopt}([mTNF/(drug)_{>1}]-\tau_{death-Drug})\Delta t} & ; [mTNF/(drug)_{>1}] \geq \tau_{death-Drug} \end{cases} \quad \text{(D.3)}$$

This description for the drug-induced cell death is in line with the approach we used to describe TNF-induced apoptosis, one of the processes that serve as the link between the single-cell/molecular scale TNF/TNFR kinetics and the cellular/tissue scale dynamics in the baseline model (Chapter 3) [1]. We assume that drug-induced death events, apoptosis and CDC, occur with equal chances. The difference between the consequences of apoptosis and CDC is only significant if the target cell is an infected or a chronically infected macrophage. Cell lysis as a result of CDC leads to the release of intracellular bacteria to the environment similarly to death due to age or bursting of a chronically infected macrophage as described in Chapter 3 [1]. However, drug-induced apoptosis, similarly to TNF-induced apoptosis, kills a fraction (we assume half) of intracellular bacteria [9].

D.4 Parameter estimation

We estimated values of the base model parameters, including ABM parameters, single-cell molecular scale TNF/TNFR kinetic parameters as well as TNF response (NF-κB activation and apoptosis) parameters based on available experimental data or via uncertainty analysis as described in Chapter 3 and [1]. TNF inhibitor-associated parameter values are estimated based on literature data on human TNF-neutralizing drugs and are listed in Table D.1. Blood concentrations of TNF inhibitors are consistent with average steady state blood concentrations reported for human TNF-neutralizing drugs (C_p = constant) [2]. When pharmacokinetic fluctuations of the concentration of a drug in blood is particularly of interest, we use $C_p = f(t)$; where $f(t)$ is the blood concentration-time profile as reported in literature for the drug.

D.5 Sensitivity analysis

When computational models include parameters describing a large number of known biological processes, it is critical to understand the role that each of these parameters plays in determining output. Sensitivity analysis is a technique to identify critical parameters of a model and quantify how input uncertainty impacts model outputs. Latin hypercube sampling (LHS) is an algorithm that allows multiple parameters to be varied and sampled simultaneously in a computationally efficient manner [10]. We have previously used LHS sensitivity analysis as described in [1] to analyze the impact of base granuloma model parameter values on outputs, including bacterial and immune cell numbers, TNF concentration, granuloma size and caseation. Here, we use sensitivity analysis to investigate whether the significance of the base model parameters in the

presence of TNF inhibitors in the tissue differs from their significance in the absence of TNF inhibitors. We use base model parameter ranges as specified in Chapter 3 and [1] for sensitivity analysis. Results of sensitivity analysis will help us identify critical immune processes that impact granuloma function following anti-TNF treatments. The correlation of model outputs with each parameter is quantified via calculation of a partial rank correlation coefficient (PRCC). PRCC values vary between -1 (perfect negative correlation) and +1 (perfect positive correlation) and can be differentiated based on *p*-values derived from Student's *t* test. LHS simulations sampled each parameter 250 times. Each sampled parameter set was run twice and averages of the outputs were used to calculate PRCC values. The choice of the number of simulations is determined by the desired significance level for the PRCC [10,11]. Here, 250 runs imply that PRCC values above +0.24 or below -0.24 are significantly different from zero ($p < 0.001$).

D.6 Computer simulations and visualization

The model was implemented in C++. We use Qt, a C++ framework for developing cross-platform applications with a graphical user interface (GUI), to visualize and track different aspects of the granuloma, including the structure and molecular concentration gradients, as it forms and is maintained. Simulations can be run with or without graphical visualization. Simulations were run on Linux and Mac operating systems.

Table D.1 Model parameters associated with TNF neutralization reactions, definitions, and values.

Parameter	Parameter description	Value	Reference
D_{drug} (cm^2/s) *	Diffusion coefficient of drug	2.3×10^{-8}	[12,13]
k_c (cm/s) †	Drug permeability in the lung tissue	1.1×10^{-8}-1.1×10^{-7}	[14]
C_p (M)	Blood concentration of the drug	1.25×10^{-8} (etanercept) 3.67×10^{-8} (adalimumab) 7.5×10^{-8} (infliximab)	[2]
$k_{on\_TNF/Drug}$ ($M^{-1}s^{-1}$)	TNF/drug association rate constant	2.6×10^{5} (etanercept) 1.33×10^{5} (adalimumab) 5.7×10^{4} (infliximab)	[15,16]
$k_{off\_TNF/Drug}$ (s^{-1})	TNF/drug dissociation rate constant	1.3×10^{-3} (etanercept) 7.31×10^{-5} (adalimumab) 1.1×10^{-4} (infliximab)	[15,16]
k_{deg_Drug} (s^{-1})	Drug degradation rate constant	1×10^{-6}	[3]
k_{deg} (s^{-1})	sTNF degradation rate constant	4.58×10^{-4}	[17]
k_{TACE} (s^{-1})	Rate constant for TNF release by TACE activity	4.4×10^{-4} (macrophages) 4.4×10^{-5} (T cells)	[18-22]
$k_{death\text{-}Drug} = k_{apopt}$ ($(\#/cell)^{-1}s^{-1}$)	Rate constant for drug-induced cell death and TNF-induced apoptosis	1.33×10^{-9}	Estimated [1]
$\tau_{death\text{-}Drug}$ (#/cell)	Concentration threshold for drug-induced cell death	5-80	Estimated

* Diffusion coefficient of the drug in tissue/granuloma was estimated in line with estimates for diffusible factors of similar molecular weight in tumors [12,13].

† Drug permeability into lung tissue was estimated based on estimated tissue:blood concentration ratios for most antibodies reported to be in the range of 0.1-0.5 [14].

Table D.2 Definition of species involved in TNF neutralization, reactions, their rates (r_i) and model equations.

Membrane-bound reaction species		***Soluble reaction species***	
$mTNF$	Membrane-bound TNF	$sTNF$	Extracellular soluble TNF
$mTNF/(drug)_1$	1:1 mTNF/drug complex	$Drug$	TNF-neutralizing drug
$mTNF/(drug)_2$	1:2 mTNF/drug complex	$sTNF/(drug)_1$	1:1 sTNF/drug complex
$mTNF/(drug)_3$	1:3 mTNF/drug complex	$sTNF/(drug)_2$	1:2 sTNF/drug complex
		$sTNF/(drug)_3$	1:3 sTNF/drug complex

TNF neutralization reactions		
1*	$mTNF + Drug \leftrightarrow mTNF/(drug)_1$	$r_1 = k_{on\_TNF/Drug}[mTNF][Drug] - k_{off\_TNF/Drug}[mTNF/(drug)_1]$
2†	$mTNF/(drug)_1 + Drug \leftrightarrow mTNF/(drug)_2$	$r_2 = k_{on\_TNF/Drug}[mTNF/(drug)_1][Drug] - k_{off\_TNF/Drug}[mTNF/(drug)_2]$
3	$mTNF/(drug)_2 + Drug \leftrightarrow mTNF/(drug)_3$	$r_3 = k_{on\_TNF/Drug}[mTNF/(drug)_2][Drug] - k_{off\_TNF/Drug}[mTNF/(drug)_3]$
4	$mTNF/(drug)_1 \rightarrow sTNF/(drug)_1$	$r_4 = k_{TACE}[mTNF/(drug)_1]$
5	$mTNF/(drug)_2 \rightarrow sTNF/(drug)_2$	$r_5 = k_{TACE}[mTNF/(drug)_2]$
6	$mTNF/(drug)_3 \rightarrow sTNF/(drug)_3$	$r_6 = k_{TACE}[mTNF/(drug)_3]$
7	$sTNF + Drug \leftrightarrow sTNF/(drug)_1$	$r_7 = k_{on\_TNF/Drug}[sTNF][Drug] - k_{off\_TNF/Drug}[sTNF/(drug)_1]$
8	$sTNF/(drug)_1 + Drug \leftrightarrow sTNF/(drug)_2$	$r_8 = k_{on\_TNF/Drug}[sTNF][sTNF/(drug)_1] - k_{off\_TNF/Drug}[sTNF/(drug)_2]$
9	$sTNF/(drug)_2 + Drug \leftrightarrow sTNF/(drug)_3$	$r_9 = k_{on\_TNF/Drug}[sTNF][sTNF/(drug)_2] - k_{off\_TNF/Drug}[sTNF/(drug)_3]$
10	$sTNF/(drug)_1 \rightarrow Drug$ (sTNF degradation)	$r_{10} = k_{deg}[sTNF/(drug)_1]$
11	$sTNF/(drug)_2 \rightarrow 2Drug$ (sTNF degradation)	$r_{11} = k_{deg}[sTNF/(drug)_2]$
12	$sTNF/(drug)_3 \rightarrow 3Drug$ (sTNF degradation)	$r_{12} = k_{deg}[sTNF/(drug)_3]$
13	$sTNF/(drug)_1 \rightarrow degradation$	$r_{13} = k_{deg\_Drug}[sTNF/(drug)_1]$
14	$sTNF/(drug)_2 \rightarrow degradation$	$r_{14} = k_{deg\_Drug}[sTNF/(drug)_2]$
15	$sTNF/(drug)_3 \rightarrow degradation$	$r_{15} = k_{deg\_Drug}[sTNF/(drug)_3]$
16	$Drug \rightarrow degradation$	$r_{16} = k_{deg\_Drug}[Drug]$

Model equations for TNF neutralization-associated reactions ‡

$$\frac{\partial[mTNF]}{\partial t} = -r_1$$

$$\frac{\partial[mTNF/(drug)_1]}{\partial t} = r_1 - r_2 - r_4$$

$$\frac{\partial[mTNF/(drug)_2]}{\partial t} = r_2 - r_3 - r_5$$

$$\frac{\partial[mTNF/(drug)_3]}{\partial t} = r_3 - r_6$$

$$\frac{\partial[sTNF]}{\partial t} = -r_7$$

$$\frac{\partial[sTNF/(drug)_1]}{\partial t} = (\frac{\rho}{N_{av}})r_4 + r_7 - r_8 - r_{10} - r_{13}$$

$$\frac{\partial[sTNF/(drug)_2]}{\partial t} = (\frac{\rho}{N_{av}})r_5 + r_8 - r_9 - r_{11} - r_{14}$$

$$\frac{\partial[sTNF/(drug)_3]}{\partial t} = (\frac{\rho}{N_{av}})r_6 + r_9 - r_{12} - r_{15}$$

$$\frac{\partial[Drug]}{\partial t} = -(\frac{\rho}{N_{av}})(r_1 + r_2 + r_3) - r_7 - r_8 - r_9 + r_{10} + 2r_{11} + 3r_{12} - r_{16}$$

* Drug binding to mTNF is only relevant to Class 2 and Class 3 TNF-neutralizing drugs.

† Sequential binding of drug to sTNF and mTNF is only relevant to Class 3 TNF neutralizing drugs.

‡ When a membrane-bound molecule releases to the extracellular space (i.e. the micro-compartment occupied by the cell), or when a soluble molecule binds to the cell membrane, a scaling factor (ρ/N_{av}) is required, where ρ is the cell density in the micro-compartment and can be computed as $(dx)^{-3}$ assuming that each micro-compartment is a cube of side dx, and N_{av} is the Avogadro's number.

Table D.3 PRCC values for the LHS sensitivity analysis of the effect of cellular/tissue scale and TNF-associated molecular scale parameters on model outcomes during treatment with etanercept at a permeability coefficient of $k_c = 1.1\times10^{-7}$ cm/s (Only parameters with significant PRCC values are indicated).

	Selected model outputs			
Model parameters	Total number of bacteria	Average sTNF concentration	Granuloma size	Caseation
δ_{chem}	+0.37	+0.35	+0.33	+0.33
T_{moveM}	-0.49	-0.50	-0.45	-0.37
$\tau_{recTgam}$	+0.44	+0.23		
T_{recr}				-0.29
α_{Bi}	+0.23	+0.24	+0.27	+0.57
δ_{TNF}				
$k_{synthMac}$	-0.51	-0.33	-0.39	
$k_{synthTcell}$			+0.27	
$k_{TACEMac}$				
K_{d1}		+0.30	+0.25	
k_{apop}				
$k_{NF\text{-}\kappa B}$	-0.32	-0.31	-0.29	-0.34
$\tau_{NF\text{-}\kappa B}$	+0.27	+0.21		+0.22

Table D.4 PRCC values for the LHS sensitivity analysis of the effect of cellular/tissue scale and TNF-associated molecular scale parameters on model outcomes during treatment with infliximab at a permeability coefficient of $k_c = 1.1\times10^{-7}$ cm/s (Only parameters with significant PRCC values are indicated).

	Selected model outputs			
Model parameters	Total number of bacteria	Average sTNF concentration	Granuloma size	Caseation
δ_{chem}	+0.34	+0.32	+0.32	+0.22
T_{moveM}	-0.36	-0.39	-0.37	+0.24
$\tau_{recTgam}$	+0.26	+0.27	+0.28	
T_{recr}				
α_{Bi}	+0.39	+0.36	+0.42	+0.55
δ_{TNF}				
$k_{synthMac}$	-0.49		-0.39	-0.37
$k_{synthTcell}$				
$k_{TACEMac}$	+0.24	+0.44	+0.32	+0.29
K_{d1}		+0.24		
k_{apop}	-0.27	-0.25	-0.24	-0.23
$k_{NF\text{-}\kappa B}$	-0.19			
$\tau_{NF\text{-}\kappa B}$				

D.7 References

1. Fallahi-Sichani M, El-Kebir M, Marino S, Kirschner DE, Linderman JJ (2011) Multiscale computational modeling reveals a critical role for TNF-{alpha} receptor 1 dynamics in tuberculosis granuloma formation. J Immunol 186: 3472-3483.

2. Nestorov I (2005) Clinical pharmacokinetics of TNF antagonists: How do they differ?. Semin Arthritis Rheum 34: 12-18.

3. Tracey D, Klareskog L, Sasso EH, Salfeld JG, Tak PP (2008) Tumor necrosis factor antagonist mechanisms of action: A comprehensive review. Pharmacol Ther 117: 244-279.

4. St Clair EW, Wagner CL, Fasanmade AA, Wang B, Schaible T, et al. (2002) The relationship of serum infliximab concentrations to clinical improvement in rheumatoid arthritis: Results from ATTRACT, a multicenter, randomized, double-blind, placebo-controlled trial. Arthritis Rheum 46: 1451-1459.

5. Menart V, Gaberc-Porekar V, Jevsevar S, Pernus M, Meager A, et al. (2000) Early events in TNFa-p55 receptor interations--experiments with TNF dimers. Pflugers Arch 439: R113-5.

6. Corti A, Fassina G, Marcucci F, Barbanti E, Cassani G (1992) Oligomeric tumour necrosis factor alpha slowly converts into inactive forms at bioactive levels. Biochem J 284 (Pt 3): 905-910.

7. Wong M, Ziring D, Korin Y, Desai S, Kim S, et al. (2008) TNFalpha blockade in human diseases: Mechanisms and future directions. Clin Immunol 126: 121-136.

8. Dinarello CA (2005) Differences between anti-tumor necrosis factor-alpha monoclonal antibodies and soluble TNF receptors in host defense impairment. J Rheumatol Suppl 74: 40-47.

9. Oddo M, Renno T, Attinger A, Bakker T, MacDonald HR, et al. (1998) Fas ligand-induced apoptosis of infected human macrophages reduces the viability of intracellular mycobacterium tuberculosis. J Immunol 160: 5448-5454.

10. Blower SM, Dowlatabadi H (1994) Sensitivity and uncertainty analysis of complex models of disease transmission: An HIV model, as an example. Int Stat Rev 62: 229-243.

11. Marino S, Hogue IB, Ray CJ, Kirschner DE (2008) A methodology for performing global uncertainty and sensitivity analysis in systems biology. J Theor Biol 254: 178-196.

12. Nugent LJ, Jain RK (1984) Extravascular diffusion in normal and neoplastic tissues. Cancer Res 44: 238-244.

13. Pluen A, Boucher Y, Ramanujan S, McKee TD, Gohongi T, et al. (2001) Role of tumor-host interactions in interstitial diffusion of macromolecules: Cranial vs. subcutaneous tumors. Proc Natl Acad Sci U S A 98: 4628-4633.

14. Lobo ED, Hansen RJ, Balthasar JP (2004) Antibody pharmacokinetics and pharmacodynamics. J Pharm Sci 93: 2645-2668.

15. Kim MS, Lee SH, Song MY, Yoo TH, Lee BK, et al. (2007) Comparative analyses of complex formation and binding sites between human tumor necrosis factor-alpha and its three antagonists elucidate their different neutralizing mechanisms. J Mol Biol 374: 1374-1388.

16. Song MY, Park SK, Kim CS, Yoo TH, Kim B, et al. (2008) Characterization of a novel anti-human TNF-alpha murine monoclonal antibody with high binding affinity and neutralizing activity. Exp Mol Med 40: 35-42.

17. Cheong R, Bergmann A, Werner SL, Regal J, Hoffmann A, et al. (2006) Transient IkappaB kinase activity mediates temporal NF-kappaB dynamics in response to a wide range of tumor necrosis factor-alpha doses. J Biol Chem 281: 2945-2950.

18. Fallahi-Sichani M, Schaller MA, Kirschner DE, Kunkel SL, Linderman JJ (2010) Identification of key processes that control tumor necrosis factor availability in a tuberculosis granuloma. PLoS Comput Biol 6: e1000778.

19. Newton RC, Solomon KA, Covington MB, Decicco CP, Haley PJ, et al. (2001) Biology of TACE inhibition. Ann Rheum Dis 60 Suppl 3: iii25-32.

20. Crowe PD, Walter BN, Mohler KM, Otten-Evans C, Black RA, et al. (1995) A metalloprotease inhibitor blocks shedding of the 80-kD TNF receptor and TNF processing in T lymphocytes. J Exp Med 181: 1205-1210.

21. Solomon KA, Covington MB, DeCicco CP, Newton RC (1997) The fate of pro-TNF-alpha following inhibition of metalloprotease-dependent processing to soluble TNF-alpha in human monocytes. J Immunol 159: 4524-4531.

22. Bueno C, Rodriguez-Caballero A, Garcia-Montero A, Pandiella A, Almeida J, et al. (2002) A new method for detecting TNF-alpha-secreting cells using direct-immunofluorescence surface membrane stainings. J Immunol Methods 264: 77-87.

Appendix E

Supplementary information for Chapter 7

E.1 Monte Carlo (MC) simulation procedure

The two-dimensional cell membrane surface was modeled as a 700 by 700 triangular lattice with periodic boundary conditions and a lattice spacing of 0.5 nm. Low diffusivity regions with uniform distribution and defined surface area (2-30% of the cell membrane) were designated as raft regions on the lattice. Simulations were initiated by placing receptor molecules (hexagons with a diameter of 5 nm, the approximate diameter of a single GPCR) randomly on the lattice. Placement on all lattice sites, whether in raft or non-raft regions, was equally likely. No two molecules were allowed to occupy the same lattice site. Thus, if the selected site was occupied, a new random lattice site was selected. Simulations were then run by random choosing of a single receptor and probability-based selection of an event (movement, dimerization, monomerization, ligand binding or unbinding) to occur at each time step. Possible events are limited to movement, dimerization and monomerization in the absence of ligand. The time step of each simulation was calculated from the fastest event in the system, either a reaction event or a move event controlled by diffusivity, and total number of receptors. Thus, the inverse of the rate constant for the fastest event, divided by total number of receptors, was used as the MC time step. The rate constant for move event was calculated as $k_{move} = 6D/l^2$; where l is the triangular lattice spacing and D is the diffusion coefficient. To ensure that the model results are independent of MC time step, simulations were run with time steps

smaller than the MC time step and results were shown to be indistinguishable. Simulations were written in C++ and were run on a Mac Pro with 2 × 2.66 GHz Dual-Core Intel Xeon processors.

During the simulation, receptors were randomly picked at each time step to react (dimerization, monomerization, ligand binding or unbinding) and move based on probability of these events. The probability of dimerization (and monomerization) was the same for all ligand-bound receptors but different from unligated ones. The probability of movement was determined by the location of receptor (raft or non-raft region). Details of the simulation procedure during a single time step of simulation are described below.

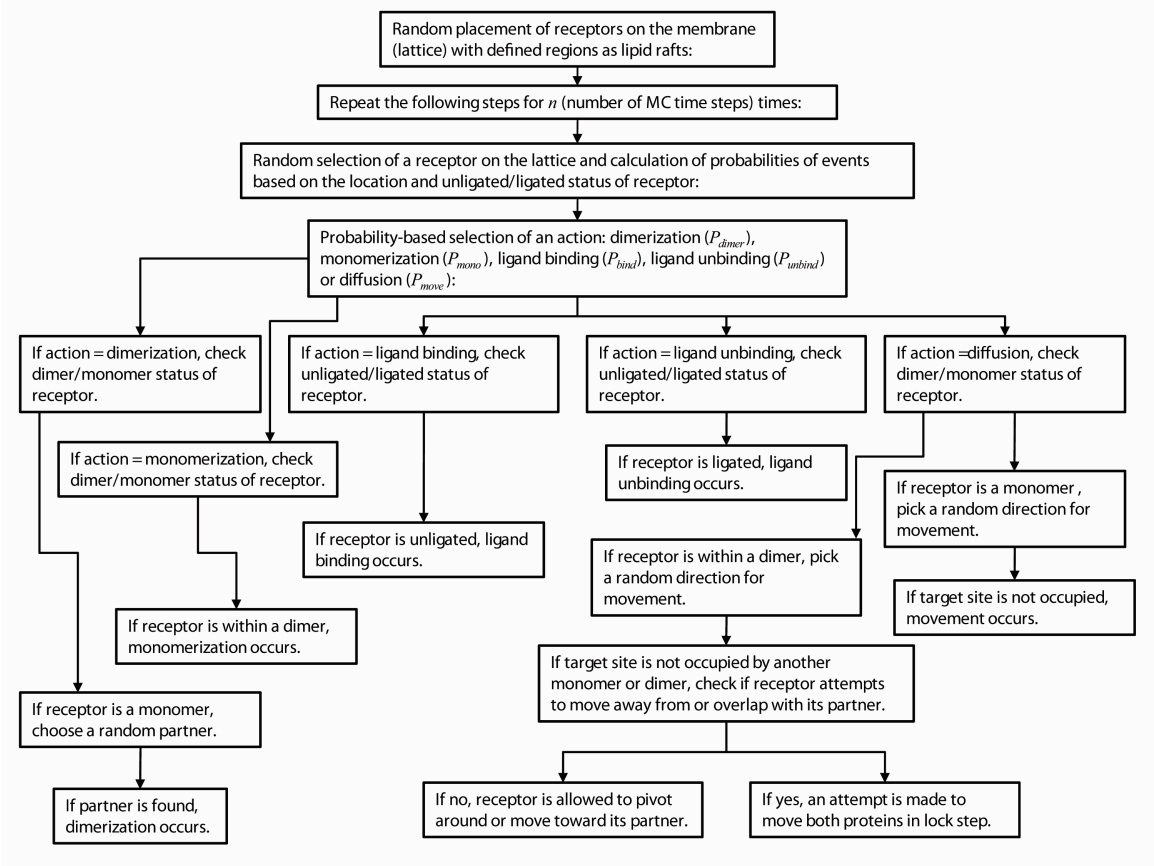

With a discrete-time model like the one used here, the dimerization and monomerization reactions can be modeled as Poisson processes. As a result, the probabilities of dimerization and monomerization can be derived from the reaction rate constants k_{dimer} and k_{mono} using a Poisson distribution. With sufficiently small time-steps (Δt), this relationship simplifies such that the probability of a reaction is approximately proportional to the reaction rate constant as shown below [1].

$$P_{mono} = 1 - e^{-k_{mono}\Delta t} \approx k_{mono}\Delta t \tag{E.1}$$

$$P_{\dim er} = 1 - e^{-k_{\dim er}\Delta t} \approx k_{\dim er}\Delta t \tag{E.2}$$

Similarly, the probabilities of ligand binding to receptors and ligand unbinding from receptors can be calculated using the following equations:

$$P_{bind} = 1 - e^{-k_f[L]\Delta t} \approx k_f[L]\Delta t \tag{E.3}$$

$$P_{unbind} = 1 - e^{-k_r\Delta t} \approx k_r\Delta t \tag{E.4}$$

where, $[L]$ is the ligand concentration and k_f and k_r are ligand/receptor association and dissociation rate constants, respectively.

The probability of a diffusion event, P_{move}, was calculated using the translational diffusion coefficient D_t of the membrane for GPCRs. For a single particle exhibiting Brownian diffusion on a triangular lattice, the probability of a particle moving at least one lattice spacing, l, in one iteration time step, Δt, can be expressed as:

$$P_{move} = 1 - \exp\left(\frac{-6D_t\Delta t}{l^2}\right) \approx \frac{6D_t\Delta t}{l^2} \tag{E.5}$$

Thus, at small time step values, the probability of a move is nearly proportional to the diffusion coefficient of the cell membrane which was assumed to be smaller for the lipid rafts compared with the non-raft region.

E.2 Receptor phosphorylation can be regulated by lipid rafts

Using the ODE model (Fig. 7.2B) we also asked whether dimerization-mediated receptor clustering in lipid rafts affects receptor phosphorylation. Receptor clustering into lipid rafts with a high concentration of G-protein relative to the non-raft region ($r = 0.8$) may enhance their diffusion-limited phosphorylation by kinases (GRKs) recruited by βγ-subunits of G-proteins. However, the level of enhancement in the number of phosphorylated receptors in the cell membrane depends on the rate of receptor internalization (Fig. E.5). Recent experiments have shown that dimerization of the thyrotropin-releasing hormone (TRH) receptor potentiates hormone-dependent GRK-mediated receptor phosphorylation [2]. Although disruption of the plasma membrane integrity by cholesterol depletion has been reported to impair the effectiveness of TRH signaling via G-proteins [3], no data are available on how dimerization of TRH receptors influences their organization on the membrane. Our combined model of receptor dimerization and G-protein signaling can connect these experimental observations and predicts the increase in the level of receptor phosphorylation due to dimerization-mediated enrichment of receptors in lipid rafts.

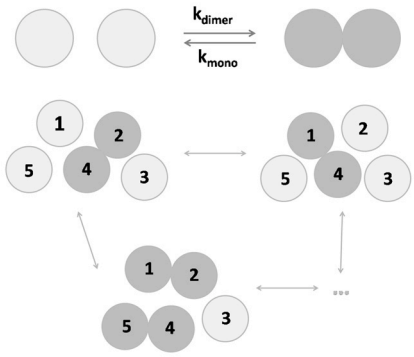

Fig. E.1 Formation of oligomers via diffusion-limited partner switching.

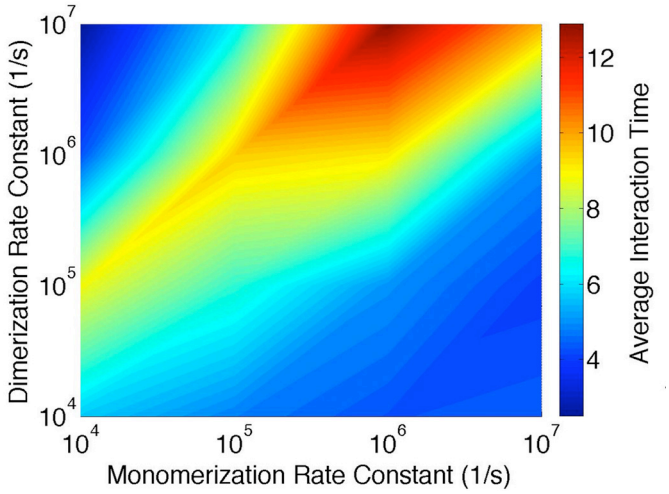

Fig. E.2 Variation of average receptor-receptor interaction time with k_{mono} and k_{dimer}. MC Simulations were run with receptor density of 18% and membrane diffusion coefficient of 10^{-9} cm^2/s. Dimensionless average interaction time is indicated by color.

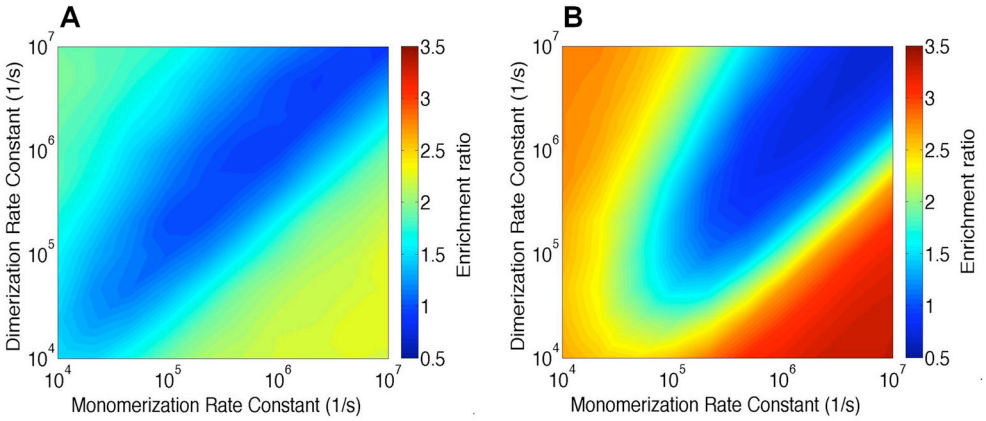

Fig. E.3 Predicted variation of enrichment ratio with k_{mono} and k_{dimer} for different values of diffusion coefficient in lipid raft and non-raft regions of the cell membrane. Diffusion coefficients in lipid raft and non-raft regions are respectively (A) 10^{-11} cm^2/s and 10^{-10} cm^2/s, and (B) 10^{-11} cm^2/s and 10^{-9} cm^2/s. Simulations were run to equilibrium with receptor density of 18%. In this set of simulations, rafts make up 20% of the simulated membrane and raft diameter is 50 nm.

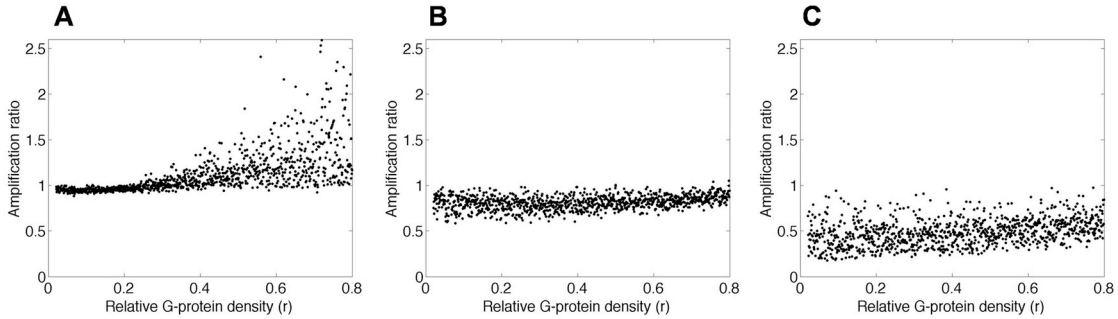

Fig. E.4 Scatter plots for the effect of relative G-protein density (*r*) on the model outcome, signal amplification ratio, at three levels of lipid raft coverage: (A) 2%, (B) 10%, and (C) 30%. Ranges for all other parameters are indicated in Table 7.1. The largest values of receptor dimerization-dependent enrichment ratio (found from MC simulations) were used.

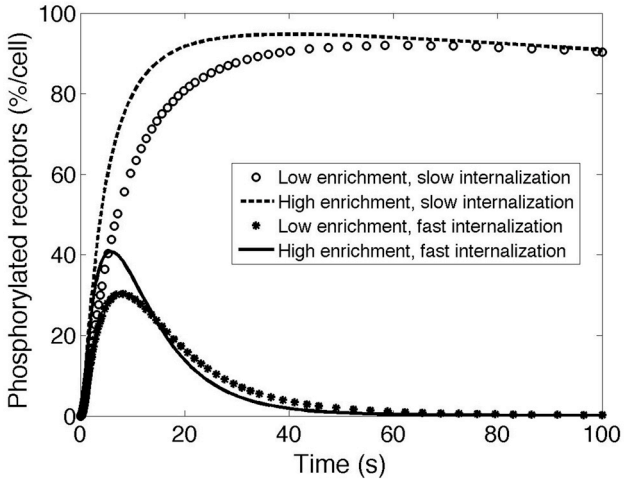

Fig. E.5 Predicted effect of receptor localization within lipid rafts on the number of phosphorylated receptors in the membrane. Results are shown for two different values of receptor enrichment ratio (2.5 and 4.5 for low and high level of enrichment, respectively) based on MC simulation results. Receptor clustering in lipid rafts enhances their G-protein dependent phosphorylation. k_{int} for the fast and slow receptor internalization was assumed to be 10^{-1} s^{-1} and 10^{-3} s^{-1} respectively. Relative G-protein density in lipid rafts, *r*, was assumed to be 0.8. Membrane diffusivities in the raft and non-raft regions and lipid raft size and coverage are the same as Fig. 7.6A. Other parameter values are as listed in Table 7.1.

E.3 Reference

1. Rowley RL (1994) Statistical mechanics for thermophysical property calculations. Englewood Cliffs, NJ: Prentice-Hall.

2. Song GJ, Jones BW, Hinkle PM (2007) Dimerization of the thyrotropin-releasing hormone receptor potentiates hormone-dependent receptor phosphorylation. Proc Natl Acad Sci U S A 104: 18303-18308.

3. Ostasov P, Bourova L, Hejnova L, Novotny J, Svoboda P (2007) Disruption of the plasma membrane integrity by cholesterol depletion impairs effectiveness of TRH receptor-mediated signal transduction via G(q)/G(11)alpha proteins. J Recept Signal Transduct Res 27: 335-352.